Measurements of DiLepton Channels at LHCb

Jonathan Plews

A thesis presented for the degree of
Doctor of Philosophy

Particle Physics Group
School of Physics and Astronomy
The University of Birmingham

22nd December 2021

UNIVERSITY OF
BIRMINGHAM

University of Birmingham Research Archive

e-theses repository

This unpublished thesis/dissertation is copyright of the author and/or third parties. The intellectual property rights of the author or third parties in respect of this work are as defined by The Copyright Designs and Patents Act 1988 or as modified by any successor legislation.

Any use made of information contained in this thesis/dissertation must be in accordance with that legislation and must be properly acknowledged. Further distribution or reproduction in any format is prohibited without the permission of the copyright holder.

Abstract

Measurements of the Drell-Yan cross-section provide insight into the structure of the proton. Measurements are made at LHCb, via the dimuon channel, as a double differential cross-section with respect to dimuon mass and rapidity, and with respect to dimuon mass and transverse momentum in the ranges $4 < m_{\mu\mu} < 120\,\text{GeV}$, $2.5 < y < 4.5$ and $1 < p_{\text{T}} < 500\,\text{GeV}$. Dimuon candidates are selected from $1.63\,\text{fb}^{-1}$ of data taken at LHCb in 2016 and fit as a function of minimum muon $\sqrt{\chi^2_{\text{IP}}}$ using templates for components of the signal and the relevant backgrounds.

A search for the lowest spin-triplet state of true muonium ($\mu^+\mu^-$) is also proposed. True muonium offers an opportunity to test standard model physics in a purely muonic system. It is suggested that decays of $\mathcal{TM} \to e^+e^-$ could be detected at LHCb, produced from the decays of $\eta \to \gamma^*\gamma$, where γ^* mixes with $\mathcal{TM}$. Two searches are proposed, an inclusive search where only the dielectron pair is selected and an exclusive search where the photon is also selected and the η meson is reconstructed. It is shown that in order to discover true muonium to 5σ significance, LHCb would be required to achieve reconstruction efficiencies of $\varepsilon_{e^+e^-} > 20\%$ and $\varepsilon_{\gamma e^+e^-} > 12\%$, within the fiducial acceptance.

Author's Contribution

For the Drell-Yan cross-section measurement analysis outlined in chapter 4, I have worked on the data selection, template production, template fitting and yield uncertainties. The estimation of the selection efficiencies were performed by Laurent Dufour, while the track reconstruction corrections were obtained by Stephen Farry. Fiducial corrections to previous analyses for the resonance cross-checks were performed by Philip Ilten. Stephen Farry made the final cross-section plots, while the theoretical predictions were obtained by Katharina Müller.

For the study of a potential search for true muonium, outlined in chapter 5, I performed simulations of true muonium production using Pythia and cross-section predictions made in previous works. I also modified an existing VELO material tool to calculate the material distances traversed by true muonium candidates. I used these, with the dissociation cross-section predicted in previous works, to estimate the loss of signal due to dissociation. The background predictions and efficiencies required for a significant discovery were calculated by Xabier Cid Vidal, Philip Ilten, Brian Shuve and Yotam Soreq.

Acknowledgements

I would like to thank Phil Ilten for being an excellent supervisor with an inordinate wealth of knowledge, it has been a great experience working with you.

I would also like to acknowledge the help of Laurent Dufour, Steve Farry and Katharina Müller, with whom I have worked closely on the Drell-Yan analysis for the majority of my PhD.

Thanks is also given to Nigel Watson for his endless supply of advice and for making himself available, even at weekends. Also in the Birmingham LHCb group, I would like to thank Simone Bifani for his suggestions and expertise, as well as Tim, Nathaniel, Kristian, Ryan, Naomi and Paul, with whom I shared an office, for their companionship and sanity checks.

Finally I would like to thank my family and friends for supporting me through the last four years.

To my parents
For helping me through the hardest times

Contents

List of Figures

List of Tables

Glossary

VELO	Vertex Locator, the first detector at LHCb, for precisely resolving primary vertices
RF Foil	Aluminium casing around the VELO to protect sensors from radio frequency induced heating
TT	Tracker Turicensis, the first tracking station using silicon microstrip technology
IT	Inner Tracker, the inner parts of tracking stations T1-T3 which use silicon microstrip technology
OT	Outer Tracker, the outer parts of tracking stations T1-T3 which use straw-tubes
RICH	Ring Imaging Cherenkov detectors used for particle identification
ECAL	Electromagnetic Calorimeter, for measuring the energy of photons, electrons and pions
HCAL	Hadronic Calorimeter, for measuring the energy of heavier hadrons
MUON Chambers	Detectors used for identifying muon candidates
Level-0 Trigger	Hardware trigger used for quickly triggering events from partially reconstructed information
High Level Trigger	Software trigger used for triggering on more specific criteria
Turbo Stream	A data stream for rapidly selecting events that meet specific criteria online

PV	Primary vertex, the position of the proton-proton collision associated with the signal candidate
TIS	Triggered Independent of Signal, the event meets the criteria of the line but was triggered by something else
TOS	Triggered On Signal, the event meets the criteria of the line and triggered the readout
`ProbNNmu`	PID variable for muons, values from 0 to 1 returned by a neural network given kinematic information
`isMuon`	Boolean PID variable for muons
`isMuonTight`	Boolean PID variable for muons, more restrictive than `isMuon`
IP	Impact Parameter, the perpendicular distance between particle trajectory and the PV
DOCA	Distance Of Closest Approach between two particle trajectories

Chapter 1

Introduction

At the dawn of the twentieth century, atomic theory was almost universally accepted by the scientific community. However, cracks had already begun to appear in the indivisible nature of the atom. In 1897, Thomson's cathode ray experiments had identified the particle that would come to be known as the electron, raising questions about the distribution of electric charge in atoms [1]. The Geiger-Marsden gold foil experiments, 1908-1913, famously showed α particles being deflected by a dense positive charge at the centre of an atom, leading Rutherford to propose the atomic nucleus and the proton [2].

The first hints of quantum mechanics were examined at the same time. In 1900, Planck found that thermodynamic black-body problems could be resolved by the quantisation of light [3]. His work was expanded upon in 1905 by Einstein who explained the photoelectric effect by describing light as discrete quanta that would come to be known as photons [4]. Following the discovery of the proton, Bohr developed a rudimentary model of the hydrogen atom, explaining the Rydberg formula with discreet transitions between electron energy levels [5]. The issue of photons was finally resolved in 1923 by Compton, who performed scattering experiments showing light behaving as a particle with momentum [6].

In 1932 the apparent discrepancy between the charge and mass of heavier nuclei

was solved by the discovery of the neutron by Chadwick [7]. This raised further questions about the forces in the nucleus that must stop the protons repelling each other. In 1934, Yukawa proposed a nuclear force mediated by a "medium" particle, between an electron and a proton, which he called a meson [8]. He calculated that the meson should have a mass approximately 300 times that of the electron. It was not until 1947 that this was associated with the pion, which acts as the nuclear mediator in a low energy approximation [9].

The atomic model had looked fairly neat and complete. More complex ideas had appeared, such as the famous equation derived by Dirac in 1927, leading to the prediction of the existence of the positron and, by extension, antimatter [10, 11]. In addition, in 1932 Pauli proposed the existence of a very light-weight neutral particle to resolve the apparent non-conservation of energy in β decay, which Fermi dubbed the neutrino [12, 13]. The neutrino would not be directly detected until 1955, when the Cowan-Reines experiment detected anti-electron neutrinos produced by a nuclear reactor through inverse β decay [14].

With renewed interest in the field, the late 1940's and early 1950's would show that the picture was nowhere close to complete. This period saw the discovery of heavier particles in both cloud chamber experiments and novel collider experiments, later known as the K^0 and Λ and a host of others. Many of these "strange" particles had long measured lifetimes, suggesting that they decayed through a mechanism that was weaker than those previously observed. In 1953 Gell-Mann and Nishijima independently proposed a quantum number Gell-Mann called *strangeness* that was conserved in all interactions except for the weak interaction [15, 16].

Gell-Mann went on to order the newly discovered particles into multiplets according to their electric charge and strangeness, which he referred to as the Eightfold Way [17]. Similar to the way in which the periodic table allowed the prediction of new elements, the geometric pattern of the multiplets suggested the existence of a particle with a charge of -1 and a strangeness of -3, which was discovered in 1964,

later known as Ω^- [18].

Gell-Mann, and independently Zweig, expanded upon the Eightfold way by introducing the quark model where all baryons and mesons are constituted of *up*, *down* or *strange* quarks [19, 20]. In the same year, Greenberg proposed a new quantum number known as *colour charge*, to prevent baryons with three seemingly identical quarks from violating the Pauli exclusion principle [21].

The quark model was vindicated via deep inelastic scattering experiments performed at the Stanford Linear Accelerator Center (SLAC) from 1967 to 1973. The angle of electrons scattering inelastically off protons was measured, and an excess was found at large angle, indicating internal proton structure. The subsequent analysis confirmed that the proton has an internal structure [22].

The quark model was expanded following the discovery of the J/ψ meson in 1974, which was explained by the introduction of a fourth flavour of quark, subsequently known as *charm* [23, 24, 25]. This allowed for the expansion of the hadron multiplets and the prediction of a collection of *charmed* particles, the discovery of which provided compelling evidence for the quark model. With ever higher energy experiments, a similar course of events followed the discovery of the Υ meson in 1977 and the proposal of the *bottom* quark [26].

The neutrino sector had grown more complex in the 1960's. The Homestake experiment showed a deficit in the expected electron neutrino flux from nuclear reactions in the sun, giving rise to the solar neutrino problem [27]. Neutrinos were also found to have flavour when the muon neutrino was discovered in 1962 [28]. Hence, when the tau, τ, lepton was discovered at SLAC in 1975, it was expected to have a counterpart tau neutrino [29]. The solar neutrino problem was resolved when the Super-Kamiokande and Sudbury Neutrino Observatories found evidence for oscillations between neutrino flavours in late 1990's and early 2000's, requiring neutrinos to have mass [30, 31].

Experiments in the 1960's showed that charge-parity (CP) symmetry could be

broken in kaon decays. This was explained in 1974 by flavour changing neutral current loop mechanisms that required a third generation of quarks. With the discovery of the *bottom* quark, expectation of the discovery of the heavier *top* quark grew.

With the expansion of the table of elementary particles, many theories were proposed to explain how they behave. The description of three of the apparently fundamental forces using quantum fields led to composition of the Standard Model of particle physics which was developed in the 1960's and 70's. The model predicts six quarks in three generations, three charged leptons and three neutrinos. It also combines quantum electrodynamics, quantum chromodynamics and the weak field theory, as well as introducing the Higgs mechanism by which particles obtain mass [32]. These forces are propagated by intermediary bosons: the photon, gluon, $W^{\pm}$ and Z bosons, and the Higgs boson.

Evidence for the Standard Model has mounted in the following years. With the discovery of the gluon in 1978 [33], the $W^{\pm}$ and Z bosons in 1983 [34, 35], the *top* quark in 1995 [36] and the tau neutrino in 2000 [37], the twentieth century closed with the Standard Model as the most complete theory of elementary particle physics. The last particle in the model, the elusive Higgs boson, was discovered in 2012 by the ATLAS and CMS experiments at CERN [38, 39].

The Standard Model is not a complete description of the universe, however, and leaves loose ends to be tied in. The model does not give an explanation of gravitation or the baryon asymmetry in the universe. Astronomical observations suggest a "dark matter" that has led some to predict a "dark sector" of particles that only weakly interact with those in the Standard Model. As a result, the Standard Model is being rigorously tested to find the areas it does not accurately predict, which may be where new physics beyond the Standard Model could be discovered.

This thesis details the author's own contribution to this process as an analyst on the LHCb experiment at CERN. The following writing reports the measurement

of the production cross-section of dimuons via the Drell-Yan process and describes a proposed search for the bound state of a muon and antimuon, known as true muonium.

Chapter 2

Theory

2.1 The Standard Model

The Standard Model (SM) of particle physics is the most complete currently available theory of fundamental particles and the forces that govern their behaviour. The model describes mechanisms for three of the four known fundamental forces of physics, excluding only gravity. The Standard Model has been experimentally verified to high precision over a wide range of energy scales and processes, though it is clear that it is not the final picture and experimental work is ongoing to find areas where nature deviates from the model [40].

2.1.1 Fermions

The fundamental, point-like particles which exist in the Standard Model can be classified into two groups: fermions and bosons, shown in figure 2.1. Fermions are characterised by a half-integer unit of spin, the intrinsic angular momentum of the particle, and are defined by Fermi-Dirac statistics and the Pauli exclusion principle. The Standard Model defines three generations of particles, which are further divided into quarks and leptons, alongside their corresponding anti-particles.

The quarks are defined as *up*-type or *down*-type with an electric charge of $+\frac{2}{3}$

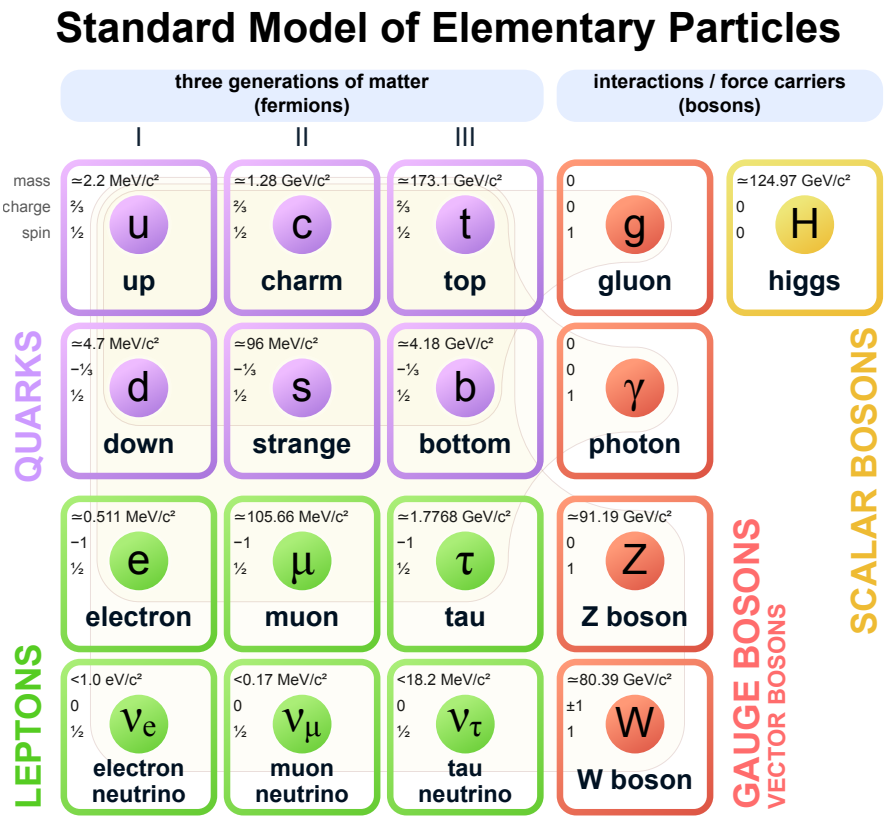

Figure 2.1: Chart of the elementary particles predicted by the Standard Model, showing mass, electric charge and spin [41].

and $-\frac{1}{3}$ respectively and a colour charge. Due to these charges, quarks can interact with both the electromagnetic and strong forces, as well as the weak force. Quarks are only observed in composite bound states with no net colour. These are known as hadrons and include baryons (qqq), mesons ($q\bar{q}$) as well as more exotic states known as tetra-quark ($q\bar{q}q\bar{q}$) and penta-quark ($qqqq\bar{q}$) states.

The Standard Model describes leptons in pairs of a charged lepton and corresponding chargeless neutrino. Neutrinos have a very small mass and were previously thought to be massless, though the mechanism through which this arises is currently uncertain. All leptons couple to the weak force, while charged leptons also couple to the electromagnetic force.

Higher generations of charged fermions have larger masses than the previous one. Heavier quarks and charged leptons have shorter lifetimes and decay to lighter

generations via the weak force, the only mechanism for flavour changing in the Standard Model.

2.1.2 Bosons

Bosons are characterised by an integer spin and follow Bose-Einstein statistics. The Standard Model defines four types of gauge boson of spin 1, which arise from the requirement that the quantum field theories are invariant under local gauge transformations. Gauge bosons mediate interactions between fundamental fermions, acting as a force carrier through a particle exchange, transferring energy and momentum from one fermion to another by exchanging a gauge boson.

The photon is the mediator for the electromagnetic force. They are massless, resulting in an infinite range but with a coupling strength that decreases with the distance between the two fermions. Photons couple with the electric charge of a particle, meaning that all fermions except neutrinos are affected by the electromagnetic force.

The strong force is mediated by gluons, which are also massless. Gluons hold both a colour and anti-colour charge which allows interactions with quarks and also gluon self interaction. Asymptotic freedom, where the coupling strength of the strong force decreases at larger energy scales, leads to the confinement of quarks and gluons in hadronic bound states.

The weak force is mediated by the exchange of $W^{\pm}$ and Z^0 bosons, which were discovered by the UA1 and UA2 experiments in 1983 and have masses of 80.4 and 91.2 GeV/c^2 respectively [34, 35]. It is this mass that gives the weak force a very short range. At high energies the weak force and electromagnetic force unify into a single force; this is known as Electroweak Unification.

The final component of the Standard Model is the Higgs Mechanism by which particles obtain mass. This involves the interaction of the $W^{\pm}$ and Z^0 bosons with a scalar field known as the Higgs Field. This interaction is then mediated by a massive

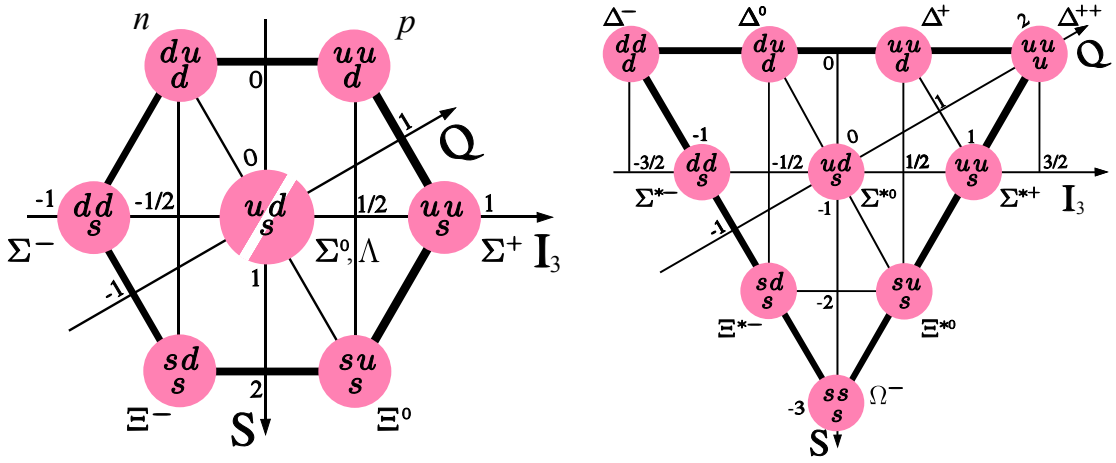

Figure 2.2: Allowed baryon states for up, down and strange quarks shown as multiplets for (left) $J = \frac{1}{2}$ and (right) $J = \frac{3}{2}$ [42, 43].

scalar boson known as the Higgs boson with a mass of 125 GeV/c^2. Interaction with this field also allows fermions to have mass.

2.1.3 Motivation for Colour Charge

The need for quarks to hold a colour charge arises from the interpretation of baryons as a three-quark bound state. The existence of flavour symmetric states with spin-$\frac{3}{2}$, such as the Ω^- (sss) discovered at BNL in 1964, seemingly violates the Pauli exclusion principle as the three quarks have the same flavour and spin. To resolve this an additional quantum number with three values is required.

These three values are labelled *red*, *green* and *blue* and are considered analogous to the electric charge, hence the term *colour charge*. Similarly, the behaviour of particles with colour charge is known as *chromodynamics*, analogous to electrodynamics. Quarks carry a single unit of colour charge, while antiquarks carry an *anti-colour*; *anti-red*, *anti-green* or *anti-blue*. Gluons, acting as exchange particles, carry both a colour charge and anti-colour.

The argument for colour manifests neatly in the *uds* baryon multiplets. Fermi-Dirac statistics require baryons to have a totally antisymmetric wavefunction under quark interchange. The total baryon wavefunction can be factorised into components

for space, spin and flavour, with the new inclusion of colour

$$\psi_{\text{baryon}} = \psi_{\text{space}} \times \psi_{\text{spin}} \times \psi_{\text{flavour}} \times \psi_{\text{colour}} \tag{2.1}$$

The spatial component is by definition symmetrical in the ground state. The existence of the spin-$\frac{3}{2}$ flavour symmetric states mentioned above, Ω^-, Δ^- and Δ^{++}, also forces both the spin and flavour wavefunctions to be symmetrical. This then requires the colour wavefunction to be antisymmetric.

The colour wavefunction persists to the spin-$\frac{1}{2}$ octet. Here, however, the spin wavefunction exhibits a mixed symmetry such that it is symmetric under the interchange of only one pair of quarks. To preserve the total antisymmetry of the wavefunction the flavour wavefunction must have a complementary mixed symmetry such that the product $\psi_{\text{spin}} \times \psi_{\text{flavour}}$ is fully symmetric. This restricts the flavour wavefunction such that spin-$\frac{1}{2}$ triple-flavour states, uuu, ddd and sss, are forbidden, and allows two uds states. The non-existence of the spin-$\frac{1}{2}$ flavour symmetric states and the observation of the Σ^0 and Λ^0 baryons are therefore evidence of colour charge, as predicted by the multiplets shown in figure 2.2.

2.2 Quantum Field Theory

Quantum Field Theories (QFTs) are a theoretical approach which arises from the unification of special relativity and quantum mechanics used to describe elementary particles and their interactions via the fundamental forces. A quantum field theory is specified by its corresponding Lagrangian density, and can be considered to have local gauge symmetry if this Lagrangian is invariant under a continuous local gauge transformation, such as

$$\phi(x) = e^{i\alpha(x)}\phi(x) \tag{2.2}$$

where $\phi(x)$ is the plane-wave solution to the Schrödinger equation and $\alpha(x)$ is a locally variable phase shift.

2.2.1 Quantum Electrodynamics

Quantum electrodynamics (QED) is the QFT that describes the interaction of charged fermions with an electromagnetic field. Starting from the Dirac equation, the Lagrangian of a free fermion of mass m and charge e in a non-interacting electromagnetic field is,

$$\mathcal{L} = -\frac{1}{4}F_{\mu\nu}F^{\mu\nu} + \bar{\psi}(i\gamma^{\mu}\partial_{\mu} - m)\psi \tag{2.3}$$

where $F_{\mu\nu}$ is the electromagnetic field tensor and γ^{μ} are the Dirac matrices. Here one can ensure the Lagrangian is invariant under a local transformation by making the replacement

$$\partial_{\mu} \rightarrow D_{\mu} = \partial_{\mu} - ieA_{\mu} \tag{2.4}$$

introducing A_{μ}, which is the electromagnetic field potential representing the photon. The full QED Lagrangian is now

$$\mathcal{L} = -\frac{1}{4}F_{\mu\nu}F^{\mu\nu} + \bar{\psi}(i\gamma^{\mu}\partial_{\mu} - m)\psi + e\bar{\psi}\gamma^{\mu}\psi A_{\mu} \tag{2.5}$$

which now contains the interaction term which directly couples the electromagnetic field with the fermion charge. This satisfies the U(1) gauge symmetry, giving rise to a single gauge boson, the photon.

2.2.2 Electroweak Unification

Left-handed fermions and right-handed anti-fermions have a quantum number known as weak isospin, denoted as T. Fermions form doublets of $T_3 = \frac{1}{2}$ and $-\frac{1}{2}$, the third

component of T, which behave in the same way under the weak force; for example, the charge current interaction of an electron and electron neutrino via coupling with a W boson can be expressed as

$$\begin{pmatrix} \nu_e \\ e^- \end{pmatrix} \begin{pmatrix} 0 & 1 \\ 0 & 0 \end{pmatrix} \begin{pmatrix} \nu_e & e^- \end{pmatrix} = \begin{pmatrix} \nu_e \\ e^- \end{pmatrix} \sigma_+ \begin{pmatrix} \nu_e & e^- \end{pmatrix} \tag{2.6}$$

and

$$\begin{pmatrix} \nu_e \\ e^- \end{pmatrix} \begin{pmatrix} 0 & 0 \\ 1 & 0 \end{pmatrix} \begin{pmatrix} \nu_e & e^- \end{pmatrix} = \begin{pmatrix} \nu_e \\ e^- \end{pmatrix} \sigma_- \begin{pmatrix} \nu_e & e^- \end{pmatrix} \tag{2.7}$$

for the W^+ and W^- coupling, respectively. These transformation matrices can be related to the Pauli matrices, here given as

$$\sigma_x = \begin{pmatrix} 0 & 1 \\ 1 & 0 \end{pmatrix}, \quad \sigma_y = \begin{pmatrix} 0 & -i \\ i & 0 \end{pmatrix}, \quad \sigma_z = \begin{pmatrix} 1 & 0 \\ 0 & -1 \end{pmatrix} \tag{2.8}$$

by the following relationship:

$$\sigma_\pm = \sigma_x \pm i\sigma_y \tag{2.9}$$

The three Pauli matrices act as generators for the SU(2) symmetry group and as a result give rise to three gauge bosons, W^+, W^- and W^0. The W^0 boson is non-physical and mixes with another boson generated by the U(1) symmetry group of QED, denoted as the B boson. The W^0 and B bosons mix via a rotation matrix to give two physical bosons, the Z^0 and the photon γ. The mixing is formalised as

$$\begin{pmatrix} \gamma \\ Z^0 \end{pmatrix} = \begin{pmatrix} \cos\theta_W & \sin\theta_W \\ -\sin\theta_W & \cos\theta_W \end{pmatrix} \begin{pmatrix} B \\ W^0 \end{pmatrix} \tag{2.10}$$

where θ_W is known as the weak mixing angle. This demonstrates the unification of the electromagnetic and weak forces, know as electroweak theory.

Local gauge symmetry is broken for electroweak theory by the introduction of masses for fundamental fermions and bosons. Mass terms can instead be introduced through the Higgs mechanism [32]. Here a weak isospin doublet can be written as

$$h = \begin{pmatrix} h_+ \\ h_0 \end{pmatrix} = \frac{1}{\sqrt{2}} \begin{pmatrix} h_3 + ih_4 \\ h_1 + ih_2 \end{pmatrix} \tag{2.11}$$

where four real scalar fields, h_1 - h_4, can be expressed as a pair of complex scalar fields, h_+ and h_0. The free Lagrangian for this doublet is obtained from the Klein-Gordon equation, where the mass terms are replaced by a stable potential with a non-zero vacuum expectation value, v. The symmetry of this potential can be spontaneously broken by choosing a gauge where $h_2 = h_3 = h_4 = 0$ and h_1 is the only non-zero field. The doublet h can then be expressed as

$$h = \frac{1}{\sqrt{2}} \begin{pmatrix} 0 \\ v + H \end{pmatrix} \tag{2.12}$$

where h_1 is expanded as the neutral scalar field H around v. The Lagrangian density then contains interaction terms which define the masses of the $W^{\pm}$ and Z^0 bosons in terms of the weak coupling g_w, weak mixing angle θ_W and v, while the mass of the Higgs boson is left as a free parameter. Yukawa couplings of fundamental fermions to the Higgs boson can be added to the Higgs Lagrangian without breaking the symmetry, giving mass terms for the fermions.

2.2.3 Quantum Chromodynamics

Quantum chromodynamics is the QFT that describes the behaviour of quarks and gluons under the strong force. As before, the Lagrangian starts as a free fermion in a non-interacting colour field

$$\mathcal{L} = -\frac{1}{4} G^a_{\mu\nu} G^{a\mu\nu} + \bar{\psi}(i\gamma^\mu \partial_\mu - m)\psi \tag{2.13}$$

where $G^a_{\mu\nu}$ is the gluon field strength tensor given by

$$G^a_{\mu\nu} = \partial_\mu A^a_\nu - \partial_\nu A^a_\mu + g_s f^{abc} A^b_\mu A^c_\nu \tag{2.14}$$

g_s is the coupling strength between quarks and the gluon field and f^{abc} are the

structure constants of the SU(3) symmetry group. Similar to the approach in QED, a transformation can be made to ensure local gauge invariance,

$$\partial_\mu \rightarrow D_{\mu ij} = \partial_\mu \delta_{ij} - i g_s t^a_{ij} A^a_\mu \tag{2.15}$$

where t^a are the generator matrices of the SU(3) group. This gives the QCD Lagrangian as

$$\mathcal{L} = -\frac{1}{4} G^a_{\mu\nu} G^{a\mu\nu} + \bar{\psi}(i\gamma^\mu \partial_\mu - m)\psi + g_s \bar{\psi}_i \gamma^\mu t^a_{ij} A^a_\mu \psi_j \tag{2.16}$$

Similar to how the generator matrices for SU(2) are represented by the Pauli matrices, the SU(3) generator matrices are represented by $t^a = \frac{1}{2}\lambda^a$, where λ^a are the eight Gell-Mann matrices,

$$\lambda^1 = \begin{pmatrix} 0 & 1 & 0 \\ 1 & 0 & 0 \\ 0 & 0 & 0 \end{pmatrix}, \quad \lambda^2 = \begin{pmatrix} 0 & -i & 0 \\ i & 0 & 0 \\ 0 & 0 & 0 \end{pmatrix}, \quad \lambda^3 = \begin{pmatrix} 1 & 0 & 0 \\ 0 & -1 & 0 \\ 0 & 0 & 0 \end{pmatrix}, \tag{2.17}$$
$$\lambda^4 = \begin{pmatrix} 0 & 0 & 1 \\ 0 & 0 & 0 \\ 1 & 0 & 0 \end{pmatrix}, \quad \lambda^5 = \begin{pmatrix} 0 & 0 & -i \\ 0 & 0 & 0 \\ i & 0 & 0 \end{pmatrix}, \quad \lambda^6 = \begin{pmatrix} 0 & 0 & 0 \\ 0 & 0 & 1 \\ 0 & 1 & 0 \end{pmatrix},$$
$$\lambda^7 = \begin{pmatrix} 0 & 0 & 0 \\ 0 & 0 & -i \\ 0 & i & 0 \end{pmatrix}, \quad \lambda^8 = \frac{1}{\sqrt{3}} \begin{pmatrix} 1 & 0 & 0 \\ 0 & 1 & 0 \\ 0 & 0 & -2 \end{pmatrix}$$

which correspond to eight unique gluons, and gives the gluon colour octet

$$\begin{aligned} &\frac{1}{\sqrt{2}}(r\bar{b} + b\bar{r}) && \frac{-i}{\sqrt{2}}(r\bar{b} - b\bar{b}) \\ &\frac{1}{\sqrt{2}}(r\bar{g} + g\bar{r}) && \frac{-i}{\sqrt{2}}(r\bar{g} - g\bar{b}) \\ &\frac{1}{\sqrt{2}}(b\bar{g} + b\bar{r}) && \frac{-i}{\sqrt{2}}(b\bar{g} - b\bar{b}) \\ &\frac{1}{\sqrt{2}}(r\bar{r} - b\bar{b}) && \frac{-i}{\sqrt{6}}(r\bar{r} + b\bar{b} - 2g\bar{g}) \end{aligned} \tag{2.18}$$

2.3 Renormalisation and Running Couplings

Predictions of observable quantities in QFT can made by considering all possible paths between the initial and final state particles via the Feynman path integral. This path integral is performed perturbatively in the relevant coupling strengths for the electroweak and strong forces. Oftentimes, to make suitably precise predictions, one must integrate over higher order perturbative processes, including internal loops. These loops can lead to divergences in the QFT which are non-physical, and can be treated through a technique known as renormalisation.

One way to consider some of the effects of renormalisation is to modify the coupling strength of interactions to "run" with the energy scale. This can be represented by the renormalisation group equation,

$$\alpha(Q) = \frac{\alpha(\mu)}{\left[1 - \beta_0 \alpha(\mu) \ln \frac{Q^2}{\mu^2}\right]} \tag{2.19}$$

where μ is a renormalisation energy scale and β_0 is the beta function, which depends on the contributions of the higher order internal loops.

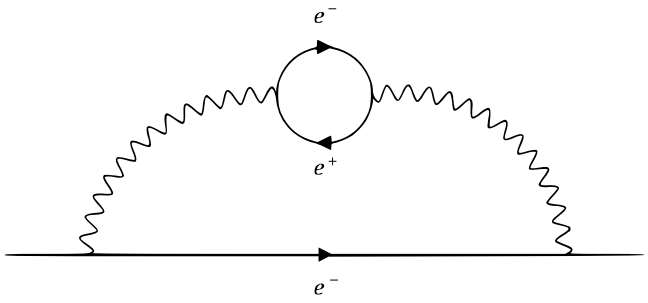

Figure 2.3: Feynman diagram[1]of the virtual e^+e^- loops that obscure the charge of the bare electron in QED.

In QED, a charged particle such as an electron can radiate and reabsorb virtual photons, which in turn can produce loops of virtual electron-positron pairs, as shown in figure 2.3. These create a *shielding effect* where the effective charge of the electron is reduced. The beta function for QED is determined by the charges of the

interacting fermions and can be expressed as

$$\beta_0 = \frac{1}{3\pi}\sum_f q_f^2 = \frac{1}{3\pi}\left[n_l + N_C\left(\frac{4}{9}n_u + \frac{1}{9}n_d\right)\right] \tag{2.20}$$

where n_l is the number of charged leptons, n_u is the number of *up*-type quarks, n_d is the number of *down*-type quarks and N_C is the number of colour charges in the model. Since β_0 is always positive, the electromagnetic coupling strength increases as the energy scale increases.

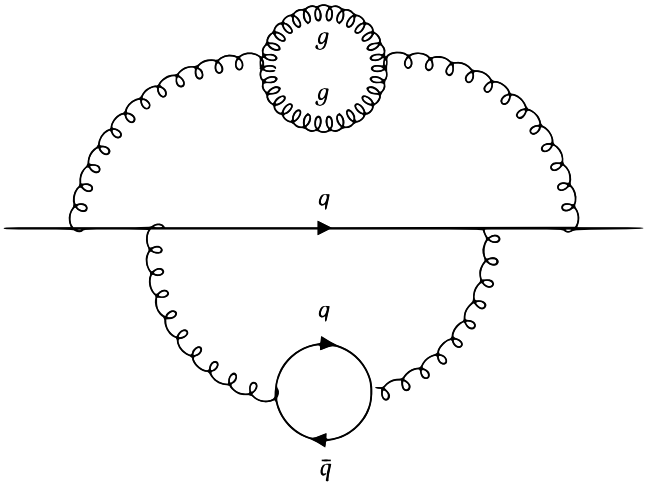

Figure 2.4: Feynman diagram of the virtual $q\bar{q}$ and gluon-gluon loops that result in a varying colour charge of the bare quark.

In QCD, the picture is made more complex by the inclusion of additional loops due to gluon-gluon interactions, as shown in figure 2.4. This leads to an *anti-shielding* effect which dominates at high energy scales, diluting the effective colour charge. The beta function for QCD is given as

$$\beta_0 = \frac{1}{108\pi}(2N_f - 11N_C) \tag{2.21}$$

where N_f is the number of quark flavours. In the standard model, $N_f = 6$ and $N_C = 3$ meaning that β_0 is negative. This results in the strong coupling strength

[1]The Feynman diagram depicts the interaction of particles by displaying spatial separation on the vertical axis and time from left to right on the horizontal, and represent the Feynman rules obtained from QFT

decreasing as the energy scale increases. Therefore, at small separations quarks hardly interact, a phenomenon known as *asymptotic freedom*, leading to bound states such as protons. Conversely, as quarks are separated, the potential energy becomes large very quickly. When this potential is large enough it becomes energetically preferable to produce a new quark-antiquark pair from the vacuum, leading to the phenomenon of hadronic *jets* in experiments.

2.4 Structure of the Proton

The proton is often described as the bound state of two *up* quarks and one *down* quark. As mentioned above, however, QCD shows gluons may form virtual pairs of quarks and antiquarks. As such the proton has a structure defined not only by the three *valence* quarks, but also by the gluons and a "sea" of low energy virtual quarks. Collectively these particles are known as *partons*.

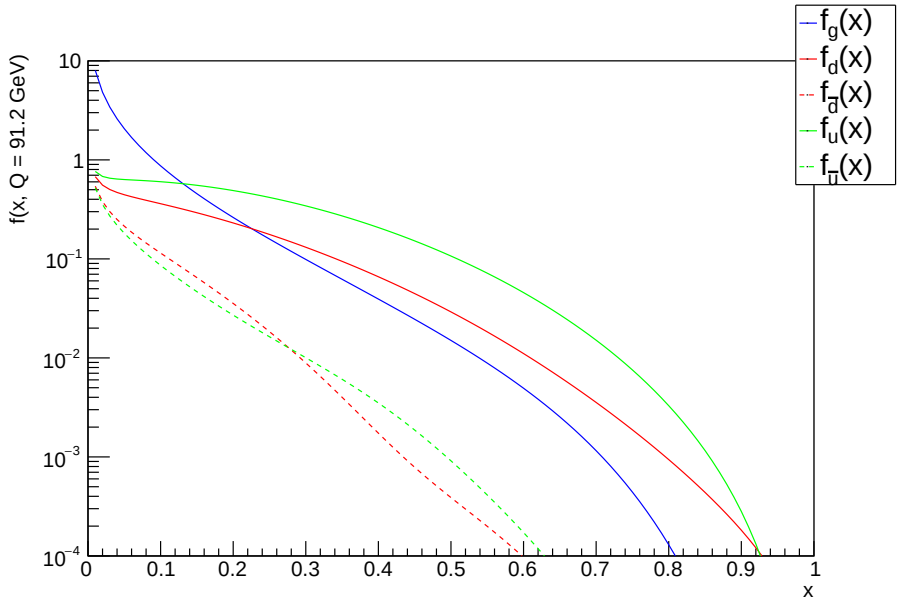

Figure 2.5: Parton density functions for gluons, quarks and antiquarks as a function of x at $Q = m_Z$, from the CT10nlo set.

As one performs collisions with increasingly energetic protons, the structure of the proton is probed in more detail to the point where the interaction is a parton-

parton collision. The rate of this hard process is expressed as a cross-section, a quantity which describes the probability of the process occurring and can be related to experimental luminosity, as shown in section 3.1.2. Since the partons have an unknown momentum fraction of the proton, the collision cross-section can be expressed by the factorisation theorem

$$\sigma_{a_1 a_2 \to X} = \sum_{p_1,\, p_2} \int \int f_{a_1}(x_{p_1}, Q^2, p_1) f_{a_2}(x_{p_2}, Q^2, p_2) \sigma_{p_1 p_2 \to X} \, \mathrm{d}x_{p_1} \, \mathrm{d}x_{p_2} \tag{2.22}$$

where the initial bound states, a_i, collide to produce the final state, X [44]. Here the cross-section is expressed in terms of the free scattering cross-section between partons p_1 and p_2, and the parton density function (PDF) of the bound state, $f_{a_i}(x_{p_i}, Q^2, p_i)$. The PDF describes the probability density of an exchange particle of energy scale Q interacting with a parton, p_i, with a longitudinal momentum fraction, the Bjorken-x. The PDF therefore controls the cross-sections of observable processes in hadronic experiments. An example of PDFs at $Q = m_Z$ is shown in figure 2.5.

As with coupling strength, PDFs are dependent on energy scale and renormalisation. The evolution of the PDF with varying energy scales is described by the DGLAP equations [45, 46, 47].

PDFs can be tested both directly, through deep inelastic scattering, or indirectly by measuring processes that come directly from the primary vertices of proton collisions. The experimental data is then fitted with the cross-section of the partonic process, convolved with the PDF model. The sensitivity of various experiments in measuring the PDF is shown in figure 2.6.

2.5 Dilepton Modes

The Standard Model is not a complete description of the elementary physics of the universe. It is therefore the aim of experimental physicists to make precise

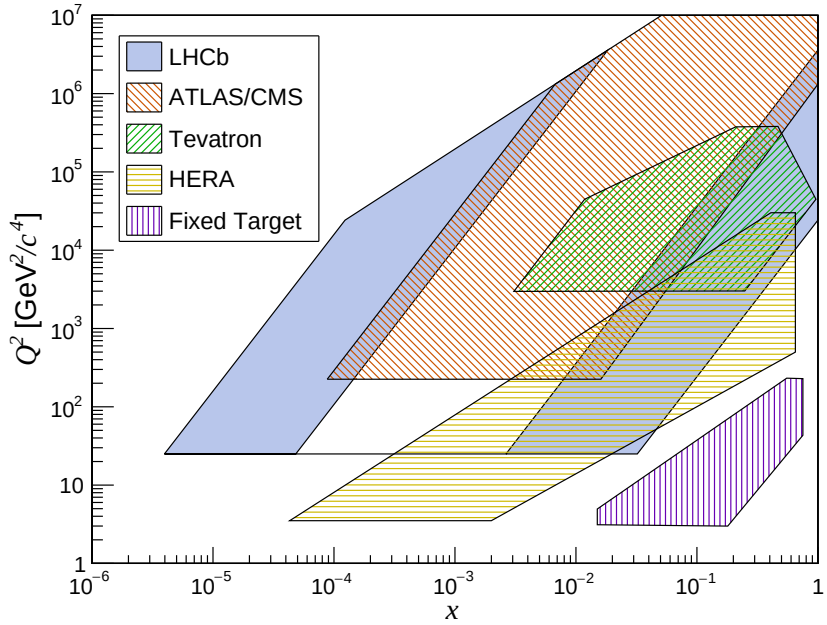

Figure 2.6: Sensitivity of various experiments to measurements of the PDFs in the phase space of Q and x.

measurements of observables that are predicted by the Standard Model, in order to identify areas that may allow for the discovery of new physics. This thesis focuses on a small fraction of the search for new physics through measurements of pairs of leptons observed at LHCb.

Dilepton production offers a theoretically clean electroweak probe of hard QCD processes, allowing for a relatively straightforward comparison between predictions and measurements. Experimentally, the invariant mass of the dilepton pair is measured, giving a spectrum of resonances from the decays of quarkonia states and real Z bosons along with a continuum produced by the Drell-Yan process.

Dimuons give an experimentally clean signature as high energy muons from the hard process will typically penetrate a detector with little deflection from material. This allows for clear identification with high resolution measurements and therefore enables precision tests of the Standard Model and searches for new physics, including previously unseen vector resonances that are not predicted by the Standard Model.

Dielectrons are typically measured with a worse mass resolution than dimuons,

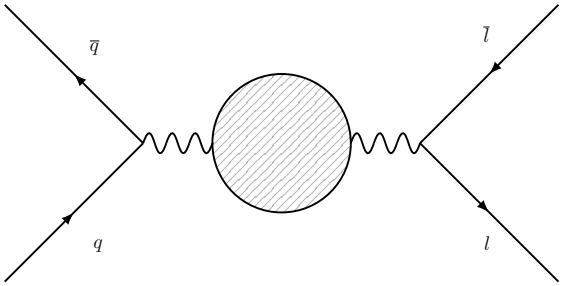

Figure 2.7: First order diagram of dilepton production in proton-proton collisions, potentially via an intermediate resonance state.

as the light mass of the electron results in multiple scattering by detector material. On the other hand, the dielectron mass spectrum extends to very low masses, $M_{ee} > 2m_e \approx 1\,\text{MeV}$, lower than that of the dimuon spectrum, $M_{\mu\mu} > 2m_\mu \approx 211\,\text{MeV}$. This allows for the searches for low mass bound states, such as true muonium, the bound state of a muon and antimuon, which is predicted to decay to a dielectron pair with an invariant mass of $\sim 2m_\mu$ [48].

This thesis presents a measurement of the Drell-Yan production cross-section via the dimuon channel, using data taken by the LHCb experiment in 2016, and a proposal for a search for true muonium at LHCb during Run 3 of data taking.

Chapter 3

Experiment

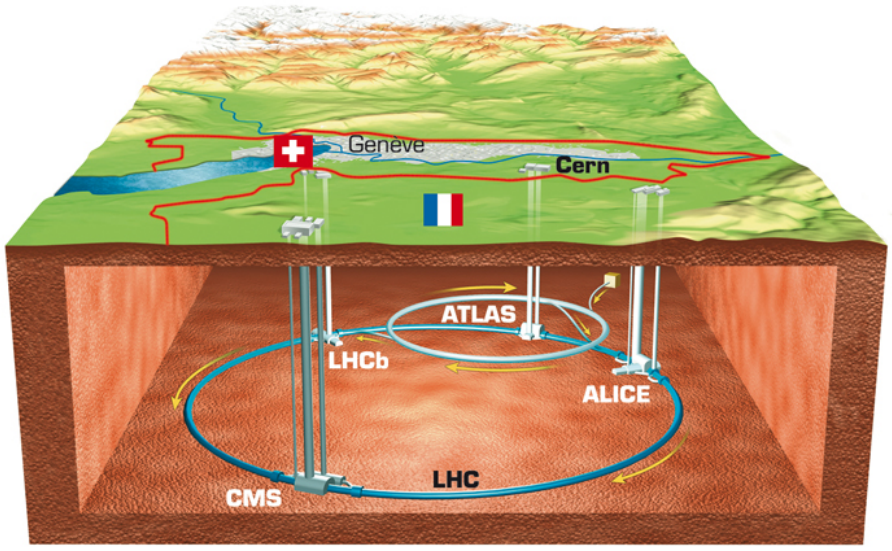

Figure 3.1: Artist's impression of the LHC [49].

3.1 The Large Hadron Collider

The Large Hadron Collider (LHC) is, at the time of writing, the highest energy particle accelerator ever built. Located at the CERN laboratory on the Swiss-French border near Geneva, the LHC is capable of colliding bunches of protons with a centre of mass energy of 14 TeV every 25 ns. This enables physicists to observe

some of the rarest high energy processes and make precise measurements in order to scrutinise the Standard Model.

3.1.1 Motivation and Design

The LHC was designed with the intention of discovering the Higgs boson and for searching for signs of supersymmetry [50, 51, 52]. In the energy range achieved by the LHC, the rate of Higgs production from gluon fusion in proton-proton collisions is larger than quark-antiquark scattering in proton-antiproton collisions. This is due to the content of the proton PDF at such high energy scales. The Tevatron, the previous record holder for high energy collisions, collided protons with antiprotons which enabled the study of quark-antiquark scattering. However, the difficulties in producing anti-protons results in a reduced experimental luminosity. A high luminosity is critical for the measurements of rare processes, as shown in section 3.1.2, and as such, proton-proton collisions were chosen for the LHC.

Synchrotron Radiation

The LHC replaced the previous Large Electron-Positron Collider (LEP), which ran between 1989 and 2000. The main technical limitation in high energy circular colliders is the synchrotron radiation emitted tangentially when a charged particle experiences radial acceleration. The energy lost by a particle of charge q per revolution of a radius r is given by

$$\Delta E = \frac{q^2 \beta^3 \gamma^4}{3\epsilon_0 r} \tag{3.1}$$

where ϵ_0 is the permittivity of free space, β is the particle velocity as a fraction of the speed of light and γ is the Lorentz factor.

For highly relativistic particles $\beta \approx 1$ and $\gamma = E/m$, thus when accelerating particles to a given energy, the energy loss due to synchrotron radiation is inversely

proportional to particle mass to the fourth power. For an electron-positron collider it quickly becomes impossible to achieve the energies allowed by a proton-proton collider, as the proton is about 2000 times heavier than the electron. It is also worth noting that losses due to synchrotron radiation can be reduced further by increasing the radius r of acceleration, explaining the 27 km circumference of the LHC.

Magnet Systems and Beam Effects

In order to perform collisions at $\sqrt{s} = 13$ TeV, protons must be accelerated to momenta of 6.5 TeV. To achieve this, the LHC uses 1232 superconducting dipole magnets, each 15 m long and generating an 8.3 T magnetic field. To minimise cost, the magnets use a 2-in-1 design where both beam pipes have separate magnetic coils but share cryostat and power infrastructure.

Perturbations in the electromagnetic fields used at the LHC can arise from the beams themselves [53]. These beam effects can cause instabilities that need to be handled in order to efficiently and effectively provide collisions. The charged particles can also induce charges and currents in the surrounding components which create magnetic fields known as wakefields. Resonant oscillations can be reduced or eliminated through Landau damping controlled by the use of octupole magnets. Sextupole modes introduced by the dipole magnets are compensated by a system of sextupole magnets [54]. Prior to collisions, the beams are focused by quadrupole magnets, reducing the cross-section of the beam and increasing the probability of collisions [55].

Accelerators and LHC Layout

Before filling the LHC ring itself, protons are accelerated by a series of smaller accelerators, as shown in figure 3.2. The protons are accelerated to 50 MeV by a linear accelerator (LINAC2) before being boosted by the Proton Synchrotron Booster (PSB) to 1.4 GeV. From here they are injected into the Proton Synchroton which

further accelerates them to 25 GeV before being filled into the Super Proton Synchrotron (SPS) where they reach 450 GeV. Finally, bunches of protons are injected from the SPS to the LHC.

The LHC ring has eight straight sections, about 500 m long, four of which are used for collisions and therefore house the main experiment detectors [56]. The general purpose detectors ATLAS and CMS occupy Points 1 and 5 respectively [57, 58]. The heavy ion ALICE experiment is located at Point 2, while b-physics focused LHCb is at Point 8 and is discussed further in section 3.2 [59]. Points 2 and 8 also contain the beam injection system.

The remaining straight sections do not have beam crossings. Points 3 and 7 are reserved for beam collimation in order to minimise background in the experiments. At Point 4, the beams are accelerated by a system of radiofrequency (RF) cavities [60]. Point 6 is assigned as the beam abort system where the beam can be safely dumped in both planned and emergency procedures.

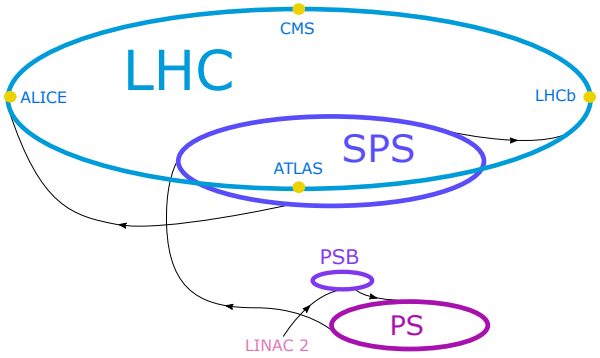

Figure 3.2: Diagram of the accelerators used to boost protons to 6.5 TeV.

3.1.2 Luminosity

The performance of a particle accelerator is often quantified by the property known as luminosity. Luminosity is directly related to the number of events that an experiment has available to study and so it is the aim of accelerators to deliver the maximum luminosity possible. This is especially true when studying a rare process

with a small production cross-section, σ. The expected production rate can then be given by

$$\frac{\mathrm{d}N}{\mathrm{d}t} = \mathcal{L} \cdot \sigma \tag{3.2}$$

and thus for a constant luminosity the total number of events expected in a given time, T, is given by

$$N = \int_0^T \mathcal{L}\,\mathrm{d}t \cdot \sigma = \mathcal{L}_{\mathrm{int}} \cdot \sigma \tag{3.3}$$

where $\mathcal{L}_{\mathrm{int}}$ is known as the integrated luminosity. This is often used as a measure of the quantity of data available for use in an analysis and is a vital quantity in cross-section measurements.

The actual luminosity delivered to an experiment by the LHC can be expressed as

$$\mathcal{L} = \frac{N_1 N_2 f N_b}{4\pi\sigma_x\sigma_y} \tag{3.4}$$

where N_1 and N_2 are the number particles in each bunch, f is the revolution frequency, N_b is the number of bunches and σ_x and σ_y are the beam widths in both dimensions, assuming a head on collision of equal Gaussian beams [61].

The experimental luminosity is measured by profiling the beam to obtain σ_x and σ_y. This is achieved using a van der Meer scan, where the two beams are scanned across each other in the transverse dimension, allowing the spread of the beam to be determined [62]. In addition to this, LHCb has the ability to fill the beam pipe with gas. This enables the profiling of the beam through beam-gas imaging, where vertices are reconstructed from collisions between beam protons and gas nuclei [63]. In contrast to van der Meer scanning, the beams do not need to be moved, reducing some of the uncertainties in the final luminosity measurement.

For the general purpose experiments, ATLAS and CMS, low cross-section pro-

cesses require a high integrated luminosity to make statistically significant measurements. The LHCb experiment, however, is designed to make precise measurements of the decays of B hadrons which in turn requires precise knowledge of primary and secondary vertices. Here it becomes advantageous to operate at a lower luminosity to reduce the number of separate p-p interactions, known as pileup. This is achieved by introducing a crossing-angle in the vertical plane to the beam interaction at Point 8 [64]. Since at these energies the production cross-section for $b\bar{b}$ pairs is high compared to Higgs production, the reduced luminosity does not result in a critical loss of data.

3.1.3 Run Schedule

The LHC was commissioned to provide proton-proton collisions at a centre of mass energy of 14 TeV. However, in 2008, a magnetic quench incident caused significant damage delaying initial testing. As a result Run 1 of LHC data taking took place from 2010 to 2013 at a reduced centre of mass energy of 7 TeV, increasing this to 8 TeV in 2012 [65].

Following the LHC's first Long Shutdown (LS1) for maintenance and upgrades, data taking restarted with Run 2 in 2015 with a centre of mass energy of 13 TeV until 2018. During this time, an integrated luminosity of $160\,\mathrm{fb}^{-1}$ was delivered to the ATLAS and CMS experiments, while around $6\,\mathrm{fb}^{-1}$ was delivered to LHCb [66].

At the time of writing the LHC is in the second Long Shutdown (LS2), where preparations are being made to increase the beam luminosity by a factor of 10 following Run 3, an upgrade known as High Luminosity LHC (HL-LHC). In Run 3 the LHC will also operate at higher luminosity and as such the experiments are taking advantage of the shutdown to install upgrades. Experiments are expected to begin data taking in March 2022 [67].

3.2 LHCb Detector

The LHCb detector is a forward arm spectrometer located at Point 8 on the LHC accelerator [68]. It is specifically designed to take advantage of the high flux of B hadrons produced in pairs, typically in the same direction, close to the beam in the 13 TeV collisions provided by the LHC. Due to the proximity of sensitive hardware to the beam, LHCb receives a reduced luminosity of bunch collisions. For example, in 2018 LHCb recorded a total integrated luminosity of $2.2\,\mathrm{fb}^{-1}$ and an average number of visible p-p interactions per bunch crossing of $\mu \sim 1.4$, compared to $60.6\,\mathrm{fb}^{-1}$ and $\mu \sim 60$ at ATLAS. Nevertheless, the experiment uses a robust and efficient trigger system to allow observations and measurements of rare processes. Additionally, the tracking system gives an excellent momentum resolution allowing for precise tests of the Standard Model.

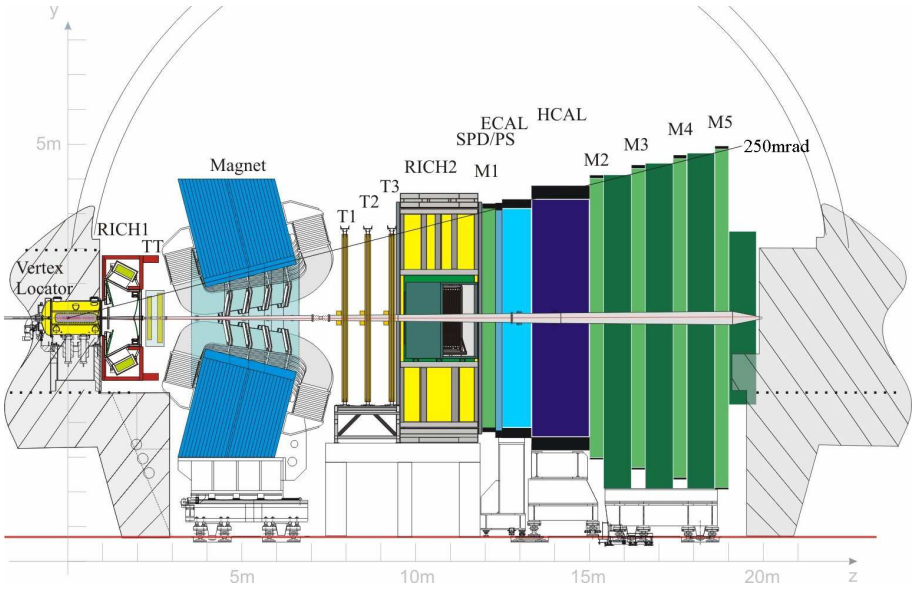

Figure 3.3: Schematic diagram of the LHCb detector during Run 1 and Run 2 [69].

A diagram of the LHCb detector is shown in figure 3.3. Here, the z-axis is defined parallel to the beam direction, while the y-axis is the vertical and the x-axis the horizontal. It is also useful to define the terms "upstream", towards the interaction point, and "downstream", away from the interaction point and the direction in which detectable particles generally travel.

3.2.1 Vertex Locator

The Vertex Locator (VELO) is the first sub-detector at LHCb. It is a high resolution tracker designed to accurately measure track trajectories from the primary vertices (PV) and identify secondary vertices from the displaced decays of heavy flavoured particles.

During Run 1 and Run 2, the VELO consisted of 42 semicircular silicon strip modules positioned perpendicular to the z-axis, centred on the beampipe. Each module is a pair of sensors, one with strips in the r direction and the other in the ϕ direction, giving both (r, z) and (r, ϕ) measurements which are combined to give a three-dimensional "hit".

The VELO can be open and closed in order to prevent exposure of the sensors to large doses of radiation. Prior to collisions the beam can be diffuse under non-stable conditions and the beam-width larger than the aperture between modules in the closed position. When closed for data taking, the modules sit at a radius of 8 mm from the beam.

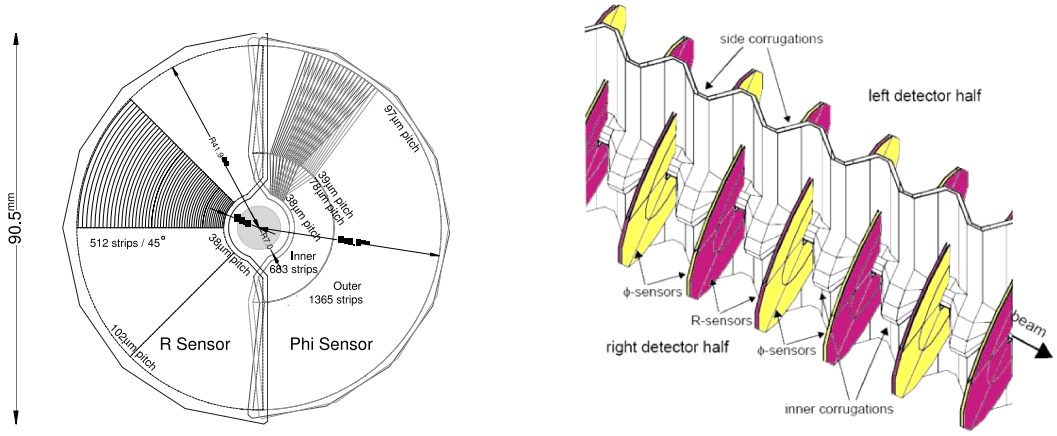

Figure 3.4: (Left) $r\phi$ geometry of VELO sensors during Run 1 and Run 2. (Right) Arrangement of VELO sensors and RF foil during Run 1 and Run 2 [69].

To further limit the degradation of the sensitive modules, each half of the VELO is enclosed in an aluminium RF box, shaped to deflect RF wakefields and reduce heating of the sensors. The thinner interface between the two boxes is known as

the RF foil and in Run 1 and Run 2 this was 300 μm thick aluminium, corrugated to minimise material interactions in the beam region. The RF boxes also allow the beam vacuum and the sensor vacuum to be kept separate, in order to minimise interactions with gaseous material while maintaining the structural rigidity of the foil.

LHCb will receive an increased instantaneous luminosity in Run 3 resulting in a higher pile-up environment. In order to effectively identify tracks and distinguish primary vertices, the VELO has been replaced with a new upgraded detector. The new VELO has 52 modules containing four silicon hybrid pixel sensors arranged in an L-shape. When the VELO is closed, the pairs of modules leave a square gap in acceptance around the beamline with the closest pixels sitting 5.1 mm from the beam. The new RF foil follows the L-shape of the modules and is made of 250 μm thick aluminium. [70]

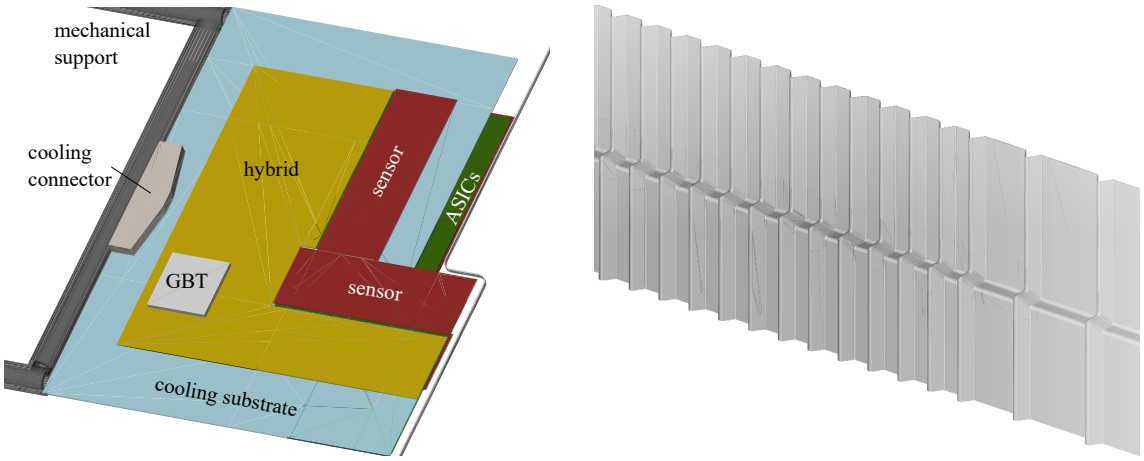

Figure 3.5: (Left) Design of the new modules used in the upgraded VELO. (Right) Shape of the upgraded RF foil [69].

3.2.2 Tracking System

LHCb makes use of additional tracking detectors both upstream and downstream of the magnet, which are shown in figure 3.6. Hits recorded in these detectors are reconstructed to form tracks, which are in turn associated with the VELO hits.

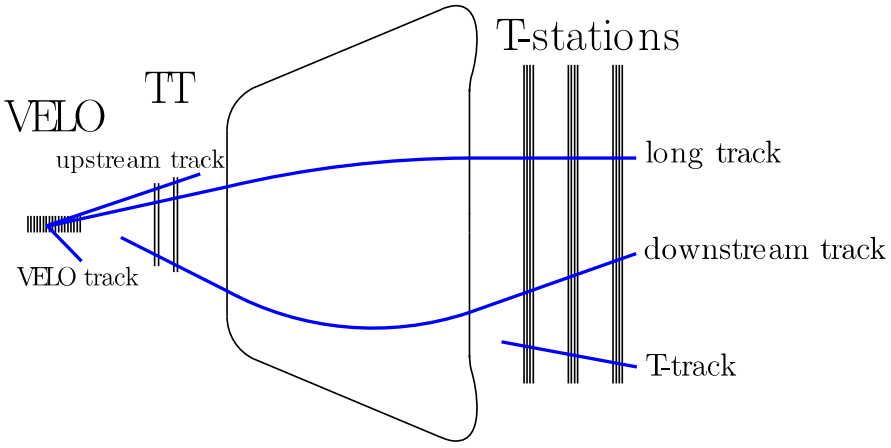

Figure 3.6: Layout of the LHCb tracking system and definitions of track types [69].

Both the Tracker Turicensis (TT) and the innermost modules of stations T1-T3, known as the Inner Tracker (IT), use silicon microstrips with a pitch of approximately 200 μm. These allow for increased spatial resolution in the region closest to the beampipe where the flux is greatest. Collectively the TT and IT are referred to as the Silicon Tracker (ST). By contrast, the outer modules of stations T1-T3 are known as the Outer Tracker (OT) and use straw-tubes to cover the larger region further from the beam, where a lower hit rate is expected.

Tracker Turicensis

The Tracker Turicensis is positioned immediately upstream of the magnet. It consists of four layers arranged on the $(x-u-v-x)$ axes from the first to the fourth layers respectively. Here the u and v axes are defined as those rotated from the x axis by $+5^\circ$ and -5° respectively, as shown in figure 3.7, which allows for better determination of tracking hits.

The first two layers consist of seven full modules on either side of a central module positioned on either side of the beam pipe, while the third and fourth layers have eight. The modules themselves are split into two half-modules of seven silicon strip sensors. The six innermost half-modules are divided into three readout sectors of four, two and one sensor each, and are therefore known as 4-2-1 type. The remaining

half-modules have two readout sectors in a 4-3 type format.

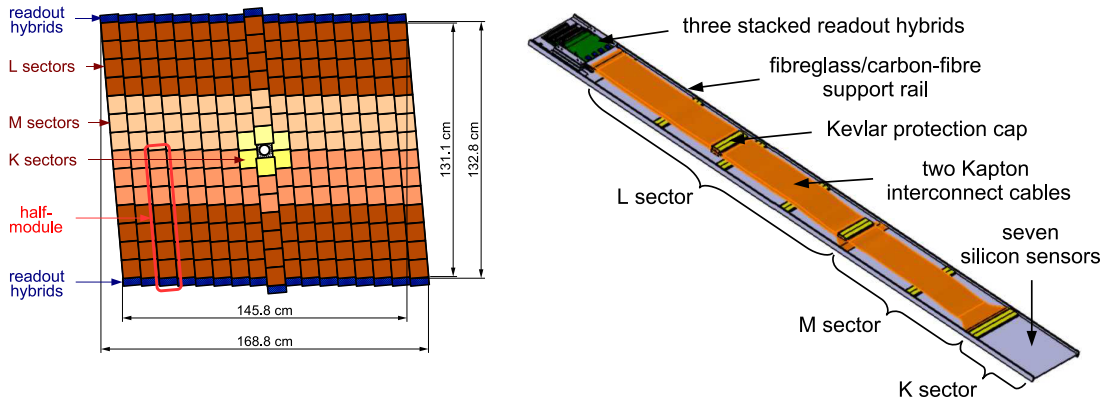

Figure 3.7: (Left) Layout of the modules and readout sectors in the third layer of the TT. (Right) Diagram of 4-2-1 type half-module [69].

Inner Tracker

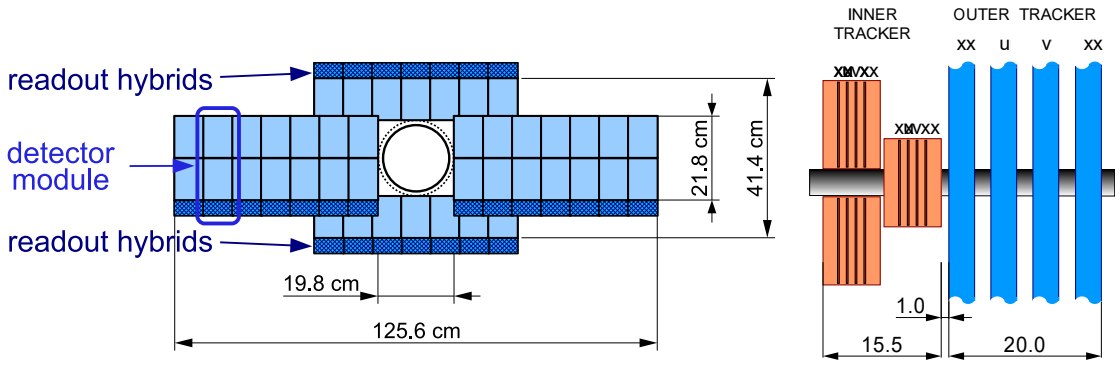

Figure 3.8: (Left) Arrangement of the IT detector boxes around the beampipe. (Right) $(x-u-v-x)$ alignment of the IT and OT layers in a single tracking station [69].

The Inner Tracker (IT) of the downstream stations T1-T3 consist of four individual detector boxes arranged in a cross-shape around the beampipe, shown in figure 3.8. Each box contains 28 modules arranged in four layers, using the same $(x-u-v-x)$ alignment as the TT. Modules in the boxes above and below the beampipe use a single silicon sensor, while those on the left and right use two sensors [71].

The sensors themselves are 11 cm long and 7.8 cm wide, with a thickness of 320

μm and a strip pitch of 198 μm. The modules have a hybrid readout which samples at 40 MHz.

Outer Tracker

The Outer Tracker (OT) of stations T1-T2 is a drift-time detector, covering the larger remaining area of acceptance not covered by the IT. The OT is an array of straw-tube modules with an inner diameter of 4.9 mm, containing a mixture of argon (70%) and CO_2 (30%) enabling a fast drift time of under 50 ns with sufficient spatial resolution.

The OT has four layers at each station arranged in the same $(x-u-v-x)$ alignment as the TT and IT. The OT enables coverage of the full acceptance of 300 mrad in the horizontal plane and 250 mrad in the vertical plane. The inner cross-shaped area covered by the IT was determined such that the OT occupancy should not exceed 10% at an instantaneous luminosity of 2×10^{32} cm^{-2}s^{-1}.

3.2.3 RICH

LHCb makes use of two Ring Imaging Cherenkov detectors (RICH) for particle identification of hadronic tracks to separate pion and kaon candidates in selected B hadron decays.

Charged particles that travel faster than the speed of light in a given medium emit Cherenkov radiation at a fixed angle, forming a cone centred on the particle trajectory. The angle, θ_C is related to the particle velocity, v, by

$$\cos\theta_C = \frac{1}{n\beta} \tag{3.5}$$

where n is the refractive index of the medium and β is the velocity as a fraction of the speed of light, v/c [72]. Thus, by measuring θ_C using a Cherenkov detector and the associated particle momentum from the tracker, an estimate of the particle mass

can be made, enabling particle identification. RICH detectors use a combination of spherical and flat mirrors to focus the cone into a ring, the radius of which allows for the calculation of θ_C, as shown in figure 3.9.

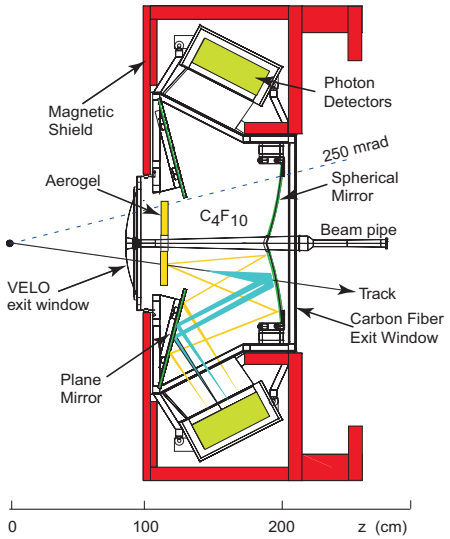

Figure 3.9: Cherenkov cones are transformed into rings using mirrors in RICH1 [69].

RICH1 is positioned upstream of the magnet and is sensitive to the lower momentum range of 1 - 60 GeV/c, using perfluorobutane gas (C_4F_{10}) with a wide radial acceptance of 25 mrad to 300 mrad (horizontal plane) and 250 mrad (vertical plane). RICH2 is downstream of magnet and the tracking stations, and is sensitive to the higher momentum range of 15 to more than 100 GeV/c, using tetrafluoromethane (CF_4), with a narrower radial acceptance of 120 mrad (horizontal) and 100 mrad (vertical).

3.2.4 Calorimeters

The calorimeter system employed by LHCb consists of a core Electromagnetic Calorimeter (ECAL) followed by a Hadronic Calorimeter (HCAL), and is preceded by the Scintillating Pad Detector (SPD) and Pre-Shower detector (PS).

Collectively, these detectors measure the energy of electrons, photons and hadrons by triggering electromagnetic and hadronic particle showers. Electromagnetic

showers are precipitated by Bremsstrahlung and pair production, dividing the initial energy of the incoming particle over several radiation lengths until pair production is no longer energetically viable. Hadronic showers are technically similar but result from more complex hadronic processes via the strong interaction, involving secondary hadron production.

The calorimetry system has two main purposes: particle identification and triggering. It provides information for the identification of electrons, photons and hadrons by associating tracks of charged particles with energy deposits. Charged particles can also be distinguished by the ratio of the energy deposit to the momentum of associated track, E/p, which gives a fraction of the total energy lost in the calorimeter that is typically high for electrons, low for muons and intermediate for pions. Transverse energy information also allows for fast rejection of lower energy events at the Level-0 trigger.

Scintillating Pad Detector/Pre-Shower detector

The Scintillating Pad Detector (SPD) and Pre-Shower detector (PS) allow for fast background rejection and the distinguishing of photon and charged particle signals. The SPD and PS both use arrays of square scintillating plastic pads of three sizes: 4×4, 6×6 and $12 \times 12\,\mathrm{cm}^2$ in the inner, middle and outer regions respectively, as shown in figure 3.10. The two planes of scintillators are separated by 15 mm of lead, corresponding to 2.5 X_0.

Electromagnetic Calorimeter

LHCb uses a sampling calorimeter with shashlik technology, which uses alternating layers of 2 mm thick lead absorbers, 120 µm thick reflecting paper and 4 mm thick plastic scintillator detectors, readout by wavelength shifting (WLS) fibres. In total, 66 layers of lead and scintillator are used, forming a stack 42 cm in length or 25 X_0.

Since the hit rate decreases at further distances from the beampipe, the ECAL is

divided into inner, middle and outer sections with decreasing granularity. The cell sizes used in these sections are $4.04 \times 4.04\,\mathrm{cm}^2$, $6.06 \times 6.06\,\mathrm{cm}^2$ and $12.12 \times 12.12\,\mathrm{cm}^2$ respectively.

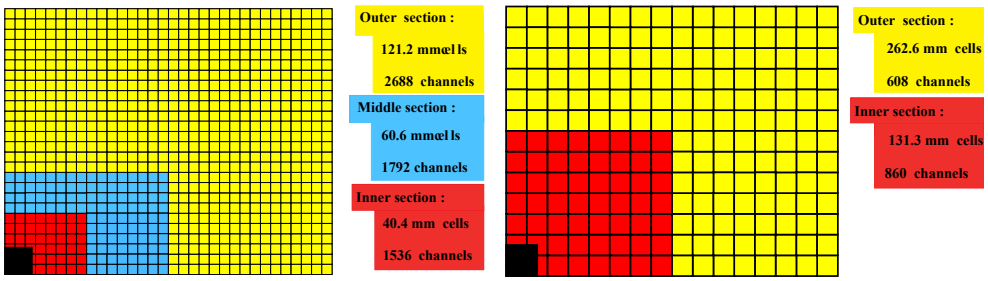

Figure 3.10: Segmentation of one quarter of (left) SPD/PS and ECAL and (right) HCAL [69].

Hadronic Calorimeter

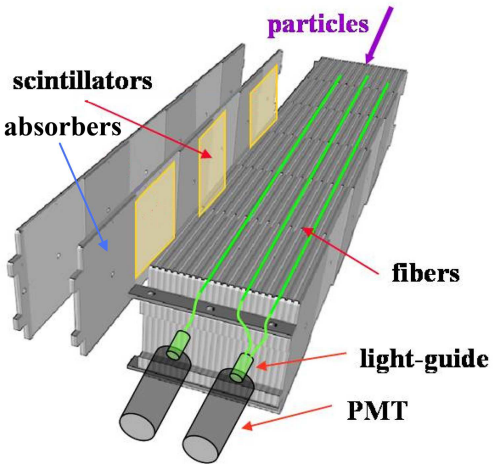

Figure 3.11: The HCAL modules are constructed from plates of iron with scintillating tiles aligned parallel to the beam axis [69].

The hadronic calorimeter (HCAL) is also a sampling calorimeter with iron absorbers and plastic scintillator active area. Unlike the ECAL, the HCAL is constructed such that the scintillating tiles are aligned parallel to the beam axis, and are interspersed with 1 cm of iron, as depicted in figure 3.11. In the longitudinal direction, the length of scintillating tiles and iron spacers correspond to the hadronic interaction length (λ_I) in steel. The light emitted by the scintillator tiles is

transmitted to photomultiplier tubes (PMTs) at the rear of the module by WLS fibres.

The HCAL is also segmented, though more coarsely than the ECAL and SPD/PS, as shown in figure 3.10. The inner section uses modules of $13.13 \times 13.13\,\mathrm{cm}^2$, while those in the outer section are $26.26 \times 26.26\,\mathrm{cm}^2$.

3.2.5 Muon System

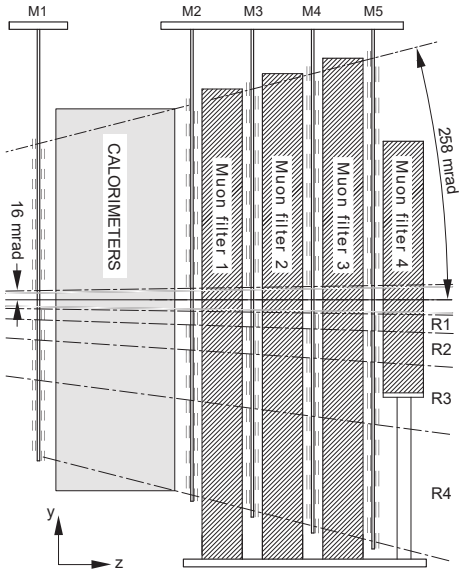

Figure 3.12: Layout of stations M1-M5 in the Muon System with iron absorbers [69].

The Muon System at LHCb consists of five substations, M1-M5, and is used for the identification of muon tracks and for providing fast information on high-p_T muons for the Level-0 trigger. M1 is situated upstream of the calorimeters, giving a more precise p_T measurement used in the hardware trigger. M2-M5 provide space-point measurements for muon tracks. They are each separated by 80 cm thick iron absorbers, which gives a total absorber thickness of $20\mathrm{X}_0$ including the calorimeters. As a result, a muon would require a minimum momentum of approximately 6 GeV/c in order to penetrate the fifth muon station.

Stations M1-M3 have a high spatial resolution in the horizontal plane and give a p_T resolution of 20%. M4 and M5 have poorer resolution and are therefore used for

the identification of higher momentum muons that penetrate all the way through the detector. The muon stations are divided into four regions R1-R4 (as shown in figure 3.12,) which scale in segmentation by the ratio 1:2:4:8 such that each region has approximately the same occupancy. Each station uses multiwire proportional chambers except for the R1 region of M1 where triple GEM detectors are used as the high particle rate would otherwise rapidly deteriorate the detector.

3.3 Trigger

During a run at the LHC, bunch crossings occur at a rate of 40 MHz. Since it is impossible to record all of this data for analysis, LHCb makes use of a trigger system to select the most interesting events at a manageable rate. The trigger system is described in detail in [73], with the key features relevant to this analysis summarised below.

The maximum rate at which all subdetectors can be read out in Run 2 is 1 MHz when running at a rate of visible interactions per bunch crossing of $\mu = 1.1$. The hardware based Level-0 (L0) trigger selects events based on information from the tracking system and the calorimeters. Further reduction is achieved using a software based High Level Trigger (HLT), which is divided into two stages: HLT1 and HLT2. HLT1 performs an inclusive selection of events based on one or two track signatures, on muon tracks displaced from the PV, or on dimuon candidates.

Events that pass the HLT1 are passed to a 10 PB disk buffer, allowing for the processing of events during inter-fill periods and for the alignment and calibration of the detector. From the buffer, events are passed to HLT2 where full event reconstruction is performed, allowing for more specific criteria to be applied to the selection. Both levels of the software trigger run using the Moore application [74]. The data flow is also described in figured 3.13.

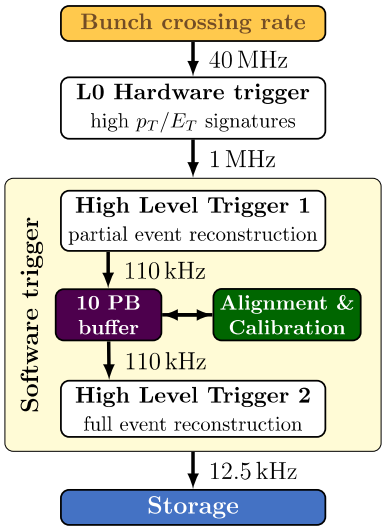

Figure 3.13: Data flow in the trigger system during Run 2 [69].

3.3.1 Level-0 Hardware Trigger

The L0 trigger selects events by requiring criteria on various signatures, collectively known as trigger lines. The Photon, Hadron and Electron lines select events based on the transverse energy, E_T, of reconstructed ECAL and HCAL clusters. The Muon, Muon High p_T and DiMuon lines select events based on the transverse momentum, p_T, of tracks in the muon stations; the DiMuon line uses the two tracks with the highest p_T. High multiplicity events can be vetoed by a cut on the number of hits recorded in the SPD.

For the calorimeter lines, ECAL and HCAL clusters are defined as the energy deposited in 2×2 cells, while the transverse energy of the cluster is defined as

$$E_T = \sum_{i=1}^{4} E_i \sin\theta_i \tag{3.6}$$

where i is the cell index, E_i is the energy deposited in the ith cell and θ_i is the angle between the z-axis and the vector between the PV and the cell centre. SPD/PS hits can be used to further distinguish between photons and electrons.

For the muon lines, the p_T of muon tracks are estimated using the direction of hits in the muon station, assuming the muon originated from the PV and received

a single kick from the magnet. The p_T resolution is approximately 25%, averaged over the relevant momentum range. The trigger line selects the two tracks with the highest p_T. In the Muon and Muon High p_T lines the decision is made solely on the highest p_T track, whereas for the DiMuon line it is the geometric mean of two momenta, $\sqrt{p_T^1 p_T^2}$.

Table 3.1: Event criteria required to trigger the L0 trigger lines in 2016 data taking [73].

L0 Line	Requirements
Hadron	$E_{\mathrm{T}} > 3.7\,\mathrm{GeV}$, $n\mathrm{SPD} < 450$
Photon	$E_{\mathrm{T}} > 2.78\,\mathrm{GeV}$, $n\mathrm{SPD} < 450$
Electron	$E_{\mathrm{T}} > 2.4\,\mathrm{GeV}$, $n\mathrm{SPD} < 450$
Muon	$p_{\mathrm{T}} > 1.8\,\mathrm{GeV}$, $n\mathrm{SPD} < 450$
Muon high p_{T}	$p_{\mathrm{T}} > 6.0\,\mathrm{GeV}$
Dimuon	$\sqrt{p_{\mathrm{T}}^1 p_{\mathrm{T}}^2} > 1.5\,\mathrm{GeV}$, $n\mathrm{SPD} < 900$

3.3.2 High Level Trigger 1

HLT1 performs a partial event reconstruction in order to rapidly make decisions. This is achieved by reconstructing the trajectories of charged particles that traverse the full tracking system, known as long tracks (see figure 3.6). Precise reconstruction of the primary vertex is also performed. Timing restrictions are too limited to be able to run particle identification algorithms, with the exception of muon identification which has the advantage of a clean signature.

Track and Vertex Reconstruction

The first step of track reconstruction is the combination of VELO hits which form a straight line that loosely points back to the beamline. This line is then extrapolated to the TT, where three associated hits are required to form an upstream track. The TT experiences the fringe of the field from the dipole magnet and momentum estimates can be made for upstream tracks with a resolution of approximately 20%. This estimate allows for the rejection of low momentum tracks.

A search window can then be defined for associated hits in the downstream tracking stations by the maximum possible deflection of charged particles with a p_T greater than 500 MeV/c. In addition, a charge estimate of the upstream track can restrict the search to only one side of the extrapolated trajectory. The selection of hits in the downstream trackers allows for the reconstruction of the final long tracks. Finally, the tracks are fitted with a Kalman filter to obtain the optimal parameter estimates.

Precise PV reconstruction is required early in the selection of displaced events. Fully reconstructed long tracks are not available at HLT1, as a result PV reconstruction is performed using only VELO tracks. This does not result in any degradation in resolution compared to using a combination of VELO tracks and long tracks, and is faster.

PV resolution can be obtained by splitting the VELO tracks used into two subsets. The PV algorithm is run over both subsets and the PVs found are matched based on the distance between them. The width of the distribution of the difference of matched PVs in a given dimension, corrected by a factor of $\sqrt{2}$, gives the corresponding resolution.

Muon Identification

Hits in the MUON detectors are examined in regions-of-interest around the extrapolated trajectories of fully fitted tracks. Tracks with a momentum $p < 3$ GeV/c are rejected as they would not be able to penetrate to the MUON detectors. Below 6 GeV/c, hits in only the first two downstream detectors, M2 and M3, are required. Between 6 and 10 GeV/c an additional hit is required in M4 or M5, and above 10 GeV/c hits are required in all four downstream stations.

At HLT1, reconstruction is only performed for tracks with $p_T > 500$ MeV/c. For lower momentum tracks a complementary muon identification algorithm is used [75]. Upstream tracks are extrapolated directly to the MUON stations where a

larger region-of-interest is used. If hits are found, the upstream track is extrapolated through the magnet using the momentum estimate and matched to hits not already used in the long-track reconstruction. This allows for muon-identification of tracks with $p_T > 80$ MeV/c which is greatly beneficial for measurements involving lower momentum muons.

3.3.3 High Level Trigger 2

Following selection by HLT1, events are fully reconstructed at HLT2. There are three major steps: track reconstruction of charge particles, reconstruction of neutral particles, and particle identification (PID). Tracks are reconstructed using the full tracker information, which is not possible at HLT1 due to timing restrictions, allowing for the most precise momentum measurements. Similarly, the most precise neutral cluster reconstruction algorithms can be used and full PID can be performed in addition to the muon identification performed at HLT1.

Track Reconstruction

Track reconstruction at HLT2 differs from that at HLT1 in that the full tracking information is available. As a result, the aim is to be able to reconstruct tracks without a minimum transverse momentum requirement. This is beneficial for the study of the decays of light particles, particularly those with three or more decay products such as charmed or strange hadrons which would not pass the $p_T > 500$ MeV/c requirement at HLT1.

The first step is to repeat the HLT1 track reconstruction. The second step aims to reconstruct lower momentum tracks. The VELO tracks and tracking station hits used to reconstruct good quality long tracks are disregarded. The remaining VELO tracks are then extrapolated through the magnetic field to define a search region for T-station hits with a maximal deflection for particles with a p_T of 80 MeV/c. TT hits are not used to avoid a loss of efficiency due to acceptance gaps in the TT.

In addition to this, a second standalone search for T-tracks is performed, where these tracks are combined with VELO tracks to form long tracks. The redundancy of the two algorithms allows for an improved efficiency of a few percent.

Displaced tracks formed by the decay products of long lived particles, such as Λ baryons and K_s^0, that decay outside of the VELO are reconstructed by extrapolating T-track segments back through the magnetic field and combining them with hits in the TT using a multivariate classifier.

Fake tracks arise from random combinations of hits or from the incorrect matching of track segments upstream and downstream of the magnet. The rejection of fakes is achieved by first fitting the tracks with a Kalman filter, providing a χ^2 value for the track quality and then using a neural network trained using the TMVA package to veto the fake tracks [76]. The input variables were the χ^2 of the Kalman filter, the χ^2 of the individual segments, the number of hits in the different tracking stations and the p_T of the track. By training on simulated events a fake rejection rate of 60% was achieved while maintaining 99% efficiency.

The final stage is the rejection of clone tracks. Clones can be created in a single pattern-recognition algorithm, or more commonly from the redundancy in pattern-recognition algorithms. Clones are identified from their shared hits in each subdetector, though only the subdetectors where both tracks have hits are considered. Ultimately, the track with the most hits is kept and the other is discarded.

Particle Identification and Neutral Reconstruction

The identification of muons at HLT2 is performed using the same algorithm as at HLT1, however the algorithm uses the full set of fitted tracks available after HLT2 reconstruction.

The RICH provides information for the discrimination of protons, pions, kaons and deuterons. The reconstruction algorithm calculates photon yields, expected Cherenkov angles, and estimates of the per-track Cherenkov angle resolution un-

der the mass hypotheses of the deuteron, proton, kaon, pion, muon and electron. All reconstructed tracks and Cherenkov photons in both RICH1 and RICH2 are considered. Finally, the algorithm returns a likelihood for each hypothesis.

Calorimeter information is used in the reconstruction of photons, electrons and π^0 mesons. A cellular automaton algorithm is used to construct clusters of energy deposits in the calorimeter which are then combined to determine the total energy of the particle.

Neutral particles are identified according to the isolation of clusters from reconstructed tracks. High energy photons and π^0 mesons cannot be distinguished as both appear as a single cluster, while low energy π^0 mesons produce a pair of well-separated clusters. Electron identification is performed by combining information from the isolation of ECAL clusters, the presence of energy clusters in the PS, energy deposited in the HCAL, and the identification of possible Bremsstrahlung photons [73].

3.3.4 Turbo Stream

With the physics event fully reconstructed at HLT2, it is questionable as to whether additional offline reconstruction is required. In response to this, the Turbo event stream was developed in 2015 for Run 2 data taking [77]. The Turbo stream allows for physics analysis to be performed online using candidates reconstructed in the trigger. This is achieved by the definition of Turbo trigger lines which select events according to specific decay criteria.

The identification of analysis-relevant particles means that it is possible to persist only these candidates to disk and for the rest of the event to be discarded. This reduces the event size by an order of magnitude, from an average of 70 kB in the Full stream to 5 kB in the Turbo. In Run 2, 2.5 kHz of the allowed 12.5 kHz trigger output rate was dedicated to the Turbo stream, this results in 20% of the trigger selections taking up a less than 2% of the total output bandwidth.

3.4 Offline Analysis

The majority of offline analysis at LHCb is performed using Ntuples of events selected by the analyst using the DaVinci application, which is based on the Gaudi framework [78]. The input to the DaVinci application is reconstructed data files in the DST or μDST format.

Prior to this, many analyses make use of a selection process known as stripping in which data is further filtered. Stripping lines define the selection criteria, grouped into common streams which are performed centrally in stripping campaigns. Alternatively, analysts can use the output of the Turbo stream to directly access the candidates reconstructed by the trigger.

Chapter 4

Measuring the Low-Mass Drell-Yan Cross-Section at LHCb

This chapter describes the measurement of dimuon production via the Drell-Yan mechanism using data taken at LHCb in 2016. The exact candidate selection and efficiencies are explained below, along with signal and background template production and fitting in order to extract the prompt signal.

4.1 Motivation

The Drell-Yan process of lepton pair production in proton-proton collisions (pp) is described in the Standard Model at leading order by an s-channel Z/γ^* exchange. At higher orders, the emission of a gluon can lead to the dilepton pair obtaining a transverse component to its momentum. Diagrams for the leading order and next-to-leading order are shown in figure 4.1.

Precise measurements of such a process can allow for accurate testing of partonic interactions and the structure of the proton. The study of this process has been fundamental in the development of theoretical perturbative calculations of quantum chromodynamics (QCD) at next-to-next-to-leading-order (NNLO). At leading order, the dilepton invariant mass, m_{ll}, and rapidity, y, are related to the momentum

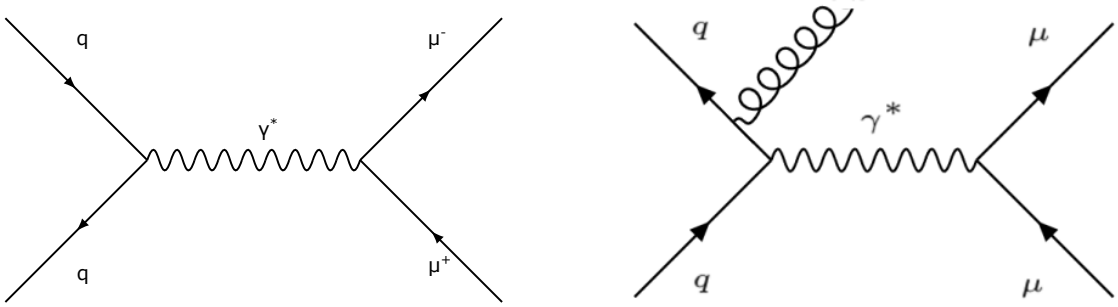

Figure 4.1: Feynman diagrams showing dimuon production via the Drell-Yan process at (left) leading order and (right) next-to-leading order, where the emission of a gluon gives the dimuon transverse momentum.

fractions, $x_+(x_-)$, of the interacting partons in the proton, such that

$$x_\pm = (m_{ll}/s)e^{\pm y} \tag{4.1}$$

where $\sqrt{s}$ is the collision centre of mass energy. Therefore, the dilepton rapidity and mass distributions are sensitive to the parton density functions (PDFs) of the proton.

Off-shell Z measurements at the LHC have reached a precision comparable or lower than the theoretical predictions, but they are restricted to regions of high momentum transfer, $Q^2 = m_{ll}^2$, and parton momentum fractions, $10^{-4} < x < 1$. Off-shell Drell-Yan production allows for a wider range of Q and x values. This provides information about PDFs at x values as low as 8×10^{-6} for momentum transfer $Q^2 = 25\,\mathrm{GeV}^2/c^4$.

The Drell-Yan process has been probed in the central rapidity region by both the ATLAS and CMS experiments at $\sqrt{s} = 7,\ 8$ and 13 TeV in the $|\eta| < 2.5$ region [79, 80]. LHCb is unique in being able to access the $2.0 < \eta < 4.5$ forward region. Measurements have previously been made by LHCb at $\sqrt{s} = 7$ TeV using 37.1 pb^{-1} of data recorded in 2010, through fits of the isolation parameter [81]. Now, additional data has been recorded in Run 2 at $\sqrt{s} = 13$ TeV with an integrated luminosity of around 5.4 fb^{-1}. This larger, more energetic sample along with new analysis techniques, pioneered by the LHCb dark photon search [82], motivate a

new measurement of the differential cross-section for Drell-Yan production through the dimuon channel. Here the measurement will be made as a double differential cross-section with respect to dimuon mass and rapidity, and a second measurement with respect to dimuon mass and transverse momentum, to probe higher order contributions, as shown in figure 4.1.

The cross-section for a given kinematic bin is expressed as

$$\sigma = \frac{\rho}{\mathcal{L}} \sum_{i=1}^{N} \frac{1}{\varepsilon_i} \tag{4.2}$$

where ρ is the signal purity, extrapolated through the template fits described in section 4.4, $\mathcal{L}$ is the integrated luminosity of the sample, i is the candidate number, N is the total number of candidates selected and ε_i is the per-candidate efficiency, evaluated using the methods described in section 4.3.

4.2 Selection

This measurement uses the 2016 proton-proton collision dataset recorded at LHCb with a total integrated luminosity of $1.63\,\text{fb}^{-1}$. Dimuon candidates are selected from the Turbo stream and recorded both in bins of candidate invariant mass versus rapidity, (m, y), and of mass versus transverse momentum, (m, p_T).

The selection requirements are motivated by the need to separate signal candidates from the expected background. Here, background dimuon candidates arise from two sources: the first is the reconstruction of muons produced in heavy flavour decays with a prompt vertex, while the second is the misidentification of hadrons, mostly pions, as the signal muons. Diagrams for these background processes are shown in figure 4.2 and they are discussed further in section 4.4.1.

Since the heavy flavour background is typically displaced, it can be reduced by requiring that candidates are consistent with having originated from the primary vertex; at LHCb this is achieved by requiring a low χ^2_IP value. The misidentification

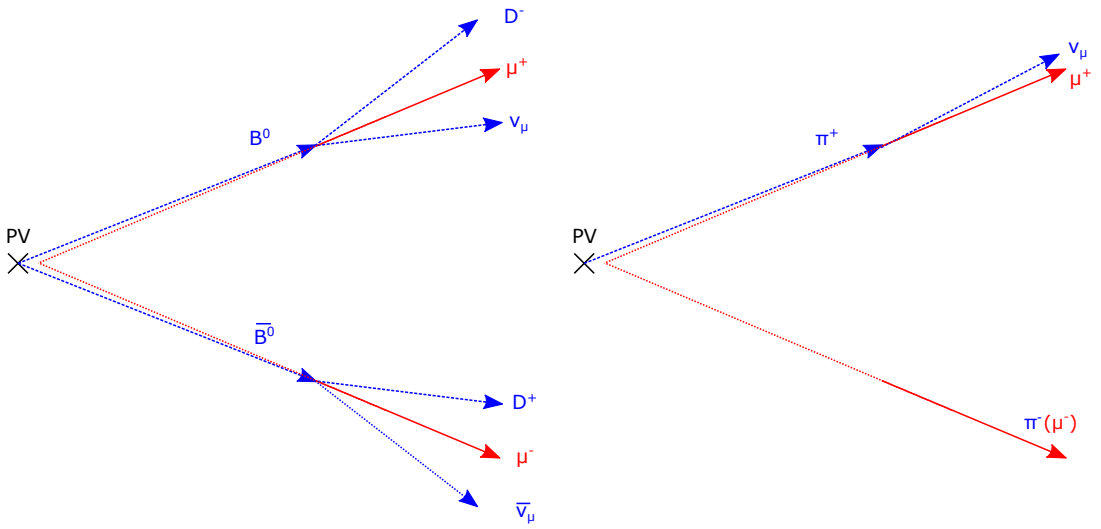

Figure 4.2: Diagrams outlining expected background processes. (Left) muons from heavy flavour decays can be reconstructed as originating from a single vertex, (right) pions can either be directly misidentified or decay in flight and the daughter muon is subsequently associated with a vertex.

background can be reduced by requiring good particle identification, which for muons at LHCb requires a high `ProbNNmu`, a value obtained from a neural network with inputs from tracking, RICH detectors, calorimetry and the MUON stations.

4.2.1 Trigger

It is required that dimuon candidates are Triggered On Signal (TOS) on the `L0DiMuon` line at the L0 trigger, `Hlt1DiMuonNoIP` at HLT1 and `Hlt2ExoticaPrmptDiMuonTurbo` at HLT2. The candidate requirements for these lines to fire the trigger are outlined in Table 4.1. Additionally, pairs of muons with the same electric charge, $\mu^{\pm}\mu^{\pm}$, referred to as same-sign dimuons, are selected for background studies.

Some requirements at the trigger level were changed over the course of data taking. To ensure uniformity, the harshest criteria are applied as post-selection requirements across the whole dataset.

The `L0DiMuon` line includes a global event cut which requires that the number of SPD hits recorded in the event is below 900 to veto busy events that require increased processing time. The efficiency of this requirement is difficult to evaluate

in data as it relies on non-pertubative QCD processes that are not well modelled in simulation. Since high pile-up events are most affected by this requirement, it is also required that there are fewer than three primary vertices distinguished by the VELO. This reduces the effect of the SPD hit efficiency and allows it to be calculated using no-bias data. This is discussed in further detail in Section 4.3.

Table 4.1: Requirements applied in the several trigger stages. Slight variations exist across the year for both HLT1 and HLT2. We enforce the stricter requirements across all the dataset offline, which simplifies the efficiency evaluation.

trigger	requirements
L0DiMuon	$\sqrt{p_{T_1} p_{T_2}} > 1.3 - 1.5$ GeV, $N_{\mathrm{SPD}} < 900$
Hlt1DiMuonNoIP	$p_{\mathrm{T}}(\mu) > 1$ GeV, $p(\mu) > 20$ GeV, $\chi^2_{\mathrm{trk}}/n_{\mathrm{dof}} < 3$, IsMuonTight, GhostProb < 0.2, DOCA < 0.2 mm, $\chi^2_{\mathrm{VX}}(\mu^+\mu^-) < 9$
Hlt2ExoticaPrmptDiMuonTurbo	$\chi^2_{\mathrm{IP}} < 6$, `ProbNNmu` > 0.95, $p_{\mathrm{T}}(\gamma^*) > 1$ GeV, $\chi^2_{\mathrm{FD}}(\gamma^*) < 45$
Hlt2ExoticaPrmptDiMuonSSTurbo	same as Hlt2ExoticaPrmptDiMuonTurbo but for $\mu^\pm\mu^\pm$ candidates

4.2.2 Offline Requirements

In addition to the requirements intrinsic in the trigger selection, a handful of extra requirements are made to the data candidates offline. The first of these is an increase in the muon transverse momentum selection, requiring both muons to have $p_{\mathrm{T}} > 1.5$ GeV/c, to limit the effects of a drop in efficiency at lower values. This also significantly reduces the misID background from softer pions.

In the LHCb dark photon search and other prompt dimuon analyses, the signal candidate is typically required to be well isolated. Since dimuon candidates produced in heavy flavour decays are generally part of a jet structure, they are produced in close association with a large multiplicity of other particles. Requiring a dimuon candidate to be produced in isolation therefore reduces the effect of these background processes, leading to a purer prompt sample.

Here, the cross-section measurement would be strongly dependent on the efficiency of any such isolation requirement. This would be difficult to evaluate accurately due to problems with simulating non-perturbative QCD processes that are not well understood, as well as the detector response. Additionally, it is shown in Section 4.4.4 that an isolation requirement would have a negligible effect on the final measurement in this analysis. As a result, no isolation requirements are made here.

Arising from the misidentification of hadrons as muons, a correlation effect was found in the LHCb dark photon search. Here, the double misID rate goes as the single muon probability when both muons share hits in the MUON chamber. This caused a feature in the dimuon mass spectrum at around 1.7 GeV/c^2, which could be removed by vetoing candidates where the two muons share tracks. The lower mass limit of this analysis is $m_{\mu\mu} \geq 5$ GeV/c^2, as theory predictions do not extend lower, and the effects of this feature do not reach that high. Therefore this veto is not necessary in this analysis.

4.3 Efficiencies

The efficiency of the selection of dimuon candidates is obtained using a combination of Monte Carlo simulation and corrections from control channels found in data. Each requirement made on a candidate gives rise to inefficiency which needs to be accurately accounted for when making a measurement. Here the total efficiency is divided into several terms, one for each requirement, listed below where each is evaluated given the previous cut:

- $\varepsilon(\text{nPV} < 3)$ - the efficiency of requiring that each event has fewer than three reconstructed primary vertices
- $\varepsilon(\text{nSPD} < 900)$ - the efficiency of the SPD requirement made in the L0 trigger line

- ε(tracking) - the efficiency of reconstructing signal tracks
- ε(vertex) - the efficiency of reconstructing dimuon decay vertices
- ε(PID & track quality) - the efficiency of additional requirements on the muon candidates such as ghost probability, track quality and PID (`ProbNNmu`)
- ε(L0) - the efficiency of requiring the `L0DiMuon` line is satisfied at the hardware trigger
- ε(HLT & offline) - the efficiency of requiring the `Hlt1DiMuonNoIP` and `Hlt2ExoticaPrmptDiMuonTurbo` lines are satisfied in the software trigger, as well as additional offline requirements (flight distance and impact parameter)

The first two requirements, nPV < 3 and nSPD < 900, are referred to as global event cuts (GECs) as they are applied to the whole event without any requirement on the signal candidate. The remaining cuts are evaluated using simulation with an additional correction obtained from data. A summary of these efficiencies and corrections is given in table 4.2. The evaluation of all efficiencies are described below.

Table 4.2: Summary of the efficiencies from simulation used as candidate weights and their corrections as the ratio of data to simulation. The average value, $< \varepsilon >$, is shown as an indication of the relative effects of each contribution to the total candidate efficiency. The product of each of these efficiencies gives the total weight for a candidate.

	Type	**Data**	**Parametrisation**	**Control channel**	$< \varepsilon >$
Tracking	Efficiency	Simulation	$(p_{\mathrm{T}}, \eta, \phi)$ single muon	Signal + Υ	95%
Tracking (low p_{T})	Correction	Data	(p, η) single muon	J/ψ	99%
Tracking (high p_{T})	Correction	Data	(p_{T}, η) single muon	Z	99%
Vertexing	Efficiency	Simulation	(y, m) dimuon	Signal	$\geq 99.5\%$
PID, χ^2_{IP} & track qual.	Efficiency	Simulation	$(p_{\mathrm{T}}, \eta, \phi)$ single muon	Signal + Υ + J/ψ	75%
PID & track qual.	Correction	Data	$(p_{\mathrm{T}}, \eta, \phi)$ single muon	Z + J/ψ	92%
L0DiMuon	Efficiency	Simulation	$(m, y, \sqrt{p_{\mathrm{T}} \times p_{\mathrm{T}}}, \log(p_{\mathrm{T}}))$ dimuon	Signal + Υ + Z	85%
L0DiMuon	Correction	Data	$(< \eta(\mu) >, \sqrt{p_{\mathrm{T}} \times p_{\mathrm{T}}})$ dimuon	J/ψ + Z	105%
HLT1+HLT2	Efficiency	Simulation	$(m, y, \sqrt{p_{\mathrm{T}} \times p_{\mathrm{T}}}, \log(p_{\mathrm{T}}))$ dimuon	Signal + Υ + Z	85%
HLT1	Correction	Data	$(\min(\eta^{\mu^+}, \eta^{\mu^-}), \sqrt{p_{\mathrm{T}} \times p_{\mathrm{T}}})$ dimuon	J/ψ + Z	97%

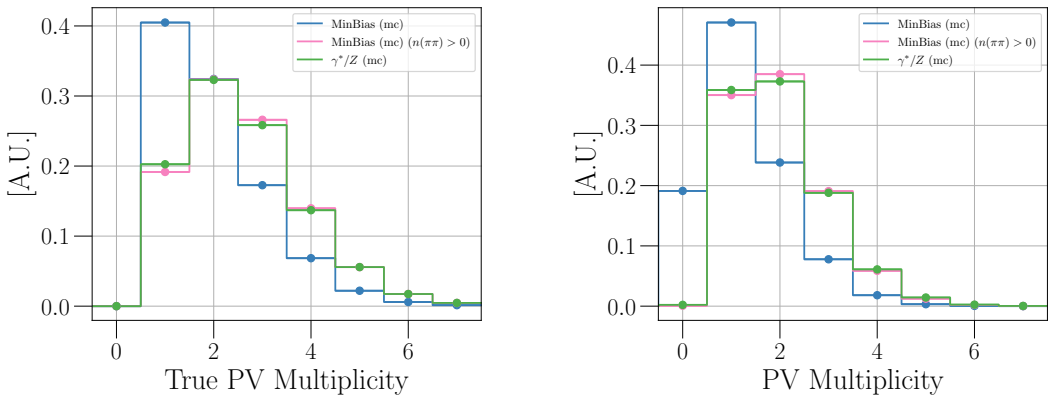

Figure 4.3: (Left) true and (right) reconstructed nPV distributions in simulation for minimum bias, $Z/\gamma^* \to \mu\mu$ and minimum bias with a requirement of a reconstructed $\pi\pi$ pair that satisfy the signal kinematic requirements.

4.3.1 Primary Vertex Multiplicity Requirement

The first requirement made on signal candidates is that they pass the `L0DiMuon` hardware trigger line. A global requirement is therefore made that the event records fewer than 900 hits in the SPD subdetector. This vetoes high multiplicity events where tracks and vertices are more likely to be misreconstructed. This introduces an inefficiency that is dependent on non-perturbative QCD processes which are not well understood and therefore it is difficult to simulate. The detector response is also difficult to predict for high occupancy events.

The effect of this requirement can be reduced by selecting lower multiplicity events. Since track multiplicity can be related to the number of collisions in the bunch crossing, this selection can be made by requiring a low number of primary vertices in the event.

The efficiency of an nPV < 3 requirement is evaluated using no-bias data. The technique is validated by comparing minimum bias and Drell-Yan MC samples, as shown in figure 4.3. Requiring that the minimum bias sample includes a reconstructed $\pi\pi$ pair brings the sample into good agreement with the signal MC. The

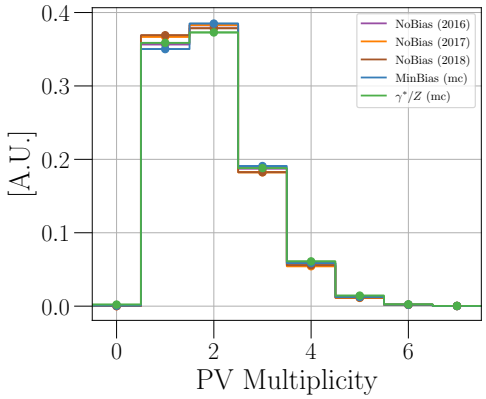

Figure 4.4: The reconstructed nPV distribution in no-bias data with the reconstructed dipion requirement, compared to the minimum bias and $Z/\gamma^* \to \mu\mu$ MC samples.

reconstructed primary vertex multiplicity in no bias data is shown in comparison to the MC samples in figure 4.4.

The efficiency of requiring fewer than three primary vertices in each event is shown in figure 4.5. The integrated efficiency in the Drell-Yan MC sample is seen to be in agreement with no-bias data with a 0.2% uncertainty. In general, the efficiency is flat as a function of the dimuon kinematics, though a slight trend is observed in the rapidity spectrum. A total uncertainty of 0.5% is assigned, giving an efficiency of $73.8 \pm 0.5\%$ for the 2016 dataset.

4.3.2 SPD Multiplicity Requirement

As discussed above, the complex effects of the requirement on the event SPD multiplicity can be reduced by the introduction of an additional requirement on primary vertex multiplicity. Figure 4.6 shows both the difficulty in accurately representing SPD multiplicity in simulation, and how the nPV < 3 requirement shifts the distribution to lower values.

The efficiency of the SPD requirement in a sample of $Z \to \mu\mu$ decays is shown in figure 4.7. Applying the primary vertex multiplicity requirement increases the efficiency in data from 98.8-99.5% to greater than 99.9%, with a flat distribution in

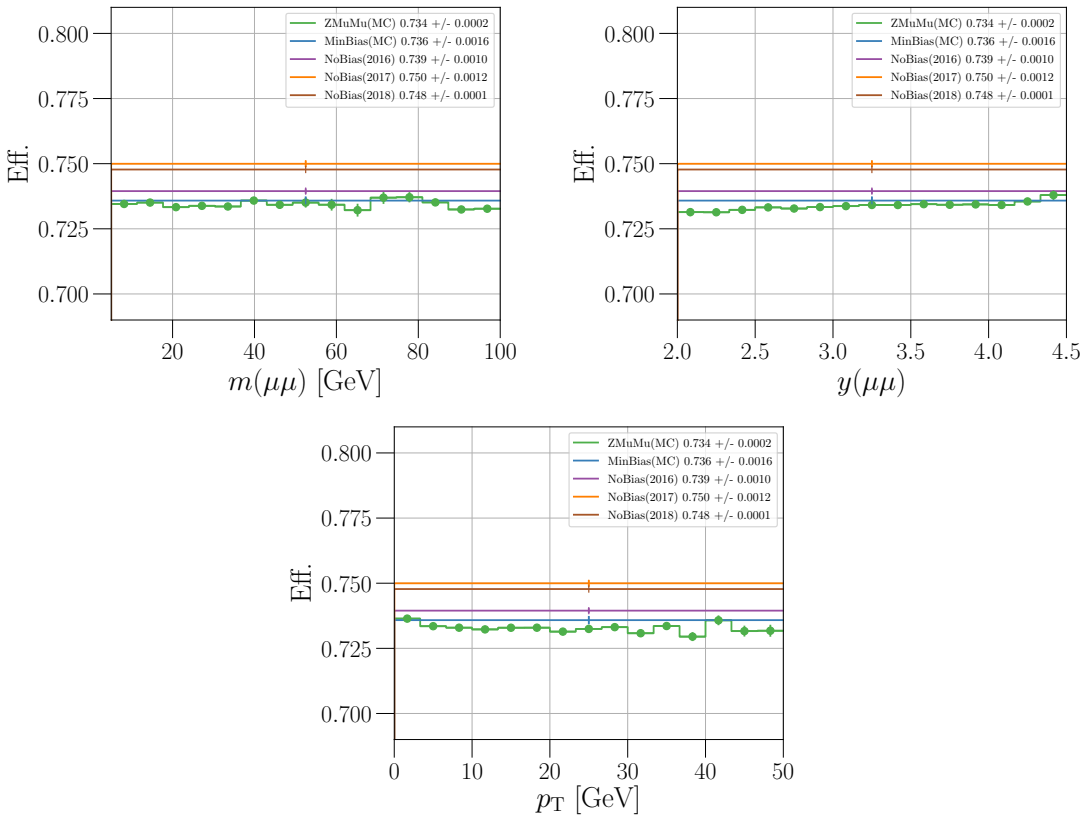

Figure 4.5: The efficiency on the nPV < 3 requirement for the Drell-Yan MC sample compared to the minimum bias MC and no bias data as a function of dimuon (top-left) mass, (top-right) rapidity and (bottom) p_{T}.

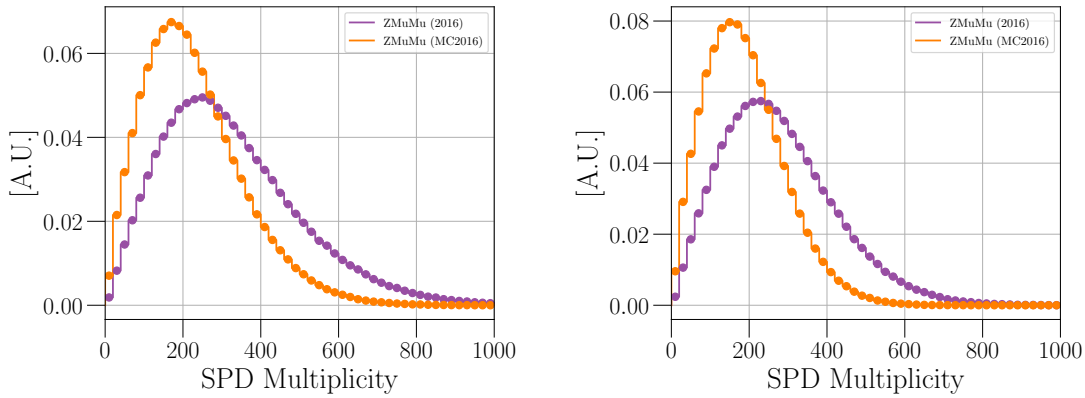

Figure 4.6: The SPD multiplicity of events containing a $Z \to \mu\mu$ decay (left) before and (right) after the nPV < 3 requirement in simulation and data.

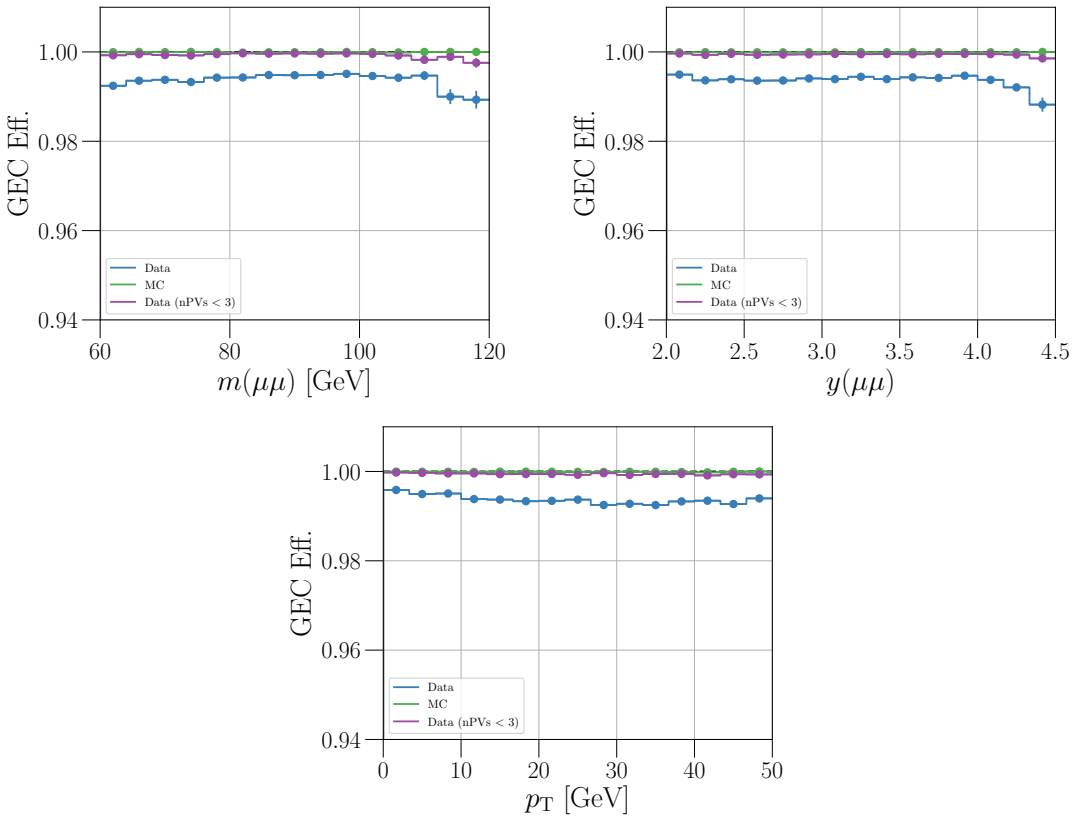

Figure 4.7: The efficiency of the nSPD < 900 requirement in events with a fully reconstructed $Z \to \mu\mu$ decay in simulation and data with and without the primary vertex multiplicity requirement as a function of dimuon (top-left) mass, (top-right) rapidity and (bottom) p_{T}.

each of the dimuon kinematic variables.

4.3.3 Track Reconstruction and Vertexing

The absolute efficiency of reconstructing single muon tracks and the efficiency of reconstructing the dimuon decay vertex are obtained from simulation. Corrections to the reconstruction efficiency are obtained in data using J/ψ and Z decays.

Tracking Efficiency

The efficiency of reconstructing single muon tracks is obtained from simulation in bins of muon pseudorapidity, transverse momentum and ϕ. The efficiency is averaged over both positively and negatively charged muons. Here, the signal Monte Carlo sample is supplemented by an $\Upsilon(1S) \to \mu\mu$ sample, which is consistent with the signal sample, to increase the total statistics. A selection of projections of the track reconstruction efficiency is shown in figure 4.8, where uncertainties are statistical. There is a little variation in the efficiency in some regions of η and ϕ, though the efficiency is generally $\sim 95\%$ per track.

Tracking Corrections

To account for potential differences in track reconstruction efficiency between data and simulation, correction factors are applied to the efficiencies obtained from simulation. These take the form of the ratio of efficiency found in data against that in Monte Carlo.

Here, the sample is split into low and high p_{T} samples with the divide at 20 GeV/c. In the low p_{T} sample, the ratios are obtained using J/ψ decays. The tag and probe method is used, where a particle is selected from an event that meets the requirements, known as the tag, then another particle is selected as the probe. The efficiency is then the number of probes that meet the requirement, divided by the total.

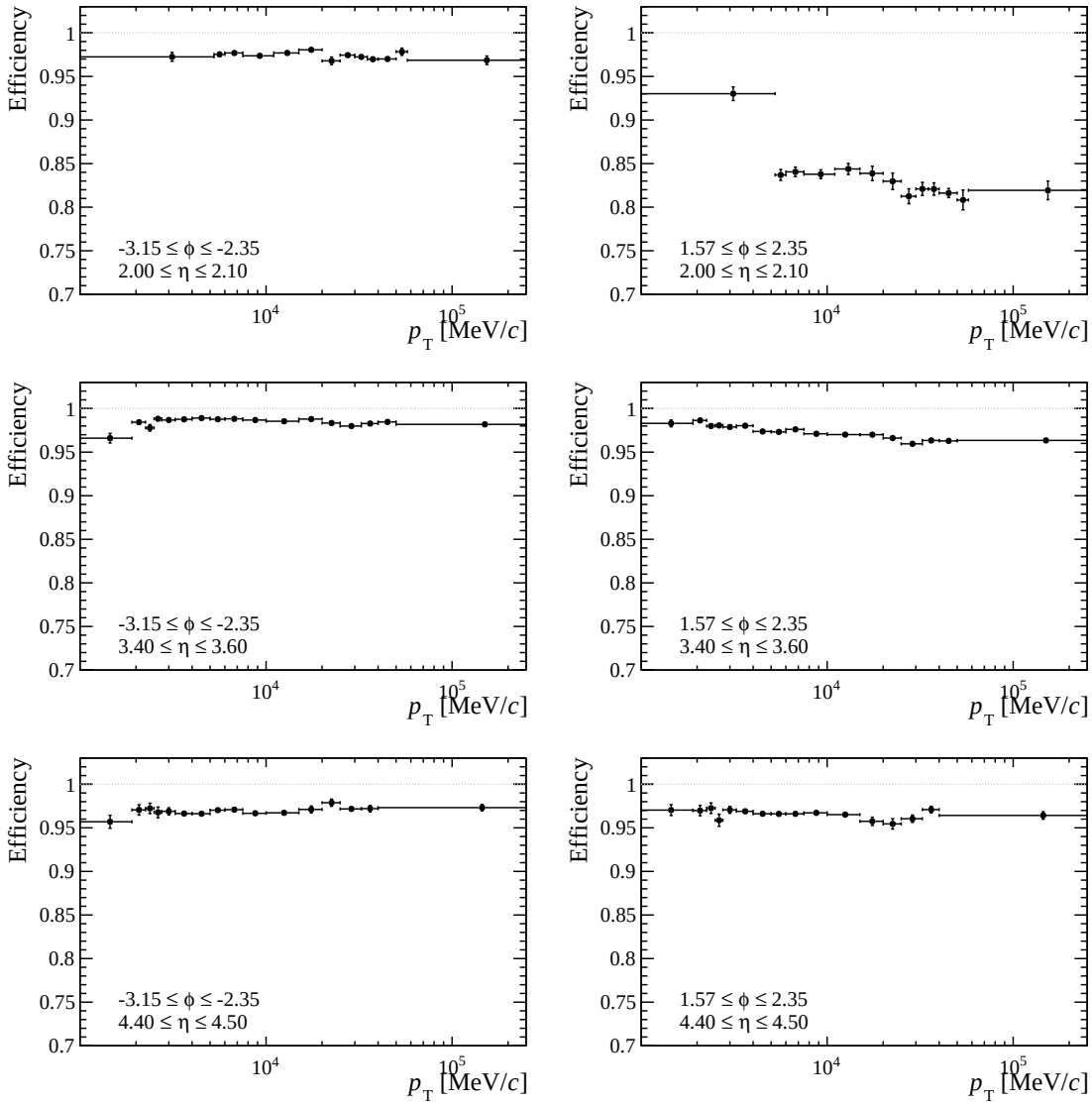

Figure 4.8: Track reconstruction efficiency in 2016 signal MC (with $\Upsilon(1S)$ decays) as a function of muon p_{T} in a selection of η, ϕ bins.

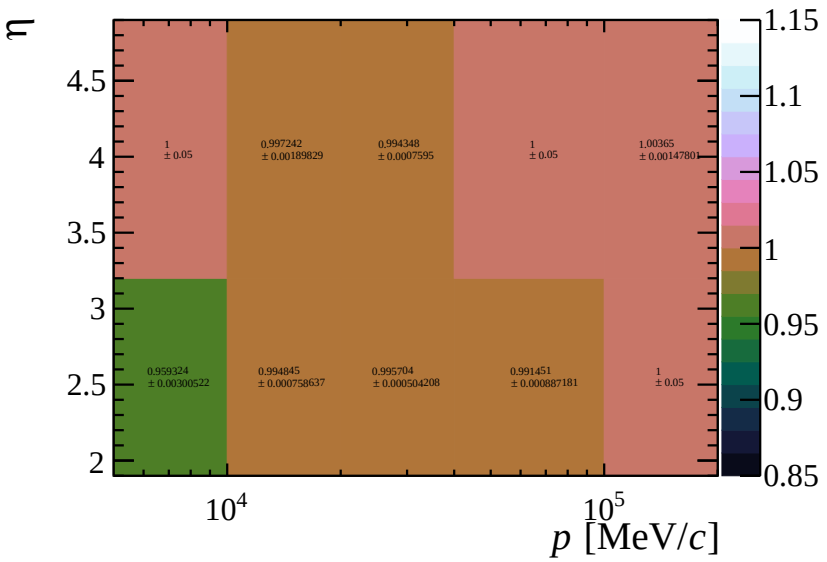

Figure 4.9: Ratio of tracking efficiencies in data to MC for muons with $p_{\mathrm{T}} < 20$ GeV/c.

The corrections are then shown in figure 4.9. In the high p_{T} sample, the tag and probe method is used again with Z decays, as in reference [83], and the ratios are shown in figure 4.10.

Vertexing

In addition to the individual track reconstruction, the efficiency of calculating the two-body decay vertices must also be considered. This efficiency is obtained from simulated Drell-Yan events described in bins of dimuon mass, $\log p_{\mathrm{T}}$ and rapidity. The efficiencies are shown for a selection of mass bins in figures 4.11 and 4.12. This gives a high efficiency of around 99.5% with only a little variation, ascribed as an uncertainty of 0.5%. As expected, lower efficiencies are found in forward decays with low mass and small opening angles.

4.3.4 PID and Track Quality Requirements

Particle identification (PID) requirements are made at the second level of the software trigger, HLT2. The efficiency of these requirements and of the track quality

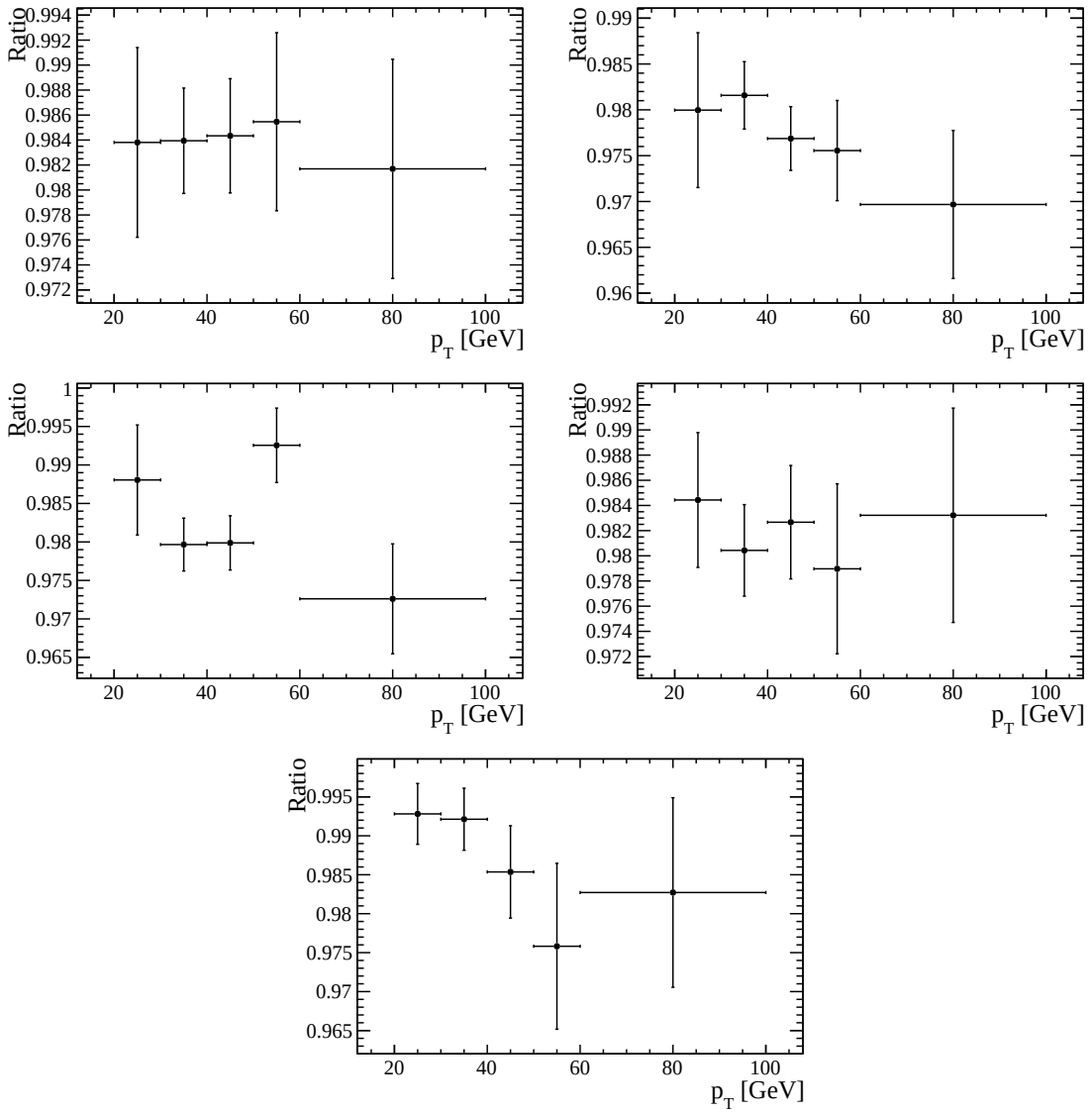

Figure 4.10: Ratio of tracking efficiencies in data to MC for muons with $p_{\mathrm{T}} > 20$ GeV/c in five equally spaced pseudorapidity bins for $2.0 < \eta < 4.5$.

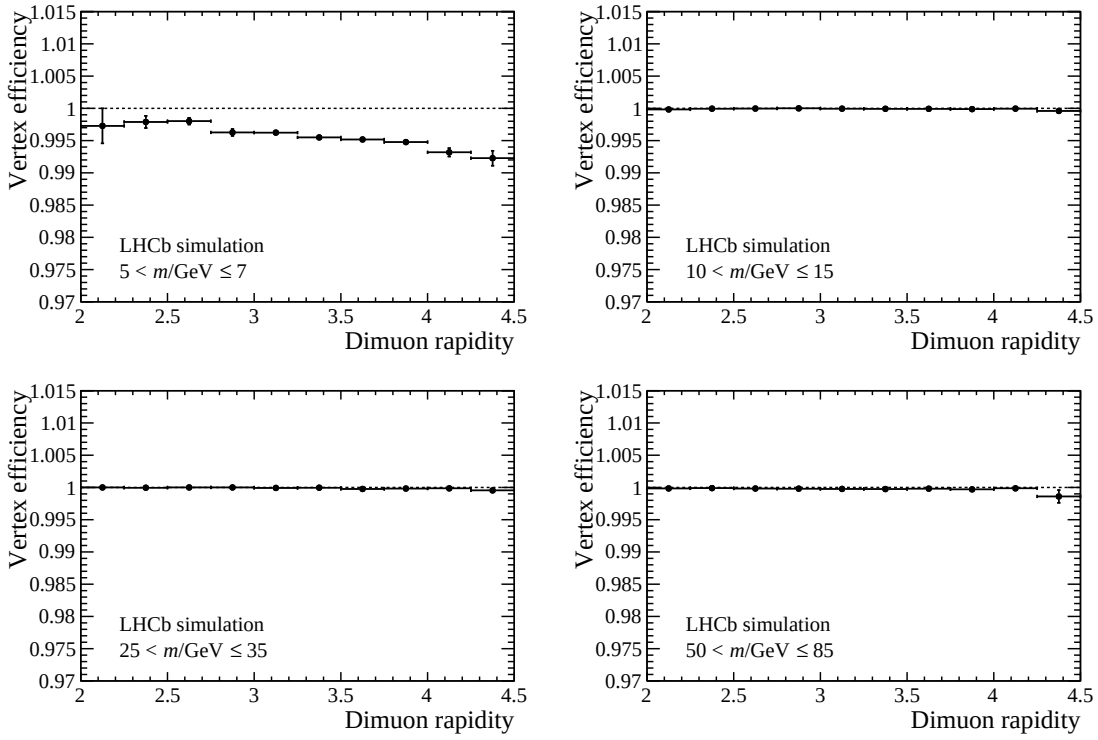

Figure 4.11: Efficiency of vertex reconstruction as a function of dimuon rapidity in a selection of mass bins.

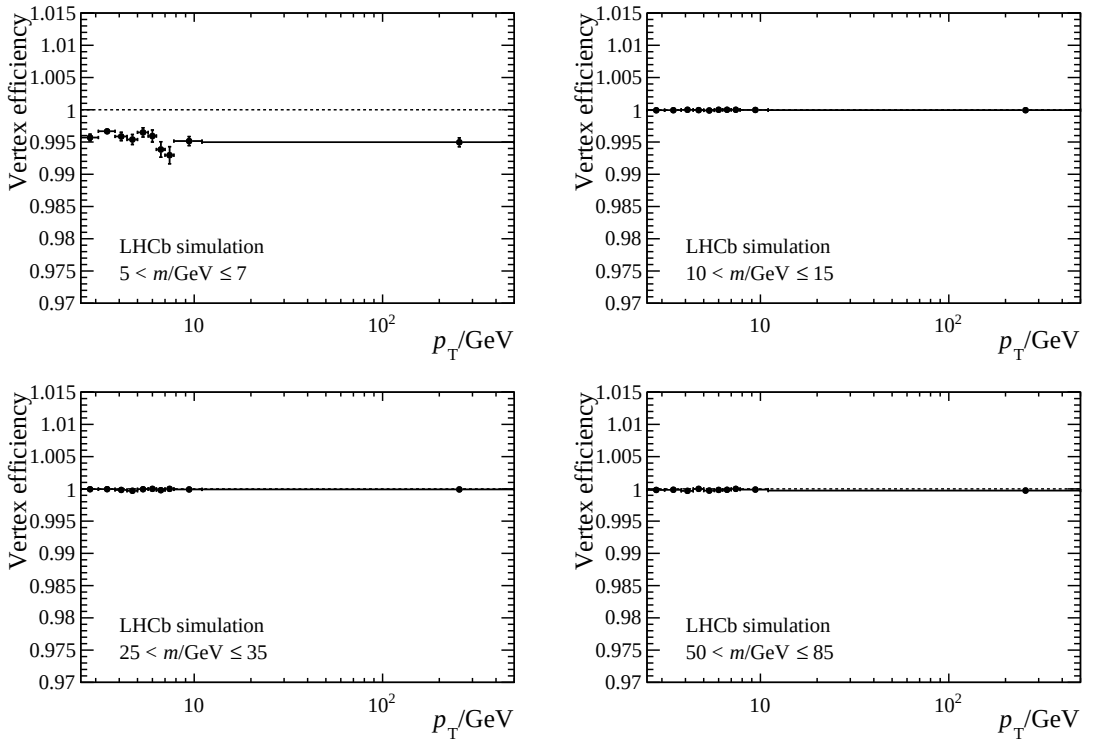

Figure 4.12: Efficiency of vertex reconstruction as a function of dimuon p_{T} in a selection of mass bins.

requirements are evaluated together in simulation and corrected using J/ψ and Z control samples in data. The efficiency is evaluated for the following requirements:

- `isMuonTight`
- Track ghost probability < 0.20
- `ProbNNmu` > 0.95
- $\chi^2_{\text{IP}} < 6$

Results of Simulation

The PID requirements, especially the `ProbNNmu` requirement, introduce a large drop in efficiency around $15 < p_{\text{T}} < 30$ GeV/c, which can be reproduced in simulated muons matched with generator-level hits, indicating that this is an issue in the `ProbNNmu` algorithm itself. Furthermore, it is not expected for the PID efficiency to be high here as the algorithm is not explicitly tuned for this region. A sample of simulated $\Upsilon(1S)$ and Z/γ^* decays is used to evaluate the efficiency in bins of single muon p_{T}, η and ϕ. Finer binning is used in the region of the efficiency drop to better define the shape. A selection of bins are shown in figure 4.13.

Correction Factors

The PID efficiencies can also be determined in data using a tag and probe method using J/ψ and Z samples. This has the benefit of the *probe* track being free of track quality requirements and also unbiased by L0 and HLT1 decisions, which are correlated with both PID and track quality requirements. In both cases, an event is only used when the *tag* track satisfies both the `L0MuonEW` and `Hlt1SingleMuonHighPT` decisions. These events are then binned in muon p_{T} and η.

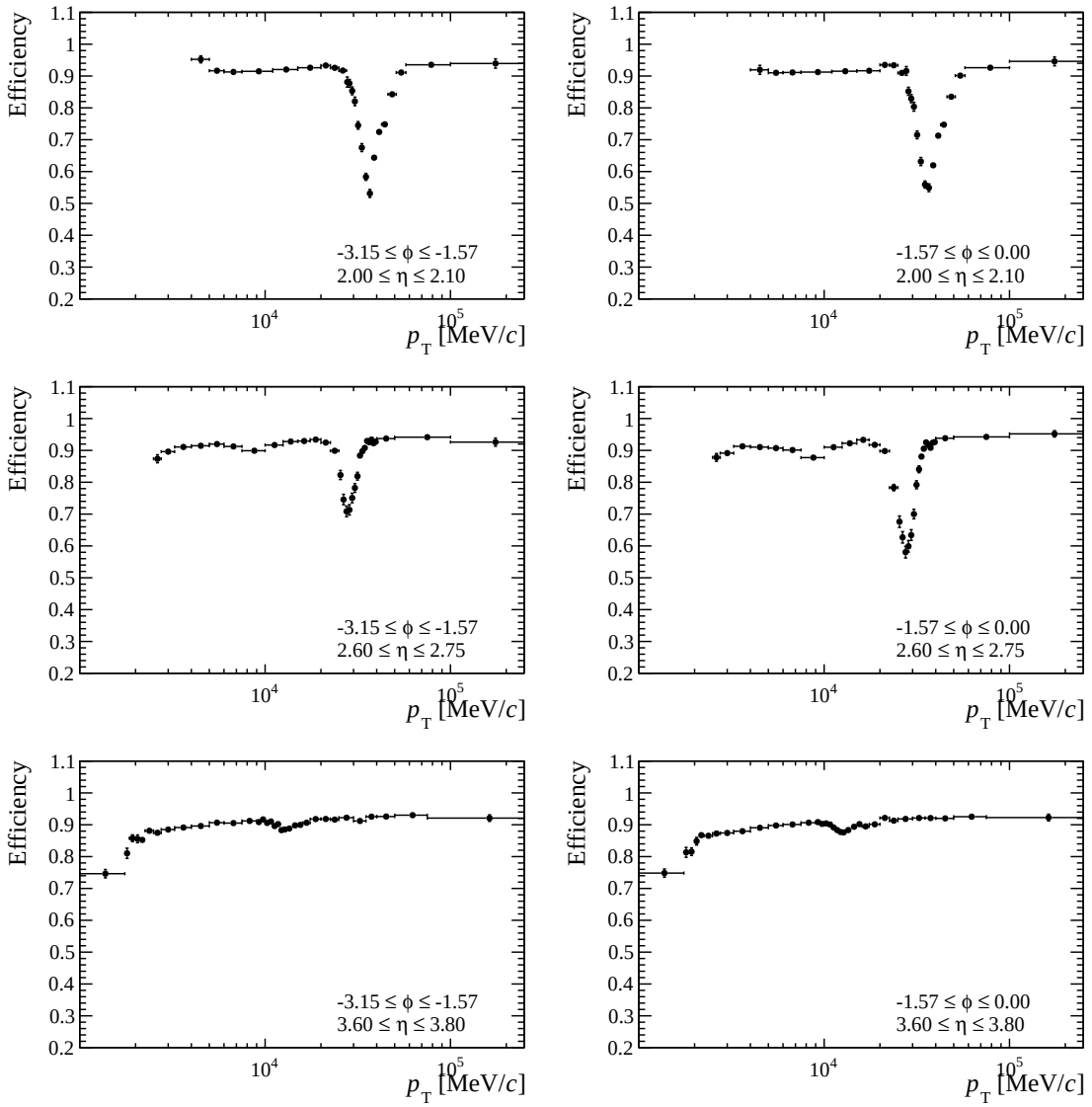

Figure 4.13: Efficiency of PID and track quality requirements as a function of muon p_{T} in a selection of η and ϕ bins. The efficiency exhibits a drop around $15 < p_{\mathrm{T}} < 30$ GeV/c, which is consistent with the performance of the `ProbNNmu` algorithm.

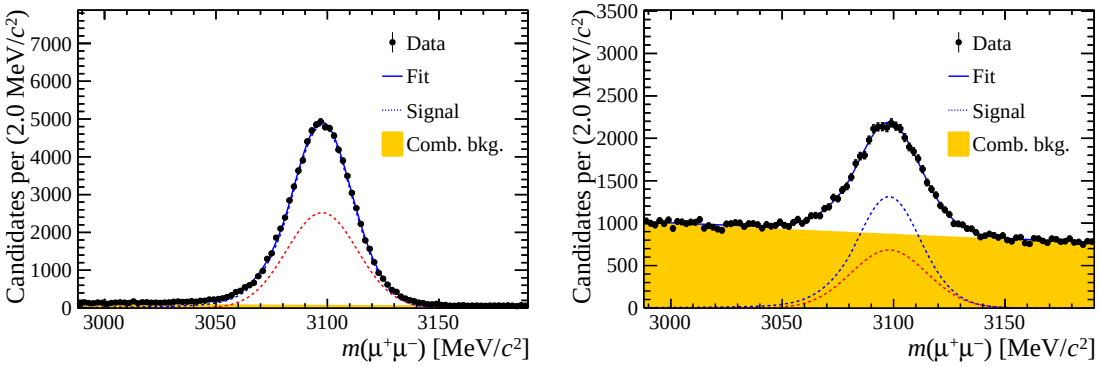

Figure 4.14: Invariant mass distribution in data at the J/ψ mass for events that (left) pass and (right) fail the PID and track quality requirements.

Analysis Method for J/ψ Decays

The signal yield in data for $J/\psi \to \mu\mu$ decays is obtained through a binned simultaneous maximum likelihood fit in dimuon mass. Here the efficiency is left as a free parameter to be determined. The signal component is defined by the sum of a Gaussian and a Crystal Ball function. The relative fraction between the Gaussian and Crystal Ball functions are constrained such that one does not dominate. This is achieved by applying a Gaussian constraint of width 5% on their relative difference. The background component is defined as exponential. An example fit is shown in figure 4.14. This method provides precise efficiencies up to $p_{\mathrm{T}} \leq 15$ GeV/c; though in some η bins this extends to $p_{\mathrm{T}} \leq 20$ GeV/c.

Analysis Method for Z Decays

For higher p_{T} muons, the efficiency is obtained from $Z \to \mu\mu$ decays where the *tag* muon is selected from the `StrippingWMuLineDecision` stripping line. The second muon is selected from the underlying event and is required to have $p_{\mathrm{T}} > 20$ GeV/c and $\chi^2_{\mathrm{IP}} < 25$, such that it is consistent with having originated from the primary vertex.

Here, the simultaneous fit uses both data and simulated events such that the efficiency *ratio* can be extracted. This is required to control non-trivial changes to

the shape of the Z peak across the kinematic intervals. The shape of the signal peak is determined from simulation, though convolved with a Gaussian to allow for resolution effects in data. The background shape is determined from same sign data using a kernel density estimator [84]. Example fits are shown in figure 4.15.

Results

The measured efficiency ratios from both the J/ψ and Z methods are shown in figure 4.16 in bins of p_{T} and η. The phase space overlap between the two samples shows a good agreement. These ratios are then applied as a correction to the absolute efficiency from simulation.

4.3.5 Hardware Trigger

The dimuon line at the Level-0 (L0) hardware trigger makes requirements on the SPD multiplicity of the event and on the product of the transverse momenta of the two muon candidates, as $\sqrt{p_{\mathrm{T}}(\mu^+) \times p_{\mathrm{T}}(\mu^-)}$. The former requirement is considered as a global event cut and the efficiency is evaluated in Section 4.3.2. Since tracks are only partially reconstructed and no fit performed at L0, momentum resolution is worse than in the offline analysis. As such, candidates that fail the momentum requirement in the trigger may be above threshold when fully reconstructed, potentially significantly so, leading to an inefficiency in the selection.

Absolute Efficiency

The efficiency of the L0 requirement is obtained using a simulated sample of $\Upsilon(1S)$ and signal decays. The effect of the `L0DiMuon` line is correlated with PID requirements as described in Section 4.3.4. To avoid bias, it is required that the simulated events pass both the PID and track quality requirements. The efficiency is then binned in dimuon mass, $\log p_{\mathrm{T}}(\mu\mu)$, dimuon rapidity and $\sqrt{p_{\mathrm{T}}(\mu^+) \times p_{\mathrm{T}}(\mu^-)}$. The binning of the last of these is fine in the threshold region, where

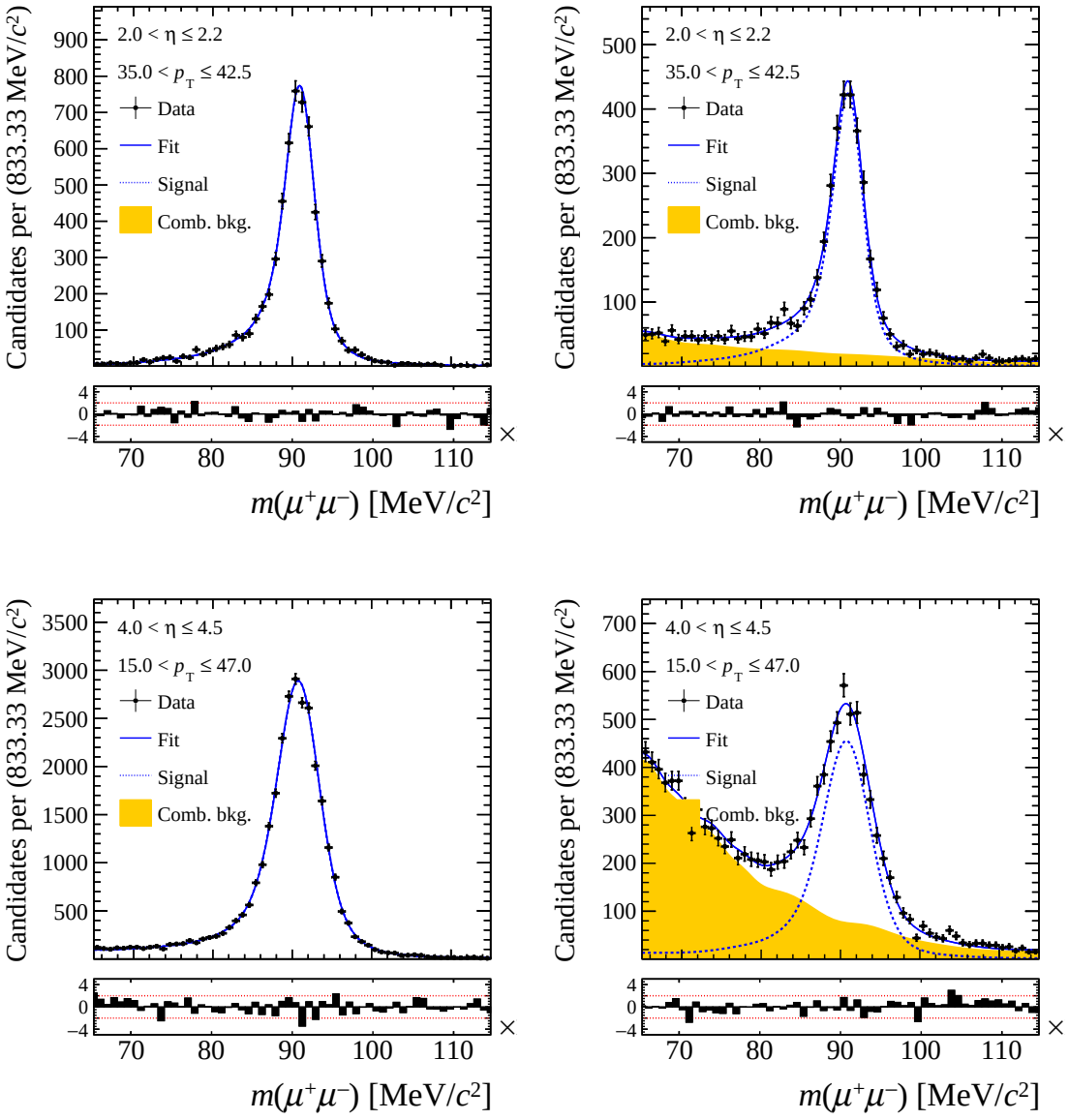

Figure 4.15: Invariant mass distribution in data at the Z mass for events that (left) pass and (right) fail the PID and track quality requirements. Two kinematic bins are shown to illustrate the differences in signal shape.

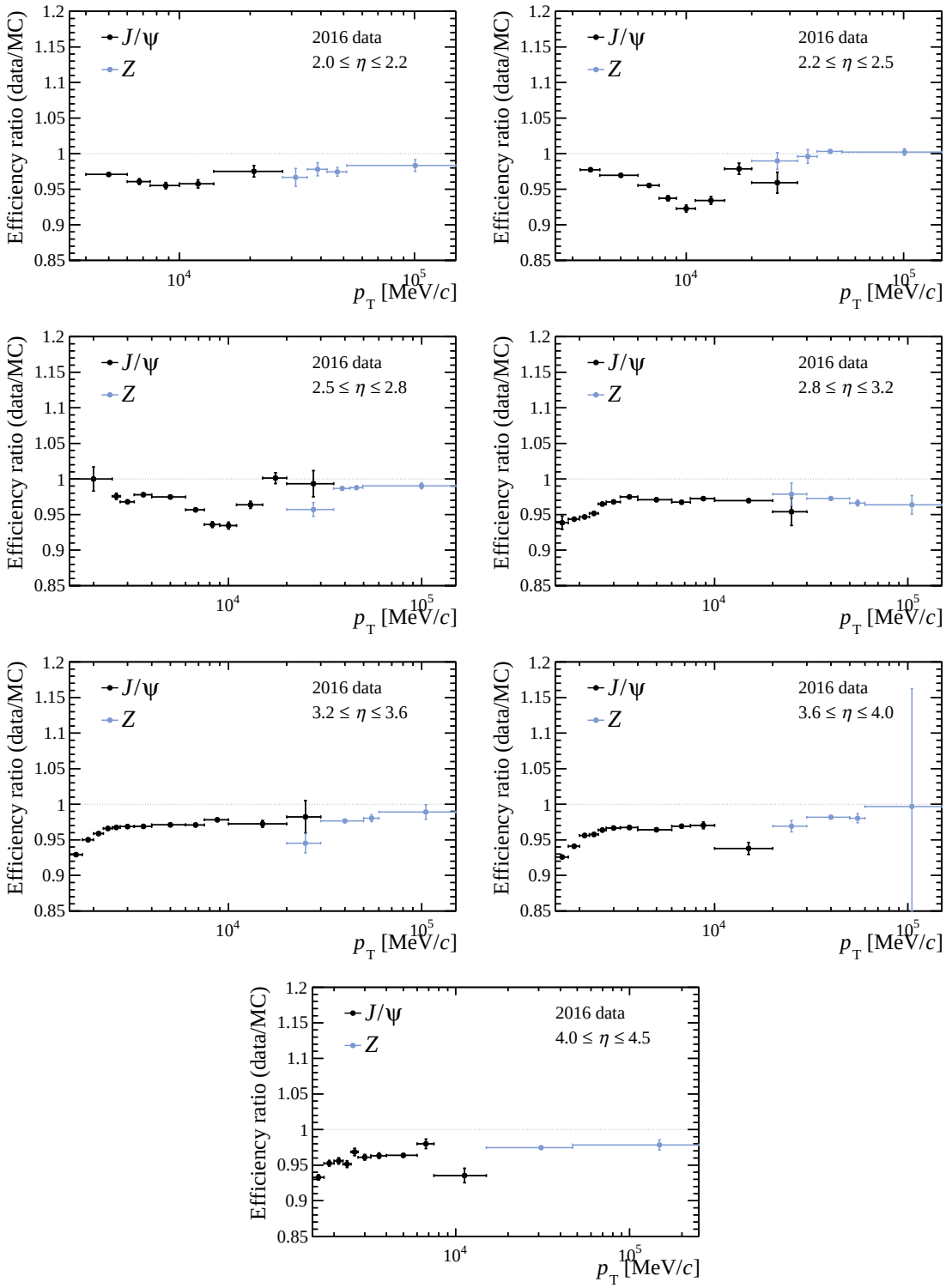

Figure 4.16: Efficiency ratios for data to simulation for PID and track quality requirements as a function of muon p_T, in bins of η.

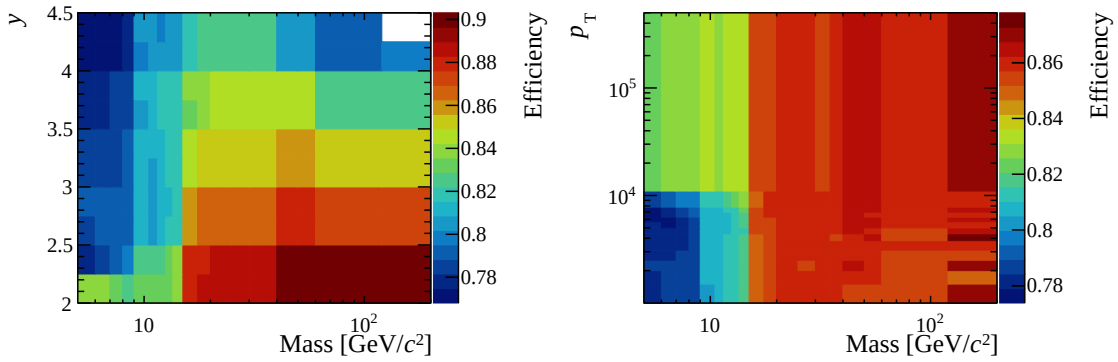

Figure 4.17: Average L0 efficiency from simulated $\Upsilon(1S)$ and signal decays binned in (left) dimuon mass and rapidity (right) dimuon mass and transverse momentum.

$\sqrt{p_{\mathrm{T}}(\mu^+) \times p_{\mathrm{T}}(\mu^-)} \leq 10$ GeV/c^2. The average efficiency of the L0 requirement is shown in figure 4.17.

Corrections from Detached J/ψ Decays

The corrections to the simulated efficiencies are evaluated for low p_{T} candidates using J/ψ decays from data. The corrections are binned in average muon pseudorapidity and $\sqrt{p_{\mathrm{T}}(\mu^+) \times p_{\mathrm{T}}(\mu^-)}$. Since J/ψ mesons are typically produced in the decays of heavy flavour particles, they are often accompanied by other particles that may also fire the hardware trigger. Detached J/ψ decays, typically produced in B meson decays, are ideal for testing the efficiency of the `L0DiMuon` line as there is often a signal from a B decay that can independently trigger the event.

Selected candidates must pass both the nSPD requirement and the PID and track quality requirements. Candidates are unbiased by the L0 trigger by requiring that they are TIS of the `L0Global` line. Candidates are also selected by the HLT1 track MVA lines. Simultaneous likelihood fits are performed as a function of dimuon mass in bins of $\sqrt{p_{\mathrm{T}}(\mu^+) \times p_{\mathrm{T}}(\mu^-)}$ and dimuon pseudorapidity. The fits use both data and simulated data and include both the efficiency and efficiency ratio as free parameters in the fit. An example fit is shown in Figure 4.18.

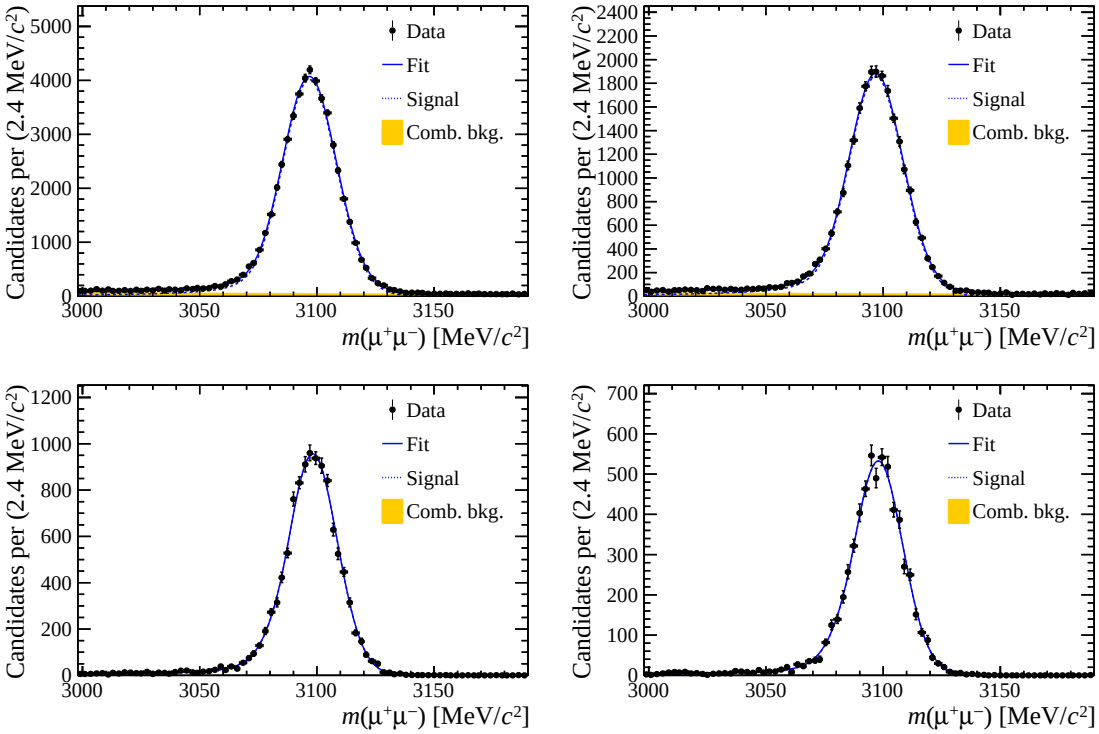

Figure 4.18: Simultaneous likelihood fit of dimuon mass around the J/ψ resonance in (top) data and (bottom) simulation for candidates that (left) pass and (right) fail the L0 dimuon trigger requirements.

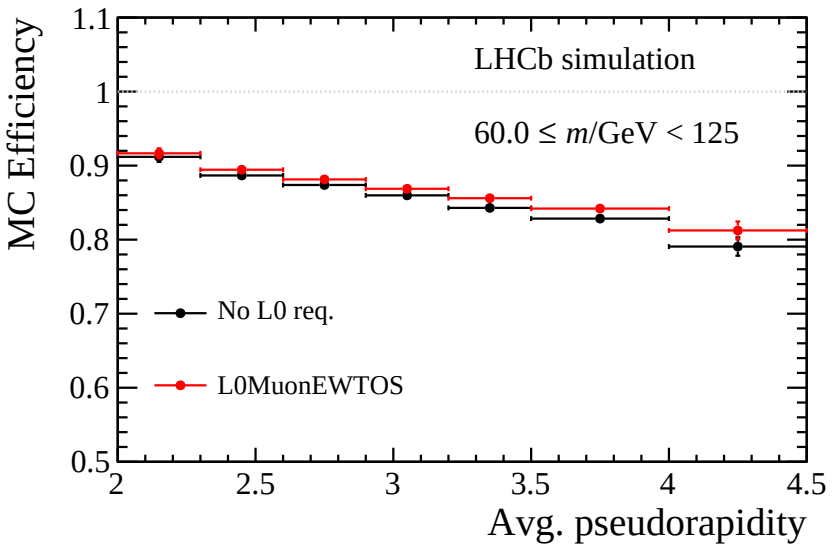

Figure 4.19: Absolute efficiency of the L0 dimuon trigger from simulation with and without the `L0MuonEW` requirement on one of the products.

Corrections from Z Decays

The correction factors for high p_T candidates are obtained from Z decays in data. Unlike the J/ψ sample, requiring other particles in the event to have fired the trigger (requiring TIS on `L0Global`) greatly reduces the sample size. Candidates are instead required to have at least one muon pass the `L0MuonEW` line. The bias introduced by this requirement is limited as PID requirements have already been made on the candidates. The effect of this on the simulated *absolute* efficiency is shown in figure 4.19 where it is found to be at the percent level. The effect is further reduced when the correction is presented as a ratio.

The efficiency ratio is determined using a "cut and count" method in the mass window from 85 to 97 GeV/c^2, where all candidates are assumed to be signal and the efficiency is given by the number that pass the requirements divided by the total. With the `L0MuonEW` requirement, the Z sample is considered large enough and pure enough for this to be acceptable.

Correction Results

The measured corrections are shown in Figure 4.20. Results from $\Upsilon(1S)$ decays are also shown, however, requiring TIS on the hardware trigger reduces the statistics of this sample and it is only included for illustration. The behaviour as a function of the p_T product is relatively flat, though there is a trend in pseudorapidity.

4.3.6 Software Trigger

Most of the requirements made by the HLT1 and HLT2 trigger lines have already been considered by the per-track and L0 requirements analysed above. Further inefficiency is however expected from the differences between HLT1 and HLT2 reconstruction as well as from requirements on the flight distance, impact parameter and reconstructed vertex quality.

Efficiencies from Simulation

The full HLT efficiency is determined in a similar way to the hardware trigger, using a signal Monte Carlo simulation and binned in dimuon mass, rapidity and the logarithm of the dimuon transverse momentum. The results are given in figure 4.21 and show an average efficiency of about 85% with a per bin variation of around 5% and little p_{T} dependence. At high rapidity, low statistics limit the use of a finer binning in p_{T}.

Correction Factors

The correction factors for differences in the efficiency of the HLT1 requirement between simulation and data are determined using J/ψ, $\Upsilon(1S)$ and Z decays with all the previously mentioned requirements applied. The corrections are given as a ratio between data and simulation in bins of the average muon pseudorapidity. The samples are combined using a fit and the resulting corrections are given in table 4.3.

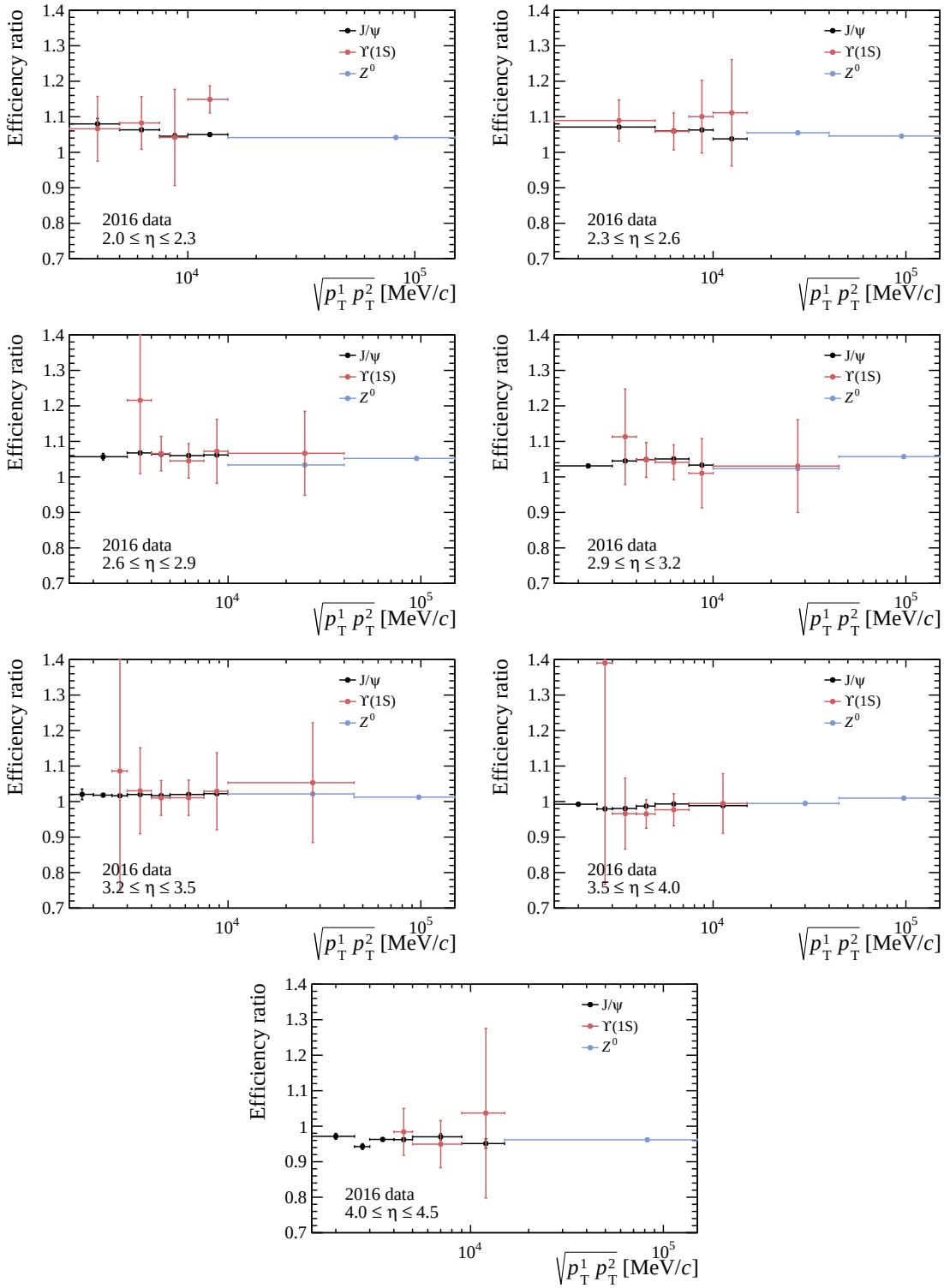

Figure 4.20: Measured efficiency data/MC ratios for the L0 dimuon trigger as a function of the geometric mean of muon transverse momentum in bins of average pseudorapidity.

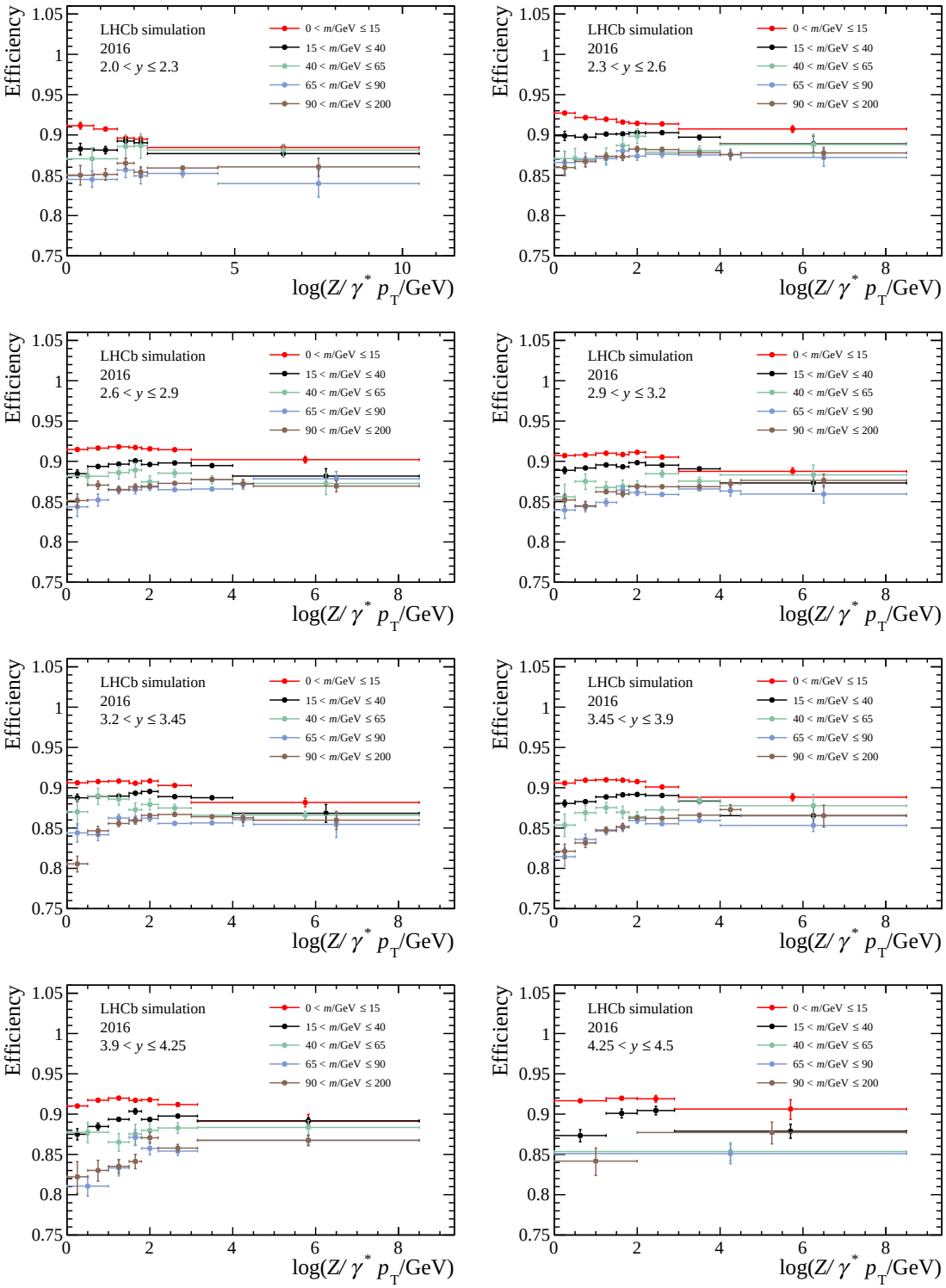

Figure 4.21: Measured efficiency for the HLT1, HLT2 and offline requirements in bins of dimuon mass and rapidity, shown as a function of the logarithm of the dimuon transverse momentum.

Table 4.3: Efficiency corrections for the HLT1 requirements in bins of average muon pseudorapidity.

η interval	Correction [%]
2.0-2.5	96.9 ± 0.6
2.5-2.9	97.7 ± 0.4
2.9-3.4	97.9 ± 0.4
3.4-3.9	98.2 ± 0.4
3.9-4.5	98.2 ± 0.4

4.3.7 Efficiency Weighting

Ultimately, template fits are performed to extract the Drell-Yan signal from the dataset. This is performed in bins of dimuon mass and rapidity, or in bins of dimuon mass and transverse momentum. As a result, all other information regarding the dimuon candidate and the constituent muons is lost. Since many of the requirements are made using this information, it is necessary to consider these efficiencies prior to fitting.

This is achieved by weighting the dataset by the per candidate efficiency, such that the total integral in a given fit bin is given by

$$N = \sum_i \frac{1}{\varepsilon_i} \tag{4.3}$$

where ε_i is the product of all the non-GEC efficiencies, which are summarised in table 4.2. The average efficiency for candidates in a selection of bins is shown in figure 4.22.

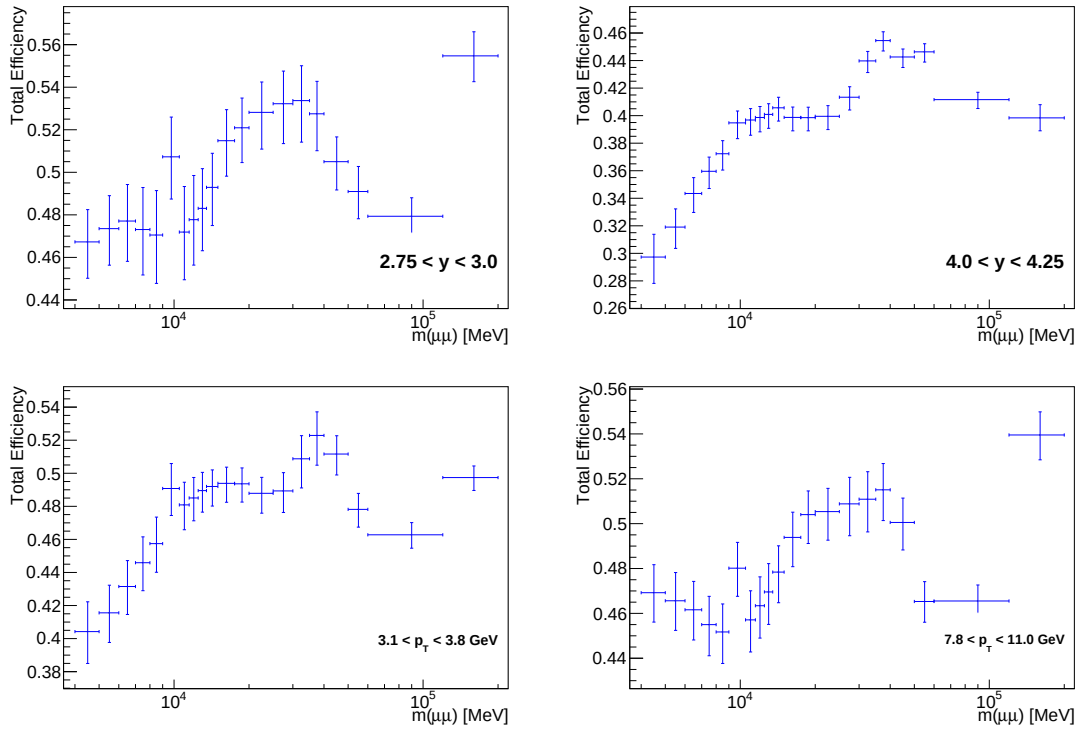

Figure 4.22: The average efficiencies of 2016 dimuon candidates as a function of dimuon mass in a selection of (top) rapidity, (bottom) transverse momentum bins. The uncertainties are evaluated using the methods described in section 4.5.2.

4.4 Signal Extraction

The Drell-Yan process gives an explicitly prompt signal. The size of this signal is extracted from the data selection by fitting templates that represent the signal and background processes to the data distribution and measuring their relative contributions. The fits are performed as a function of the minimum muon χ^2_{IP}, a variable that offers good separation between prompt and displaced candidates. The process for producing the templates and fitting the data is described in this section.

4.4.1 Backgrounds

The prompt Drell-Yan signal has two main sources of background dimuons in the selected dataset: dimuons reconstructed from displaced decays and from tracks misidentified as muons.

MisID Background

The misidentification (MisID) background arises from hadrons, most typically pions, being misidentified as muons. The two main mechanisms for this are known as decay-in-flight and punch-through.

The former dominates lower momentum pions which may travel a shorter mean distance in the laboratory frame before decaying to a muon and neutrino. If the subsequent hits in the MUON chambers are consistent with the pion track, it is possible for the track to be misidentified as a muon.

Conversely, punch-through dominates at higher momentum where the pion is energetic enough to penetrate all the way through to the MUON chambers and directly cause hits. Misidentified pions can be reconstructed as prompt dimuon candidates in a number of ways:

- 2×MisID - a pair of MisID pions are reconstructed with a prompt vertex
- MisID + HF - a MisID pion forms a vertex with a genuine muon from a heavy flavour decay
- MisID + $W \to \mu$ - As above but with a muon from a real W decay
- MisID + $Z \to \mu$ - As above but one muon from the Z decay falls outside of the detector acceptance

Displaced Background

The displaced background arises from pairs of muons produced in heavy flavour quark decays which can be erroneously reconstructed as originating from a prompt decay vertex. These candidates most frequently arise from the decay chains of $b\bar{b}$ and $c\bar{c}$ pairs produced in the pp collision:

- $b \to \mu + \bar{b} \to \mu$
- $b \to c\mu \to \mu\mu$
- $c \to \mu + \bar{c} \to \mu$

Here a hadronisation model is used, though this has a minimal impact on the final template. Also considered are the decays of ditaus from heavy flavour meson and Z boson decays:

- $Z/\gamma^* \to \tau\tau \to \mu\mu$
- $\Upsilon(1S)/\Upsilon(2S)/\Upsilon(3S) \to \tau\tau \to \mu\mu$
- $\chi_{b0}/\chi_{b1}/\chi_{b2} \to \Upsilon(1S)\gamma \to \tau\tau \to \mu\mu$

4.4.2 Template Production

The Drell-Yan signal yield is extracted via a template fit of the data as a function of $\sqrt{\chi^2_{\text{IP}}}$. The templates for both the prompt signal and the displaced and MisID backgrounds are produced through several methods which are described below.

MisID Template

Both the shape and size of the MisID background is determined by the selection of same-sign dimuons ($\mu^\pm\mu^\pm$), obtained from the same dataset as the opposite-sign sample, using the HLT2 trigger line `Hlt2ExoticaPrmptDiMuonSSTurbo` described in Table 4.1.

The same-sign sample is dominated by misidentified tracks with reconstructable vertices. Same-sign candidates can also be constructed from real muons, notably from semi-leptonic decays of pairs of oscillating neutral B mesons. The contribution of these candidates is estimated using a Pythia simulation. The production cross-section of same-sign dimuon candidates that satisfy the kinematic criteria and the prompt vertex requirements is found to be approximately 2 nb at generator level. As detector effects are not included, prompt vertex requirements are based on a parameterisation of the IP resolution, discussed in further detail in the following section regarding the displaced template production.

The same-sign dipion production cross-section is also estimated following a similar procedure and found to be approximately 7 mb. The single track misID probability is taken to be 1% [81]. This gives a 2×MisID dipion cross-section of approximately 700 nb, dominating the contribution from oscillating neutral B mesons, which account for less that 0.3% of selected candidates in generator level studies.

As a result, it is assumed that all candidates in the same-sign dimuon sample originate from misidentified pion tracks and misreconstructed vertices. At higher masses, $m_{\mu\mu} > 4\,\text{GeV}$, the rate of dipion production is the same in the same-sign and opposite-sign selection. This allows the use of the same-sign min $\sqrt{\chi^2_{\text{IP}}}$ distribution as the MisID template shape.

Displaced Template

There are two stages for generating a min $\sqrt{\chi^2_{\text{IP}}}$ template from data: first obtaining a set of true IP values from simulation and secondly smearing these by the IP resolution, $\sigma(\text{IP})$, to account for detector and reconstruction effects.

Simulations performed with Pythia 8.2 are used to obtain the true IP distributions for each heavy flavour decay listed in Section 4.4.1. The simulations are run using the Monash tune and with `hardccbar` and `hardbbbar` hard process settings. To ensure an even coverage in lower cross-section regions, the simulation is performed

in bins of the propagator $\hat{p}_T$ and weighted by the production cross-section.

Pairs of opposite sign muons are selected that satisfy the fiducial requirements, i.e. if they are considered prompt, $\mathrm{IP}/\sigma(\mathrm{IP}) < 6$, and have a reconstructable vertex, $\mathrm{DOCA} < 2\,\mathrm{mm}$ and $\mathrm{DOCA}/\sigma(\mathrm{DOCA}) < 9$. Here, the resolution on the IP is defined as $\sigma(\mathrm{IP}) = (11.6 + 23.4/p_{\mathrm{T}}[\mathrm{GeV}])$ [mm], a parameterisation obtained from previous detector performance, and $\sigma(\mathrm{DOCA}) = \sqrt{\sigma(\mathrm{IP},\mu_1)^2 + \sigma(\mathrm{IP},\mu_2)^2}$ [85]. The $\mathrm{IP}/\sigma(\mathrm{IP})$ for μ_1 vs μ_2 is then recorded as a two-dimensional histogram to preserve the correlations between both muons. This differs from the dark photon analysis, where the second muon $\mathrm{IP}/\sigma(\mathrm{IP})$ was sampled from a uniform distribution.

The true $\mathrm{IP}/\sigma(\mathrm{IP})$ distributions then need to be corrected for detector and reconstruction effects that are present in the observed data. This is achieved through a data driven method using the selected dimuon dataset. For each dimuon candidate:

1. $\mathrm{IP}/\sigma(\mathrm{IP},\ \mathrm{sim})$ for each muon is sampled from the Pythia simulation
2. $\mathrm{IP}/\sigma(\mathrm{IP},\ \mathrm{sim})$ for each muon is independently smeared in the parallel and perpendicular by sampling a standard Gaussian distribution centred on the sampled value and zero respectively, as demonstrated in figure 4.23
3. $\sigma(\mathrm{IP},\ \mathrm{data})$ is obtained from each muon by taking $\mathrm{IP}/\sqrt{\chi^2_{\mathrm{IP}}}$ from data
4. The smeared $\mathrm{IP}/\sigma(\mathrm{IP},\mathrm{sim})$ is multiplied by $\sigma(\mathrm{IP},\ \mathrm{data})$ to obtain the smeared IP
5. The new vector IP is calculated using a uniformly sampled ϕ and the $\mathrm{IP}/\sigma(\mathrm{IP},\ \mathrm{data})$ of both muons is calculated
6. The minimum muon $\mathrm{IP}/\sigma(\mathrm{IP},\ \mathrm{data})$ is recorded as min $\sqrt{\chi^2_{\mathrm{IP}}(\mu)}$ in bins of the dimuon mass and rapidity or mass and transverse momentum
7. These steps are repeated ten times for each event

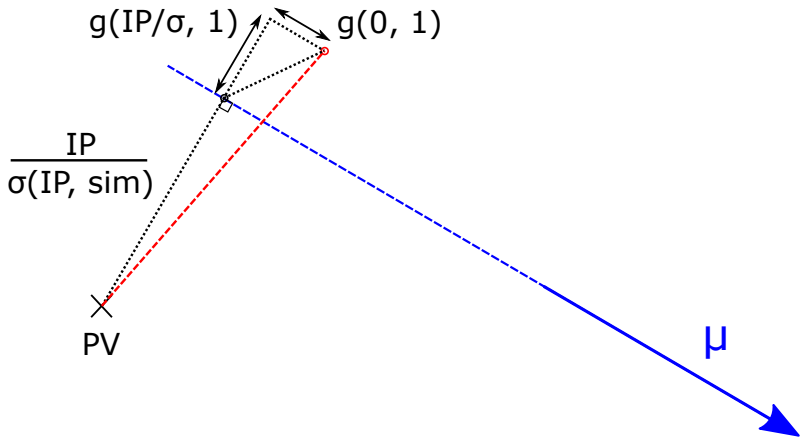

Figure 4.23: Diagram of smearing the true IP/σ(IP) from simulation to account for detector and reconstruction effects. The new IP/σ(IP) is the sum in quadrature of the samples of two Gaussian distributions, $g(\mu, \sigma)$, representing the components parallel and perpendicular to the vector IP.

Through this method, templates are produced for each decay type simulated. The full displaced template is then made by summing the component templates weighted by their production cross-sections. An example template showing the relative heavy flavour contributions is shown in figure 4.24.

This generative method makes the assumption that the detector effects are distributed according to a Gaussian distribution. Since these effects are dominated by multiple scattering of the muons in the detector material, they are better described by a Moliere distribution with wider tails. As such, a non-Gaussian tails correction is applied to all generated templates.

These corrections are obtained by comparing the shape of generated prompt templates to the min $\sqrt{\chi^2_{\rm IP}(\mu)}$ distributions in data at the mass of the $\Upsilon(1S)$ and Z resonances, which are produced in almost exclusively prompt decays.

The generated prompt templates are produced using the same method as the displaced templates described above, except the true IP is taken to be zero. The normalised min $\sqrt{\chi^2_{\rm IP}(\mu)}$ distributions are taken within $3\sigma_{\mu\mu}$ of the PDG $\Upsilon(1S)$ and Z masses[1]. The ratio of the generated templates to the data distributions at the

[1]The values of $\sigma_{\mu\mu}$ are taken from the Dark Photon analysis and were obtained from mass fits to dimuon resonances [86]

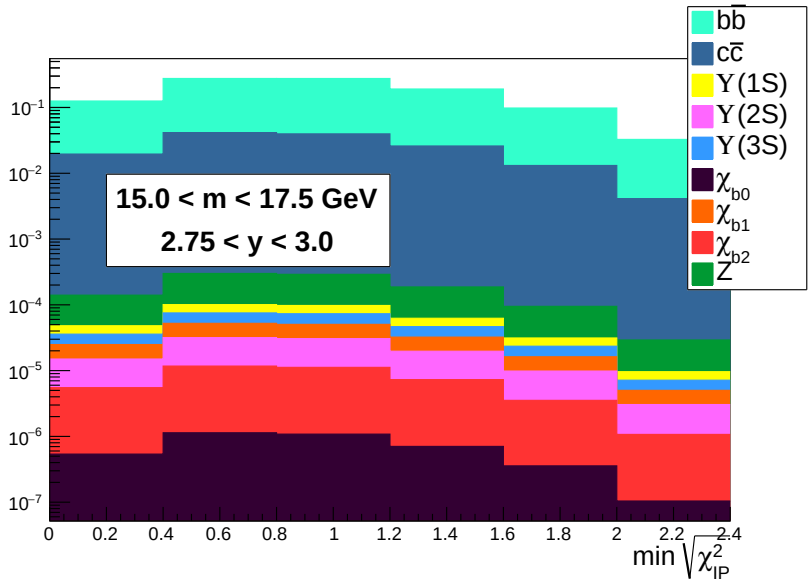

Figure 4.24: Example of the relative contributions of the heavy flavour decay modes to the total displaced template.

resonances are then interpolated as a function of $1/m_{\mu\mu}$ to obtain the non-Gaussian tails corrections for generated templates.

The $1/m_{\mu\mu}$ assumption arises from the effects of the multiple scattering of the muons, which depends on $1/p_{\mathrm{T}}$ of the muons as less energetic particles are deflected more in material interactions. Since the dimuon mass is correlated with the single muon momenta and the interpolation is made as a function of mass, a $1/m$ relationship is chosen here. This assumption is validated by a cross-check in Monte Carlo simulation and is discussed in detail below.

Prompt Template

The prompt signal template is produced from data using an interpolative method. The method is very similar to that used to obtain the non-Gaussian tails correction for the displaced template.

Here the normalised min $\sqrt{\chi^2_{\mathrm{IP}}(\mu)}$ distributions in data are directly interpolated between the $\Upsilon(1S)$ and Z resonances as a function of $1/m_{\mu\mu}$ in the chosen bins of dimuon y or p_{T}. The validity of this method can be seen by comparing the final distributions to a generated prompt template, weighted by the non-Gaussian tails

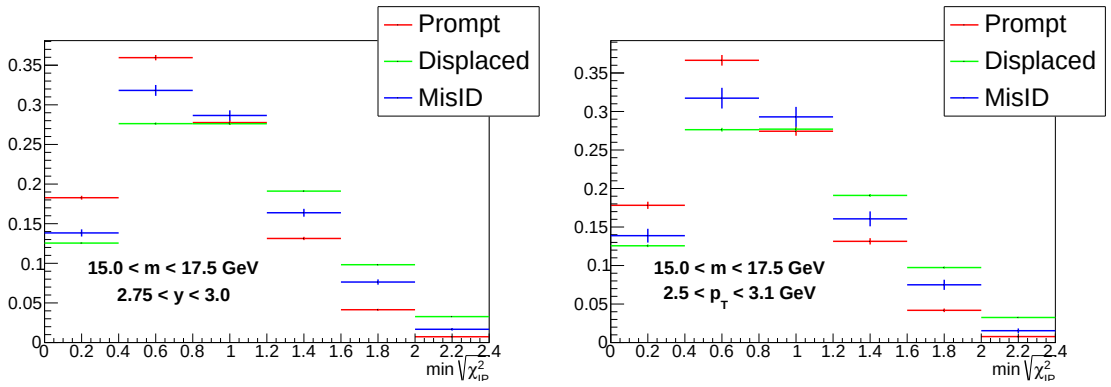

Figure 4.25: Normalised prompt, displaced and MisID templates produced in example bins; the prompt template peaks towards lower values of min $\sqrt{\chi^2_{\text{IP}}}$ while the displaced template peaks at higher values and the MisID template lies in between.

corrections, as shown below.

A comparison of the prompt, displaced and MisID template shapes is shown in Figure 4.25.

4.4.3 Uncertainty on Templates

The accuracy of the min $\sqrt{\chi^2_{\text{IP}}(\mu)}$ fits is dependent on the shape of the templates and the accuracy of their representation of the physical processes. As such, the uncertainty on the template shapes is considered within the fits. These uncertainties arise from the template production methods, the true IP simulations and the assumption of the $1/m_{\mu\mu}$ function used in the interpolative methods.

The methods of estimating these uncertainties are described here. The uncertainties themselves are included in the fit minimisation by allowing the template shapes to vary within an envelope defined by the uncertainties and controlled by nuisance parameters.

Template Production Uncertainty

The accuracy of the template production methods can be understood by comparing the template shapes to those produced by alternative methods.

First, the uncertainty on the prompt template shape is estimated by comparing

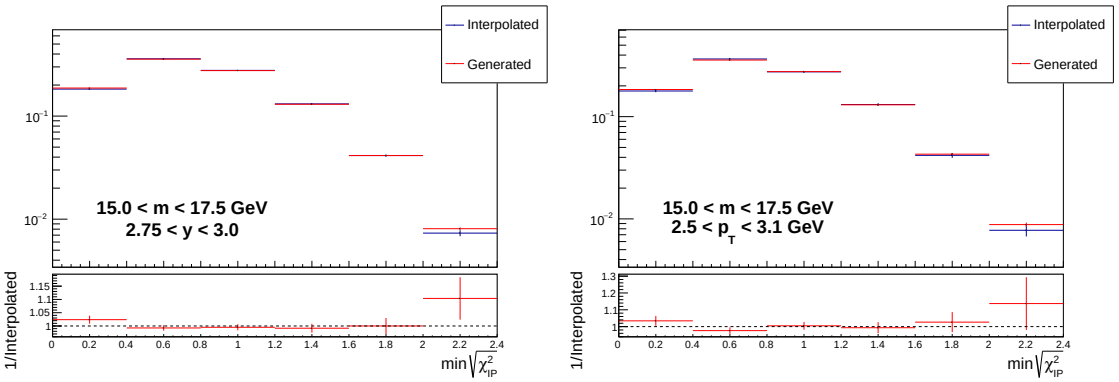

Figure 4.26: Comparison of prompt templates produced using the nominal interpolation method and the alternative generative method, shown in example bins.

the nominal interpolated template to a template generated from data. The generated prompt template is produced using the same method as the displaced template, with the true IP taken as zero, and weighted by the same non-Gaussian tails correction. The difference between the interpolated and generated prompt templates is then taken to be the shape uncertainty on each given bin, as shown in figure 4.26.

The shape of the displaced template is dependent on the processes included in the true IP simulation and their relative cross-sections. As a result, the displaced template is dominated by dimuon candidates from $b\bar{b}$ and $c\bar{c}$ decays, which account for more than 99% of the total cross-section considered.

An uncertainty on the template shape can be estimated by varying the relative $b\bar{b}$ and $c\bar{c}$ production cross-sections. Here, the $b\bar{b}$ cross-section is increased by 25%, while the $c\bar{c}$ cross-section is decreased by 25%. Here, 25% is chosen as this is roughly the uncertainty on the cross-section ratio of $b\bar{b}$ and $c\bar{c}$ production in Pythia [87]. Similarly, another template is produced where the $c\bar{c}$ cross-section is instead inflated. Both templates are then compared to the nominal to estimate a two-sided uncertainty in each bin due to the relative $b\bar{b}$ and $c\bar{c}$ contributions, which is shown in figure 4.27.

The displaced template also depends on the definition of the IP resolution used in the smearing of the simulated true IP. The nominal method makes the assertion that $\sigma(\text{IP}) = \text{IP}/\sqrt{\chi^2_{\text{IP}}}$, where IP and χ^2_{IP} are taken from the data event. Alternatively,

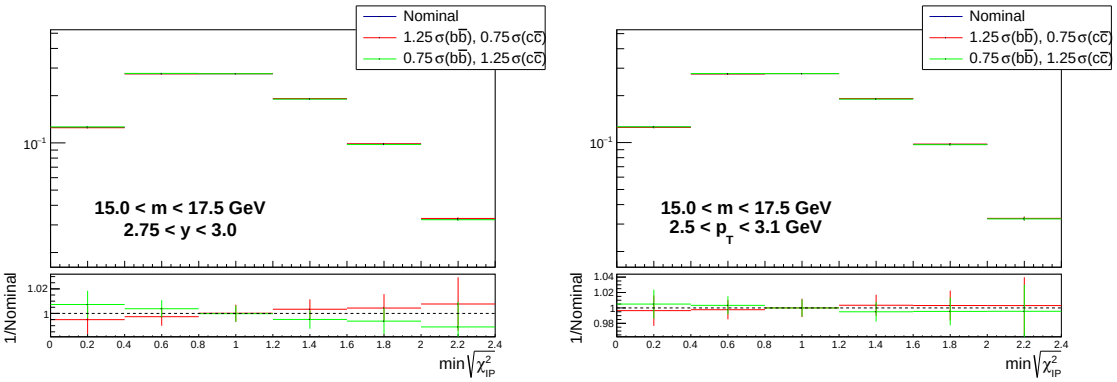

Figure 4.27: Comparison of displaced template produced with the nominal heavy flavour cross-sections and with inflated $b\bar{b}$ or $c\bar{c}$ cross-sections, shown in example bins.

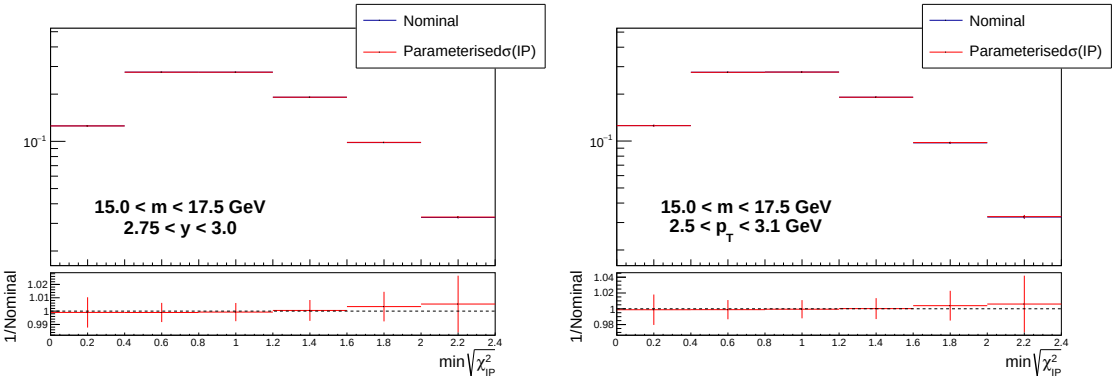

Figure 4.28: Comparison of displaced template produced using the nominal impact parameter resolution from data and using the parameterised resolution, shown in example bins.

the parameterised form of the resolution can be used, giving $\sigma(\text{IP}) = (11.6 + 23.4/p_{\text{T}}[\text{GeV}])$ [mm] where p_{T} is also taken from the data event. A template produced with the parameterised resolution is then compared to the nominal shape to obtain an estimate for the uncertainty due to the resolution definition in each bin. The difference between the two templates is shown in figure 4.28.

Validity of the $1/m$ Assumption

The validity of the $1/m_{\mu\mu}$ assumption made in the production of the interpolated prompt template and the evaluation of the non-Gaussian tails correction is confirmed using Monte Carlo simulation. Events are selected from a Drell-Yan signal MC

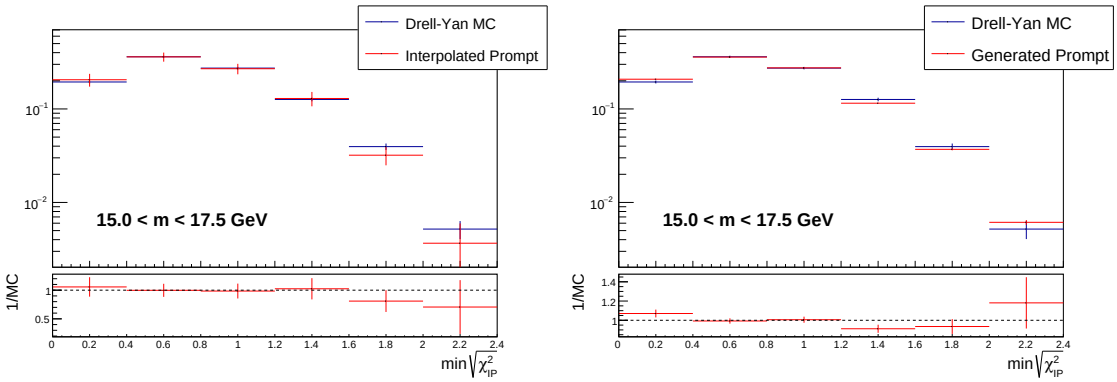

Figure 4.29: (Left) interpolated and (right) generated prompt templates produced from signal Monte Carlo compared to the same MC. The envelopes are then used in the fit to represent the uncertainty on the $1/m$ assumption in both methods.

sample using the same criteria described in Section 4.2 and binned in the same way as the data. Prompt templates are also produced from the same MC sample.

The first template is an interpolated prompt template, obtained using the same method as in data only seeded by the signal MC events. The second template is a generated prompt template, weighted by a non-Gaussian tails correction obtained by comparing the shape of the unweighted template to that of the MC sample.

The templates are then compared directly to the min $\sqrt{\chi^2_{\rm IP}}$ distribution in Monte Carlo in figure 4.29, showing a good agreement. The uncertainty due to the $1/m_{\mu\mu}$ assumption is then estimated to be the difference between the template and the simulation. The uncertainty from both the interpolated and generated templates are used in the fit.

4.4.4 Min $\sqrt{\chi^2_{\rm IP}}$ Fits

The prompt signal yield is obtained by fitting the signal and background templates to data across six bins of min $\chi^2_{\rm IP}$. This is achieved by minimising a modified χ^2 variable,

$$\chi^2 = \sum_{i=1}^{6} \frac{(N_i^{\rm data} - \tilde{N}_i^{\rm misid} - \tilde{N}_i^{\rm prompt} - \tilde{N}_i^{\rm displ})^2}{\sigma_i^2} + \sum_j a_j^2 \qquad (4.4)$$

where, in bin i, N_i^{data} is the efficiency weighted number of events, $\tilde{N}_i^{\text{misid}}$, $\tilde{N}_i^{\text{prompt}}$ and $\tilde{N}_i^{\text{displ}}$ are the sizes of the MisID, prompt and displaced templates respectively, and σ_i is the uncertainty on the data. Finally, a_j represent a set of nuisance parameters that control the shape of the templates.

The size of the MisID template is given by the number of events selected from the same-sign dimuon sample, also weighted by the selection efficiency. The template shape, however, is allowed to vary within the statistical uncertainty up to $\pm 3\sigma$ in each min χ^2_{IP} bin. The MisID contribution is then given as

$$\tilde{N}_i^{\text{misid}} = N_i^{\text{misid}} + a_i \sigma_i^{\text{misid}} \tag{4.5}$$

where N_i^{misid} is the weighted number of same-sign events and σ_i^{misid} is the uncertainty in bin i. The nuisance parameters a_1 - a_6 control the shape variation in each bin.

The sizes of the prompt and displaced templates are allowed to vary. The template shapes are also allowed to vary within both the statistical uncertainty and the systematic uncertainties outlined in section 4.4.3, however, unlike the MisID template, the first bin is fixed in order to preserve the shape. The prompt template contribution in bin i is given as

$$\tilde{N}_i^{\text{prompt}} = \begin{cases} i = 1 & p_0 n_i^{\text{prompt}} \\ i > 1 & p_0 \left(\frac{n_i^{\text{prompt}} + a_{i+5}\sigma_i^{\text{prompt}} + a_{17}\sigma_i^{\text{gen}} + a_{20}\sigma_i^{\text{int}}}{1 + a_{i+5}\sigma_i^{\text{prompt}} + a_{17}\sigma_i^{\text{gen}} + a_{20}\sigma_i^{\text{int}}} \right) \end{cases} \tag{4.6}$$

where n_i^{prompt} is the size of the normalised template and p_0 is the prompt yield parameter. As in the MisID contribution, a_7 - a_{11} are the nuisance parameters that allow the shape to vary within the statistical uncertainty, σ_i^{prompt}. The additional nuisance parameters, a_{17} and a_{20}, allow for variation representing the uncertainty from the generated prompt template and the $1/m_{\mu\mu}$ assumption in the interpolated template, which are given by σ_i^{gen} and σ_i^{int} respectively. The effect of the shape variation is limited by a penalty factor.

Similarly, the displaced contribution is given by

$$\tilde{N}_i^{\text{displ}} = \begin{cases} i = 1 & p_1 n_i^{\text{displ}} \\ i > 1 & p_1 \left(\frac{n_i^{\text{displ}} + a_{i+10}\sigma_i^{\text{displ}} + a_{18}\sigma_i^{\text{param}} + a_{19}\sigma_i^{\text{HF}} + a_{21}\sigma_i^{\text{cor}}}{1 + a_{i+10}\sigma_i^{\text{displ}} + a_{18}\sigma_i^{\text{param}} + a_{19}\sigma_i^{\text{HF}} + a_{21}\sigma_i^{\text{cor}}} \right) \end{cases} \tag{4.7}$$

where n_i^{displ} is now the size of the normalised displaced template and p_1 is the displaced yield parameter. The nuisance parameters a_{12} - a_{16} allow for shape variation within statistical uncertainty, while a_{18}, a_{19} and a_{21} control variation due to the uncertainties from the IP resolution definition, the heavy flavour production cross-sections and the $1/m_{\mu\mu}$ assumption in the non-Gaussian tails correction, given by σ_i^{param}, σ_i^{HF} and σ_i^{cor} respectively.

For each bin in dimuon mass and rapidity, or in mass and transverse momentum, equation 4.4 is minimised using MINUIT [88]. This returns values for the prompt and displaced yields with uncertainties, as well as the nuisance parameters, giving the template sizes and shapes that best match the data.

Example fits are shown in Figures 4.30 and 4.31, while the full results are shown in Appendix A.

It is possible for numerical minimisation techniques to fail to converge on a minimum point or to instead find a local instead of the desired global minimum. This method of template production gives fits that reliably converge, even in cases of low statistic data. On the other hand, the prompt yield returned for a given bin can vary considerably depending on the initial parameters given, indicating fits converging on local minima.

To counter this, fits are performed 100 times with initial parameters sampled from a uniform distribution, whilst nuisance parameters always start at zero. The parameters from the iteration which gives the minimum value of the χ^2 in equation 4.4 are then given as the initial parameters for a final fit which gives the final prompt yield.

The final fit results are shown in figures 4.32 and 4.33, showing the contributions

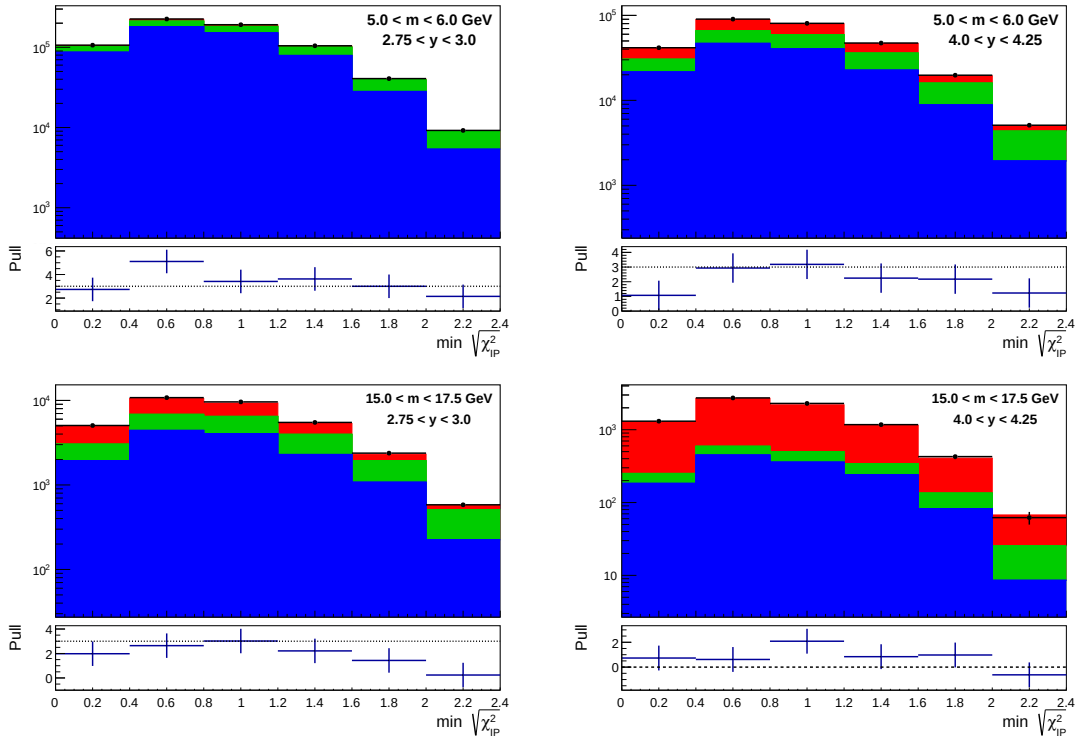

Figure 4.30: Example fits of data in bins of dimuon mass and rapidity as a function of min $\sqrt{\chi^2_{\rm IP}}$, where the components are shown as (red) prompt, (green) displaced and (blue) MisID.

of each template and therefore indicating the measured signal purity of each bin.

Isolation Cut Cross-Check

Since the dimuons in the displaced heavy flavour backgrounds are typically produced through the decays of $b\bar{b}$ or $c\bar{c}$ pairs, they are often closely associated with jet structures in the event. It is for this reason that in the LHCb dark photon search, it was required that both signal muons were well isolated in order to improve the purity of the sample. This was measured by running an anti-k_T algorithm with $R = 0.5$, seeded by the muons, to find the jet objects that contain these tracks [89]. The isolation is then defined as

$$\text{iso} = \frac{p_{\rm T}(\mu)}{p_{\rm T}(\text{jet})} \tag{4.8}$$

and in the dark photon search it is required that both muons satisfy iso > 0.7.

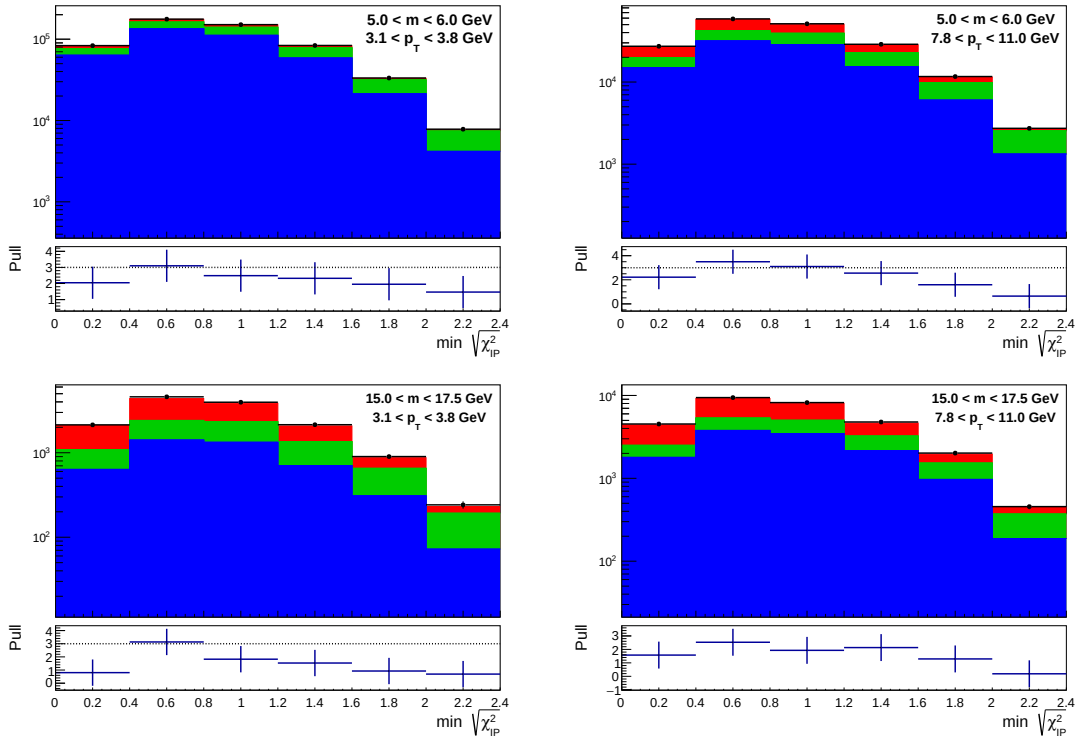

Figure 4.31: Example fits of data in bins of dimuon mass and transverse momentum as a function of min $\sqrt{\chi^2_{\mathrm{IP}}}$, where the components are shown as (red) prompt, (green) displaced and (blue) MisID.

The dark photon search was not dependent on the efficiency of the isolation cut as a bump hunt was performed relative to prompt side-band data, meaning that the efficiency cancels in the signal and background. In this Drell-Yan analysis, the cross-section measurement would be strongly affected by inaccuracies in the evaluation of the efficiency of any isolation cut. The efficiency of isolation cuts are inherently difficult to evaluate as the detector response for jets, and hence the isolation parameter, is difficult to model in Monte Carlo simulation.

Here, the necessity of any isolation requirement is considered by examining the effects of isolation cuts on, first, the shapes of the data and templates in min $\sqrt{\chi^2_{\mathrm{IP}}}$ and, secondly, the prompt yields of the fits.

The changes in the min $\sqrt{\chi^2_{\mathrm{IP}}}$ with isolation requirements can be seen in data in figure 4.34. Here it can be seen that a more isolated sample shifts the distribution to lower values of min $\sqrt{\chi^2_{\mathrm{IP}}}$, such that a more prompt selection is made giving a

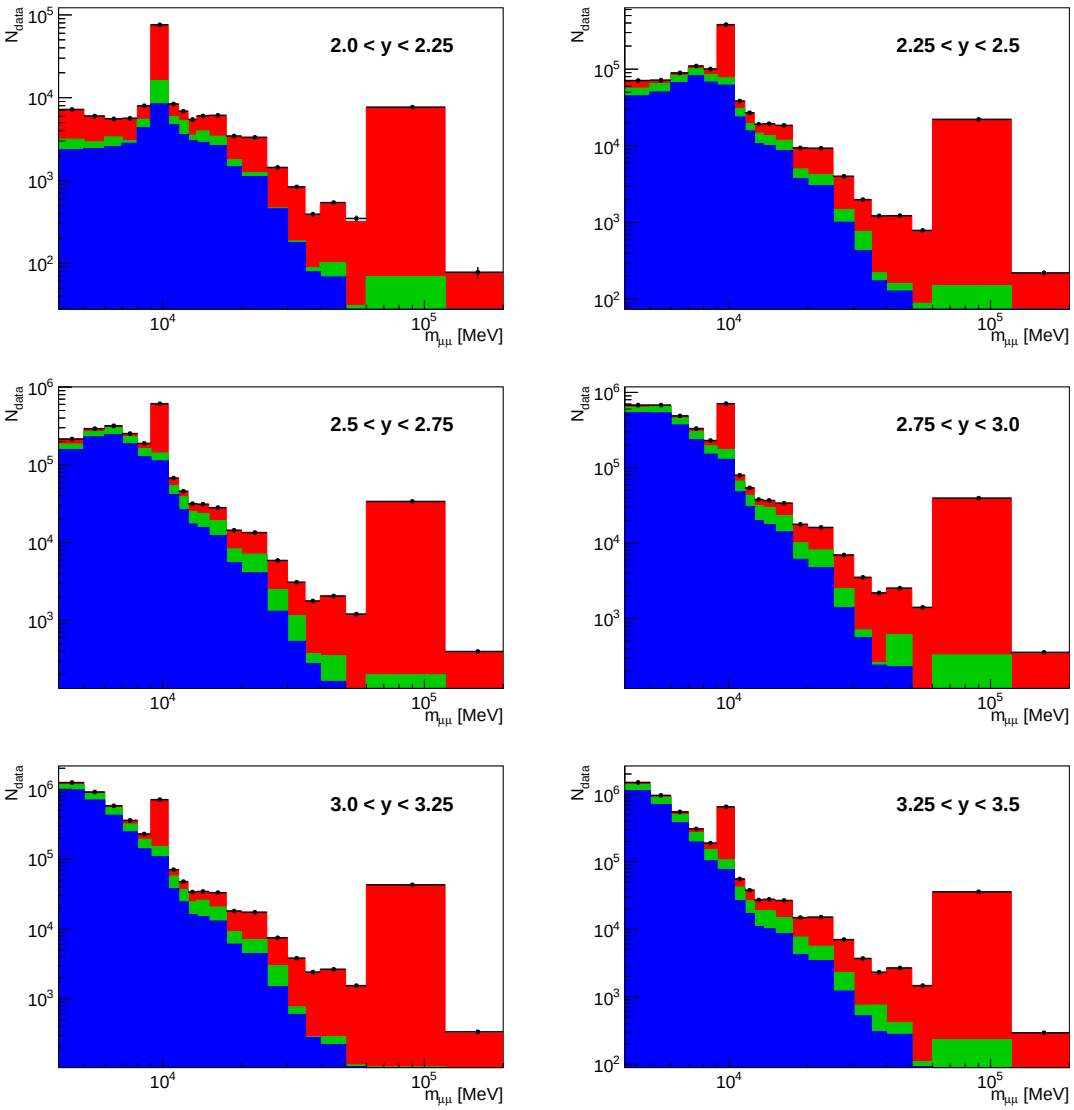

Figure 4.32: Fit results showing fractional contributions of (red) prompt signal, (green) displaced background and (blue) MisID background, as a function of dimuon mass in bins of dimuon rapidity, showing prompt resonances at $\Upsilon(1S)$ and Z masses.

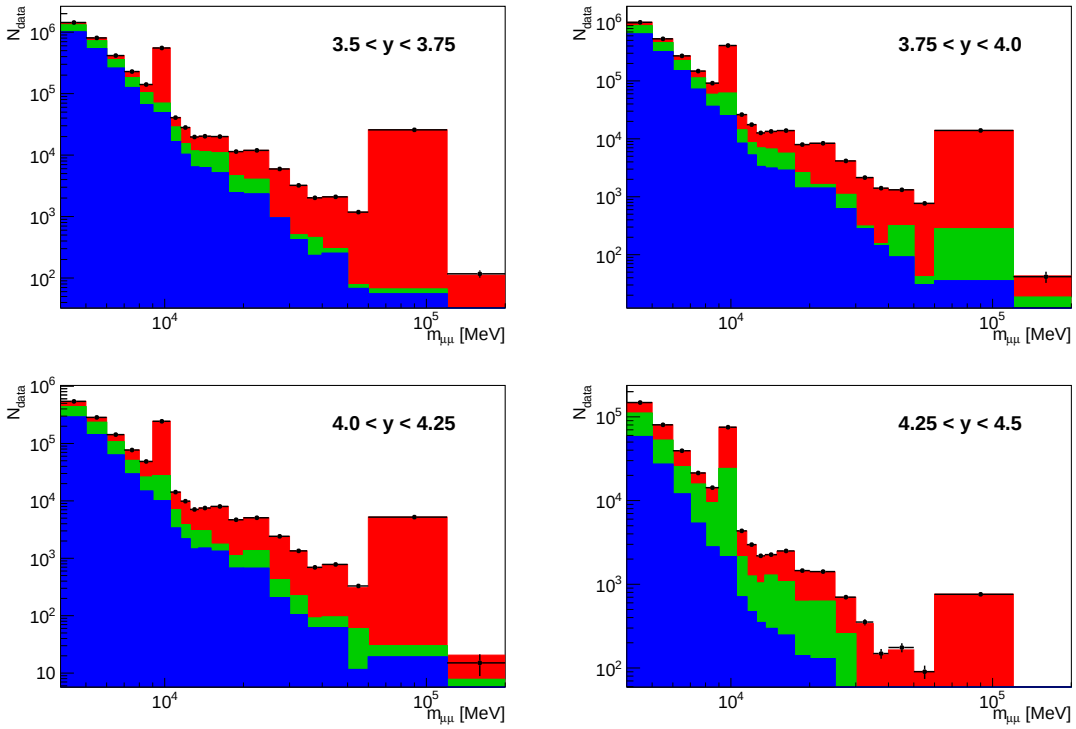

Figure 4.32: Fit results showing fractional contributions of (red) prompt signal, (green) displaced background and (blue) MisID background, as a function of dimuon mass in bins of dimuon rapidity, showing prompt resonances at $\Upsilon(1S)$ and Z masses.

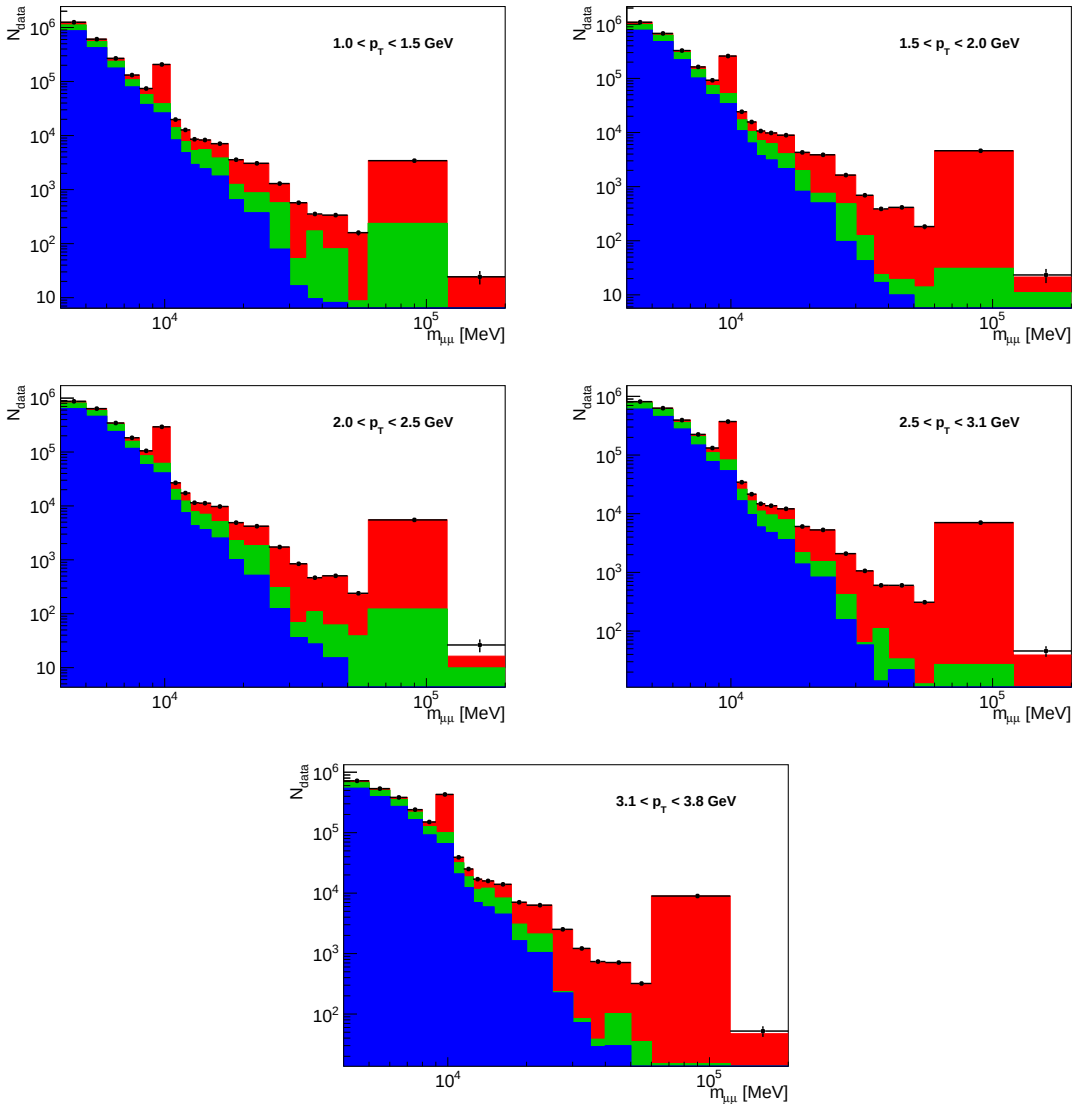

Figure 4.33: Fit results showing fractional contributions of (red) prompt signal, (green) displaced background and (blue) MisID background, as a function of dimuon mass in bins of dimuon transverse momentum, showing prompt resonances at $\Upsilon(1S)$ and Z masses.

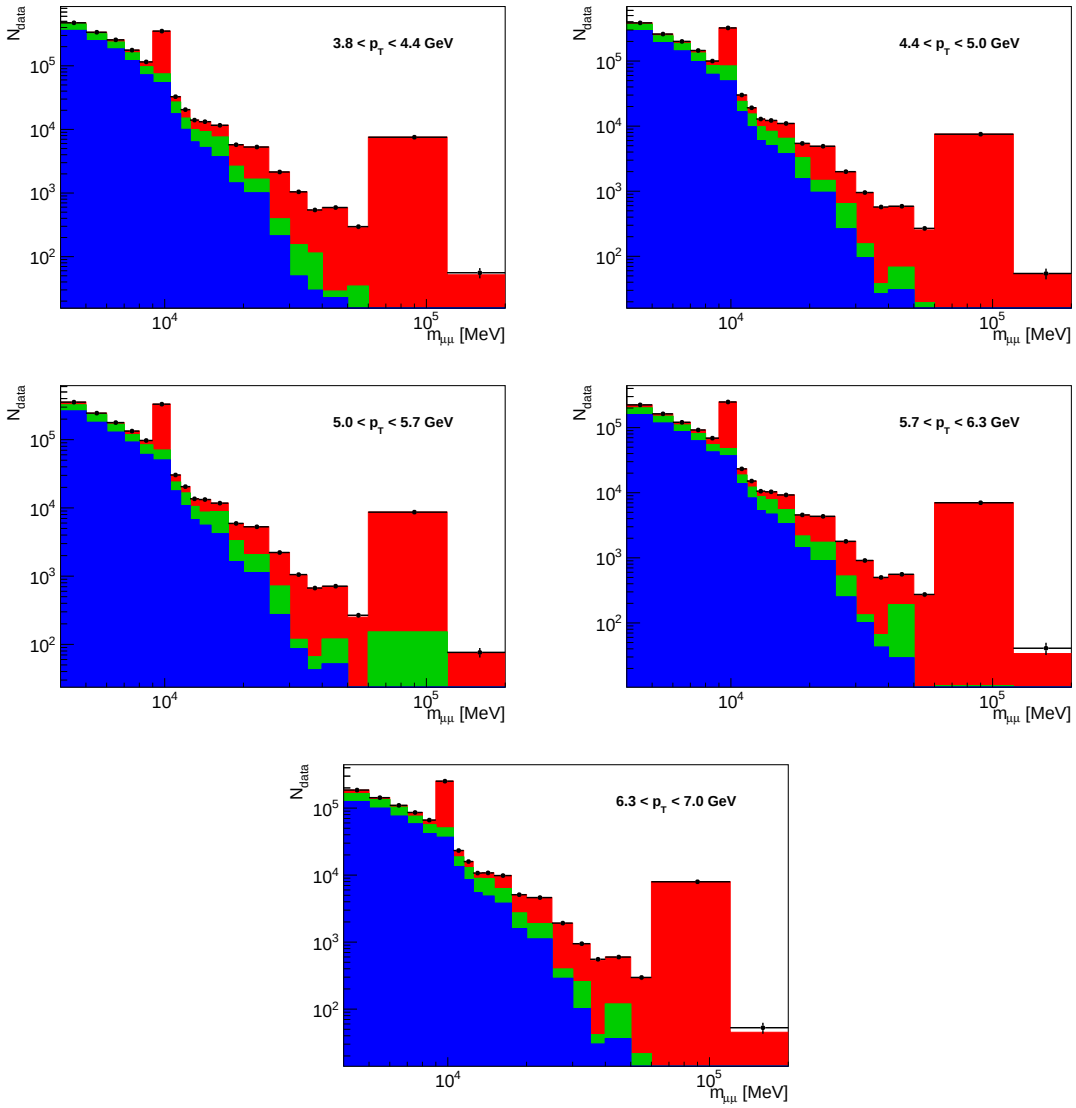

Figure 4.33: Fit results showing fractional contributions of (red) prompt signal, (green) displaced background and (blue) MisID background, as a function of dimuon mass in bins of dimuon transverse momentum, showing prompt resonances at $\Upsilon(1S)$ and Z masses.

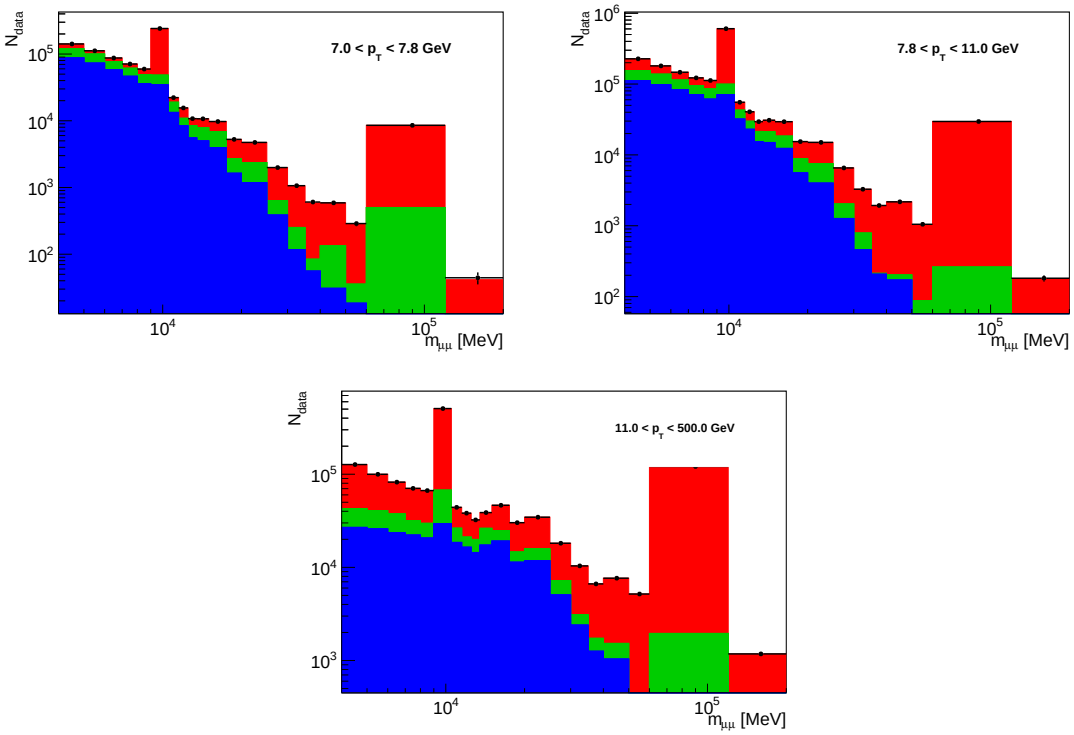

Figure 4.33: Fit results showing fractional contributions of (red) prompt signal, (green) displaced background and (blue) MisID background, as a function of dimuon mass in bins of dimuon transverse momentum, showing prompt resonances at $\Upsilon(1S)$ and Z masses.

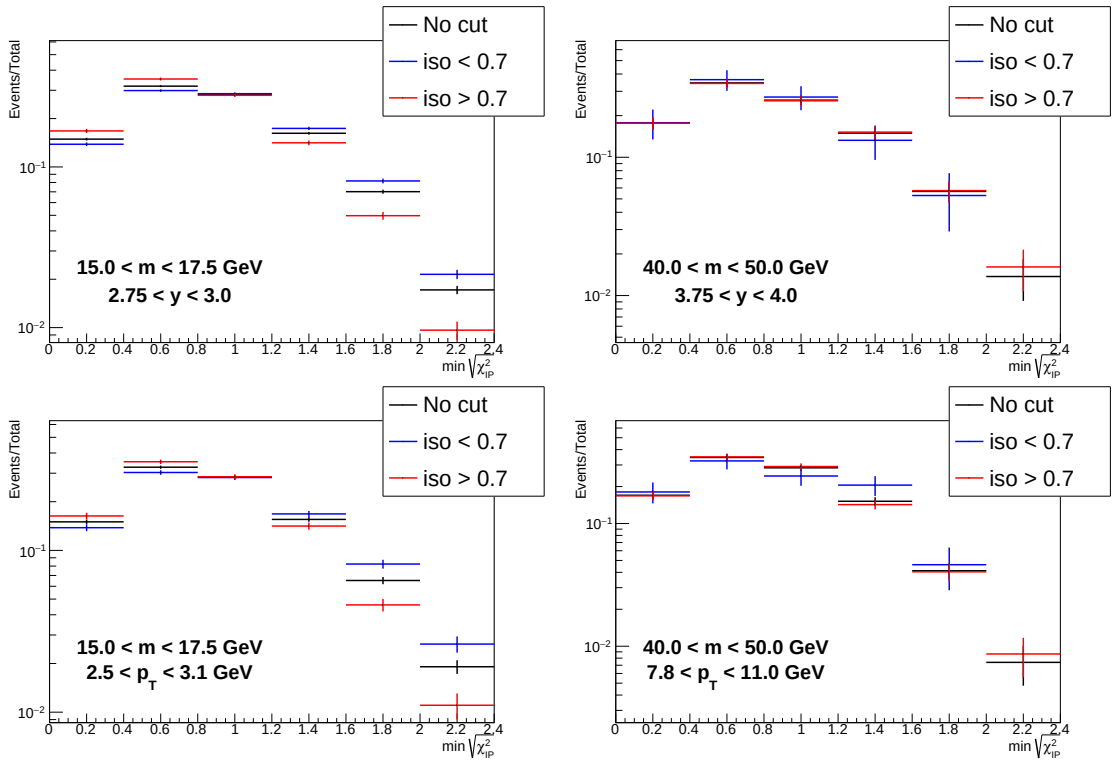

Figure 4.34: The effects of an isolation requirement on opposite sign dimuon candidates in data in a selection of (top) dimuon mass and rapidity and (bottom) mass and p_{T} bins.

more pure dataset. It should also be noted that the difference between a high and low isolation sample is less significant in higher mass bins.

Figure 4.35 shows the same comparison in the same-sign sample. Here there is little difference between a high and low isolation selection, though the sample is limited by statistics at higher masses, which is another reason that avoiding an isolation cut is desirable.

Figures 4.36 and 4.37 compare interpolated prompt and generated displaced templates produced from data with isolation requirements. Here it can be seen that the effect of isolation requirements on the template shape is minimal, especially in the displaced templates. The most significant differences are seen in the low p_{T} region of the interpolated prompt templates. This implies that the changes in the distribution shapes in data with isolation cuts, shown in figure 4.34, are due to the changes in the relative contributions of prompt and displaced processes.

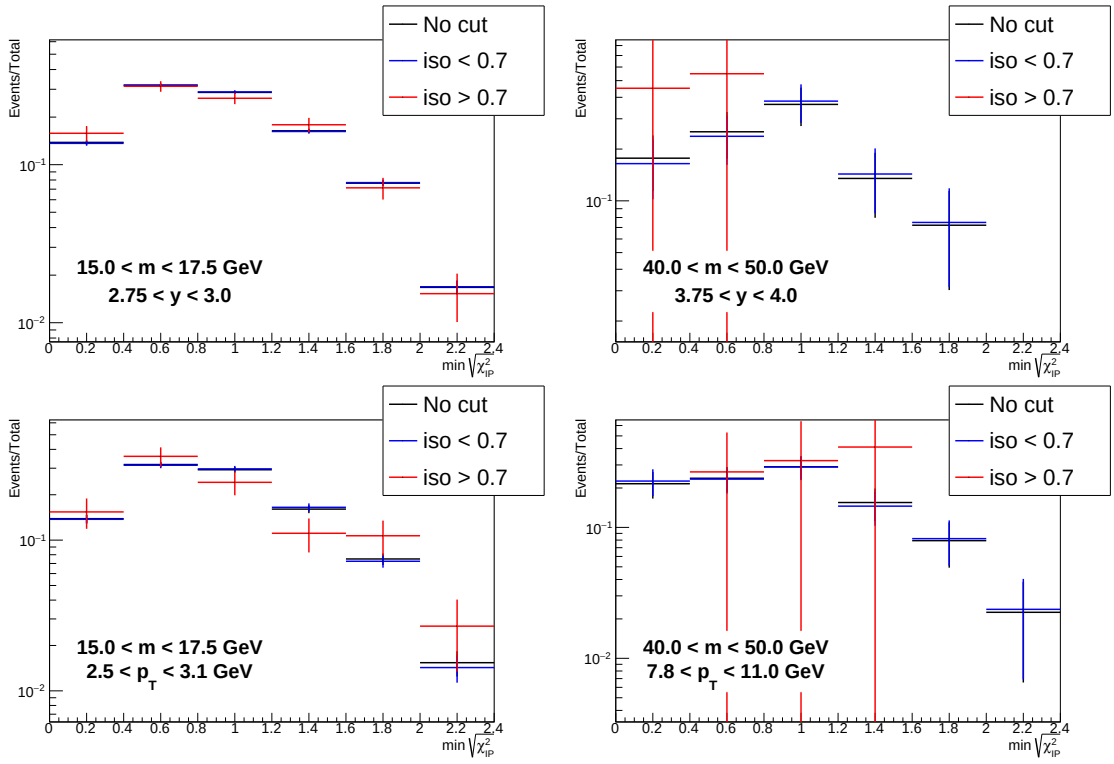

Figure 4.35: The effects of an isolation requirement on same sign dimuon candidates in data, i.e. the MisID template, in a selection of (top) dimuon mass and rapidity and (bottom) mass and p_{T} bins.

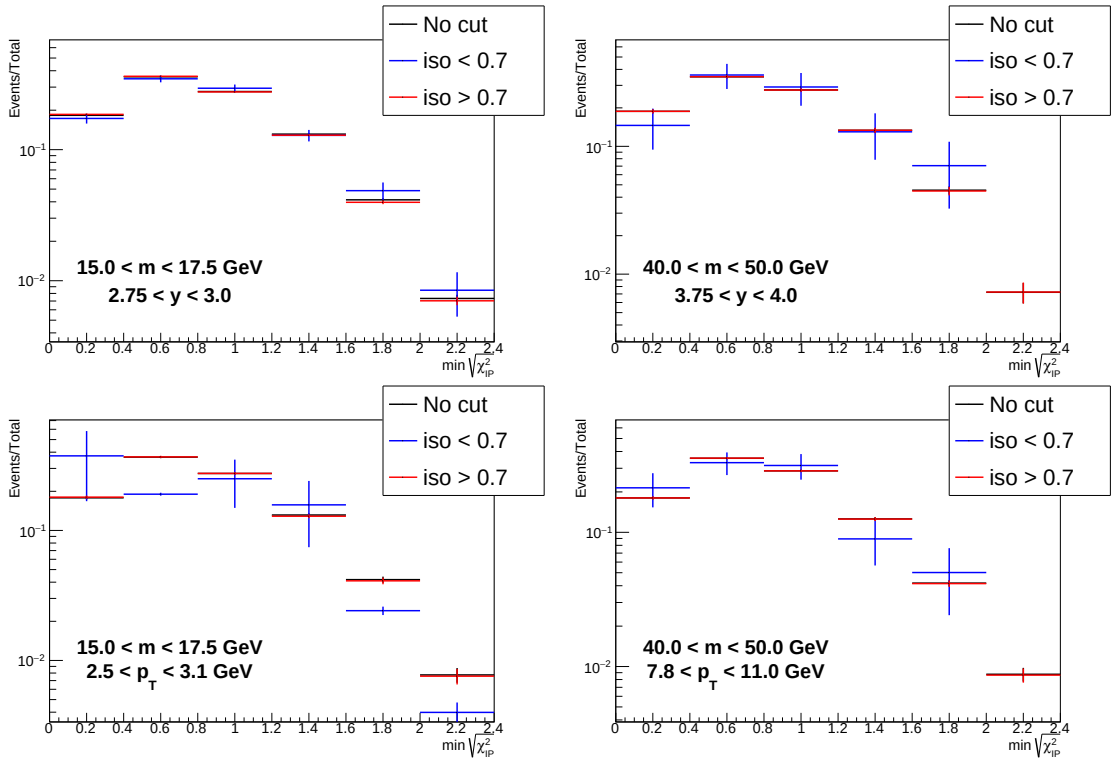

Figure 4.36: The effects of an isolation requirement on the interpolated prompt template in a selection of (top) dimuon mass and rapidity and (bottom) mass and p_{T} bins.

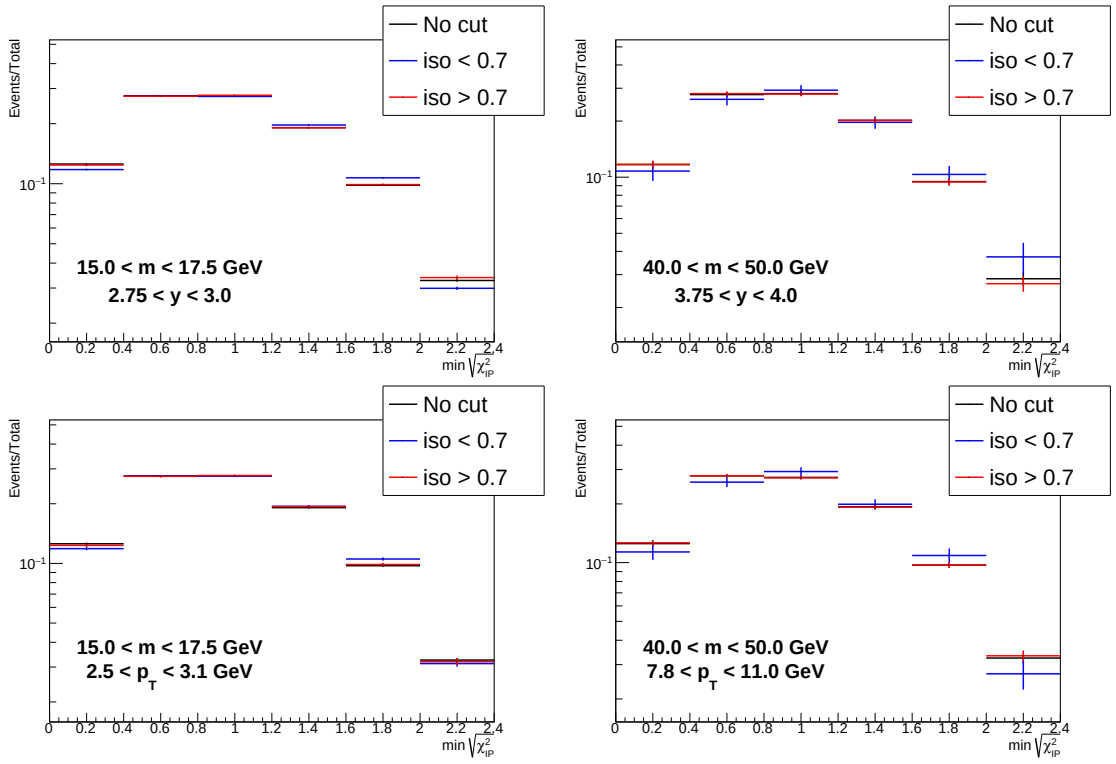

Figure 4.37: The effects of an isolation requirement on the nominal displaced template in a selection of (top) dimuon mass and rapidity and (bottom) mass and p_{T} bins.

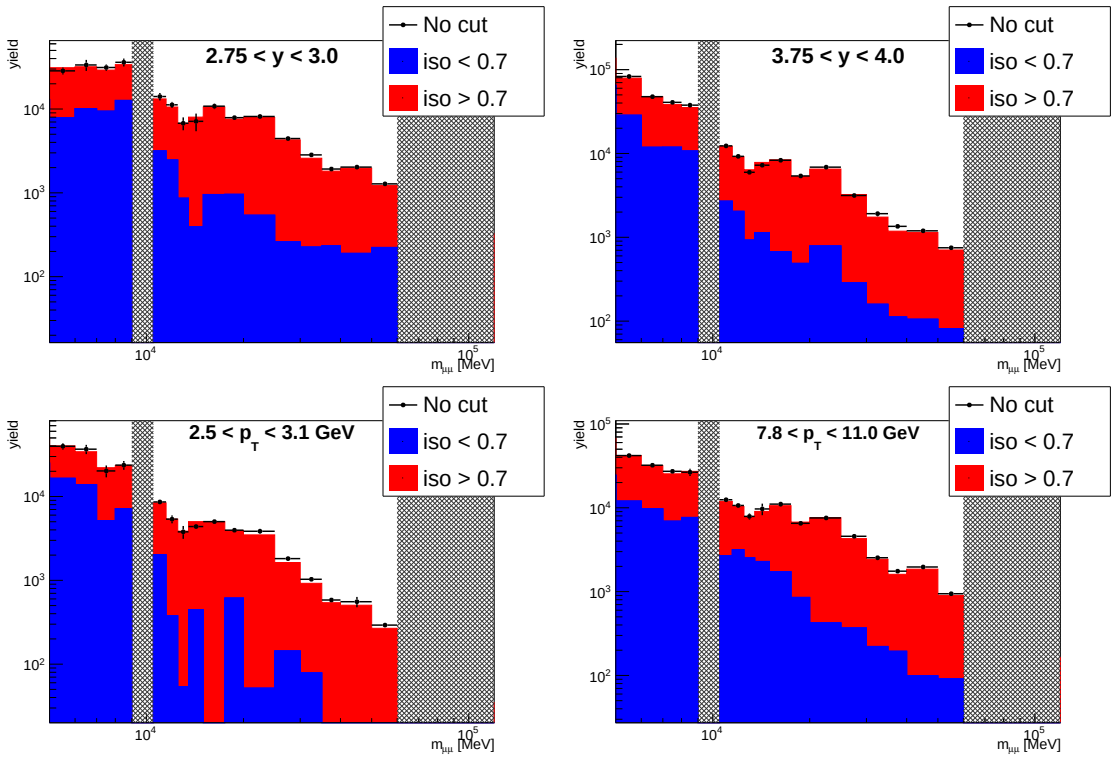

Figure 4.38: The effects of an isolation requirement on total fit yield as a function of dimuon mass in a selection of (top) dimuon rapidity and (bottom) p_{T} bins, where the Υ and Z resonances are excised.

Since the effect of an isolation cut on template shapes is negligible, fits can be performed using templates without any such requirement. In figure 4.38, the sum of the yields from the fits of high and low isolation data is compared to the yield for data with no requirement, showing good agreement. It can therefore be shown that a consistent prompt yield can be obtained without making any isolation requirements, and consequently it is unnecessary to evaluate the isolation efficiency.

Efficiency Weighting Cross-Check

It is important to understand the effects of weighting events by the reciprocal efficiency on the min $\sqrt{\chi^2_{\mathrm{IP}}}$ shapes of data and templates, and how these in turn affect the purity of the fits. First, weighted and unweighted data are directly compared; example bins are shown in figure 4.39.

Here, the difference in shape between the weighted and unweighted data is neg-

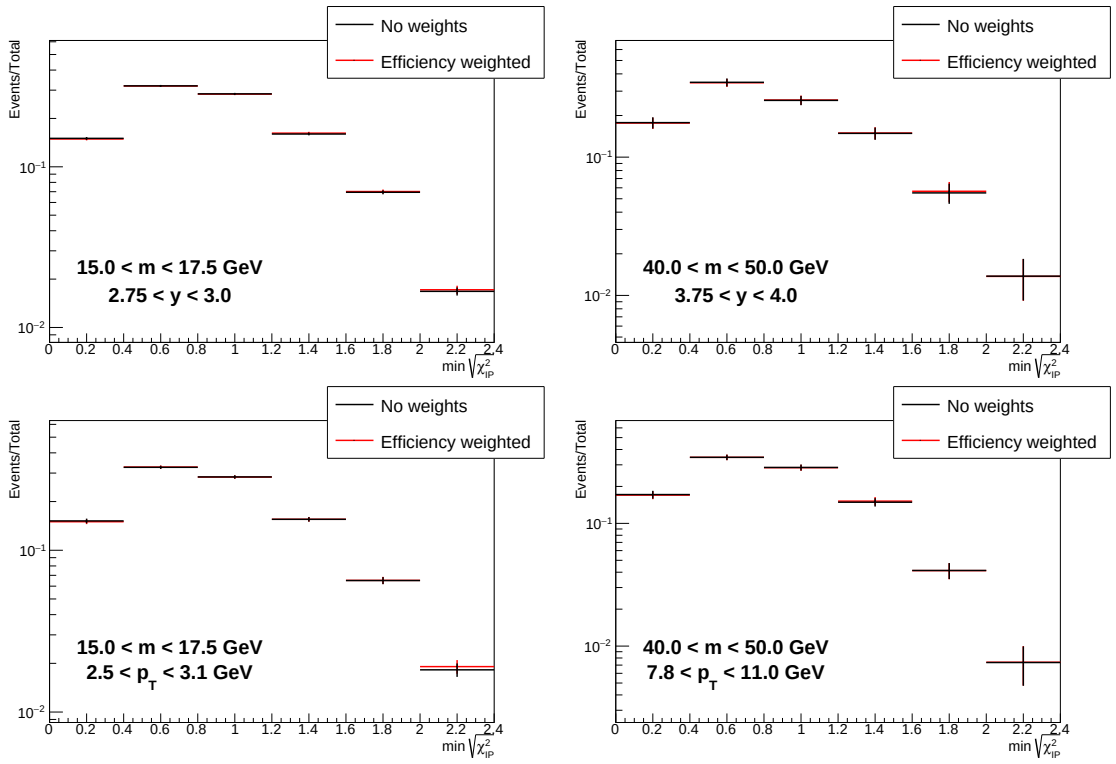

Figure 4.39: The effects of weighting events by efficiency on the min $\sqrt{\chi^2_{\rm IP}}$ shape of data in a selection of (top) dimuon mass and rapidity and (bottom) mass and $p_{\rm T}$ bins.

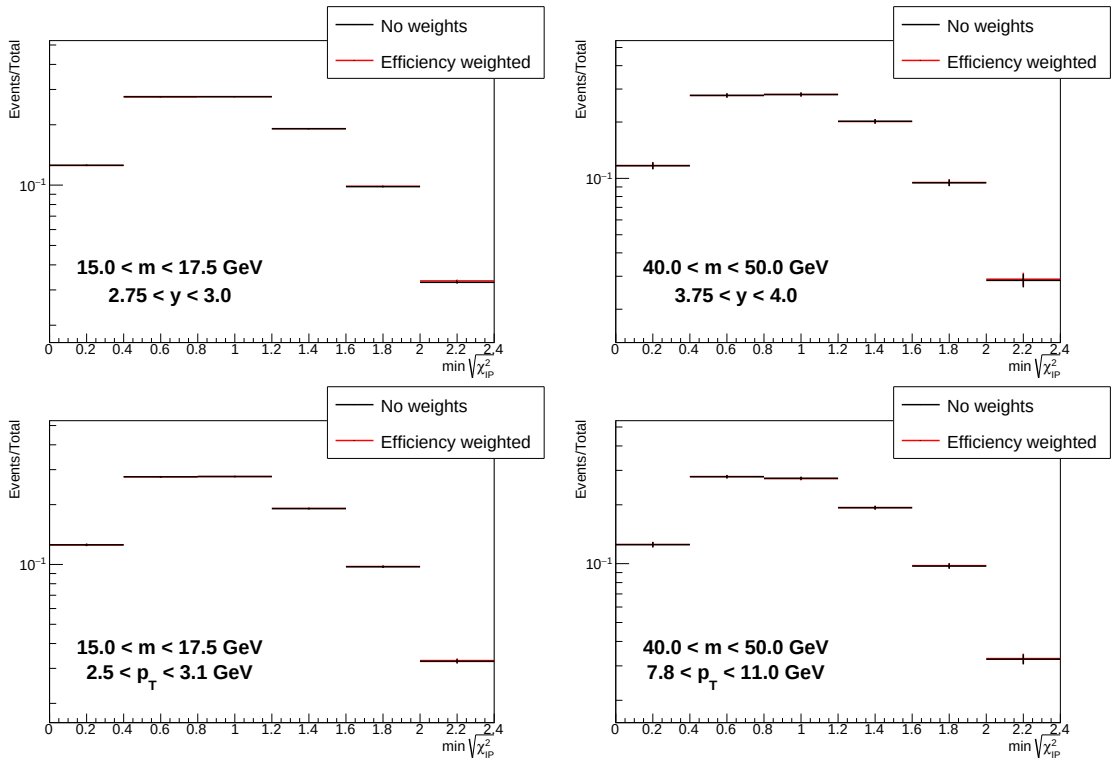

Figure 4.40: The effects of weighting events by efficiency on the min $\sqrt{\chi^2_{\text{IP}}}$ shape of the nominal displaced template in a selection of (top) dimuon mass and rapidity and (bottom) mass and p_{T} bins.

ligible. Since the shape of the interpolated prompt template depends exclusively on the min $\sqrt{\chi^2_{\text{IP}}}$ distribution of the data, the template shape will also be unaffected by the efficiency weighting.

The effect on the displaced template is assessed by producing a template weighted by the efficiencies. First, new non-Gaussian tails corrections are calculated by comparing an efficiency weighted generated prompt template to weighted data. Then the efficiency weighted displaced template is generated, including the new corrections. Finally, this is compared to the template with no efficiency weighting, shown in figure 4.40, which shows a negligible effect.

Since the efficiency weights have no significant effect on the min $\sqrt{\chi^2_{\text{IP}}}$ shapes of either the data or the templates, the fractional yields of the fits do not depend on variations in the efficiencies. This enables studies of the efficiencies, such as those on the uncertainties due to the weights, to be made without performing new fits.

4.5 Systematic Uncertainties

The systematic uncertainties on the prompt yield arise from two sources: the uncertainty due to the quality of the fit and the uncertainty on the efficiency weights. As described in section 4.4.3, uncertainties in the template shape due to the template production methods and the $1/m_{\mu\mu}$ assumption in interpolation are included in the fit by allowing the shape to vary within these envelopes. As a result, the full shape uncertainty is absorbed by the fit uncertainty.

The effects of migrations between neighbouring bins must also be taken into account. A previous analysis of Z production at LHCb, using a similar selection and binning to this analysis, found that the these effects are negligible for the rapidity distribution [90]. In p_T, where migrations were found to be comparable to statistical fluctuations, unfolding studies were performed but were found to have a negligible effect on the final result. No unfolding has been performed for the current analysis, assuming the similarities with the previous selection, therefore no systematic uncertainty is assigned. Future studies will need to be performed for verification prior to publication.

4.5.1 Fit Uncertainty

The total uncertainty on the fit result is given by the error on the prompt yield parameter, p_0 in equation 4.6, returned by the `MINUIT` minimiser. This uncertainty includes both statistical and systematic components. Here, the components are separated by making the assumption that the total uncertainty is

$$\sigma^2_{\text{total}} = \sigma^2_{\text{stat}} + \sigma^2_{\text{sys}} \tag{4.9}$$

Here, σ_{total} is already known from the fitter. It is possible to estimate σ_{stat} by rerunning the fit where the nuisance parameters are fixed to the values obtained in the nominal fit. This means that the template shapes are not allowed to vary in the

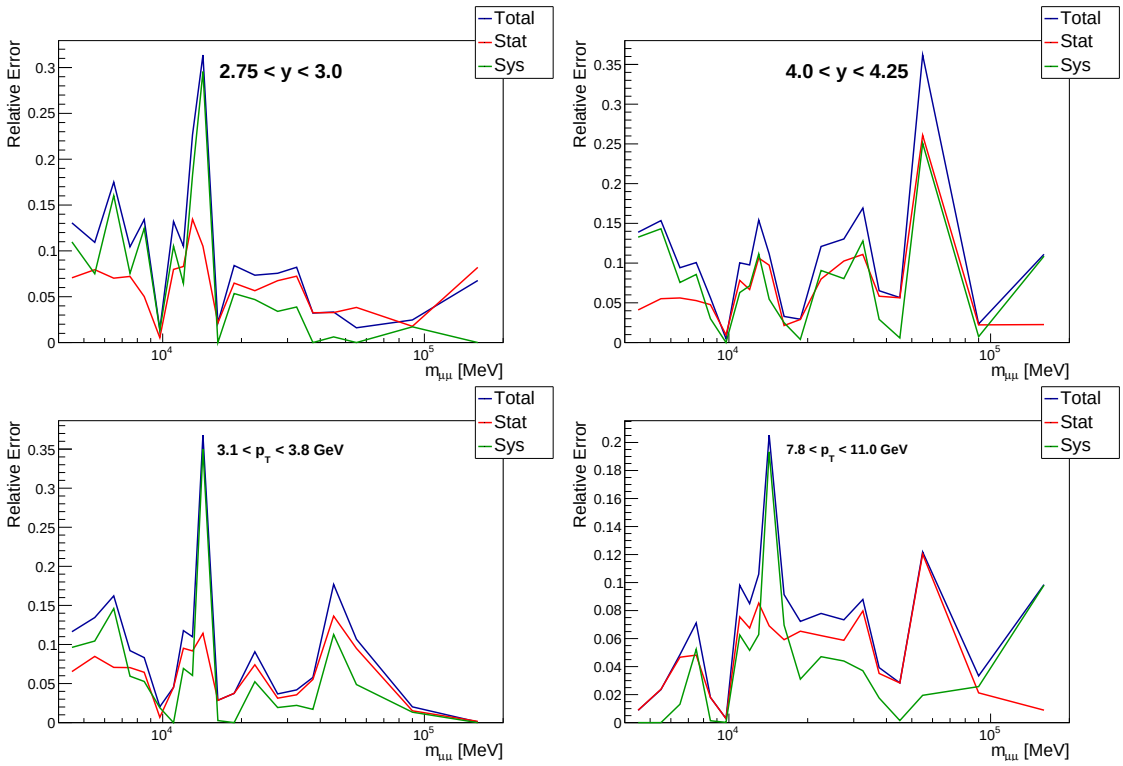

Figure 4.41: Example fit uncertainty in bins of (top) dimuon rapidity and (bottom) dimuon transverse momentum, as a function of dimuon invariant mass. The total uncertainty returned by the fitter, σ_{total}, is shown in blue while the statistical and systematic components are shown in red and green respectively.

fit and the only uncertainty considered is the statistical uncertainty on the data, given as σ_i in equation 4.4. With this estimate, the systematic uncertainty can be obtained from

$$\sigma_{\text{sys}} = \sqrt{\sigma^2_{\text{total}} - \sigma^2_{\text{stat}}} \tag{4.10}$$

Examples of the fit uncertainties are shown in figure 4.41. In regions where backgrounds are high, such as at low mass, the systematic uncertainty dominates. Conversely, at high masses, the systematic component goes to zero and the statistical dominates.

4.5.2 Efficiency Weight Uncertainty

The uncertainty on the prompt yield due to the efficiency weighting is evaluated by varying the efficiency values obtained in section 4.3 and observing the changes in yields. Since the effect of the efficiency weights on the fit results is negligible, as shown in section 4.4.4, fitting these variations is unnecessary. Instead, the effects on the weighted integral of the data in each fit bin is observed. Two studies are performed, a deterministic study and a toy study, and are described below.

Deterministic Study

Efficiencies are obtained per event by referring to a set of maps which are binned according to the kinematic variables of the dimuon candidate or constituent muons. The deterministic study of the uncertainties on the efficiency weighting involves varying the value of the efficiency maps one bin at a time. The efficiency uncertainties arise from a statistical component from evaluations in MC, and a systematic component to account for correlation between bins from the MC-data corrections.

New maps are produced where a single bin is raised or lowered by the statistical error on the efficiency for that bin, representing a $1\sigma_{\text{stat}}$ uncertainty. Additional maps are required where all bins are raised or lowered by the systematic error assigned to the efficiency, $1\sigma_{\text{sys}}$, for correlations between bins. A simple example is shown figure 4.42. Histograms are then filled, using the fit binning, with the dataset weighted by the efficiencies from each of the new maps. For a given bin, the weighted integral is then

$$N_{\text{eff}} = \sum_i \frac{1}{\varepsilon_i} \tag{4.11}$$

where ε_i is the efficiency obtained from the map for candidate i. The deterministic uncertainty is obtained by adding in quadrature the deviations of the weighted integral from the nominal values for each map, which is given as

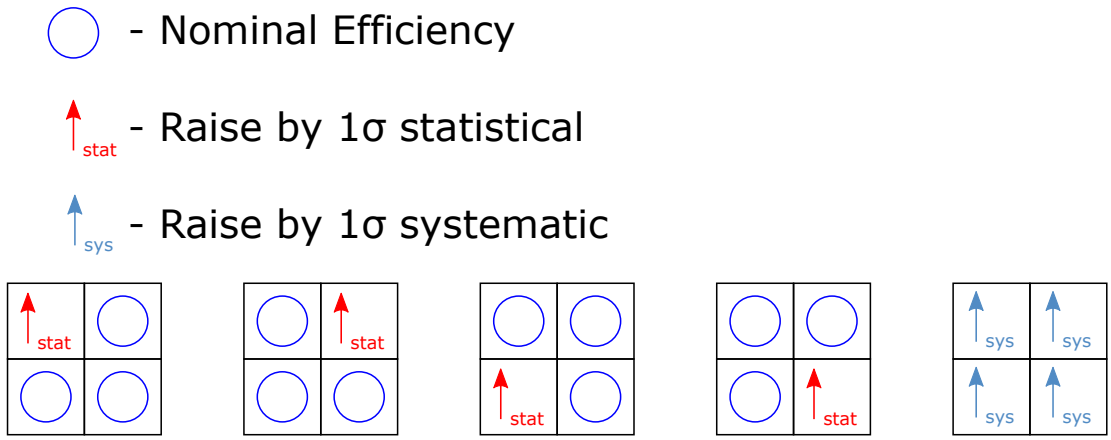

Figure 4.42: An example of the required "raised" maps for an efficiency map with 2×2 binning. For a general two dimensional case with binning $m \times n$, there are mn maps where the efficiency in a single bin raised by the statistical uncertainty and a single map where all bins are raised by the systematic uncertainty to account for correlations in the uncertainties between the map bins. This set is accompanied by an equivalent set where the bins are instead lowered, in total requiring $2(mn + 1)$ maps. This can also be expanded to higher dimensional binning.

$$\sigma_{\text{det}} = \sqrt{\sum_j \left(\frac{N_{\text{nominal}} - N_j}{N_{\text{nominal}}} \right)^2} \tag{4.12}$$

where j is the map index. Using the "raised" maps, those where the efficiency has been increased by 1σ, give the lower uncertainty on the yield while using the "lowered" maps give the upper uncertainty.

Since the efficiency maps are factorised according to their source, separate maps must be produced for each efficiency. When obtaining the efficiency from an altered map of one source, the nominal efficiency must be used from the remaining sources. This is demonstrated in an example with two sources of efficiencies in figure 4.43.

Toy Study

The toy study of efficiency weight uncertainties works similarly to the deterministic study. Instead of creating a new efficiency map for each bin, new toy maps are built where for each bin the efficiency is randomly sampled.

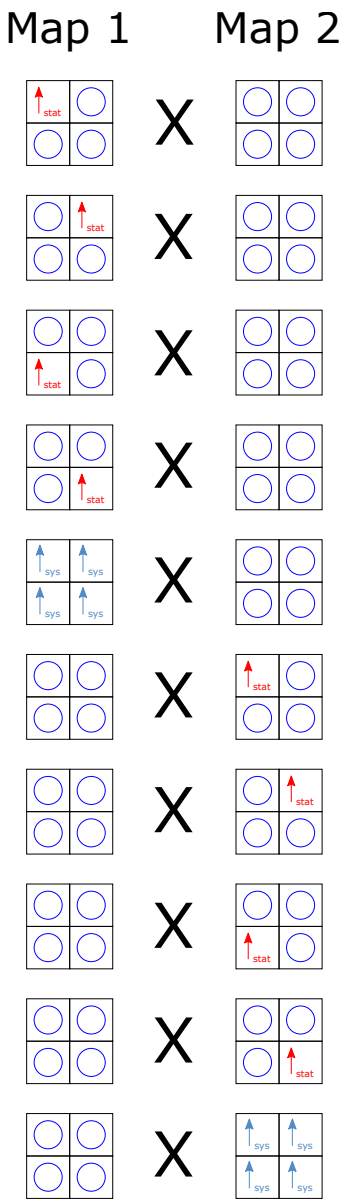

Figure 4.43: An example of how "raised" maps can be produced when considering efficiencies from two factorised sources. First the efficiencies in Map 1 are raised, as in figure 4.43, while those in Map 2 are held at their nominal values. Following this, the process is repeated where Map 2 is raised and Map 1 is held. This can be extended to N efficiency sources which, if each map has an $m \times n$ binning, requires a total of $2N^2(mn+1)$ maps, increasing quadratically. The nominal efficiency maps are repeated, reducing the computational requirement.

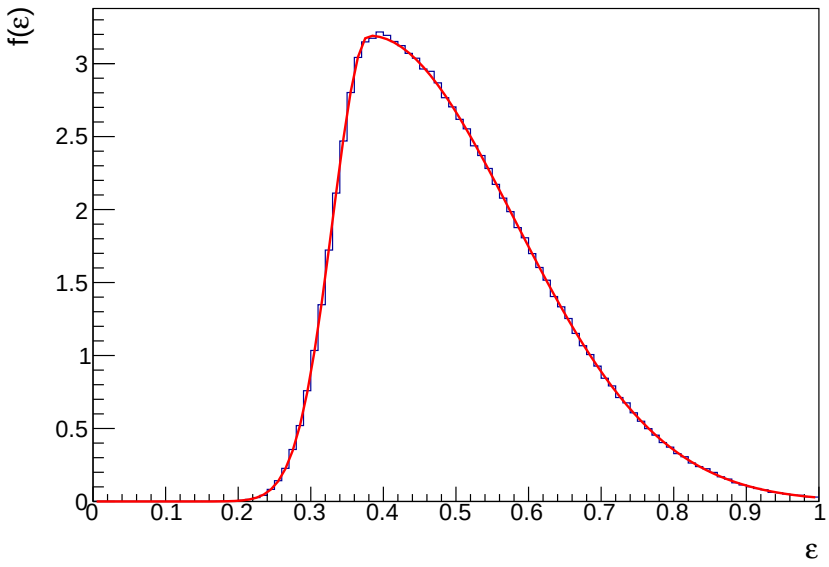

Figure 4.44: Example of an exaggerated asymmetric distribution sampled in the toy study, built from two Gaussian distributions with $\mu = 0.5$, $\sigma_- = 0.05$ and $\sigma_+ = 0.2$. Also shown is a histogram of 1000000 samples.

The new efficiencies are sampled according to the statistical uncertainty on the efficiency, with an additional component from the systematic uncertainty to account for correlations between bins. The statistical component is sampled from a distribution constructed from two Gaussian distributions where the widths are taken as the upper and lower statistical uncertainty, normalised to be continuous at the peak and translated such that the mean of the total distribution is the nominal efficiency. An example distribution is shown in figure 4.44. The systematic component is constant for each bin and is obtained by sampling a Gaussian distribution with a mean of zero and a width of the systematic uncertainty on the efficiency.

A total of 1000 toy maps are produced for each source of efficiency considered. Again, histograms are filled with the dataset weighted per candidate by each set of toy maps. For a given bin, this gives a distribution of 1000 weighted integrals. The upper and lower uncertainties are taken as $\pm 34.1\%$ of the integral of this distribution from the nominal efficiency, as demonstrated in figure 4.45.

The results of both the deterministic and toy studies are shown in figure 4.46.

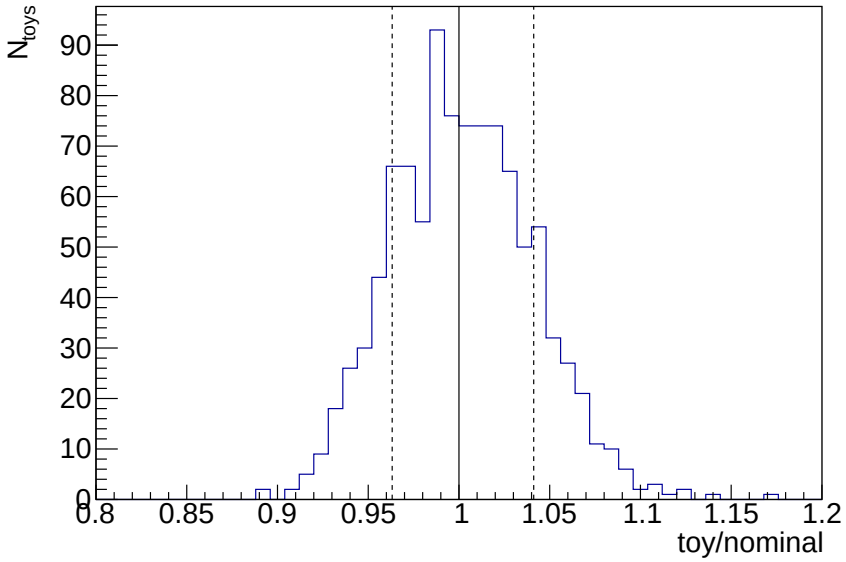

Figure 4.45: Example of the distribution of 1000 toy efficiencies as a ratio of the nominal efficiency. Also shown are the upper and lower uncertainties, taken as ±34.1% of the integral from the nominal efficiency.

Here it can be seen that both studies give consistent uncertainties, trending from a high uncertainty at low masses to lower values at high masses, typically between 2 - 5 %. Between the two studies, the most noticeable difference is the separation between the upper and lower uncertainties which is larger in the toy study, indicating a more asymmetric result.

4.6 Results

The prompt dimuon production cross-section in a given bin can be expressed as

$$\sigma = \frac{\rho}{\mathcal{L}} \sum_{i=1}^{N} \frac{1}{\varepsilon_i} \tag{4.13}$$

where ρ is the prompt purity in the bin, $\mathcal{L}$ is the integrated luminosity of the sample, i is the candidate index and ε_i is the full selection efficiency of the candidate i.

Since the muon kinematic information of the constituent muons, and therefore per candidate efficiencies, is not available post-fitting the total efficiency for the fit

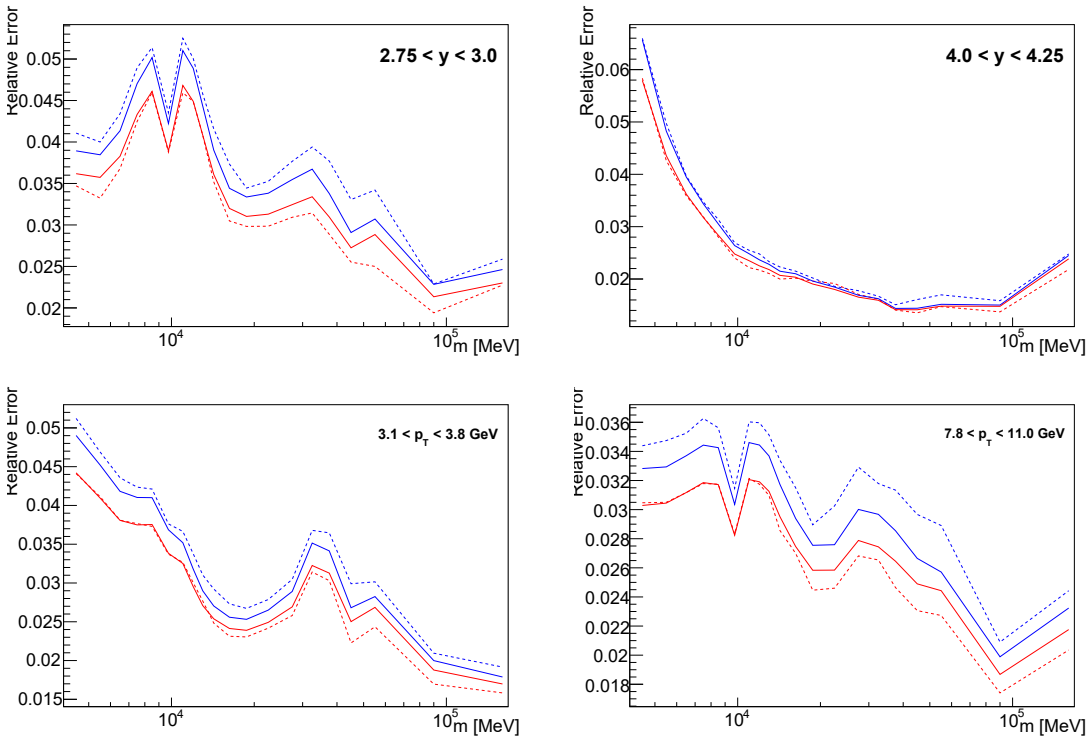

Figure 4.46: Example efficiency uncertainty in bins of (top) dimuon rapidity and (bottom) dimuon transverse momentum, as a function of dimuon invariant mass. The solid lines represent the results of the deterministic study, while the dashed lines show the toy study. The red line shows the upper uncertainty while the blue line shows the lower uncertainty.

bin cannot be obtained by summing over candidates. To overcome this, as has been discussed, most efficiencies have been applied as candidate weights prior to the fits. This leaves only the global efficiencies, ε_{nPV} and ε_{SPD}, giving the final form of the cross-section as,

$$\sigma = \frac{n_{\text{prompt}}}{\mathcal{L} \times \varepsilon_{\text{nPV}} \times \varepsilon_{\text{SPD}}} \tag{4.14}$$

where n_{prompt} is the prompt yield obtained from the template fit. The integrated luminosity of the 2016 dataset is measured as 1.63 ± 0.03 fb^{-1}. The efficiency of the primary vertex multiplicity requirement is given as a constant $73.8 \pm 0.5\%$ and the SPD multiplicity efficiency is taken to be 100% efficient, as measured in 4.3.

4.6.1 Resonance Cross-Checks

The presence of resonant dimuon modes in the dataset allows for cross-checks of this method of cross-section measurement. LHCb has made measurements of dimuon production through the decays of both the Z boson and $\Upsilon(1S)$ state, both of which can be evaluated in this analysis [91, 90, 92].

Since the previous measurements use different selection requirements it is required that they are corrected to the fiducial phase space used in this current analysis. This is achieved using Pythia, where the p_{T} distribution of the generated sample is weighted to match the distribution of the data. Ultimately, the correction is on the order of $\sim 1\%$. Fits are performed using the 2016 dataset binned according to the previous analyses.

For the $\Upsilon(1S) \to \mu\mu$ measurement, a $\pm 3\sigma$ signal window is taken around the peak where the resolution, $\sigma = 60$ MeV/c^2, is obtained from the fits used in the previous analysis. Four side-band bins are also defined, 8.26 - 8.62 GeV/c^2 and 8.62 - 8.98 GeV/c^2 below the peak and 10.655 - 11.015 GeV/c^2 and 11.015 - 11.375 GeV/c^2 above the $\Upsilon(3S)$ peak. The prompt yield of the side-bands are fit with a linear background model to obtain an estimation of the background in the signal bin. Equation 4.14 is used with the background-subtracted yield to obtain the result shown in Figure 4.47.

For the $Z/\gamma^* \to \mu\mu$ measurement, it is assumed that the sample is effectively 100% prompt and so no background fit is performed. The full prompt yield is then used to measure the cross-section which is shown in Figure 4.48.

These cross-checks indicate that, in most regions, the current method produces results that are consistent with the previous analysis. The area of largest deviation is at the high dimuon p_{T} region of the $\Upsilon(1S)$ resonance.

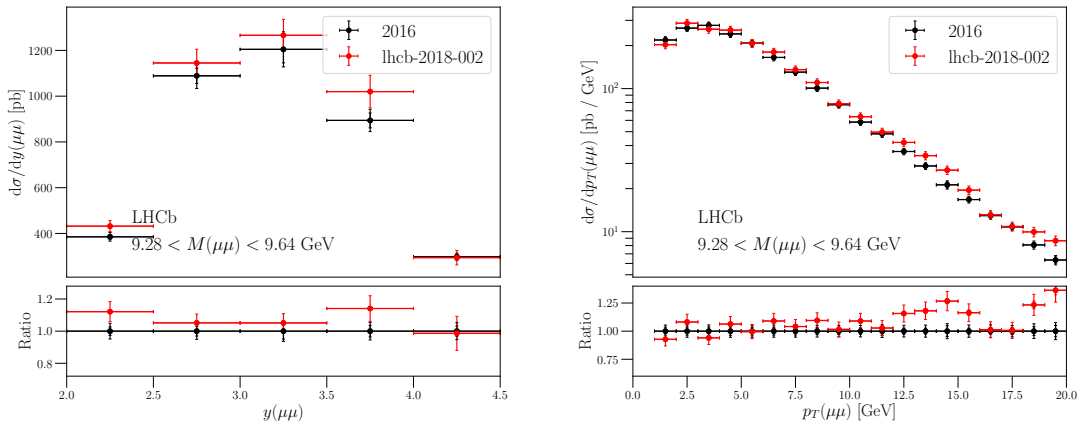

Figure 4.47: Measured cross-section of $\Upsilon(1S) \to \mu\mu$ as a function of (left) dimuon rapidity and (right) dimuon transverse momentum, compared to the previous LHCb measurement.

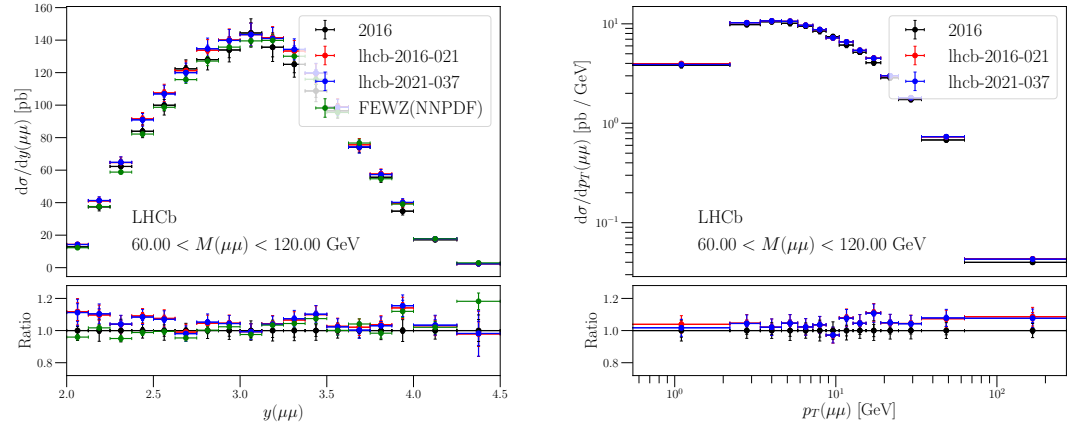

Figure 4.48: Measured cross-section of $Z/\gamma^* \to \mu\mu$ as a function of (left) dimuon rapidity and (right) dimuon transverse momentum, compared to the previous LHCb measurement.

4.6.2 Double Differential Drell-Yan Cross-Section

The final measurement of the double differential Drell-Yan cross-section is shown in Figures 4.49 and 4.50 as a function of dimuon mass and in bins of rapidity and transverse momentum respectively.

Here, comparisons are made to theoretical predictions made using the NNLOjet parton-level event generator and a massive variable flavour number scheme (MVFNS) described in references [93] and [94]. The measurements are seen to be in generally good agreement. These measurements can then be fit with a convolution of the parton scattering cross-section and a PDF and contribute to the improvement of PDF models and, hence, understanding of the structure of the proton.

4.7 Conclusion

To summarise, the Drell-Yan production cross-section has been measured through the dimuon channel, doubly differentially in both dimuon muon mass and rapidity, and in dimuon mass and transverse momentum, in the acceptance of the LHCb experiment.

This is achieved by selecting dimuon candidates from the 2016 Turbo stream and fitting the min $\sqrt{\chi^2_{\text{IP}}}$ distribution with templates produced from data. The templates represent the prompt signal, background from displaced heavy flavour decays, and background from tracks misidentified as muons.

The selection efficiency is evaluated in simulation using Drell-Yan and dimuon resonance Monte Carlo samples. Corrections for the differences between simulation and data are applied in the form of efficiency ratios. A global requirement that each candidate comes from an event with fewer than three primary vertices is made in order to more accurately evaluate the SPD multiplicity requirement made by the L0 trigger. The nPV and nSPD requirements are considered globally, whereas the remaining efficiencies are applied to the data sample as candidate weights.

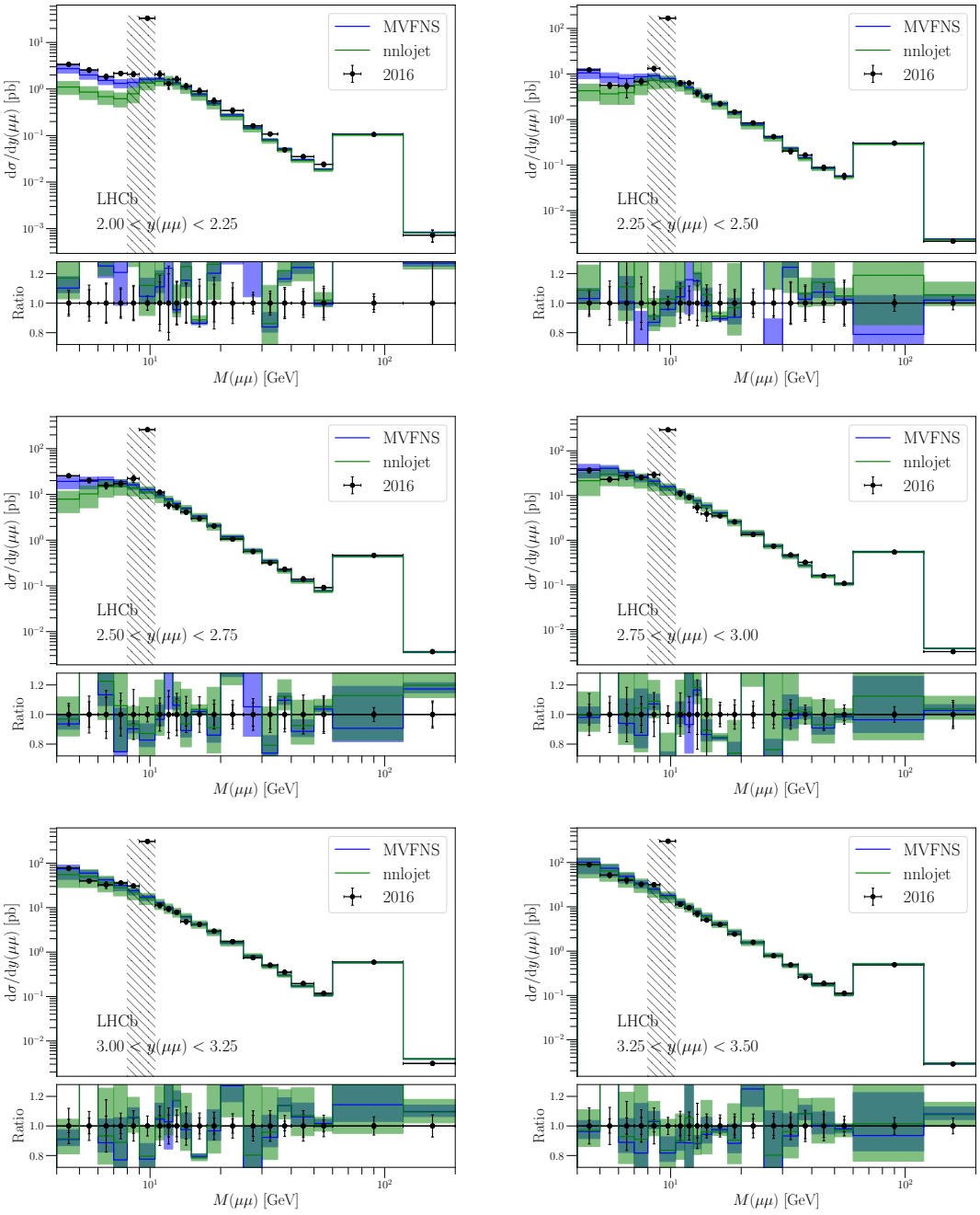

Figure 4.49: Measured cross-section of dimuon production through the Drell-Yan process as a function of dimuon invariant mass, shown in bins of dimuon rapidity and compared to the available theoretical predictions.

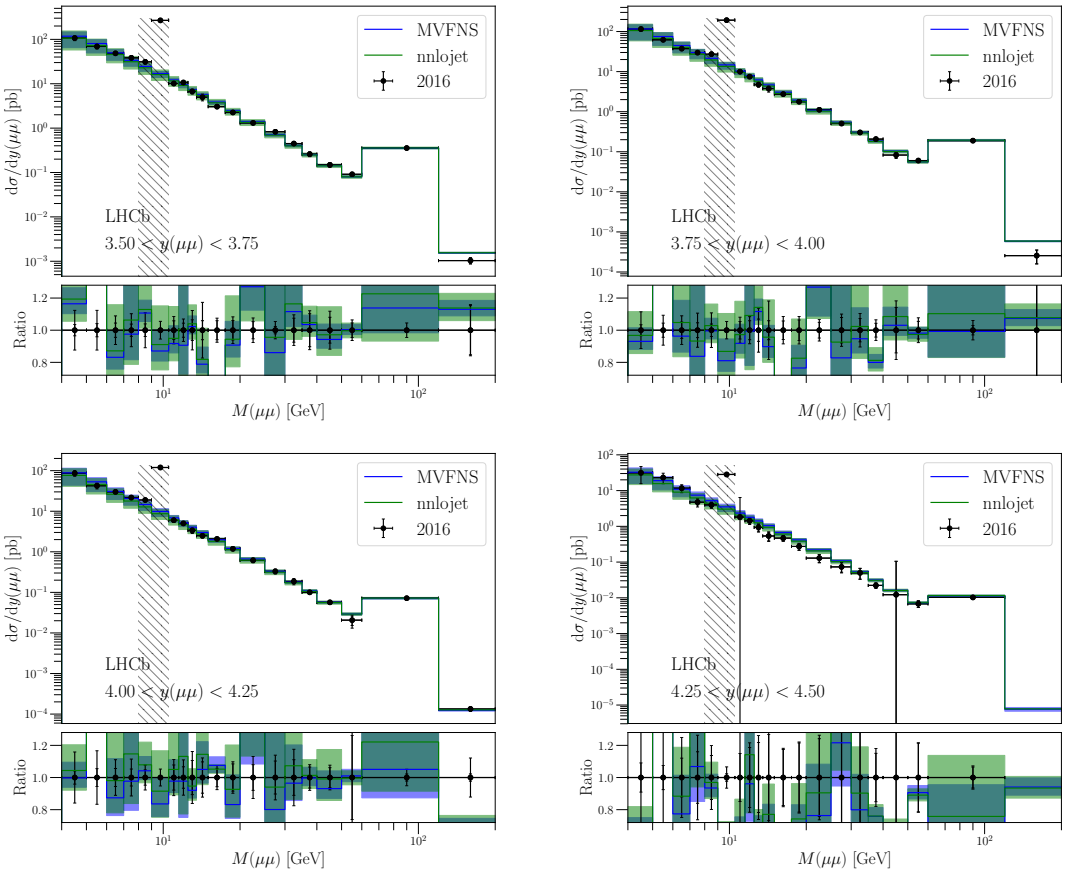

Figure 4.49: Measured cross-section of dimuon production through the Drell-Yan process as a function of dimuon invariant mass, shown in bins of dimuon rapidity and compared to the available theoretical predictions.

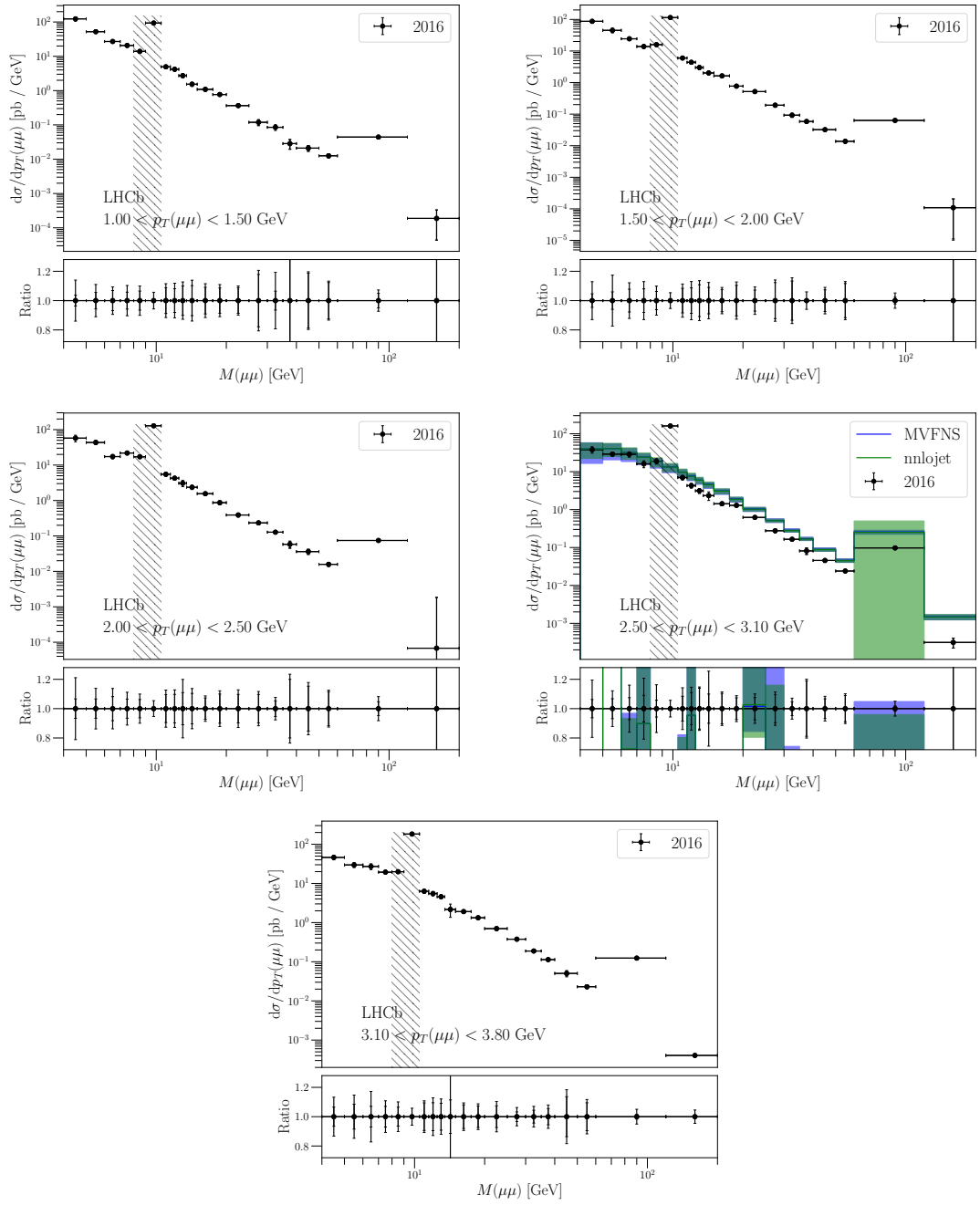

Figure 4.50: Measured cross-section of dimuon production through the Drell-Yan process as a function of dimuon invariant mass, shown in bins of dimuon transverse momentum and compared to the available theoretical predictions.

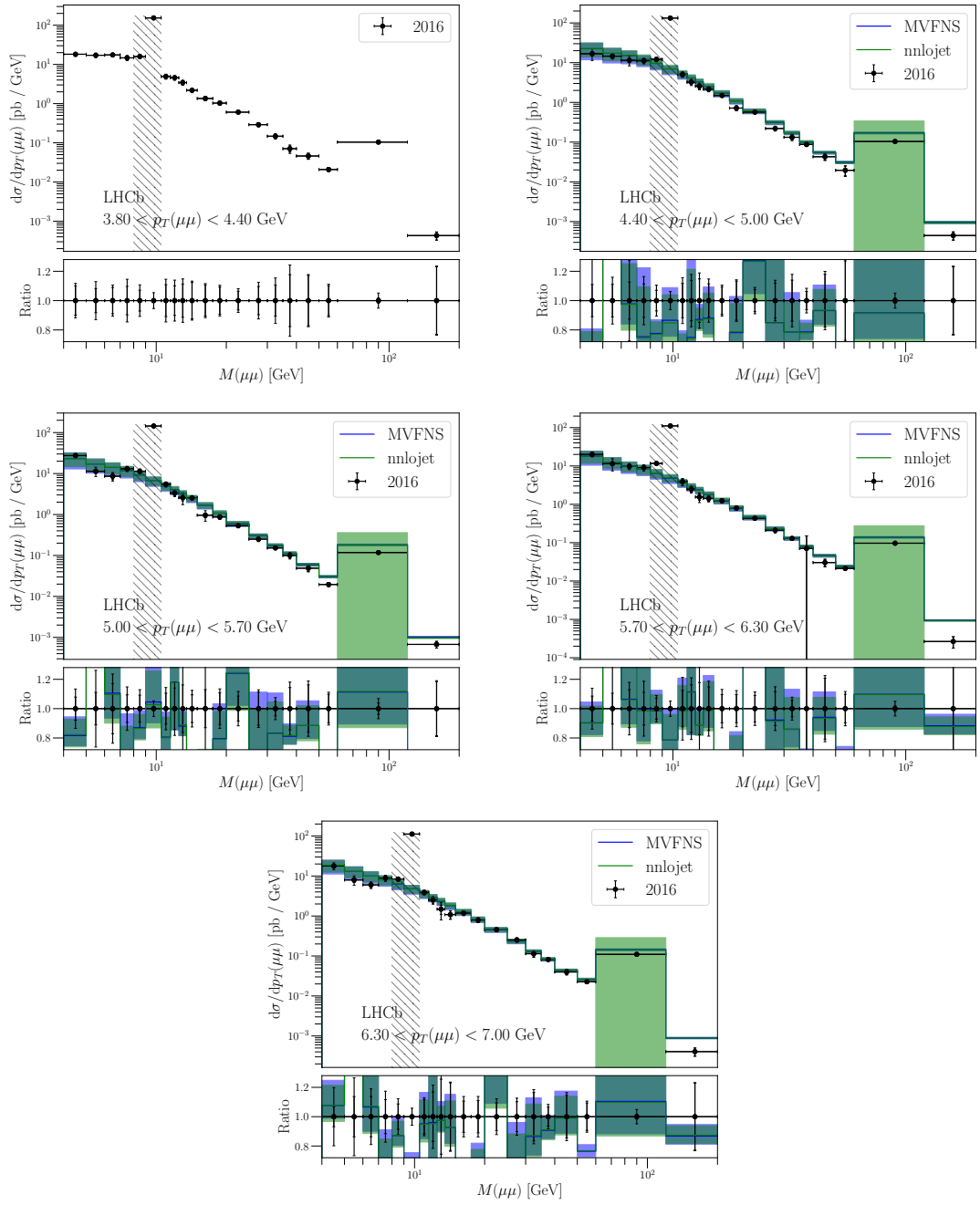

Figure 4.50: Measured cross-section of dimuon production through the Drell-Yan process as a function of dimuon invariant mass, shown in bins of dimuon transverse momentum, compared to theoretical predictions from Pythia.

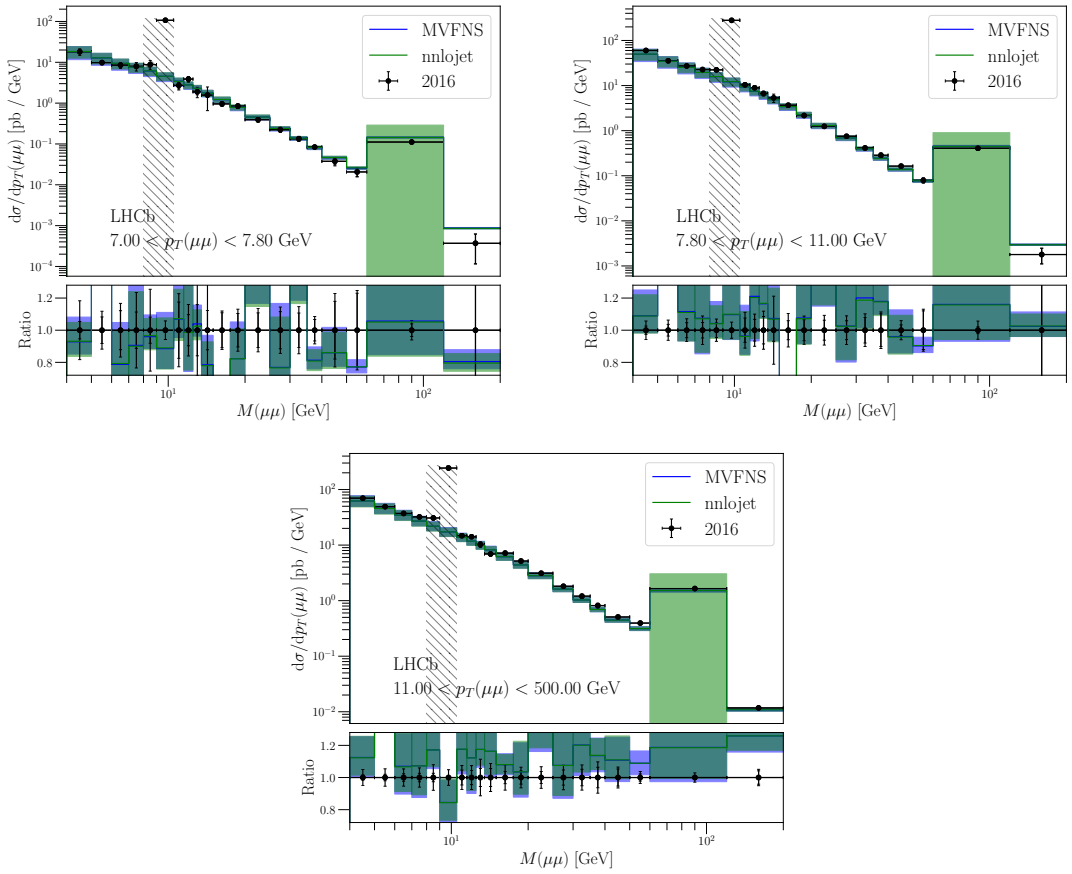

Figure 4.50: Measured cross-section of dimuon production through the Drell-Yan process as a function of dimuon invariant mass, shown in bins of dimuon transverse momentum, compared to theoretical predictions from Pythia.

The cross-section measurements are validated by a cross-check where the same method is used to measure the $\Upsilon(1S)$ and Z dimuon decay cross-sections. These cross-check measurements are found to align with good agreement to the measurements made previously by LHCb.

Finally, the Drell-Yan differential cross-section measurement is presented in comparison to theoretical predictions from NNLOjet and a MVFNS. The measurement is found to be in good agreement with the predictions.

Time constraints mean that this result is given using only the $1.63\,\text{fb}^{-1}$ 2016 dataset. There are small differences in the 2017 and 2018 selection recorded at LHCb, but the full Run 2 dataset is estimated to contain $5.4\,\text{fb}^{-1}$ which would allow for a more precise measurement in the near future.

Chapter 5

Discovering True Muonium at LHCb

This chapter describes the study of the potential of the LHCb experiment to discover the $\mu^+\mu^-$ true muonium ($\mathcal{TM}$) bound state. This work was published as reference [48].

5.1 Motivation

Electromagnetic interactions between oppositely charged particles allow for bound states. Atoms are the most common of these, consisting of a positively charged nucleus of protons and neutrons, governed by the strong interaction, with bound electrons.

More exotic states have also been observed such as positronium (a bound state of e^+e^-) and muonium (a bound state of μ^+e^-). The properties of these leptonic bound states are predicted by quantum electrodynamics (QED). Therefore precise measurements of mass and energy spectra of these particles allow for tests of standard model QED.

Heavier bound states are predicted but yet to be observed. The measurement of the properties of these states would be a unique probe that is sensitive to beyond the standard model (BSM) physics. The focus of this study is the bound state of a muon and anti-muon, $\mu^+\mu^-$, known as true muonium and the potential of the LHCb

experiment to discover its lowest spin-1 state.

Several experimental results show discrepancies in muonic systems. For example, the 2010 measurement of the charge radius of the proton obtained by measuring the Lamb shift ($2S_{1/2}$ to $2P_{1/2}$) in muonic hydrogen ($p^+\mu^-$) differed by 5.0σ from the same measurement in electronic hydrogen [95, 96]. A subsequent measurement in 2016 using muonic deuterium gave consistent results [97].

Another source of tension is the muon anomalous magnetic moment, given by

$$a = \frac{g-2}{2} \tag{5.1}$$

where g is the gyromagnetic ratio or g-factor. The g-factor is predicted to be 2 by the Dirac equation but higher order perturbations also contribute. For muons, QED contributions are currently calculated to eighth order and electroweak contributions to second order, however hadronic contributions must be evaluated experimentally [98]. The most precise measurement was made by the Muon g-2 experiment (combined result from Brookhaven and Fermilab) which gives

$$a_\mu = 116592061(41) \times 10^{-11} \tag{5.2}$$

which is in excess of the standard model prediction by 4.2σ [99, 100].

LHCb has tested potential new physics in muon physics through the R_K and R_{K^*} measurements, which are defined as

$$R_{K^{(*)}} = \frac{\mathcal{B}(B^+ \to K^{(*)+}\mu^+\mu^-)}{\mathcal{B}(B^+ \to K^{(*)+}e^+e^-)} \tag{5.3}$$

$B \to K^{(*)}l^+l^-$ decays occur flavour changing neutral current (FCNC) loops which are particularly sensitive to new physics as new force propagators may provide additional contributions. In the standard model, all charged leptons interact equally with the electroweak force. This lepton universality means the standard model predicts an $R_{K^{(*)}}$ close to unity, with the differences arising only from phase space

restrictions due to the difference in lepton masses. The most recent result from LHCb gives

$$R_K(1.1 < q^2 < 6.0\text{GeV}^2/c^4) = 0.846^{+0.044}_{-0.041} \tag{5.4}$$

which deviates from the standard model prediction by 3.1σ, evidence for the violation of lepton universality [101].

True muonium offers a unique opportunity to make measurements of a purely muonic system. Precise measurements of the mass, lifetime and energy levels of true muonium could reveal deviations from the standard model prediction which may indicate new physics in the form of unobserved particles exchanged between the constituent muons.

5.2 Properties and Signature Decay

The most promising spin state for discovery is the 1^3S_1 triplet state, denoted as $\mathcal{TM}$ from here on, which dominantly decays to an electron-positron pair, e^+e^-. By contrast, the spin singlet state ($^1S_0$) decays to pairs of photons which are generally harder to reconstruct experimentally [48].

The vector state $\mathcal{TM}$ undergoes kinetic mixing with the photon, similar to that of the dark photon. The dark photon has also been a point of study at LHCb [102]. The coupling of the dark photon to the SM photon, via kinetic mixing, is given by the Lagrangian

$$\mathcal{L} \subset \frac{\varepsilon}{2} F_{\mu\nu} F'^{\mu\nu} \tag{5.5}$$

where $F_{\mu\nu}$ and $F'^{\mu\nu}$ are the dark photon and SM photon field strengths respectively. The phenomenology of $\mathcal{TM}$ is similar to that of the dark photon at energies close to the $\mathcal{TM}$ mass. As a result, the projected reaches of future dark photon experiments

can provide a rough guide to $\mathcal{TM}$ sensitivity as shown in the phase space plot in figure 5.1.

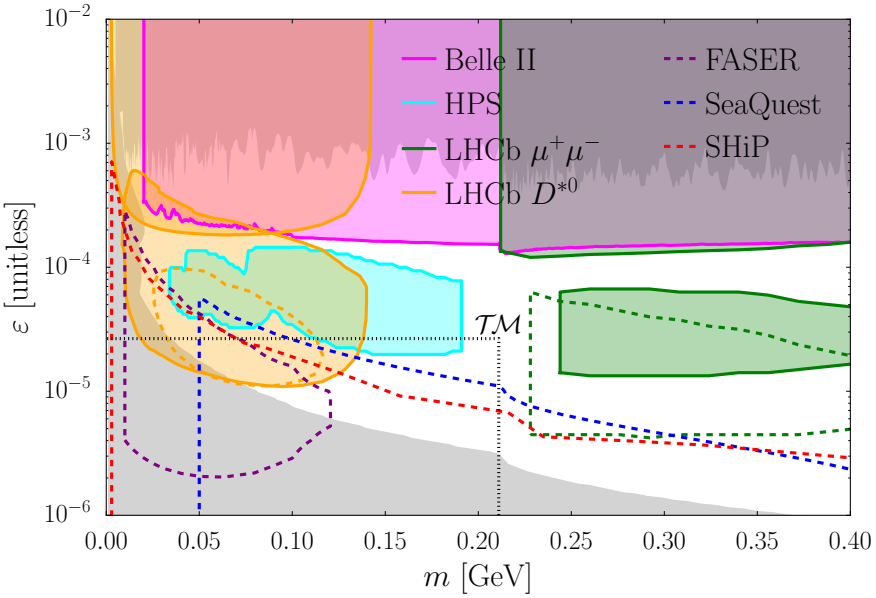

Figure 5.1: Parameter space in dark photon mass and kinetic mixing with (grey) previous limits and future reach of (magenta) Belle II, (purple) FASER, (cyan) HPS and (green & yellow) LHCb. Dashed lines show studies expected to be affected by $\mathcal{TM}$ dissociation (see section 5.3). $\mathcal{TM}$ shown with mass and kinetic mixing from equations 5.6 and 5.7.

The mass and kinetic mixing of $\mathcal{TM}$ predicted by leading order QED are

$$m_{\mathcal{TM}} = 2m_\mu - B_E \approx 211 \text{ MeV} \tag{5.6}$$

$$\varepsilon_{\mathcal{TM}} = \alpha^2/2 \approx 2.66 \times 10^{-5} \tag{5.7}$$

where $B_E \approx m_\mu \alpha^2/4 = 1.41$ keV is the $\mathcal{TM}$ binding energy, estimated in the non-relativistic limit.

As previously noted, $\mathcal{TM}$ decays through kinetic mixing to a dielectron final state with a branching fraction of $\text{BR}(\mathcal{TM} \to e^+e^-) \approx 98\%$. The subdominant decay mode has a final state of a triplet of photons with $\text{BR}(\mathcal{TM} \to 3\gamma) \approx 1.7\%$. The lifetime of $\mathcal{TM}$ is estimated at leading order to be

$$\tau_{\mathcal{TM}} \approx \frac{6}{\alpha^5 m_\mu} = 1.8 \times 10^{-12} \text{ s} \tag{5.8}$$

Given the forward acceptance and the resulting high boost at LHCb, along with the proper lifetime of 0.53 mm, $\mathcal{TM}$ decays will produced displaced vertices comparable to those of the B meson decays that LHCb was designed to resolve.

5.3 Dissociation of True Muonium

The most significant phenomenological difference between $\mathcal{TM}$ and the dark photon arises due to the fact that $\mathcal{TM}$ is a bound state of constituent particles rather than an elementary particle. This allows the interaction of the constituent muons with the material of experiment hardware, causing dissociation into an unbound $\mu^+\mu^-$ pair with an invariant mass slightly higher than the $\mathcal{TM}$ mass.

The cross-section for dissociation is estimated to be $\sigma(\mathcal{TM} \to \mu^+\mu^-) \approx 13Z^2$ b, where Z is the atomic number of the material being traversed. At LHCb, the first material traverse by long-lived particles is the VELO RF foil (see section 3.2.1), made of aluminium which has $Z = 13$. If the $\mathcal{TM}$ particle were to penetrate the foil, the next material is the silicon sensors which have $Z = 14$. Given the similar atomic numbers and number densities of aluminium and silicon, the mean free path for $\mathcal{TM}$ traversing the LHCb detector is estimated to be

$$\lambda^{-1} = \sigma(\mathcal{TM} \to \mu^+\mu^-)n_a \approx 13 \text{ mm}^{-1} \tag{5.9}$$

where the number density $n_a \approx 6.0(5.0) \times 10^{19}$ atoms/mm^3 for aluminium(silicon). The probability of a $\mathcal{TM}$ candidate dissociating is given by

$$\mathcal{P}_{\text{dis}} = 1 - e^{-x/\lambda} \tag{5.10}$$

where x is the distance traversed in the material.

For the Run 3 VELO upgrade, the RF foil will have a thickness of 0.25 mm and the silicon sensors will have a thickness of 0.2 mm. This results in a minimum dissociation probability for every interaction between $\mathcal{TM}$ and the VELO material of $\mathcal{P}_{\text{dis}} \gtrsim 90\%$.

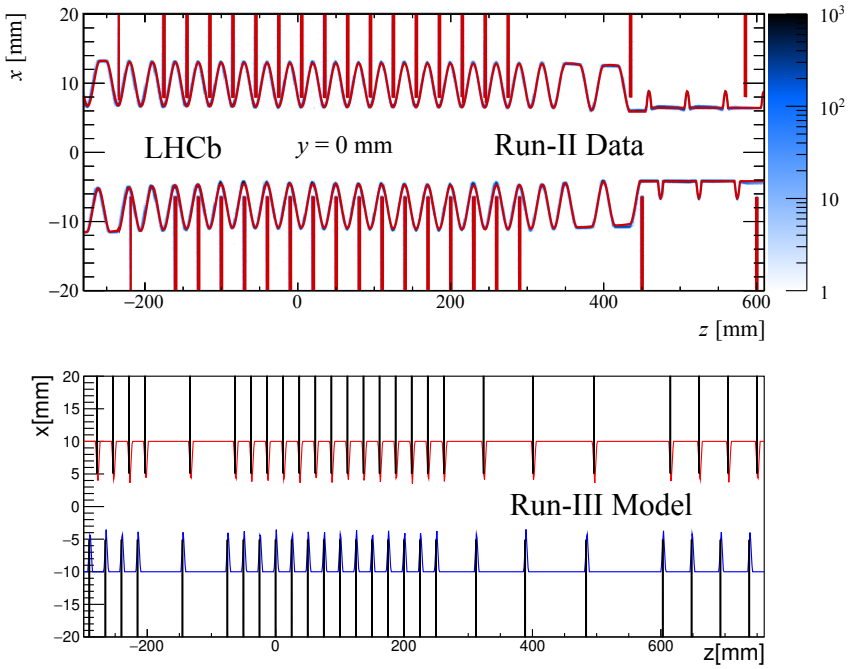

Figure 5.2: VELO structure for (top) Run 2, fitted to beam-gas data and (bottom) Run 3, from model.

The effects of dissociation are estimated by simulating $\mathcal{TM}$ decays using Pythia and calculating x using a model of the RF foil, shown for Run 2 and Run 3 in figure 5.2. The foil model is obtained through the modification of an existing material tool, where two instances of the foil are translated such that the distance between them is equal to the material thickness. Intersections of particle trajectories with the foil surface are calculated using numerical root finding methods.

For a given candidate, if the distance from the PV and the decay vertex is greater than the distance to first intersection with the foil, the transversed distance, x, and the probability of dissociation are calculated. A random number is uniformly sampled and if this is less than the dissociation probability, the candidate is marked as "dissociated" and removed from the sample. For candidates that do not dissoci-

ate, the process is repeated for the next intersection with material until it has either decayed or dissociated.

From this simulation, it is expected that in Run 3 approximately 50% of $\mathcal{TM}$ produced will dissociate before they can decay to the e^+e^- signal. The radial flight distance of $\mathcal{TM}$ candidates that do decay is shown in figure 5.3. The signal typically has a larger boost than the background, giving a flatter distribution that falls sharply at approximately 5 mm due to dissociation.

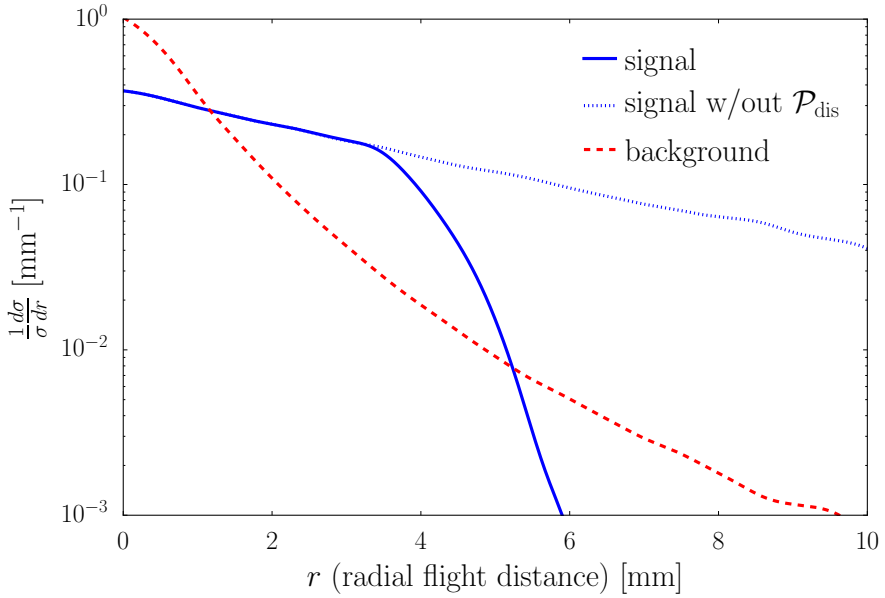

Figure 5.3: Normalised radial flight distance of $\mathcal{TM} \to e^+e^-$ decays (solid blue) with dissociation, (dotted blue) without dissociation, and (dashed red) expected e^+e^- background from B decays.

Dissociation, therefore, gives rise to a potential signal of $\mu^+\mu^-$ produced in areas of high material density. This signal, however, would be very difficult to reconstruct at LHCb and would suffer from large, irreducible backgrounds. Firstly, the two muons would be produced with essentially collinear trajectories, resulting in shared hits in both the VELO and the Muon chambers, meaning that the identification of a dimuon signature would be difficult. Secondly, the signal itself is indistinguishable from $\gamma \to \mu^+\mu^-$ pair production in the material which can no longer be vetoed using material maps without eliminating the signal. As a result, only the $\mathcal{TM} \to e^+e^-$ signal is considered for discovery at LHCb.

5.4 Proposed Search at LHCb

It is proposed to search for $\mathcal{TM}$ as a displaced e^+e^- resonance. Due to the phenomenological similarities with the dark photon, the signal rate can be calculated directly from the off-shell photon rate given by prompt e^+e^- data [103, 82, 87].

For any initial state, Y, and final state, X, the ratio between the number of $Y \to X\ \mathcal{TM} \to Xe^+e^-$ signal events, $S_{\mathcal{TM}}$, and $Y \to X\gamma^* \to Xe^+e^-$ background events, B_{EM}, remains fixed. For the invariant mass range $|m_{ee} - m_{\mathcal{TM}}| < 2\sigma_{m_{ee}}$, where $\sigma_{m_{ee}}$ is the dielectron mass resolution, this ratio is given by

$$\frac{S_{\mathcal{TM}}}{B_{\text{EM}}} \approx \frac{3\pi}{16}\frac{m_\mu}{\sigma_{m_{ee}}}\alpha^3 \approx \frac{20\text{ MeV}}{\sigma_{m_{ee}}}1.2 \times 10^{-6} \tag{5.11}$$

The dominant source of off-shell photons in this mass range is from the decay of η mesons via the $\eta \to \gamma\gamma^*$ mode. The focus is therefore on searching for $\mathcal{TM}$ produced via $\eta \to \gamma\ \mathcal{TM}$ and decaying via $\mathcal{TM} \to e^+e^-$.

The expected number of signal events is estimated from simulation using Pythia 8.2 [104]. This gives values for both the total pp cross-section, $\sigma_{pp} = 100$ mb, and the average number of η mesons produced per collision, $N_\eta = 0.83$, which are in agreement with LHCb measurements [105, 87]. The branching ratio for $\mathcal{TM}$ production in this way is $\text{BR}(\eta \to \gamma\mathcal{TM}) = 4.8 \times 10^{-10}$, which agrees well with equation 5.11 using the differential $\eta \to \gamma e^+e^-$ shape from Pythia [106]. This gives an expected $\mathcal{TM}$ production cross-section in the fiducial region of

$$\sigma^{\text{fid}}_{\mathcal{TM}} = \sigma_{pp}N_\eta\text{BR}(\eta \to \gamma\mathcal{TM}) \approx 40\text{ pb} \tag{5.12}$$

Here, two search strategies are considered: (i) an inclusive search with an e^+e^- final state where the photon is not selected and the η meson is not reconstructed, and (ii) an exclusive search where the final state is γe^+e^- and the η is reconstructed.

Both methods have their advantages. The inclusive search is simpler and is therefore expected to have lower systematic uncertainties. In addition the inclusive

search can in principle select $\mathcal{TM}$ candidates from any production mechanism. On the other hand, the exclusive search would have reduced background rates. Since full-detector simulation and data-driven background estimates are currently unavailable for Run 3 at LHCb, it is impossible to say which strategy is optimal. Therefore the potential sensitivity of both methods are estimated here.

The precise performance of LHCb in Run 3 is unknown but the relevant mass resolutions can be estimated from current analyses. The e^+e^- mass resolution in the region of $m_{\mathcal{TM}}$ is estimated to be $\sigma_{m_{ee}} \approx 20$ MeV, based on the $K^0_s \to \pi^+\pi^-e^+e^-$ analysis at LHCb [107]. The γe^+e^- resolution is estimated to be $\sigma_{m_{\gamma ee}} \approx 50$ MeV, based on χ_c and radiative B^0_s decays [108, 109].

5.4.1 Selection Criteria

The same selection criteria are applied to the electrons and $\mathcal{TM}$ candidate for both the inclusive (i) and exclusive (ii) searches, and are shown in detail below.

Requirements on $e^{\pm}$:

- $p(e^{\pm}) > 10$ GeV
- $p_T(e^{\pm}) > 0.5$ GeV
- Non-zero transverse impact parameter, $\mathrm{IP}_T(e^{\pm}) > 3\sigma_{\mathrm{IP}_T(e)}$, where $\sigma_{\mathrm{IP}_T(e)}$ is the IP_T resolution

Requirements on the reconstructed $\mathcal{TM}$ candidate:

- $p_T(\mathcal{TM}) > 1.0$ GeV
- $|m_{ee} - m_{\mathcal{TM}}| < 2\sigma_{m_{ee}}$
- Distance of closest approach (DOCA) between electrons must be consistent with zero; $\mathrm{DOCA}(e^+, e^-) < 3\sigma_{\mathrm{DOCA}(e^+,e^-)}$

For the exclusive (ii) search, additional criteria are required of the associated photon and the reconstructed η meson.
Requirements on the photon:

- $p(\gamma) > 5$ GeV
- $p_T(\gamma) > 0.65$ GeV

Requirements on the reconstructed η meson:

- $|m_{\gamma ee} - m_\eta| < 2\sigma_{m_{\gamma ee}}$

For both cases, data will be collected using a dielectron trigger. During Run 1 and Run 2, single electrons were selected by the L0 hardware trigger using tight kinematic cuts that are not efficient for these searches, although a new dielectron trigger line was made available in 2018. However, LHCb is moving to full online reconstruction with triggerless readout for Run 3, allowing the reconstruction of lower momentum signals, including that of $\mathcal{TM}$ decays, at a higher efficiency.

5.4.2 Background Reduction

The dominant background with this selection is from displaced B-hadron decays, with a lesser component from D-hadron decays as these rarely produce e^+e^- candidates in the chosen kinematic region. Photon conversions in the detector material are also a potential background. These can be significantly reduced via a material veto used in the LHCb inclusive dark photon search [102]. Similarly, background from $\eta \to \gamma e^+ e^-$ decays will be minimal due to the prompt nature of the resulting vertex.

B-hadrons typically decay to a high multiplicity of tracks, whereas $\mathcal{TM}$ decays are isolated. As a proxy for dedicated B-decay vetoes, the following additional selections are made:

- The $\mathcal{TM}$ candidate is well isolated from other tracks: tracks with $p_T(\text{trk}) > 0.5$ GeV and $\text{IP}_\text{T}(\text{trk}) > 3\sigma_{\text{IP}_\text{T}}(\text{trk})$ must satisfy $\text{DOCA}(\text{trk}, e) > 3\sigma_{\text{DOCA}}(\text{trk}, e)$

- The opening angle, θ, between the flight vector and momentum vector of the $\mathcal{TM}$ candidate must be consistent with zero, which is demonstrated in figure 5.4

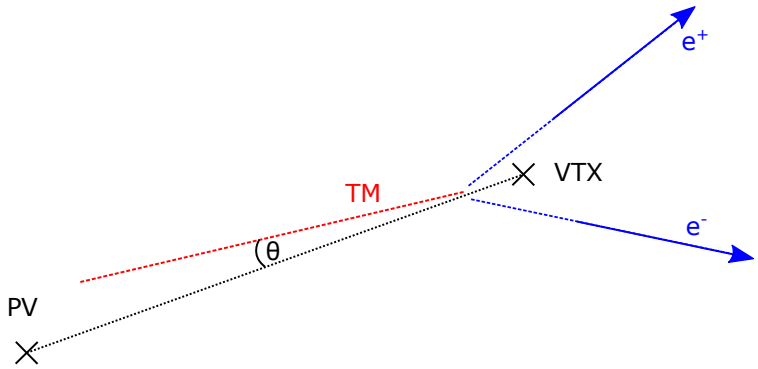

Figure 5.4: Diagram demonstrating the opening angle, θ, between the flight vector, from the primary vertex to the decay vertex, and the momentum vector of the $\mathcal{TM}$ candidate, from the sum of the electron momenta, which is required to be consistent with zero.

Expected Yields and Significance

The number of expected signal and background events in a Run 3 dataset can then be predicted for both strategies, with the baseline requirement and following both of these background reduction requirements, and are shown in table 5.1.

Table 5.1: Expected signal and background yields for $\mathcal{TM}$ selection criteria.

requirement	$S^{(\text{i})}_{\mathcal{TM}}$	$B^{(\text{i})}_{\text{tot}}$	$S^{(\text{ii})}_{\mathcal{TM}}$	$B^{(\text{ii})}_{\text{tot}}$
base	3.4×10^3	3.2×10^7	1.6×10^3	5.4×10^6
$\text{DOCA}(\text{trk}, e)$	3.0×10^3	8.5×10^6	1.3×10^3	1.1×10^6
θ	1.5×10^3	1.8×10^4	6.4×10^2	1.9×10^3
efficiency	4.4×10^{-1}	5.6×10^{-4}	4.0×10^{-1}	3.5×10^{-4}

Less than 0.1% of signal events satisfy the baseline selection criteria, mostly due to inefficient p_T requirements that cannot be loosened. The efficiencies of the background reduction criteria are approximately 40% for signal events and between $10^{-4} - 10^{-3}$ for background, allowing for effective background reduction.

Finally, the efficiency of reconstructing the final state particles, ε_f, must also be considered. Since these efficiencies are currently unknown for Run 3 and Run 4, they are left as an unknown parameter in the expression for signal significance. However, the current experimental performance can be used as a reference point. From the $B \to J/\psi K^{*0}$ analysis it is estimated that $\varepsilon_{e^+e^-} > 10\%$, while from the analysis of the ratio of χ_c to J/ψ production it is estimated that $\varepsilon_{\gamma e^+e^-} \approx 0.3\varepsilon_{e^+e^-} > 3\%$ [110, 108].

The background rate in the signal region can be estimated from the sidebands and as a result the significance is expected to be limited by the statistical uncertainty. This technique was used in the LHCb dark photon search, where the significance was greatly improved by the inclusion of known background structures [102, 111]. This analysis benefits from a well defined signal region where the shape of the B-hadron background has been demonstrated to be well modelled, and as such the same is expected here.

The significance of the $\mathcal{TM}$ signal is therefore expected to be approximately given by

$$\sigma_{\text{stat}} \approx \frac{S_{\mathcal{TM}}}{\sqrt{B_{\text{tot}}}} \sqrt{\frac{\varepsilon_f \mathcal{L}}{15 \text{ fb}^{-1}}} \tag{5.13}$$

where $S_{\mathcal{TM}}$ and B_{tot} are the expected number of signal and background events given in Table 5.1, ε_f is the final state reconstruction efficiency and $\mathcal{L}$ is the integrated luminosity of the selected dataset. Using the expected Run 3 dataset of 15 fb^{-1}, $\mathcal{TM}$ can be discovered with $\sigma_{\text{stat}} > 5$ when $\varepsilon_{e^+e^-} > 20\%$ and $\varepsilon_{\gamma e^+e^-} > 12\%$ for the inclusive and exclusive searches respectively. Given the current LHCb performance and the move to triggerless readout in Run 3, these efficiencies are realistic.

Figure 5.5 shows the required luminosity for the discovery of $\mathcal{TM}$ as a function of ε_f. Figure 5.6 shows the expected differential cross-sections with respect to the e^+e^- invariant mass, assuming a final state reconstruction efficiency of 20% and 6% for the inclusive and exclusive searches respectively.

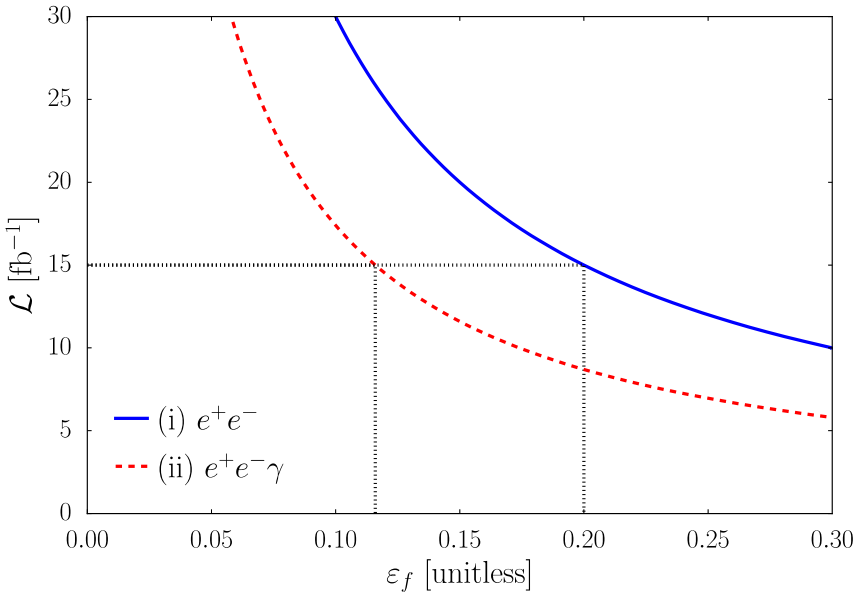

Figure 5.5: Integrated luminosity required for $\sigma_{\text{stat}} > 5$ as a function of ε_f, the final state reconstruction efficiency, for the (blue) inclusive, (red) exclusive search.

5.5 Conclusion

In summary, the measurement of the properties of the true muonium bound state would allow scrutiny of the standard model muonic interactions, potentially revealing new physics.

Here it is predicted that the LHCb experiment will be able to discover the 1^3S_1 spin triplet state of true muonium ($\mathcal{TM}$), produced by the decay of η mesons, through its decay to a dielectron pair. With the expected boost at LHCb and the predicted lifetime of $\mathcal{TM}$, approximately 50% of signal candidates are lost due to dissociation in the detector material. The decay vertices of the candidates that do not dissociate will be displaced from the primary vertex, similar to those of B

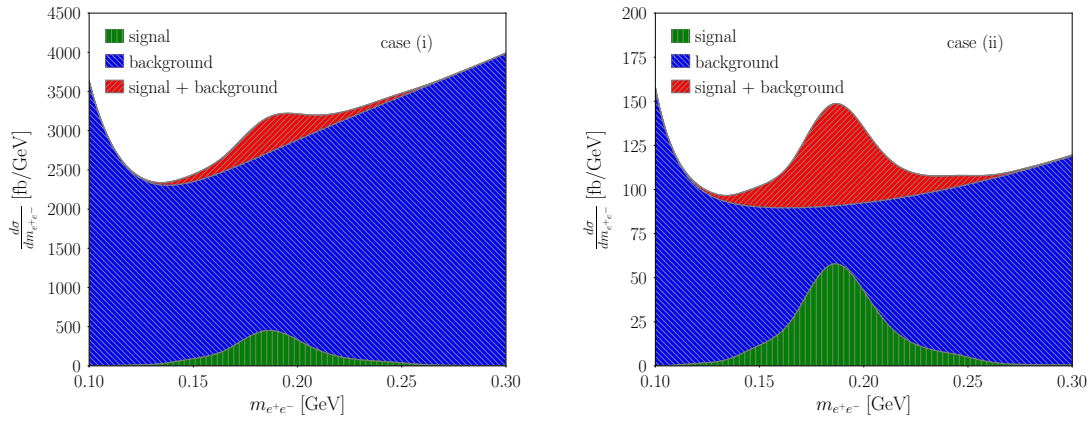

Figure 5.6: Differential cross-sections of expected $\mathcal{TM}$ signal and combinatoric background at LHCb, assuming the normalisation given in Table 5.1 for (left) the inclusive search, case i, (right) the exclusive search, case ii. Here ε_f is assumed to be 20% and 6% for the inclusive and exclusive searches respectively. With these conditions, a 5σ discovery can be made with a luminosity of (i) 15 fb^{-1}, (ii) 30 fb^{-1}. The invariant mass distribution of the combinatoric background is obtained from simulation.

hadron decays.

Two search strategies have been suggested. The first is an inclusive search, selecting only the dielectron candidates in the relevant invariant mass window, which in principle could select $\mathcal{TM}$ candidates from any production mode. The second strategy is an exclusive search where the photon from the η decay is also selected and the η meson itself is reconstructed.

Both strategies employ a material veto to reduce background from photon conversions in the VELO material. The dominant background are dielectrons from displaced B-hadron decays. This is reduced by additionally requiring that the $\mathcal{TM}$ candidate is well isolated and that the candidate flight vector and momentum vector are consistent. These requirements result in excellent separation between signal and background.

Finally, the efficiency of the reconstruction of the final state particles is also considered. From the current LHCb performance it is estimated that $\varepsilon_{e^+e^-} > 10\%$ and $\varepsilon_{\gamma e^+e^-} > 3\%$. The efficiencies required for a 5σ discovery in a 15 fb^{-1} dataset are estimated to be 20% and 12% for the inclusive and exclusive strategies respectively.

These improvements are believed to be reasonable given the current detector and trigger upgrades.

Chapter 6

Conclusions

Measurements of the Drell-Yan production cross-section have been made through the dimuon channel; double differentially with respect to the dimuon candidate mass and rapidity, and also with respect to the candidate mass and transverse momentum. Both measurements were made using dimuon candidates selected from the data taken by the LHCb experiment in 2016 using a dedicated High Level Trigger line in the Turbo stream. The total dataset has an integrated luminosity of $1.63\,\text{fb}^{-1}$, though the data taken in 2017 and 2018 gives the potential for this to be increased to $5.4\,\text{fb}^{-1}$ in the near future.

The dataset is weighted by the selection efficiency of each candidate. The per candidate efficiency is evaluated using simulated sets of signal and dimuon resonance events. The efficiencies are also corrected for differences between Monte Carlo and data using additional samples.

The main backgrounds in this analysis arise from displaced heavy flavour decays and from misidentification. The displaced background is dominated by the decays of particles formed in the hadronisation of $b\bar{b}$ and $c\bar{c}$ pairs, from which muons may be erroneously reconstructed as being produced with a prompt vertex. The misidentification of hadrons, typically pions, can also lead to the selection of candidates consisting of one or more misidentified tracks.

The separation of these backgrounds from the prompt signal is achieved using a template fit of the data as a function of the minimum muon $\sqrt{\chi^2_{\rm IP}}$. Templates are produced for the prompt signal and displaced background using data driven methods, while the MisID template is taken from a selection of same-sign dimuon candidates. The fits are performed by minimising a modified χ^2 variable, where template shapes are allowed to vary according to their uncertainties, using MINUIT.

This method of cross-section measurement is validated by also measuring the dimuon production cross-section from $\Upsilon(1S)$ and Z decays. These measurements are compared to those made previously at LHCb in dedicated analyses, and are found to be in good agreement. The final cross-section measurements are found to be in agreement with theoretical predictions. These measurements offer insight into a region of phase space that has not been measured previously; in the forward acceptance region only available with LHCb, at $\sqrt{s} = 13\,\text{TeV}$. This will contribute to increasingly accurate measurements of the structure of the proton and predictions of backgrounds in the searches for rare processes.

In addition to this measurement, a search for the so far undiscovered true muonium bound state has also been proposed. The production of $^3\text{S}_1$ triplet state true muonium, $\mathcal{TM}$, is expected to be most prolific in the decays of η mesons at LHCb, via the $\eta \to \gamma^*\gamma$ mode. The most feasible detection channel is the dominant decay to a dielectron pair, $\mathcal{TM} \to e^+e^-$, which is the most straightforward at LHCb.

Simulations of $\mathcal{TM}$ decays in the LHCb upgrade VELO have shown that approximately 50% of candidates produced will be lost to dissociation in material interactions. The reconstruction of $\mathcal{TM}$ candidates from the dissociated muons is rejected as they would be produced almost collinear and thus be difficult to reconstruct. As dissociation occurs in the material, candidates would also be indistinguishable from photon conversions.

Two search methods have been suggested: an inclusive search in which only the electrons selected and $\mathcal{TM}$ candidate reconstructed, and an exclusive search where

the photon is also selected and the η candidate reconstructed. Backgrounds from photon conversions are reduced by a material veto, while background from B decays are reduced by requiring that candidates are well isolated and the candidate flight vector is consistent with its momentum vector.

Finally the reconstruction efficiencies are estimated in order to make a 5σ discovery with $15\,\text{fb}^{-1}$ of data taken at LHCb in Run III. For the inclusive search it will be required that $\varepsilon_{e^+e^-} \approx 20\%$, while for the exclusive search $\varepsilon_{\gamma e^+e^-} \approx 12\%$. Given the improvements being made to the detector and trigger in the current upgrade, these efficiencies appear reasonable and LHCb is expected to be capable of discovering true muonium in Run III.

References

[1] J. J. Thomson. "XL. Cathode Rays". In: *The London, Edinburgh, and Dublin Philosophical Magazine and Journal of Science* 44.269 (1897), pp. 293–316. DOI: 10.1080/14786449708621070. eprint: https://doi.org/10.1080/14786449708621070.

[2] E. Rutherford. "LXXIX. The scattering of α and β particles by matter and the structure of the atom". In: *The London, Edinburgh, and Dublin Philosophical Magazine and Journal of Science* 21.125 (1911), pp. 669–688. DOI: 10.1080/14786440508637080. eprint: https://doi.org/10.1080/14786440508637080.

[3] M. Planck. "Zur Theorie des Gesetzes der Energieverteilung im Normalspectrum". In: *Verhandlungen der Deutschen Physikalischen Gesellschaft* 4.4 (1900), pp. 146–151. DOI: 10.1002/phbl.19480040404.

[4] A. Einstein. "Über einen die Erzeugung und Verwandlung des Lichtes betreffenden heuristischen Gesichtspunkt". In: *Annalen der Physik* 322.6 (1905), pp. 132–148. DOI: https://doi.org/10.1002/andp.19053220607. eprint: https://onlinelibrary.wiley.com/doi/pdf/10.1002/andp.19053220607.

[5] N. Bohr. "I. On the constitution of atoms and molecules". In: *The London, Edinburgh, and Dublin Philosophical Magazine and Journal of Science* 26.151 (1913), pp. 1–25. DOI: 10.1080/14786441308634955. eprint: https://doi.org/10.1080/14786441308634955.

[6] A. H. Compton. "A Quantum Theory of the Scattering of X-rays by Light Elements". In: *Physical Review* 21.5 (May 1923), pp. 483–502. DOI: 10.1103/PhysRev.21.483.

[7] J. Chadwick. "The Existence of a Neutron". In: *Proceedings of the Royal Society of London Series A* 136.830 (June 1932), pp. 692–708. DOI: 10.1098/rspa.1932.0112.

[8] H. Yukawa. "On the Interaction of Elementary Particles. I". In: *Proceedings of the Physico-Mathematical Society of Japan. 3rd Series* 17 (1935), pp. 48–57. DOI: 10.11429/ppmsj1919.17.0_48.

[9] C. M. G. Lattes et al. “PROCESSES INVOLVING CHARGED MESONS”. In: *Nature* 159 (1947), pp. 694–697. DOI: 10.1038/159694a0.

[10] P. A. M. Dirac and R. H. Fowler. “The quantum theory of the electron”. In: *Proceedings of the Royal Society of London. Series A, Containing Papers of a Mathematical and Physical Character* 117.778 (1928), pp. 610–624. DOI: 10.1098/rspa.1928.0023. eprint: https://royalsocietypublishing.org/doi/pdf/10.1098/rspa.1928.0023.

[11] C. D. Anderson. “The Positive Electron”. In: *Physical Review* 43.6 (Mar. 1933), pp. 491–494. DOI: 10.1103/PhysRev.43.491.

[12] L. M. Brown. “The idea of the neutrino”. In: *Physics Today* 31.9 (Sept. 1978), pp. 23–28. DOI: 10.1063/1.2995181.

[13] E. Fermi. “Versuch einer Theorie der β-Strahlen. I”. In: *Zeitschrift fur Physik* 88.3-4 (Mar. 1934), pp. 161–177. DOI: 10.1007/BF01351864.

[14] C. L. Cowan et al. “Detection of the Free Neutrino: A Confirmation”. In: *Science* 124.3212 (July 1956), pp. 103–104. DOI: 10.1126/science.124.3212.103.

[15] T. Nakano and K. Nishijima. “Charge Independence for V-particles”. In: *Progress of Theoretical Physics* 10.5 (Nov. 1953), pp. 581–582. DOI: 10.1143/PTP.10.581.

[16] M. Gell-Mann. “The interpretation of the new particles as displaced charge multiplets”. In: *Il Nuovo Cimento* 4.S2 (Apr. 1956), pp. 848–866. DOI: 10.1007/BF02748000.

[17] M. Gell-Mann. “The Eightfold Way: A Theory of Strong Interaction Symmetry”. In: (Mar. 1961). DOI: 10.2172/4008239.

[18] V. E. Barnes et al. “Observation of a Hyperon with Strangeness Minus Three”. In: *Phys. Rev. Lett.* 12 (1964), pp. 204–206. DOI: 10.1103/PhysRevLett.12.204.

[19] M. Gell-Mann. “A schematic model of baryons and mesons”. In: *Physics Letters* 8.3 (Feb. 1964), pp. 214–215. DOI: 10.1016/S0031-9163(64)92001-3.

[20] G. Zweig. “An SU_3 model for strong interaction symmetry and its breaking; Version 2”. In: (Feb. 1964), 80 p.

[21] O. W. Greenberg. “Spin and Unitary-Spin Independence in a Paraquark Model of Baryons and Mesons”. In: *PRL* 13.20 (Nov. 1964), pp. 598–602. DOI: 10.1103/PhysRevLett.13.598.

[22] M. Riordan. “The Discovery of Quarks”. In: *Science* 256.5061 (1992), pp. 1287–1293. DOI: 10.1126/science.256.5061.1287. eprint: https://www.science.org/doi/pdf/10.1126/science.256.5061.1287.

[23] J. J. Aubert et al. “Experimental Observation of a Heavy Particle J”. In: *PRL* 33.23 (Dec. 1974), pp. 1404–1406. DOI: 10.1103/PhysRevLett.33.1404.

[24] J. .-E. Augustin et al. “Discovery of a Narrow Resonance in e^+e^- Annihilation”. In: *PRL* 33.23 (Dec. 1974), pp. 1406–1408. DOI: 10.1103/PhysRevLett.33.1406.

[25] S. L. Glashow, J. Iliopoulos and L. Maiani. “Weak Interactions with Lepton-Hadron Symmetry”. In: *PRD* 2.7 (Oct. 1970), pp. 1285–1292. DOI: 10.1103/PhysRevD.2.1285.

[26] S. W. Herb et al. “Observation of a Dimuon Resonance at 9.5 GeV in 400-GeV Proton-Nucleus Collisions”. In: *PRL* 39.5 (Aug. 1977), pp. 252–255. DOI: 10.1103/PhysRevLett.39.252.

[27] J. N. Bahcall and R. Davis. “Solar Neutrinos: A Scientific Puzzle”. In: *Science* 191.4224 (1976), pp. 264–267. DOI: 10.1126/science.191.4224.264. eprint: https://www.science.org/doi/pdf/10.1126/science.191.4224.264.

[28] G. Danby et al. “Observation of High-Energy Neutrino Reactions and the Existence of Two Kinds of Neutrinos”. In: *PRL* 9.1 (July 1962), pp. 36–44. DOI: 10.1103/PhysRevLett.9.36.

[29] M. L. Perl et al. “Evidence for anomalous lepton production in e^+e^- annihilation”. In: *PRL* 35.22 (Dec. 1975), pp. 1489–1492. DOI: 10.1103/PhysRevLett.35.1489.

[30] E. Kearns, T. Kajita and Y. Totsuka. “Detecting Massive Neutrinos”. In: *Scientific American* 281.2 (Aug. 1999), pp. 64–71. DOI: 10.1038/scientificamerican0899-64.

[31] Q. R. Ahmad et al. “Measurement of the Rate of ν_e + d –> p + p + e^- Interactions Produced by ^{8}B Solar Neutrinos at the Sudbury Neutrino Observatory”. In: *PRL* 87.7, 071301 (Aug. 2001), p. 071301. DOI: 10.1103/PhysRevLett.87.071301. arXiv: nucl-ex/0106015 [nucl-ex].

[32] P. W. Higgs. “Broken Symmetries and the Masses of Gauge Bosons”. In: *PRL* 13.16 (Oct. 1964), pp. 508–509. DOI: 10.1103/PhysRevLett.13.508.

[33] C. Berger et al. “Jet analysis of the $\Upsilon(9.46)$ decay into charged hadrons”. In: *Physics Letters B* 82.3-4 (Apr. 1979), pp. 449–455. DOI: 10.1016/0370-2693(79)90265-X.

[34] G. Arnison et al. “Experimental observation of isolated large transverse energy electrons with associated missing energy at s=540 GeV”. In: *Physics Letters B* 122.1 (1983), pp. 103–116. ISSN: 0370-2693. DOI: https://doi.org/10.1016/0370-2693(83)91177-2.

[35] G. T. J. Arnison et al. “Experimental observation of lepton pairs of invariant mass around $95 GeV/c^2$ at the CERN SPS collider”. In: *Phys. Lett. B* 126 (June 1985), 398–410. 17 p. DOI: 10.1016/0370-2693(83)90188-0.

[36] F. Abe et al. “Observation of Top Quark Production in $p\bar{p}$ Collisions with the Collider Detector at Fermilab”. In: *PRL* 74.14 (Apr. 1995), pp. 2626–2631. DOI: 10.1103/PhysRevLett.74.2626. arXiv: hep-ex/9503002 [hep-ex].

[37] DONUT Collaboration et al. “Observation of tau neutrino interactions”. In: *Physics Letters B* 504.3 (Apr. 2001), pp. 218–224. DOI: 10.1016/S0370-2693(01)00307-0. arXiv: hep-ex/0012035 [hep-ex].

[38] S. Chatrchyan et al. “Observation of a new boson at a mass of 125 GeV with the CMS experiment at the LHC”. In: *Physics Letters B* 716.1 (Sept. 2012), pp. 30–61. ISSN: 0370-2693. DOI: 10.1016/j.physletb.2012.08.021.

[39] G. Aad et al. “Observation of a new particle in the search for the Standard Model Higgs boson with the ATLAS detector at the LHC”. In: *Physics Letters B* 716.1 (Sept. 2012), pp. 1–29. ISSN: 0370-2693. DOI: 10.1016/j.physletb.2012.08.020.

[40] M. K. Gaillard, P. D. Grannis and F. J. Sciulli. “The standard model of particle physics”. In: *Reviews of Modern Physics* 71.2 (Mar. 1999), S96–S111. ISSN: 1539-0756. DOI: 10.1103/revmodphys.71.s96.

[41] *Standard Model of Elementary Particles*. [Accessed: 13/11/2021]. URL: https://en.wikipedia.org/wiki/File:Standard_Model_of_Elementary_Particles.svg.

[42] *Baryon Octet Diagram*. [Accessed: 16/11/2021]. URL: https://commons.wikimedia.org/wiki/File:Baryon-octet-small.svg.

[43] *Baryon Decuplet Diagram*. [Accessed: 16/11/2021]. URL: https://commons.wikimedia.org/wiki/File:Baryon-decuplet-small.svg.

[44] J. C. Collins, D. E. Soper and G. Sterman. “FACTORIZATION OF HARD PROCESSES IN QCD”. In: *Perturbative QCD*, pp. 1–91. DOI: 10.1142/9789814503266_0001. eprint: https://www.worldscientific.com/doi/pdf/10.1142/9789814503266_0001.

[45] Y. L. Dokshitzer. “Calculation of the Structure Functions for Deep Inelastic Scattering and e+ e- Annihilation by Perturbation Theory in Quantum Chromodynamics. (In Russian)”. In: *Sov. Phys. JETP* 46 (1977), pp. 641–653.

[46] V. Gribov and L. Lipatov. "Deep inelastic electron scattering in perturbation theory". In: *Physics Letters B* 37.1 (1971), pp. 78–80. ISSN: 0370-2693. DOI: https://doi.org/10.1016/0370-2693(71)90576-4.

[47] G. Altarelli and G. Parisi. "Asymptotic Freedom in Parton Language". In: *Nucl. Phys. B* 126 (1977), pp. 298–318. DOI: 10.1016/0550-3213(77)90384-4.

[48] X. C. Vidal et al. "Discovering true muonium at LHCb". In: *Physical Review D* 100.5 (Sept. 2019). ISSN: 2470-0029. DOI: 10.1103/physrevd.100.053003.

[49] O. Brüning, H. Burkhardt and S. Myers. "The large hadron collider". In: *Progress in Particle and Nuclear Physics* 67.3 (2012), pp. 705–734. ISSN: 0146-6410. DOI: https://doi.org/10.1016/j.ppnp.2012.03.001.

[50] "Search for the Standard Model Higgs Boson at LEP". In: *Physics Letters B* 565 (July 2003), pp. 61–75. ISSN: 0370-2693. DOI: 10.1016/s0370-2693(03)00614-2.

[51] T. Aaltonen et al. "Combination of Tevatron Searches for the Standard Model Higgs Boson in the W^+W^- Decay Mode". In: *Phys. Rev. Lett.* 104 (6 Feb. 2010), p. 061802. DOI: 10.1103/PhysRevLett.104.061802.

[52] A. Belyaev. "Supersymmetry status and phenomenology at the Large Hadron Collider". In: *Pramana* 72.1 (Mar. 2009), pp. 143–160. DOI: 10.1007/s12043-009-0012-0.

[53] S. Myers. "The Large Hadron Collider 2008-2013". In: *Int. J. Mod. Phys. A* 28 (2013), p. 1330035. DOI: 10.1142/S0217751X13300354.

[54] R. Meinke et al. "Sextupole correction magnets for the Large Hadron Collider". In: *Proceedings of the 1999 Particle Accelerator Conference (Cat. No.99CH36366)* (). DOI: 10.1109/pac.1999.792253.

[55] R. Perin and J. Vlogaert. *Magnets for the Large Hadron Collider*. Tech. rep. Geneva: CERN, Feb. 1994.

[56] L. R. Evans. "LHC accelerator physics and technology challenges". In: *6th European Particle Accelerator Conference (EPAC 98)*. July 1998, pp. 3–7.

[57] A. Airapetian et al. *ATLAS detector and physics performance: Technical Design Report, 1*. Technical design report. ATLAS. Geneva: CERN, 1999.

[58] G. L. Bayatian et al. *CMS Physics: Technical Design Report Volume 1: Detector Performance and Software*. Technical design report. CMS. Geneva: CERN, 2006.

[59] K. Aamodt et al. "The ALICE experiment at the CERN LHC". In: *JINST* 3 (2008), S08002. DOI: 10.1088/1748-0221/3/08/S08002.

[60] D. Boussard and T. P. R. Linnecar. *The LHC Superconducting RF System*. Tech. rep. Geneva: CERN, Dec. 1999.

[61] *CAS - CERN Accelerator School: Intermediate Accelerator Physics: Zeuthen, Germany 15 - 26 Sep 2003. CAS - CERN Accelerator School: Intermediate Course on Accelerator Physics*. CERN. Geneva: CERN, 2006. DOI: 10.5170/CERN-2006-002.

[62] S. van der Meer. *Calibration of the effective beam height in the ISR*. Tech. rep. Geneva: CERN, 1968.

[63] M. Ferro-Luzzi. "Proposal for an absolute luminosity determination in colliding beam experiments using vertex detection of beam–gas interactions". In: *Nuclear Instruments and Methods in Physics Research Section A: Accelerators, Spectrometers, Detectors and Associated Equipment* 553.3 (2005), pp. 388–399. ISSN: 0168-9002. DOI: https://doi.org/10.1016/j.nima.2005.07.010.

[64] B. J. Holzer, R. Versteegen and R. Alemany. "Vertical Crossing Angle in IR8". In: (Apr. 2013).

[65] R. Alemany-Fernandez et al. "Operation and Configuration of the LHC in Run 1". In: (Nov. 2013).

[66] J. Wenninger. "Operation and Configuration of the LHC in Run 2". In: (Mar. 2019).

[67] Schaeffer, Anaïs. *New schedule for CERN's accelerators and experiments*. https://home.cern/news/news/accelerators/new-schedule-cerns-accelerators-and-experiments. [Accessed: 20/03/2021]. Sept. 2020.

[68] A. A. Alves et al. "The LHCb Detector at the LHC". In: *JINST* 3.LHCb-DP-2008-001. CERN-LHCb-DP-2008-001 (2008). Also published by CERN Geneva in 2010, S08005. DOI: 10.1088/1748-0221/3/08/S08005.

[69] *LHCb material for presentations*. [Accessed: 22/12/2021]. URL: https://lhcb.web.cern.ch/speakersbureau/html/material_for_presentations.html.

[70] LHCb Collaboration. *LHCb VELO Upgrade Technical Design Report*. Tech. rep. CERN-LHCC-2013-021. LHCB-TDR-013. Nov. 2013.

[71] P. R. Barbosa-Marinho et al. *LHCb inner tracker: Technical Design Report*. Technical design report. LHCb. revised version number 1 submitted on 2002-11-13 14:14:34. Geneva: CERN, 2002.

[72] L. D. Landau et al. *Electrodynamics of Continuous Media*. Pergamon Press, 1984.

[73] R. Aaij et al. "Design and performance of the LHCb trigger and full real-time reconstruction in Run 2 of the LHC". In: *Journal of Instrumentation* 14.04 (Apr. 2019), P04013–P04013. ISSN: 1748-0221. DOI: 10.1088/1748-0221/14/04/p04013.

[74] *Moore Documentation*. [Accessed: 17/11/2021]. URL: https://lhcbdoc.web.cern.ch/lhcbdoc/moore/master/index.html.

[75] R. Aaij et al. *Optimization of the muon reconstruction algorithms for LHCb Run 2*. Tech. rep. Geneva: CERN, Feb. 2017.

[76] A. Hocker et al. *TMVA - Toolkit for Multivariate Data Analysis with ROOT: Users guide. TMVA - Toolkit for Multivariate Data Analysis*. Tech. rep. physics/0703039. TMVA-v4 Users Guide: 135 pages, 19 figures, numerous code examples and references. Geneva: CERN, Mar. 2007.

[77] S. Benson et al. "The LHCb Turbo Stream". In: *J. Phys.: Conf. Ser.* 664.LHCb-PROC-2015-013. CERN-LHCb-PROC-2015-013. 8 (May 2015), 082004. 8 p. DOI: 10.1088/1742-6596/664/8/082004.

[78] *Gaudi Documentation*. [Accessed: 19/11/2021]. URL: https://gaudi.web.cern.ch/gaudi/.

[79] ATLAS Collaboration. *Measurement of the transverse momentum distribution of Drell-Yan lepton pairs in proton-proton collisions at* $\sqrt{s} = 13$ *TeV with the ATLAS detector*. 2020. arXiv: 1912.02844 [hep-ex].

[80] CMS Collaboration. "Measurements of differential Drell-Yan production cross sections in proton-proton collisions at $\sqrt{s} = 13$ TeV". In: *Journal of High Energy Physics* 2019.12 (Dec. 2019). ISSN: 1029-8479. DOI: 10.1007/jhep12(2019)061.

[81] "Inclusive low mass Drell-Yan production in the forward region at $\sqrt{s} = 7$ TeV". In: (Mar. 2012). Linked to LHCb-ANA-2012-029.

[82] P. Ilten et al. "Proposed Inclusive Dark Photon Search at LHCb". In: *Phys. Rev. Lett.* 116 (25 June 2016), p. 251803. DOI: 10.1103/PhysRevLett.116.251803.

[83] M. Xu, H. Yin and S. Farry. *Measurement of high-p_T muon reconstruction efficiencies for studies of γ^*/Z production and angular coefficients with LHCb RunII data-sets*. Tech. rep. Geneva: CERN, Dec. 2020.

[84] E. Parzen. "On Estimation of a Probability Density Function and Mode". In: *The Annals of Mathematical Statistics* 33.3 (1962), pp. 1065–1076. DOI: 10.1214/aoms/1177704472.

[85] R. Aaij et al. "Performance of the LHCb Vertex Locator". In: *Journal of Instrumentation* 9.09 (Sept. 2014), P09007–P09007. ISSN: 1748-0221. DOI: 10.1088/1748-0221/9/09/p09007.

[86] X. Cid Vidal, P. J. Ilten and J. M. Williams. *"Search for $A' \to \mu^+\mu^-$ decays"*. https://cds.cern.ch/record/2259469. Apr. 2017.

[87] R. Aaij et al. "Search for Dark Photons Produced in 13 TeV pp Collisions". In: *Physical Review Letters* 120.6 (Feb. 2018). ISSN: 1079-7114. DOI: 10.1103/physrevlett.120.061801.

[88] F. James and M. Roos. "Minuit: A System for Function Minimization and Analysis of the Parameter Errors and Correlations". In: *Comput. Phys. Commun.* 10 (1975), pp. 343–367. DOI: 10.1016/0010-4655(75)90039-9.

[89] M. Cacciari, G. P. Salam and G. Soyez. "The anti-kt jet clustering algorithm". In: *Journal of High Energy Physics* 2008.04 (Apr. 2008), pp. 063–063. ISSN: 1029-8479. DOI: 10.1088/1126-6708/2008/04/063.

[90] R. Aaij et al. "Measurement of the forward Z boson production cross-section in pp collisions at $\sqrt{s} = 13$ TeV". In: *JHEP* 09 (July 2016), 136. 35 p. DOI: 10.1007/JHEP09(2016)136. arXiv: 1607.06495.

[91] R. Aaij et al. "Measurement of Υ production in pp collisions at $\sqrt{s}$= 13 TeV". In: *JHEP* 07 (Apr. 2018), 134. 26 p. DOI: 10.1007/JHEP07(2018)134. arXiv: 1804.09214.

[92] R. Aaij et al. *Precision measurement of forward Z boson production in proton-proton collisions at $\sqrt{s} = 13$ TeV*. 2021. arXiv: 2112.07458 [hep-ex].

[93] R. Gauld et al. *Transverse momentum distributions in low-mass Drell-Yan lepton pair production at NNLO QCD*. 2021. arXiv: 2110.15839 [hep-ph].

[94] R. Gauld. *A massive variable flavour number scheme for the Drell-Yan process*. 2021. arXiv: 2107.01226 [hep-ph].

[95] M. Niering et al. "Measurement of the Hydrogen $1S$- $2S$ Transition Frequency by Phase Coherent Comparison with a Microwave Cesium Fountain Clock". In: *Phys. Rev. Lett.* 84 (24 June 2000), pp. 5496–5499. DOI: 10.1103/PhysRevLett.84.5496.

[96] R. Pohl et al. "The size of the proton". In: *Nature* 466 (July 2010), pp. 213–216. DOI: 10.1038/nature09250.

[97] R. Pohl et al. "Laser spectroscopy of muonic deuterium". In: *Science* 353.6300 (2016), pp. 669–673. DOI: 10.1126/science.aaf2468.

[98] J. P. Miller, E. de Rafael and B. L. Roberts. "Muon (g - 2): experiment and theory". In: *Reports on Progress in Physics* 70 (May 2007), pp. 795–881. DOI: 10.1088/0034-4885/70/5/R03. eprint: hep-ph/0703049.

[99] G. W. Bennett et al. "Final Report of the Muon E821 Anomalous Magnetic Moment Measurement at BNL". In: *Phys. Rev. D* 73 (2006), p. 072003. DOI: 10.1103/PhysRevD.73.072003. arXiv: hep-ex/0602035.

[100] B. Abi et al. "Measurement of the Positive Muon Anomalous Magnetic Moment to 0.46 ppm". In: *Phys. Rev. Lett.* 126 (14 Apr. 2021), p. 141801. DOI: 10.1103/PhysRevLett.126.141801.

[101] R. Aaij et al. *Test of lepton universality in beauty-quark decays*. 2021. arXiv: 2103.11769 [hep-ex].

[102] R. Aaij et al. "Search for $A' \to \mu^+\mu^-$ Decays". In: *Physical Review Letters* 124.4 (Jan. 2020). ISSN: 1079-7114. DOI: 10.1103/physrevlett.124.041801.

[103] J. D. Bjorken et al. "New fixed-target experiments to search for dark gauge forces". In: *Phys. Rev. D* 80 (7 Oct. 2009), p. 075018. DOI: 10.1103/PhysRevD.80.075018.

[104] T. Sjöstrand et al. "An introduction to PYTHIA 8.2". In: *Computer Physics Communications* 191 (June 2015), pp. 159–177. ISSN: 0010-4655. DOI: 10.1016/j.cpc.2015.01.024.

[105] R. Aaij et al. "Measurement of the inelastic pp cross-section at a centre-of-mass energy of 13 TeV". In: *Journal of High Energy Physics* 2018.6 (June 2018). ISSN: 1029-8479. DOI: 10.1007/jhep06(2018)100.

[106] Y. Ji and H. Lamm. "Scouring meson decays for true muonium". In: *Physical Review D* 99.3 (Feb. 2019). ISSN: 2470-0029. DOI: 10.1103/physrevd.99.033008.

[107] C. Marin Benito, L. Garrido Beltran and X. Cid Vidal. *Feasibility study of $K^0_S \to \pi^+\pi^-e^+e^-$ at LHCb*. Tech. rep. Geneva: CERN, Oct. 2016.

[108] R. Aaij et al. "Measurement of the ratio of prompt χ_c to J/ψ production in pp collisions at $\sqrt{s} = 7$ TeV". In: *Physics Letters B* 718.2 (Dec. 2012), pp. 431–440. ISSN: 0370-2693. DOI: 10.1016/j.physletb.2012.10.068.

[109] R. Aaij et al. "First Experimental Study of Photon Polarization in Radiative B_s^0 Decays". In: *Physical Review Letters* 118.2 (Jan. 2017). ISSN: 1079-7114. DOI: 10.1103/physrevlett.118.021801.

[110] M. Nicol. "Analysis of the rare decay $B^0 \to K^{*0}e^+e^-$ at LHCb". Theses. Université Paris Sud - Paris XI, Dec. 2012.

[111] M. Williams. "A novel approach to the bias-variance problem in bump hunting". In: *Journal of Instrumentation* 12.09 (Sept. 2017), P09034–P09034. ISSN: 1748-0221. DOI: 10.1088/1748-0221/12/09/p09034.

Appendix A

Minimum $\sqrt{\chi^2_{\text{IP}}}$ Fits

This appendix shows the full results of the min $\sqrt{\chi^2_{\text{IP}}}$ fits used to extract the size of the prompt signal from dimuon data, as described in section 4.4. As in figures 4.30 and 4.31, the prompt signal component is shown in red, the displaced background component in green and the MisID background in blue.

Fits in Bins of Dimuon Mass and Rapidity

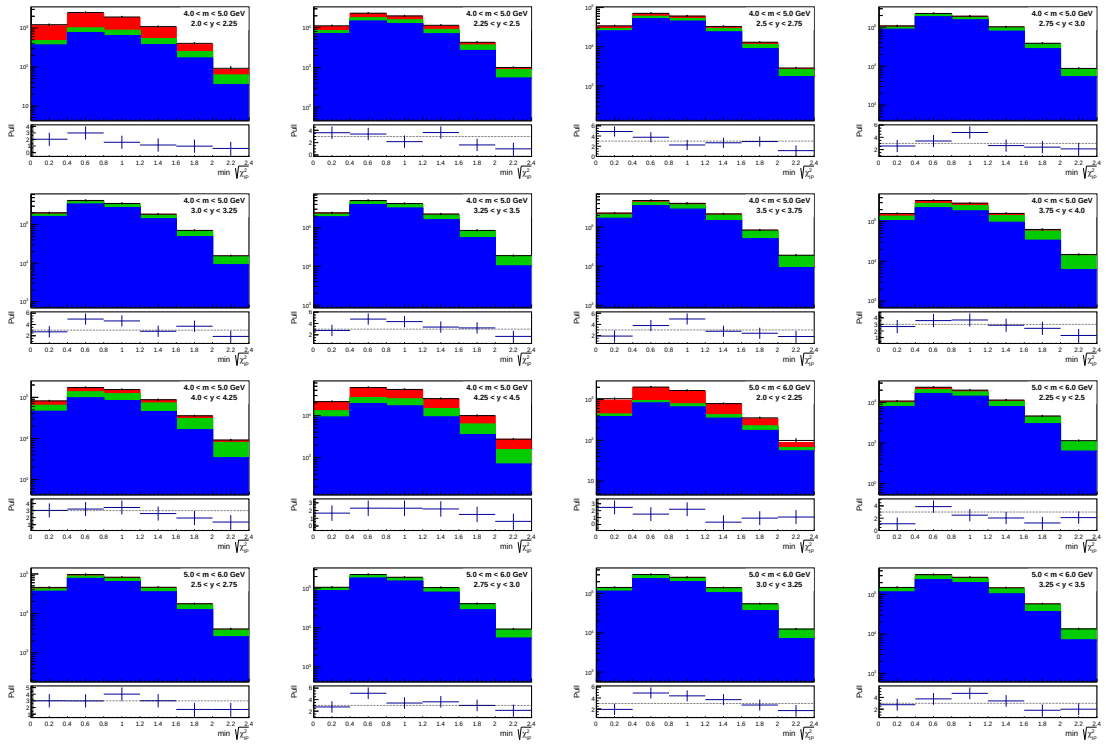

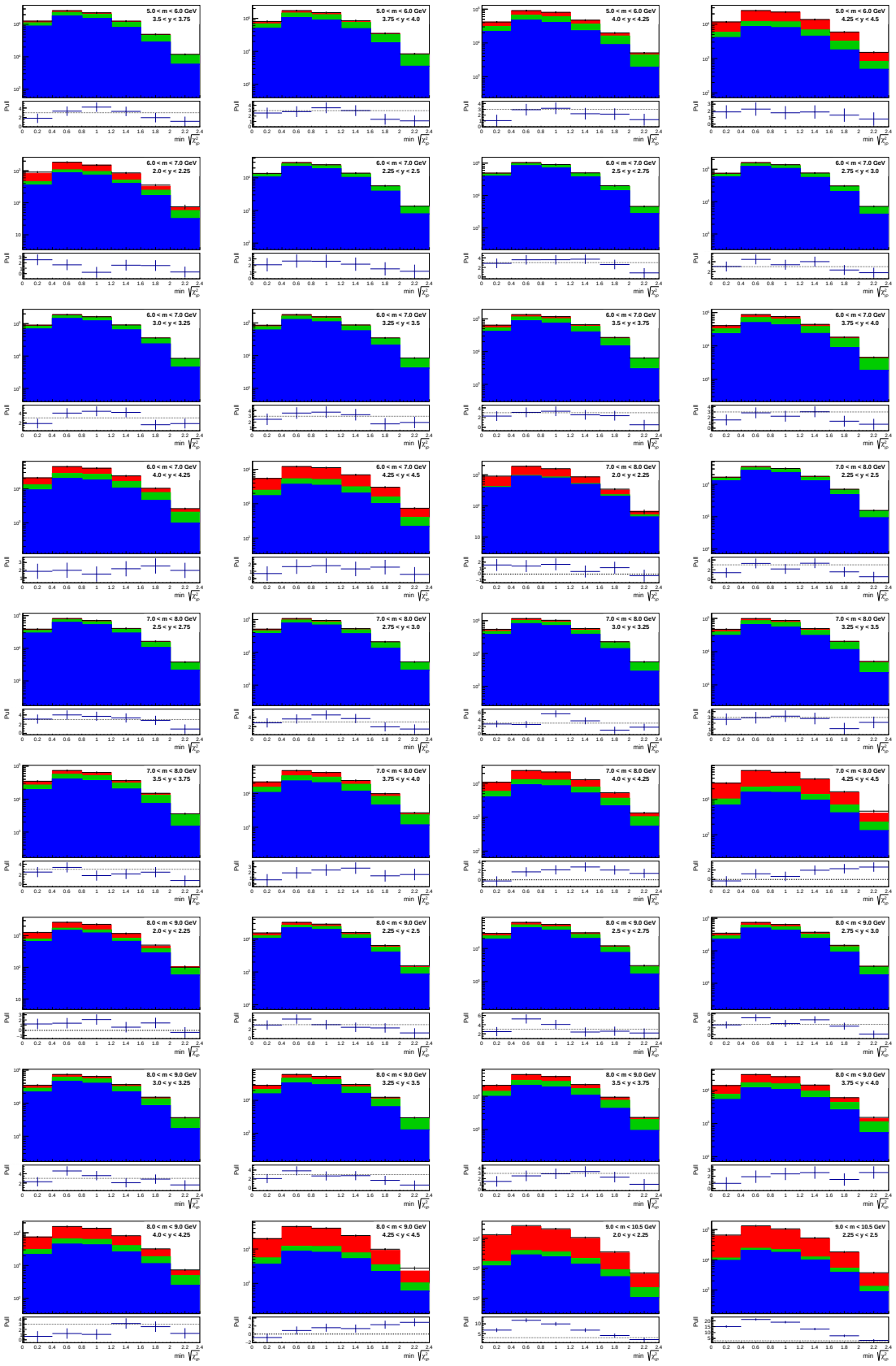
5.0 < m < 6.0 GeV
3.5 < y < 3.75
5.0 < m < 6.0 GeV
3.75 < y < 4.0
5.0 < m < 6.0 GeV
4.0 < y < 4.25
5.0 < m < 6.0 GeV
4.25 < y < 4.5
6.0 < m < 7.0 GeV
2.0 < y < 2.25
6.0 < m < 7.0 GeV
2.25 < y < 2.5
6.0 < m < 7.0 GeV
2.5 < y < 2.75
6.0 < m < 7.0 GeV
2.75 < y < 3.0
6.0 < m < 7.0 GeV
3.0 < y < 3.25
6.0 < m < 7.0 GeV
3.25 < y < 3.5
6.0 < m < 7.0 GeV
3.5 < y < 3.75
6.0 < m < 7.0 GeV
3.75 < y < 4.0
6.0 < m < 7.0 GeV
4.0 < y < 4.25
6.0 < m < 7.0 GeV
4.25 < y < 4.5
7.0 < m < 8.0 GeV
2.0 < y < 2.25
7.0 < m < 8.0 GeV
2.25 < y < 2.5
7.0 < m < 8.0 GeV
2.5 < y < 2.75
7.0 < m < 8.0 GeV
2.75 < y < 3.0
7.0 < m < 8.0 GeV
3.0 < y < 3.25
7.0 < m < 8.0 GeV
3.25 < y < 3.5
7.0 < m < 8.0 GeV
3.5 < y < 3.75
7.0 < m < 8.0 GeV
3.75 < y < 4.0
7.0 < m < 8.0 GeV
4.0 < y < 4.25
7.0 < m < 8.0 GeV
4.25 < y < 4.5
8.0 < m < 9.0 GeV
2.0 < y < 2.25
8.0 < m < 9.0 GeV
2.25 < y < 2.5
8.0 < m < 9.0 GeV
2.5 < y < 2.75
8.0 < m < 9.0 GeV
2.75 < y < 3.0
8.0 < m < 9.0 GeV
3.0 < y < 3.25
8.0 < m < 9.0 GeV
3.25 < y < 3.5
8.0 < m < 9.0 GeV
3.5 < y < 3.75
8.0 < m < 9.0 GeV
3.75 < y < 4.0
8.0 < m < 9.0 GeV
4.0 < y < 4.25
8.0 < m < 9.0 GeV
4.25 < y < 4.5
9.0 < m < 10.5 GeV
2.0 < y < 2.25
9.0 < m < 10.5 GeV
2.25 < y < 2.5
Pull
min $\sqrt{\chi^2_{ip}}$

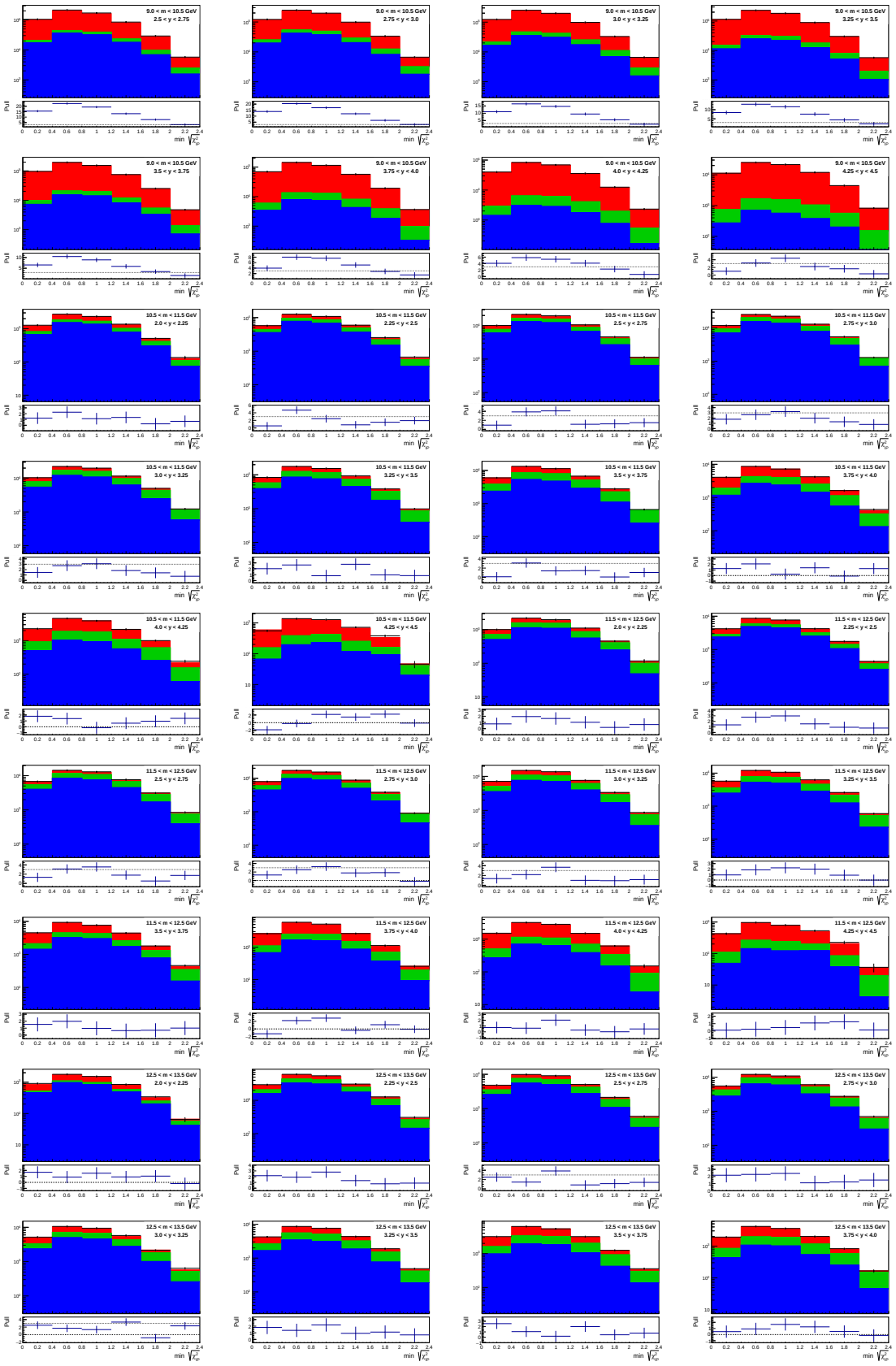
9.0 < m < 10.5 GeV
2.5 < y < 2.75
9.0 < m < 10.5 GeV
2.75 < y < 3.0
9.0 < m < 10.5 GeV
3.0 < y < 3.25
9.0 < m < 10.5 GeV
3.25 < y < 3.5
9.0 < m < 10.5 GeV
3.5 < y < 3.75
9.0 < m < 10.5 GeV
3.75 < y < 4.0
9.0 < m < 10.5 GeV
4.0 < y < 4.25
9.0 < m < 10.5 GeV
4.25 < y < 4.5
10.5 < m < 11.5 GeV
2.0 < y < 2.25
10.5 < m < 11.5 GeV
2.25 < y < 2.5
10.5 < m < 11.5 GeV
2.5 < y < 2.75
10.5 < m < 11.5 GeV
2.75 < y < 3.0
10.5 < m < 11.5 GeV
3.0 < y < 3.25
10.5 < m < 11.5 GeV
3.25 < y < 3.5
10.5 < m < 11.5 GeV
3.5 < y < 3.75
10.5 < m < 11.5 GeV
3.75 < y < 4.0
10.5 < m < 11.5 GeV
4.0 < y < 4.25
10.5 < m < 11.5 GeV
4.25 < y < 4.5
11.5 < m < 12.5 GeV
2.0 < y < 2.25
11.5 < m < 12.5 GeV
2.25 < y < 2.5
11.5 < m < 12.5 GeV
2.5 < y < 2.75
11.5 < m < 12.5 GeV
2.75 < y < 3.0
11.5 < m < 12.5 GeV
3.0 < y < 3.25
11.5 < m < 12.5 GeV
3.25 < y < 3.5
11.5 < m < 12.5 GeV
3.5 < y < 3.75
11.5 < m < 12.5 GeV
3.75 < y < 4.0
11.5 < m < 12.5 GeV
4.0 < y < 4.25
11.5 < m < 12.5 GeV
4.25 < y < 4.5
12.5 < m < 13.5 GeV
2.0 < y < 2.25
12.5 < m < 13.5 GeV
2.25 < y < 2.5
12.5 < m < 13.5 GeV
2.5 < y < 2.75
12.5 < m < 13.5 GeV
2.75 < y < 3.0
12.5 < m < 13.5 GeV
3.0 < y < 3.25
12.5 < m < 13.5 GeV
3.25 < y < 3.5
12.5 < m < 13.5 GeV
3.5 < y < 3.75
12.5 < m < 13.5 GeV
3.75 < y < 4.0
Pull
min $\sqrt{\chi^2_{ip}}$

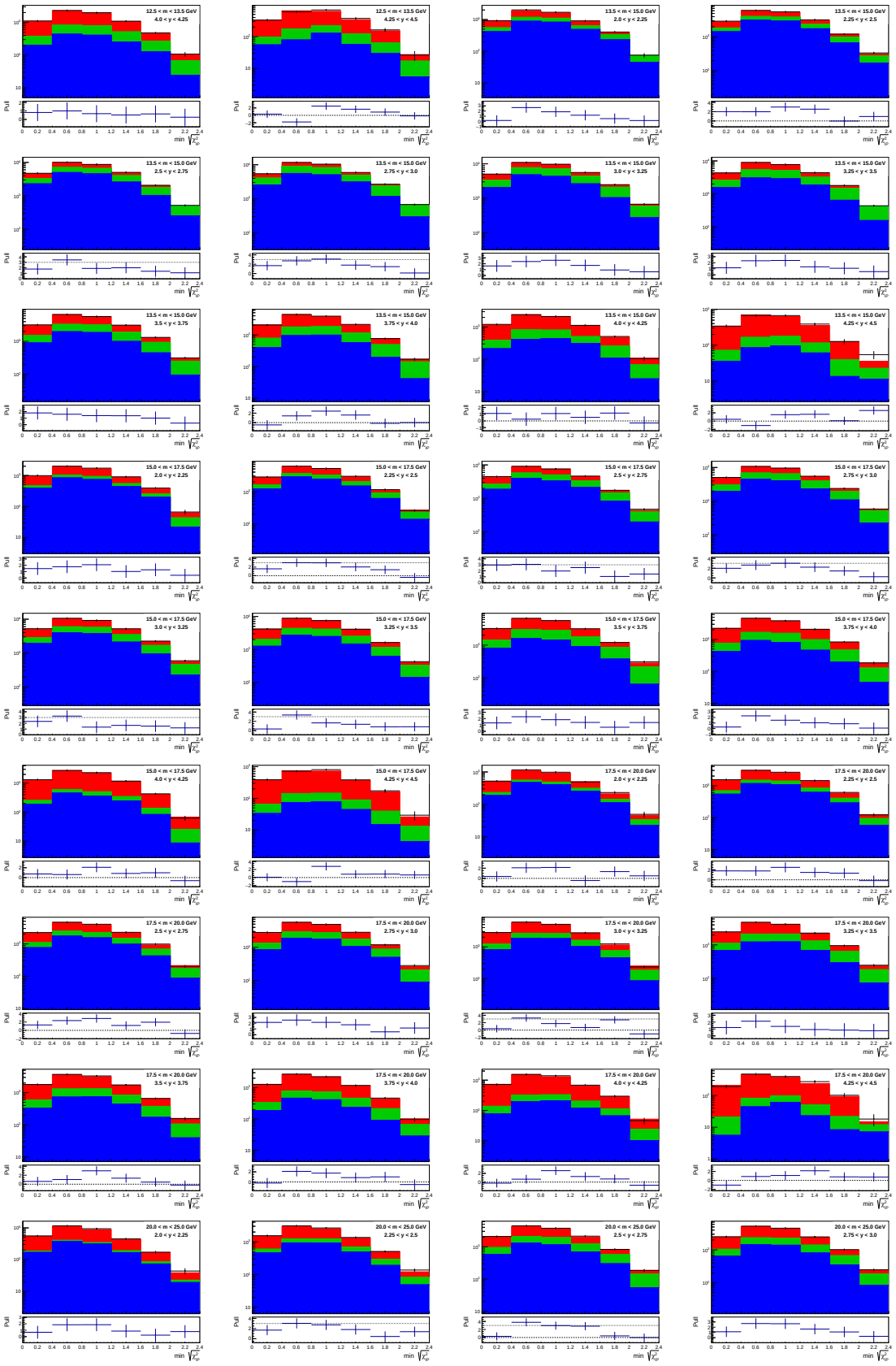
12.5 < m < 13.5 GeV
4.0 < y < 4.25
12.5 < m < 13.5 GeV
4.25 < y < 4.5
13.5 < m < 15.0 GeV
2.0 < y < 2.25
13.5 < m < 15.0 GeV
2.25 < y < 2.5
13.5 < m < 15.0 GeV
2.5 < y < 2.75
13.5 < m < 15.0 GeV
2.75 < y < 3.0
13.5 < m < 15.0 GeV
3.0 < y < 3.25
13.5 < m < 15.0 GeV
3.25 < y < 3.5
13.5 < m < 15.0 GeV
3.5 < y < 3.75
13.5 < m < 15.0 GeV
3.75 < y < 4.0
13.5 < m < 15.0 GeV
4.0 < y < 4.25
13.5 < m < 15.0 GeV
4.25 < y < 4.5
15.0 < m < 17.5 GeV
2.0 < y < 2.25
15.0 < m < 17.5 GeV
2.25 < y < 2.5
15.0 < m < 17.5 GeV
2.5 < y < 2.75
15.0 < m < 17.5 GeV
2.75 < y < 3.0
15.0 < m < 17.5 GeV
3.0 < y < 3.25
15.0 < m < 17.5 GeV
3.25 < y < 3.5
15.0 < m < 17.5 GeV
3.5 < y < 3.75
15.0 < m < 17.5 GeV
3.75 < y < 4.0
15.0 < m < 17.5 GeV
4.0 < y < 4.25
15.0 < m < 17.5 GeV
4.25 < y < 4.5
17.5 < m < 20.0 GeV
2.0 < y < 2.25
17.5 < m < 20.0 GeV
2.25 < y < 2.5
17.5 < m < 20.0 GeV
2.5 < y < 2.75
17.5 < m < 20.0 GeV
2.75 < y < 3.0
17.5 < m < 20.0 GeV
3.0 < y < 3.25
17.5 < m < 20.0 GeV
3.25 < y < 3.5
17.5 < m < 20.0 GeV
3.5 < y < 3.75
17.5 < m < 20.0 GeV
3.75 < y < 4.0
17.5 < m < 20.0 GeV
4.0 < y < 4.25
17.5 < m < 20.0 GeV
4.25 < y < 4.5
20.0 < m < 25.0 GeV
2.0 < y < 2.25
20.0 < m < 25.0 GeV
2.25 < y < 2.5
20.0 < m < 25.0 GeV
2.5 < y < 2.75
20.0 < m < 25.0 GeV
2.75 < y < 3.0
Pull
min $\sqrt{\chi^2_{ip}}$

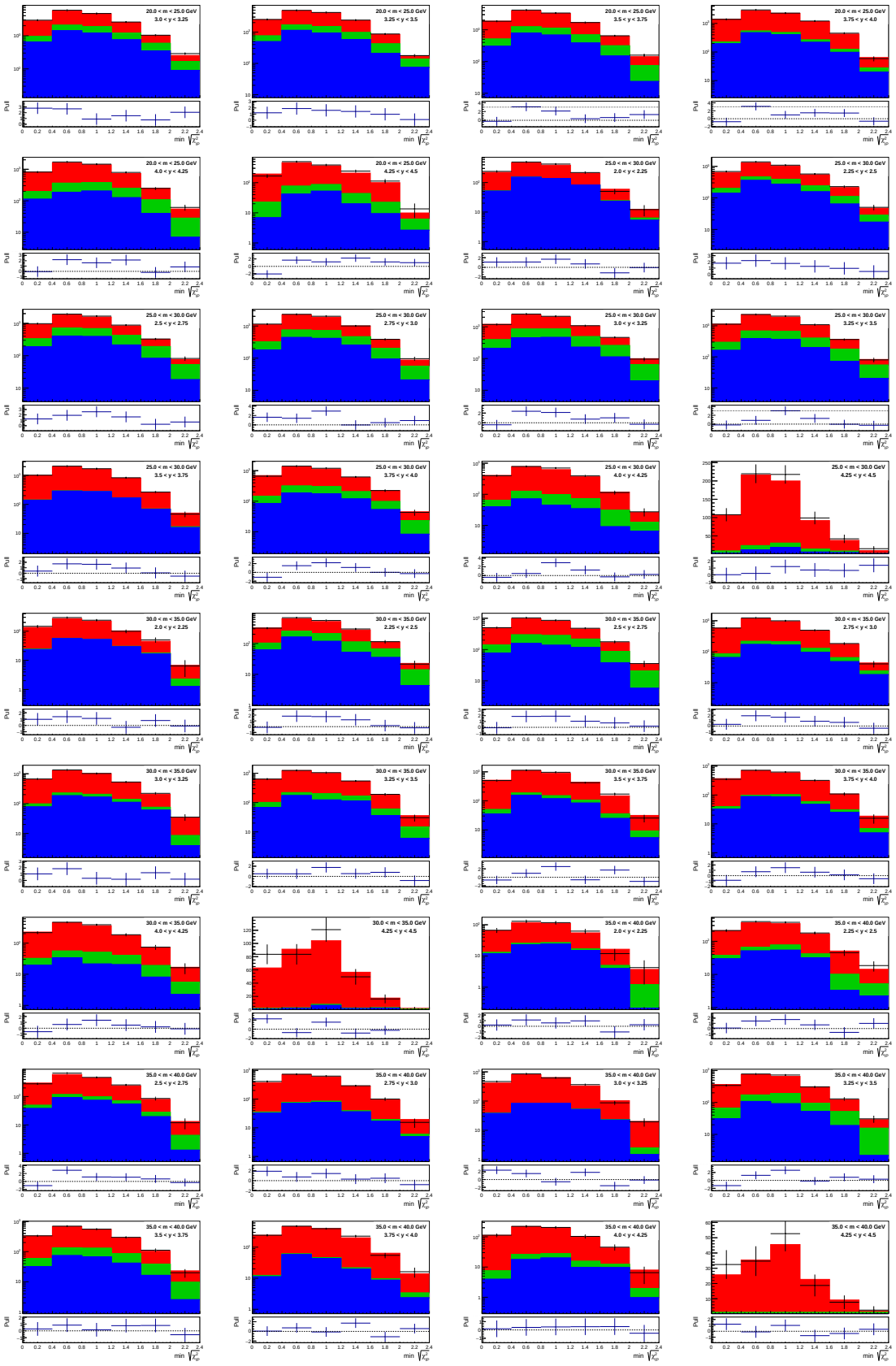
20.0 < m < 25.0 GeV
3.0 < y < 3.25
20.0 < m < 25.0 GeV
3.25 < y < 3.5
20.0 < m < 25.0 GeV
3.5 < y < 3.75
20.0 < m < 25.0 GeV
3.75 < y < 4.0
20.0 < m < 25.0 GeV
4.0 < y < 4.25
20.0 < m < 25.0 GeV
4.25 < y < 4.5
25.0 < m < 30.0 GeV
2.0 < y < 2.25
25.0 < m < 30.0 GeV
2.25 < y < 2.5
25.0 < m < 30.0 GeV
2.5 < y < 2.75
25.0 < m < 30.0 GeV
2.75 < y < 3.0
25.0 < m < 30.0 GeV
3.0 < y < 3.25
25.0 < m < 30.0 GeV
3.25 < y < 3.5
25.0 < m < 30.0 GeV
3.5 < y < 3.75
25.0 < m < 30.0 GeV
3.75 < y < 4.0
25.0 < m < 30.0 GeV
4.0 < y < 4.25
25.0 < m < 30.0 GeV
4.25 < y < 4.5
30.0 < m < 35.0 GeV
2.0 < y < 2.25
30.0 < m < 35.0 GeV
2.25 < y < 2.5
30.0 < m < 35.0 GeV
2.5 < y < 2.75
30.0 < m < 35.0 GeV
2.75 < y < 3.0
30.0 < m < 35.0 GeV
3.0 < y < 3.25
30.0 < m < 35.0 GeV
3.25 < y < 3.5
30.0 < m < 35.0 GeV
3.5 < y < 3.75
30.0 < m < 35.0 GeV
3.75 < y < 4.0
30.0 < m < 35.0 GeV
4.0 < y < 4.25
30.0 < m < 35.0 GeV
4.25 < y < 4.5
35.0 < m < 40.0 GeV
2.0 < y < 2.25
35.0 < m < 40.0 GeV
2.25 < y < 2.5
35.0 < m < 40.0 GeV
2.5 < y < 2.75
35.0 < m < 40.0 GeV
2.75 < y < 3.0
35.0 < m < 40.0 GeV
3.0 < y < 3.25
35.0 < m < 40.0 GeV
3.25 < y < 3.5
35.0 < m < 40.0 GeV
3.5 < y < 3.75
35.0 < m < 40.0 GeV
3.75 < y < 4.0
35.0 < m < 40.0 GeV
4.0 < y < 4.25
35.0 < m < 40.0 GeV
4.25 < y < 4.5
Pull
min $\sqrt{\chi^2_{ip}}$

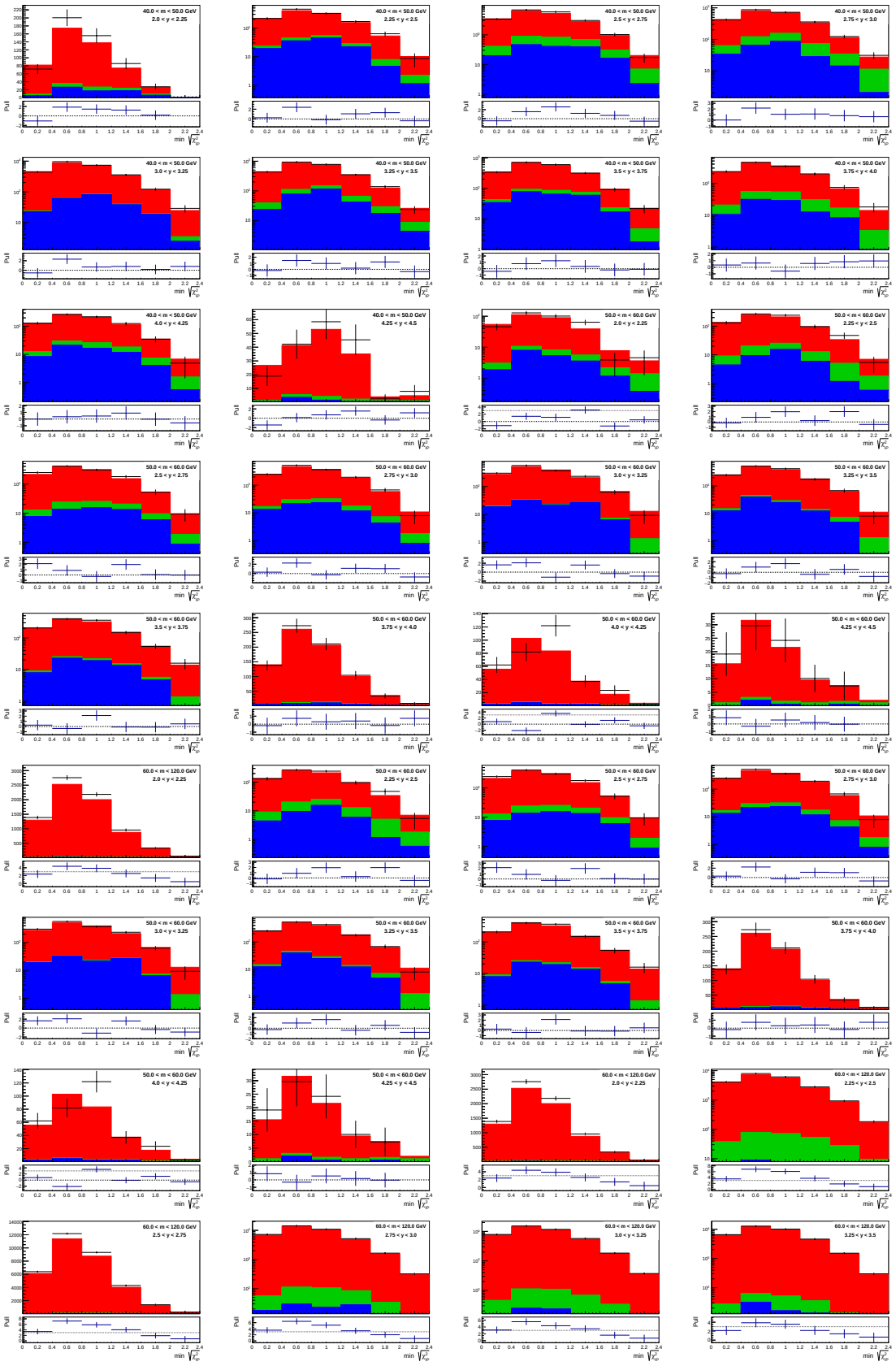
40.0 < m < 50.0 GeV
2.0 < y < 2.25
40.0 < m < 50.0 GeV
2.25 < y < 2.5
40.0 < m < 50.0 GeV
2.5 < y < 2.75
40.0 < m < 50.0 GeV
2.75 < y < 3.0
40.0 < m < 50.0 GeV
3.0 < y < 3.25
40.0 < m < 50.0 GeV
3.25 < y < 3.5
40.0 < m < 50.0 GeV
3.5 < y < 3.75
40.0 < m < 50.0 GeV
3.75 < y < 4.0
40.0 < m < 50.0 GeV
4.0 < y < 4.25
40.0 < m < 50.0 GeV
4.25 < y < 4.5
50.0 < m < 60.0 GeV
2.0 < y < 2.25
50.0 < m < 60.0 GeV
2.25 < y < 2.5
50.0 < m < 60.0 GeV
2.5 < y < 2.75
50.0 < m < 60.0 GeV
2.75 < y < 3.0
50.0 < m < 60.0 GeV
3.0 < y < 3.25
50.0 < m < 60.0 GeV
3.25 < y < 3.5
50.0 < m < 60.0 GeV
3.5 < y < 3.75
50.0 < m < 60.0 GeV
3.75 < y < 4.0
50.0 < m < 60.0 GeV
4.0 < y < 4.25
50.0 < m < 60.0 GeV
4.25 < y < 4.5
60.0 < m < 120.0 GeV
2.0 < y < 2.25
50.0 < m < 60.0 GeV
2.25 < y < 2.5
50.0 < m < 60.0 GeV
2.5 < y < 2.75
50.0 < m < 60.0 GeV
2.75 < y < 3.0
50.0 < m < 60.0 GeV
3.0 < y < 3.25
50.0 < m < 60.0 GeV
3.25 < y < 3.5
50.0 < m < 60.0 GeV
3.5 < y < 3.75
50.0 < m < 60.0 GeV
3.75 < y < 4.0
50.0 < m < 60.0 GeV
4.0 < y < 4.25
50.0 < m < 60.0 GeV
4.25 < y < 4.5
60.0 < m < 120.0 GeV
2.0 < y < 2.25
60.0 < m < 120.0 GeV
2.25 < y < 2.5
60.0 < m < 120.0 GeV
2.5 < y < 2.75
60.0 < m < 120.0 GeV
2.75 < y < 3.0
60.0 < m < 120.0 GeV
3.0 < y < 3.25
60.0 < m < 120.0 GeV
3.25 < y < 3.5
Pull
min $\sqrt{\chi^2_{ip}}$

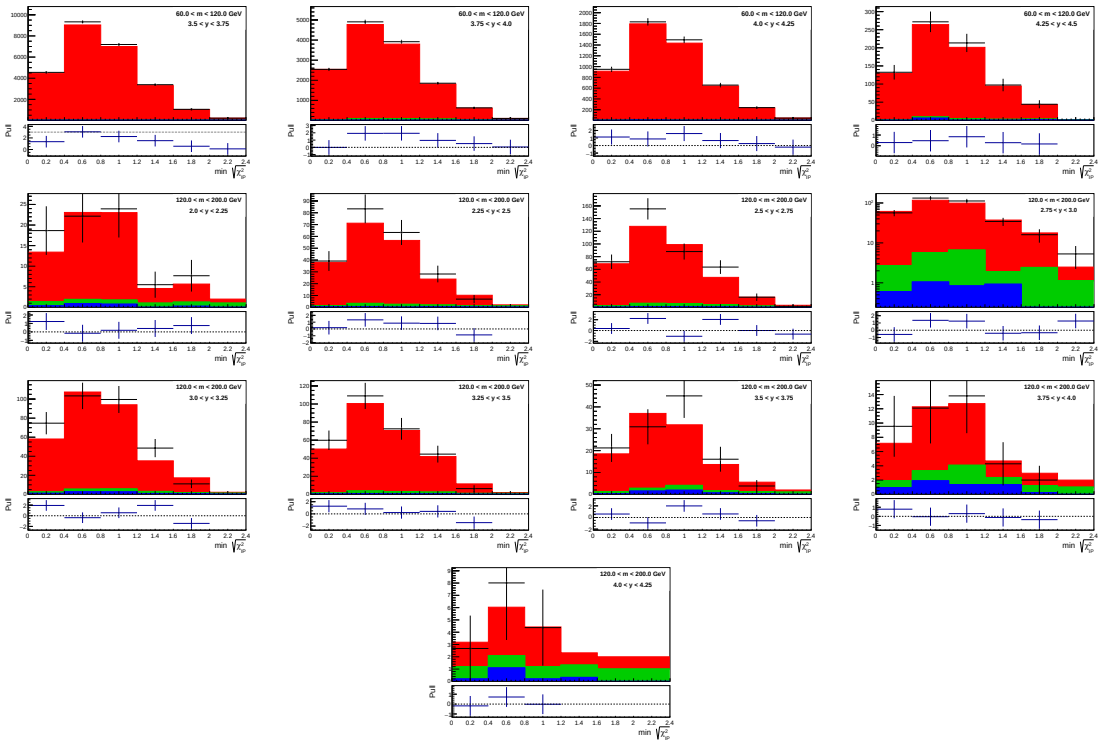

Fits in Bins of Dimuon Mass and Transverse Momentum

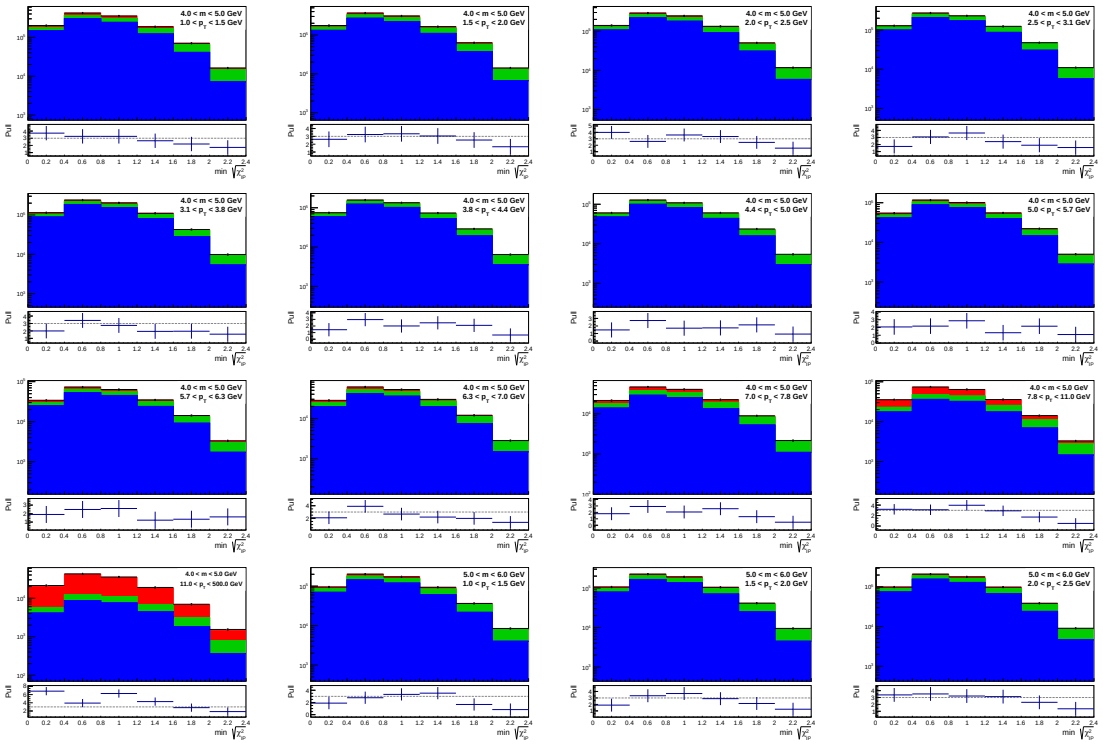

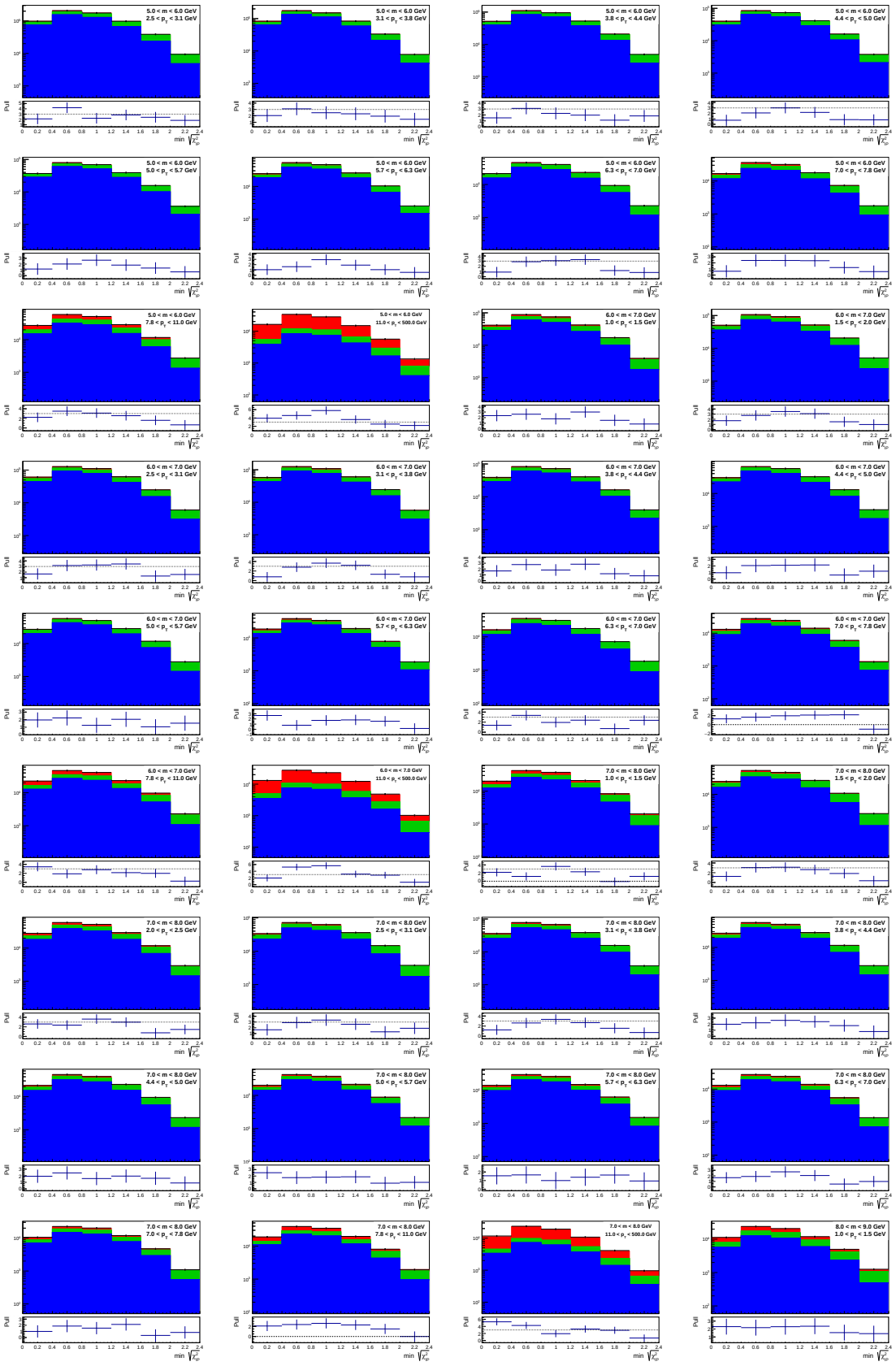
5.0 < m < 6.0 GeV
2.5 < p_T < 3.1 GeV
5.0 < m < 6.0 GeV
3.1 < p_T < 3.8 GeV
5.0 < m < 6.0 GeV
3.8 < p_T < 4.4 GeV
5.0 < m < 6.0 GeV
4.4 < p_T < 5.0 GeV
5.0 < m < 6.0 GeV
5.0 < p_T < 5.7 GeV
5.0 < m < 6.0 GeV
5.7 < p_T < 6.3 GeV
5.0 < m < 6.0 GeV
6.3 < p_T < 7.0 GeV
5.0 < m < 6.0 GeV
7.0 < p_T < 7.8 GeV
5.0 < m < 6.0 GeV
7.8 < p_T < 11.0 GeV
5.0 < m < 6.0 GeV
11.0 < p_T < 500.0 GeV
6.0 < m < 7.0 GeV
1.0 < p_T < 1.5 GeV
6.0 < m < 7.0 GeV
1.5 < p_T < 2.0 GeV
6.0 < m < 7.0 GeV
2.5 < p_T < 3.1 GeV
6.0 < m < 7.0 GeV
3.1 < p_T < 3.8 GeV
6.0 < m < 7.0 GeV
3.8 < p_T < 4.4 GeV
6.0 < m < 7.0 GeV
4.4 < p_T < 5.0 GeV
6.0 < m < 7.0 GeV
5.0 < p_T < 5.7 GeV
6.0 < m < 7.0 GeV
5.7 < p_T < 6.3 GeV
6.0 < m < 7.0 GeV
6.3 < p_T < 7.0 GeV
6.0 < m < 7.0 GeV
7.0 < p_T < 7.8 GeV
6.0 < m < 7.0 GeV
7.8 < p_T < 11.0 GeV
6.0 < m < 7.0 GeV
11.0 < p_T < 500.0 GeV
7.0 < m < 8.0 GeV
1.0 < p_T < 1.5 GeV
7.0 < m < 8.0 GeV
1.5 < p_T < 2.0 GeV
7.0 < m < 8.0 GeV
2.0 < p_T < 2.5 GeV
7.0 < m < 8.0 GeV
2.5 < p_T < 3.1 GeV
7.0 < m < 8.0 GeV
3.1 < p_T < 3.8 GeV
7.0 < m < 8.0 GeV
3.8 < p_T < 4.4 GeV
7.0 < m < 8.0 GeV
4.4 < p_T < 5.0 GeV
7.0 < m < 8.0 GeV
5.0 < p_T < 5.7 GeV
7.0 < m < 8.0 GeV
5.7 < p_T < 6.3 GeV
7.0 < m < 8.0 GeV
6.3 < p_T < 7.0 GeV
7.0 < m < 8.0 GeV
7.0 < p_T < 7.8 GeV
7.0 < m < 8.0 GeV
7.8 < p_T < 11.0 GeV
7.0 < m < 8.0 GeV
11.0 < p_T < 500.0 GeV
8.0 < m < 9.0 GeV
1.0 < p_T < 1.5 GeV
Pull
min $\sqrt{\chi^2_{ip}}$

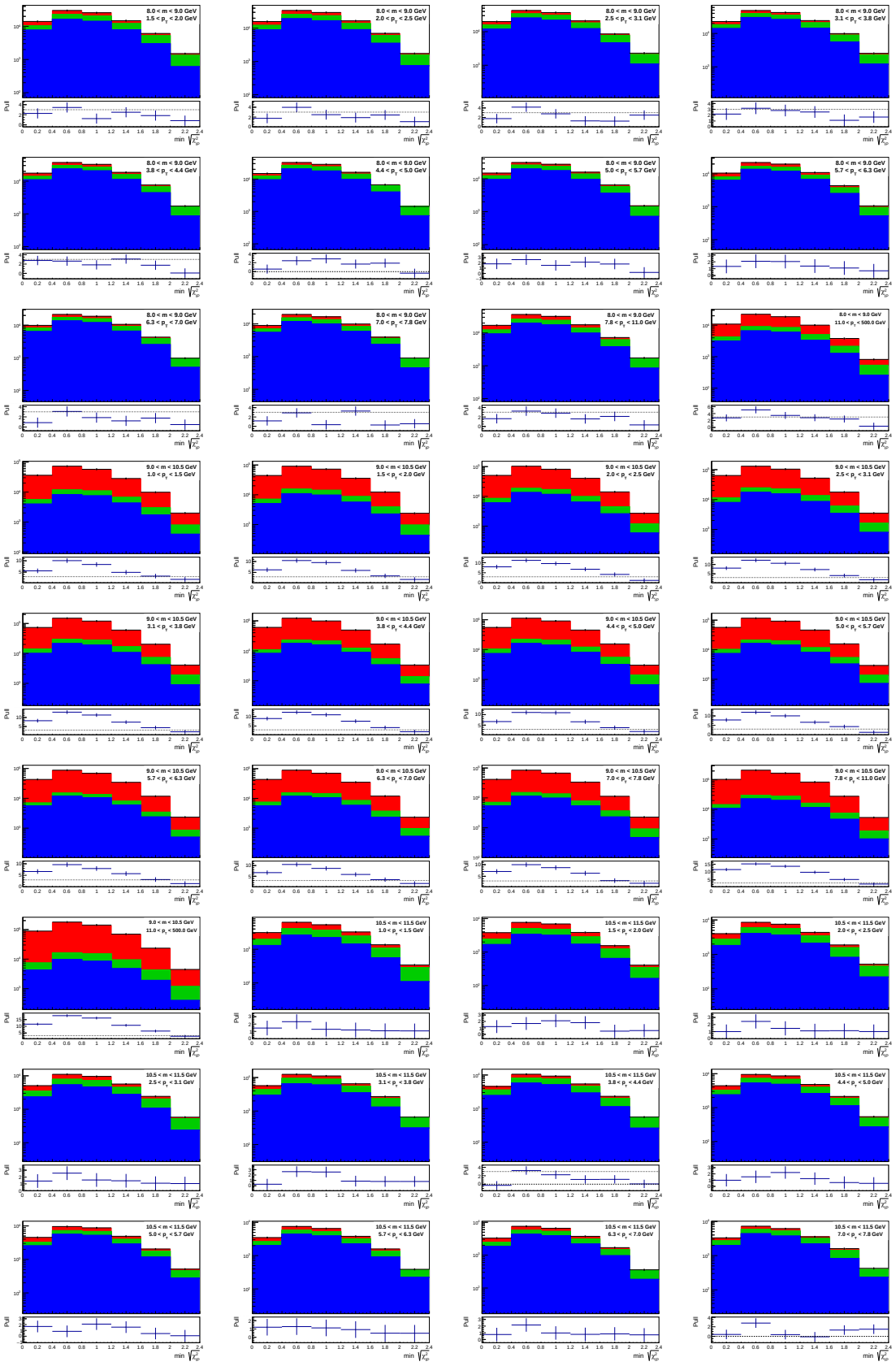
8.0 < m < 9.0 GeV
1.5 < p_t < 2.0 GeV
8.0 < m < 9.0 GeV
2.0 < p_t < 2.5 GeV
8.0 < m < 9.0 GeV
2.5 < p_t < 3.1 GeV
8.0 < m < 9.0 GeV
3.1 < p_t < 3.8 GeV
8.0 < m < 9.0 GeV
3.8 < p_t < 4.4 GeV
8.0 < m < 9.0 GeV
4.4 < p_t < 5.0 GeV
8.0 < m < 9.0 GeV
5.0 < p_t < 5.7 GeV
8.0 < m < 9.0 GeV
5.7 < p_t < 6.3 GeV
8.0 < m < 9.0 GeV
6.3 < p_t < 7.0 GeV
8.0 < m < 9.0 GeV
7.0 < p_t < 7.8 GeV
8.0 < m < 9.0 GeV
7.8 < p_t < 11.0 GeV
8.0 < m < 9.0 GeV
11.0 < p_t < 500.0 GeV
9.0 < m < 10.5 GeV
1.0 < p_t < 1.5 GeV
9.0 < m < 10.5 GeV
1.5 < p_t < 2.0 GeV
9.0 < m < 10.5 GeV
2.0 < p_t < 2.5 GeV
9.0 < m < 10.5 GeV
2.5 < p_t < 3.1 GeV
9.0 < m < 10.5 GeV
3.1 < p_t < 3.8 GeV
9.0 < m < 10.5 GeV
3.8 < p_t < 4.4 GeV
9.0 < m < 10.5 GeV
4.4 < p_t < 5.0 GeV
9.0 < m < 10.5 GeV
5.0 < p_t < 5.7 GeV
9.0 < m < 10.5 GeV
5.7 < p_t < 6.3 GeV
9.0 < m < 10.5 GeV
6.3 < p_t < 7.0 GeV
9.0 < m < 10.5 GeV
7.0 < p_t < 7.8 GeV
9.0 < m < 10.5 GeV
7.8 < p_t < 11.0 GeV
9.0 < m < 10.5 GeV
11.0 < p_t < 500.0 GeV
10.5 < m < 11.5 GeV
1.0 < p_t < 1.5 GeV
10.5 < m < 11.5 GeV
1.5 < p_t < 2.0 GeV
10.5 < m < 11.5 GeV
2.0 < p_t < 2.5 GeV
10.5 < m < 11.5 GeV
2.5 < p_t < 3.1 GeV
10.5 < m < 11.5 GeV
3.1 < p_t < 3.8 GeV
10.5 < m < 11.5 GeV
3.8 < p_t < 4.4 GeV
10.5 < m < 11.5 GeV
4.4 < p_t < 5.0 GeV
10.5 < m < 11.5 GeV
5.0 < p_t < 5.7 GeV
10.5 < m < 11.5 GeV
5.7 < p_t < 6.3 GeV
10.5 < m < 11.5 GeV
6.3 < p_t < 7.0 GeV
10.5 < m < 11.5 GeV
7.0 < p_t < 7.8 GeV
Pull
min $\sqrt{\chi^2_{ip}}$

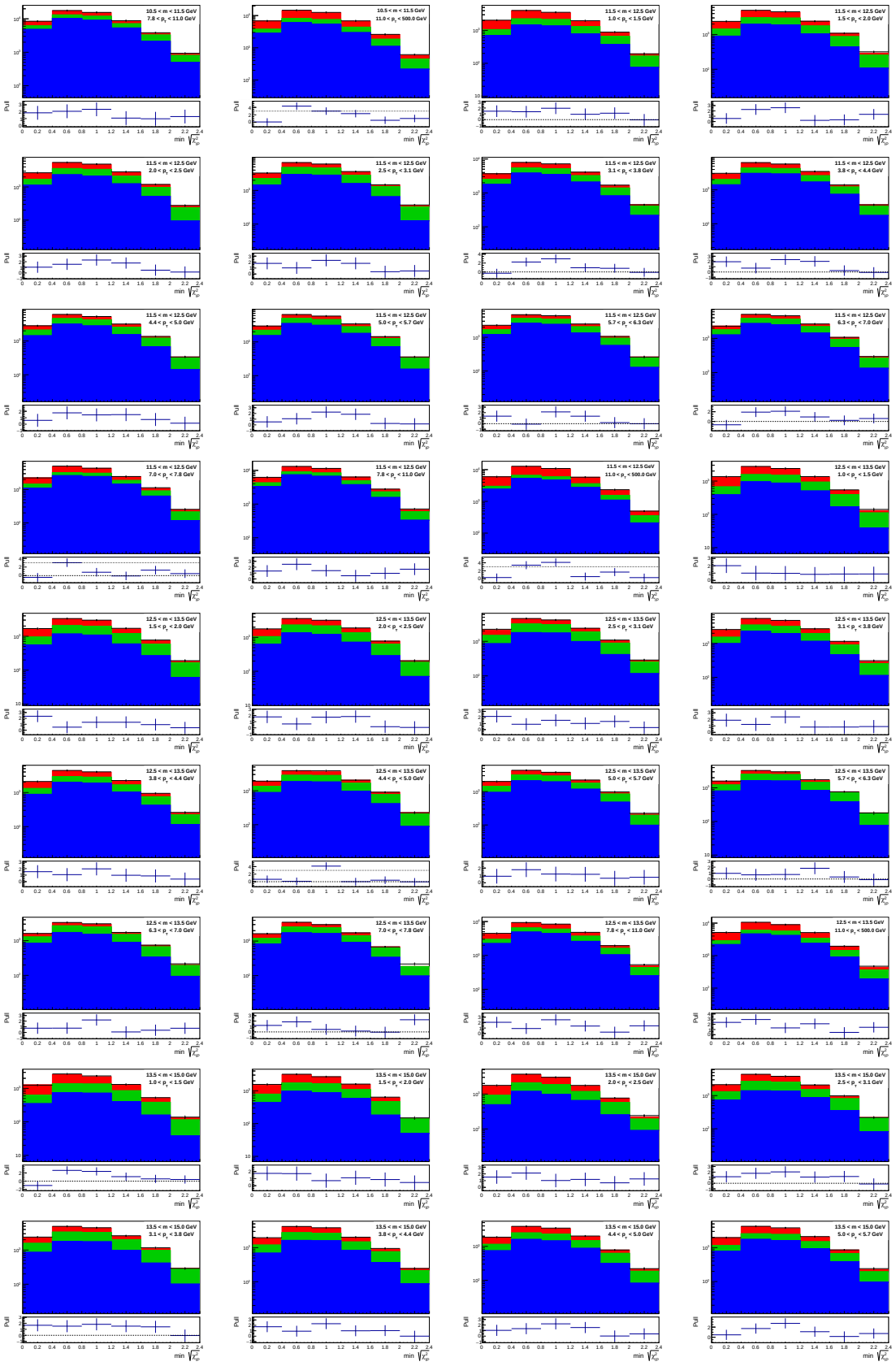
10.5 < m < 11.5 GeV
7.8 < p_T < 11.0 GeV
10.5 < m < 11.5 GeV
11.0 < p_T < 500.0 GeV
11.5 < m < 12.5 GeV
1.0 < p_T < 1.5 GeV
11.5 < m < 12.5 GeV
1.5 < p_T < 2.0 GeV
11.5 < m < 12.5 GeV
2.0 < p_T < 2.5 GeV
11.5 < m < 12.5 GeV
2.5 < p_T < 3.1 GeV
11.5 < m < 12.5 GeV
3.1 < p_T < 3.8 GeV
11.5 < m < 12.5 GeV
3.8 < p_T < 4.4 GeV
11.5 < m < 12.5 GeV
4.4 < p_T < 5.0 GeV
11.5 < m < 12.5 GeV
5.0 < p_T < 5.7 GeV
11.5 < m < 12.5 GeV
5.7 < p_T < 6.3 GeV
11.5 < m < 12.5 GeV
6.3 < p_T < 7.0 GeV
11.5 < m < 12.5 GeV
7.0 < p_T < 7.8 GeV
11.5 < m < 12.5 GeV
7.8 < p_T < 11.0 GeV
11.5 < m < 12.5 GeV
11.0 < p_T < 500.0 GeV
12.5 < m < 13.5 GeV
1.0 < p_T < 1.5 GeV
12.5 < m < 13.5 GeV
1.5 < p_T < 2.0 GeV
12.5 < m < 13.5 GeV
2.0 < p_T < 2.5 GeV
12.5 < m < 13.5 GeV
2.5 < p_T < 3.1 GeV
12.5 < m < 13.5 GeV
3.1 < p_T < 3.8 GeV
12.5 < m < 13.5 GeV
3.8 < p_T < 4.4 GeV
12.5 < m < 13.5 GeV
4.4 < p_T < 5.0 GeV
12.5 < m < 13.5 GeV
5.0 < p_T < 5.7 GeV
12.5 < m < 13.5 GeV
5.7 < p_T < 6.3 GeV
12.5 < m < 13.5 GeV
6.3 < p_T < 7.0 GeV
12.5 < m < 13.5 GeV
7.0 < p_T < 7.8 GeV
12.5 < m < 13.5 GeV
7.8 < p_T < 11.0 GeV
12.5 < m < 13.5 GeV
11.0 < p_T < 500.0 GeV
13.5 < m < 15.0 GeV
1.0 < p_T < 1.5 GeV
13.5 < m < 15.0 GeV
1.5 < p_T < 2.0 GeV
13.5 < m < 15.0 GeV
2.0 < p_T < 2.5 GeV
13.5 < m < 15.0 GeV
2.5 < p_T < 3.1 GeV
13.5 < m < 15.0 GeV
3.1 < p_T < 3.8 GeV
13.5 < m < 15.0 GeV
3.8 < p_T < 4.4 GeV
13.5 < m < 15.0 GeV
4.4 < p_T < 5.0 GeV
13.5 < m < 15.0 GeV
5.0 < p_T < 5.7 GeV
Pull
min $\sqrt{\chi^2_{ip}}$

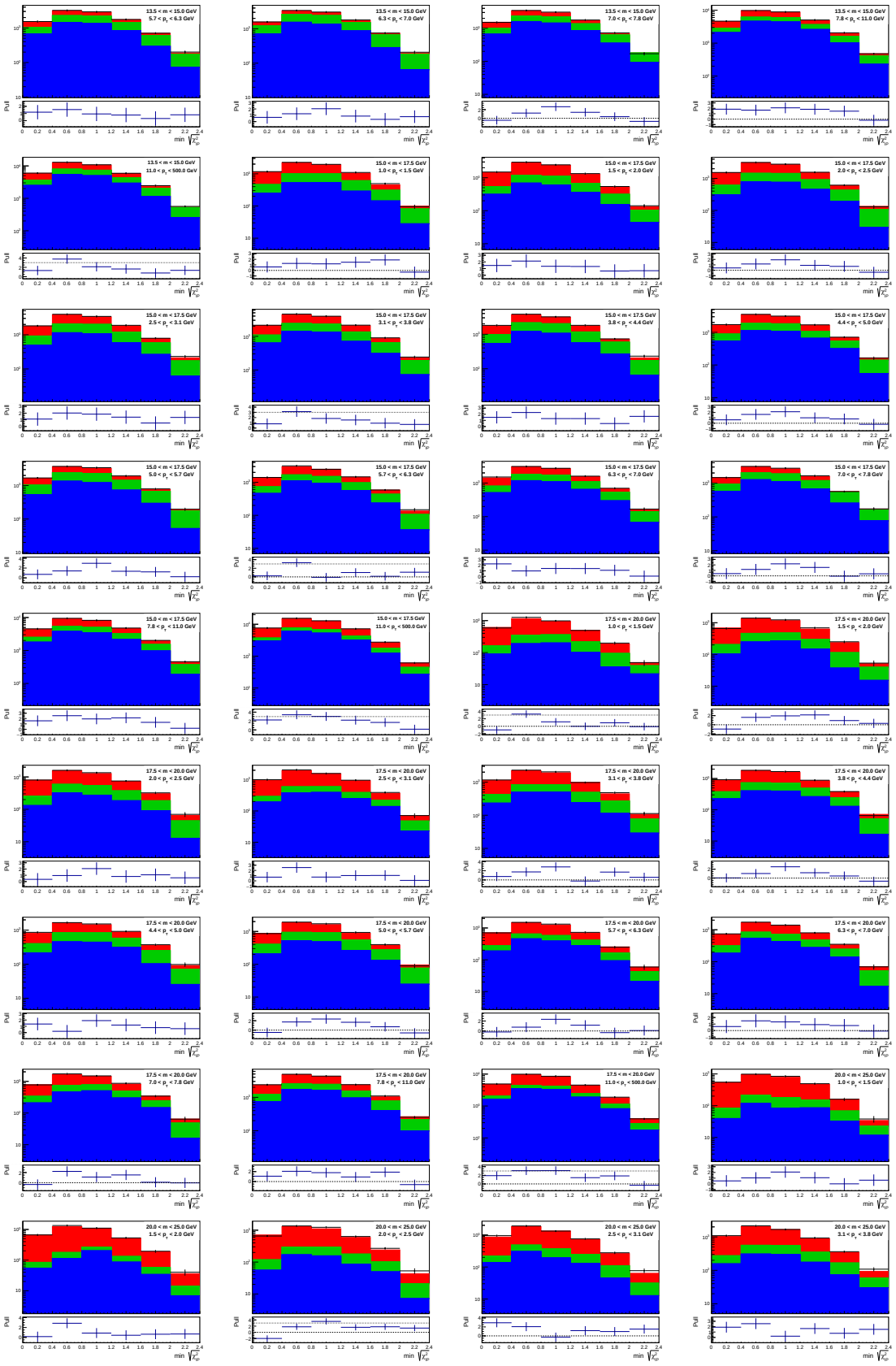
13.5 < m < 15.0 GeV
5.7 < p_t < 6.3 GeV
13.5 < m < 15.0 GeV
6.3 < p_t < 7.0 GeV
13.5 < m < 15.0 GeV
7.0 < p_t < 7.8 GeV
13.5 < m < 15.0 GeV
7.8 < p_t < 11.0 GeV
13.5 < m < 15.0 GeV
11.0 < p_t < 500.0 GeV
15.0 < m < 17.5 GeV
1.0 < p_t < 1.5 GeV
15.0 < m < 17.5 GeV
1.5 < p_t < 2.0 GeV
15.0 < m < 17.5 GeV
2.0 < p_t < 2.5 GeV
15.0 < m < 17.5 GeV
2.5 < p_t < 3.1 GeV
15.0 < m < 17.5 GeV
3.1 < p_t < 3.8 GeV
15.0 < m < 17.5 GeV
3.8 < p_t < 4.4 GeV
15.0 < m < 17.5 GeV
4.4 < p_t < 5.0 GeV
15.0 < m < 17.5 GeV
5.0 < p_t < 5.7 GeV
15.0 < m < 17.5 GeV
5.7 < p_t < 6.3 GeV
15.0 < m < 17.5 GeV
6.3 < p_t < 7.0 GeV
15.0 < m < 17.5 GeV
7.0 < p_t < 7.8 GeV
15.0 < m < 17.5 GeV
7.8 < p_t < 11.0 GeV
15.0 < m < 17.5 GeV
11.0 < p_t < 500.0 GeV
17.5 < m < 20.0 GeV
1.0 < p_t < 1.5 GeV
17.5 < m < 20.0 GeV
1.5 < p_t < 2.0 GeV
17.5 < m < 20.0 GeV
2.0 < p_t < 2.5 GeV
17.5 < m < 20.0 GeV
2.5 < p_t < 3.1 GeV
17.5 < m < 20.0 GeV
3.1 < p_t < 3.8 GeV
17.5 < m < 20.0 GeV
3.8 < p_t < 4.4 GeV
17.5 < m < 20.0 GeV
4.4 < p_t < 5.0 GeV
17.5 < m < 20.0 GeV
5.0 < p_t < 5.7 GeV
17.5 < m < 20.0 GeV
5.7 < p_t < 6.3 GeV
17.5 < m < 20.0 GeV
6.3 < p_t < 7.0 GeV
17.5 < m < 20.0 GeV
7.0 < p_t < 7.8 GeV
17.5 < m < 20.0 GeV
7.8 < p_t < 11.0 GeV
17.5 < m < 20.0 GeV
11.0 < p_t < 500.0 GeV
20.0 < m < 25.0 GeV
1.0 < p_t < 1.5 GeV
20.0 < m < 25.0 GeV
1.5 < p_t < 2.0 GeV
20.0 < m < 25.0 GeV
2.0 < p_t < 2.5 GeV
20.0 < m < 25.0 GeV
2.5 < p_t < 3.1 GeV
20.0 < m < 25.0 GeV
3.1 < p_t < 3.8 GeV
Pull
min $\sqrt{\chi^2_{ip}}$

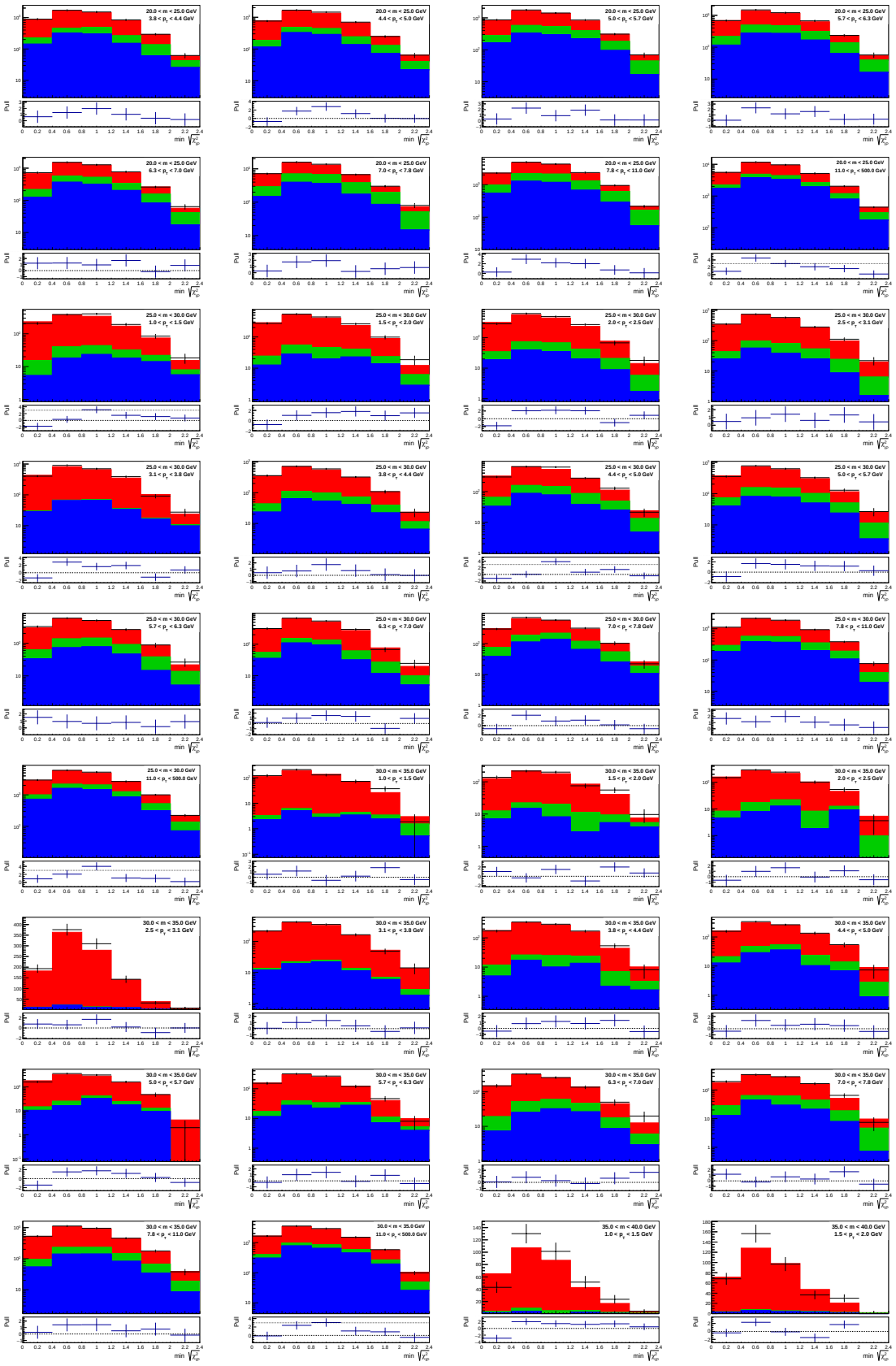
20.0 < m < 25.0 GeV
3.8 < p_t < 4.4 GeV
20.0 < m < 25.0 GeV
4.4 < p_t < 5.0 GeV
20.0 < m < 25.0 GeV
5.0 < p_t < 5.7 GeV
20.0 < m < 25.0 GeV
5.7 < p_t < 6.3 GeV
20.0 < m < 25.0 GeV
6.3 < p_t < 7.0 GeV
20.0 < m < 25.0 GeV
7.0 < p_t < 7.8 GeV
20.0 < m < 25.0 GeV
7.8 < p_t < 11.0 GeV
20.0 < m < 25.0 GeV
11.0 < p_t < 500.0 GeV
25.0 < m < 30.0 GeV
1.0 < p_t < 1.5 GeV
25.0 < m < 30.0 GeV
1.5 < p_t < 2.0 GeV
25.0 < m < 30.0 GeV
2.0 < p_t < 2.5 GeV
25.0 < m < 30.0 GeV
2.5 < p_t < 3.1 GeV
25.0 < m < 30.0 GeV
3.1 < p_t < 3.8 GeV
25.0 < m < 30.0 GeV
3.8 < p_t < 4.4 GeV
25.0 < m < 30.0 GeV
4.4 < p_t < 5.0 GeV
25.0 < m < 30.0 GeV
5.0 < p_t < 5.7 GeV
25.0 < m < 30.0 GeV
5.7 < p_t < 6.3 GeV
25.0 < m < 30.0 GeV
6.3 < p_t < 7.0 GeV
25.0 < m < 30.0 GeV
7.0 < p_t < 7.8 GeV
25.0 < m < 30.0 GeV
7.8 < p_t < 11.0 GeV
25.0 < m < 30.0 GeV
11.0 < p_t < 500.0 GeV
30.0 < m < 35.0 GeV
1.0 < p_t < 1.5 GeV
30.0 < m < 35.0 GeV
1.5 < p_t < 2.0 GeV
30.0 < m < 35.0 GeV
2.0 < p_t < 2.5 GeV
30.0 < m < 35.0 GeV
2.5 < p_t < 3.1 GeV
30.0 < m < 35.0 GeV
3.1 < p_t < 3.8 GeV
30.0 < m < 35.0 GeV
3.8 < p_t < 4.4 GeV
30.0 < m < 35.0 GeV
4.4 < p_t < 5.0 GeV
30.0 < m < 35.0 GeV
5.0 < p_t < 5.7 GeV
30.0 < m < 35.0 GeV
5.7 < p_t < 6.3 GeV
30.0 < m < 35.0 GeV
6.3 < p_t < 7.0 GeV
30.0 < m < 35.0 GeV
7.0 < p_t < 7.8 GeV
30.0 < m < 35.0 GeV
7.8 < p_t < 11.0 GeV
30.0 < m < 35.0 GeV
11.0 < p_t < 500.0 GeV
35.0 < m < 40.0 GeV
1.0 < p_t < 1.5 GeV
35.0 < m < 40.0 GeV
1.5 < p_t < 2.0 GeV
Pull
min √χ²_ip

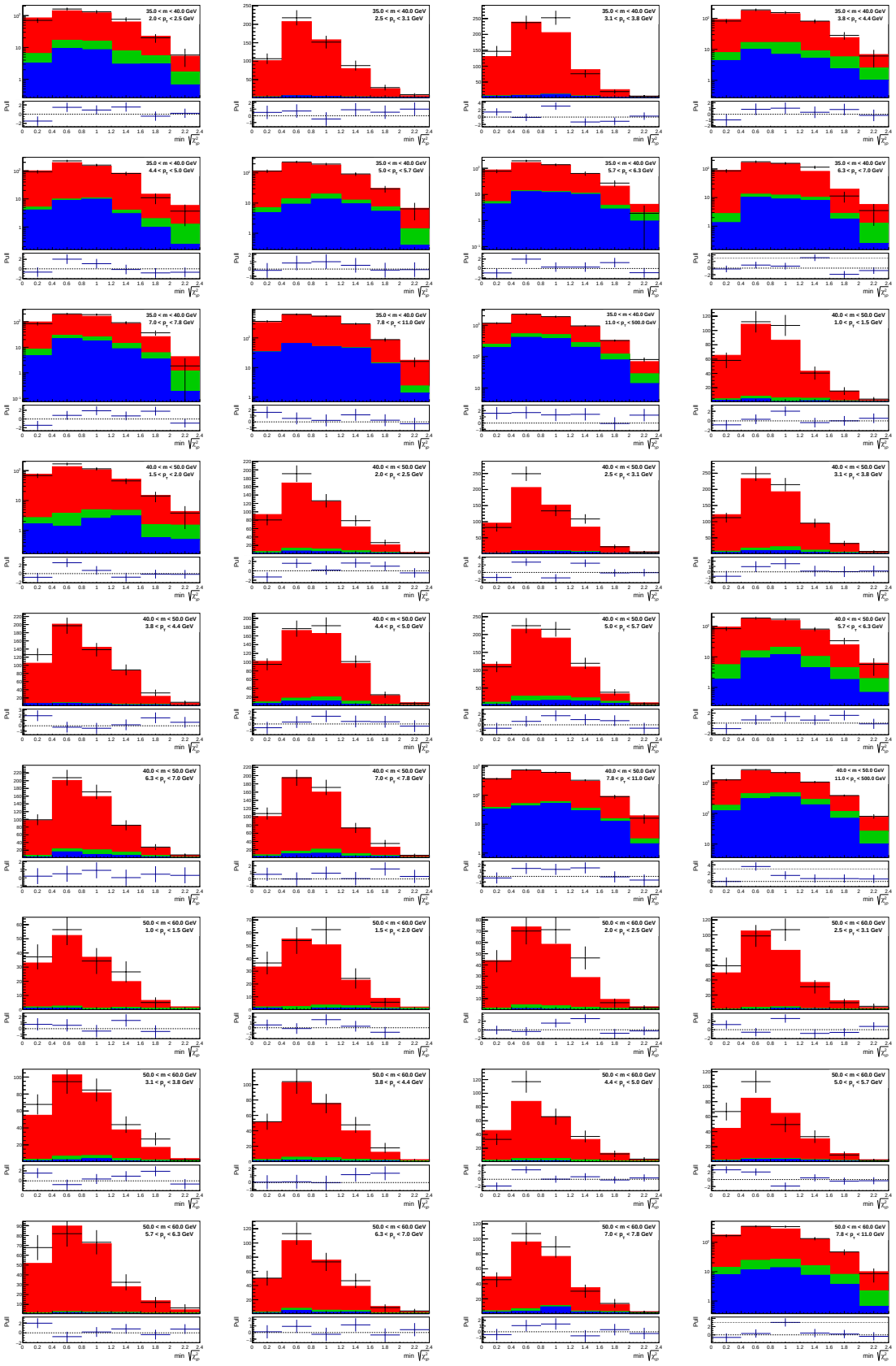
35.0 < m < 40.0 GeV
2.0 < p_t < 2.5 GeV
35.0 < m < 40.0 GeV
2.5 < p_t < 3.1 GeV
35.0 < m < 40.0 GeV
3.1 < p_t < 3.8 GeV
35.0 < m < 40.0 GeV
3.8 < p_t < 4.4 GeV
35.0 < m < 40.0 GeV
4.4 < p_t < 5.0 GeV
35.0 < m < 40.0 GeV
5.0 < p_t < 5.7 GeV
35.0 < m < 40.0 GeV
5.7 < p_t < 6.3 GeV
35.0 < m < 40.0 GeV
6.3 < p_t < 7.0 GeV
35.0 < m < 40.0 GeV
7.0 < p_t < 7.8 GeV
35.0 < m < 40.0 GeV
7.8 < p_t < 11.0 GeV
35.0 < m < 40.0 GeV
11.0 < p_t < 500.0 GeV
40.0 < m < 50.0 GeV
1.0 < p_t < 1.5 GeV
40.0 < m < 50.0 GeV
1.5 < p_t < 2.0 GeV
40.0 < m < 50.0 GeV
2.0 < p_t < 2.5 GeV
40.0 < m < 50.0 GeV
2.5 < p_t < 3.1 GeV
40.0 < m < 50.0 GeV
3.1 < p_t < 3.8 GeV
40.0 < m < 50.0 GeV
3.8 < p_t < 4.4 GeV
40.0 < m < 50.0 GeV
4.4 < p_t < 5.0 GeV
40.0 < m < 50.0 GeV
5.0 < p_t < 5.7 GeV
40.0 < m < 50.0 GeV
5.7 < p_t < 6.3 GeV
40.0 < m < 50.0 GeV
6.3 < p_t < 7.0 GeV
40.0 < m < 50.0 GeV
7.0 < p_t < 7.8 GeV
40.0 < m < 50.0 GeV
7.8 < p_t < 11.0 GeV
40.0 < m < 50.0 GeV
11.0 < p_t < 500.0 GeV
50.0 < m < 60.0 GeV
1.0 < p_t < 1.5 GeV
50.0 < m < 60.0 GeV
1.5 < p_t < 2.0 GeV
50.0 < m < 60.0 GeV
2.0 < p_t < 2.5 GeV
50.0 < m < 60.0 GeV
2.5 < p_t < 3.1 GeV
50.0 < m < 60.0 GeV
3.1 < p_t < 3.8 GeV
50.0 < m < 60.0 GeV
3.8 < p_t < 4.4 GeV
50.0 < m < 60.0 GeV
4.4 < p_t < 5.0 GeV
50.0 < m < 60.0 GeV
5.0 < p_t < 5.7 GeV
50.0 < m < 60.0 GeV
5.7 < p_t < 6.3 GeV
50.0 < m < 60.0 GeV
6.3 < p_t < 7.0 GeV
50.0 < m < 60.0 GeV
7.0 < p_t < 7.8 GeV
50.0 < m < 60.0 GeV
7.8 < p_t < 11.0 GeV
Pull
min $\sqrt{\chi^2_{ip}}$

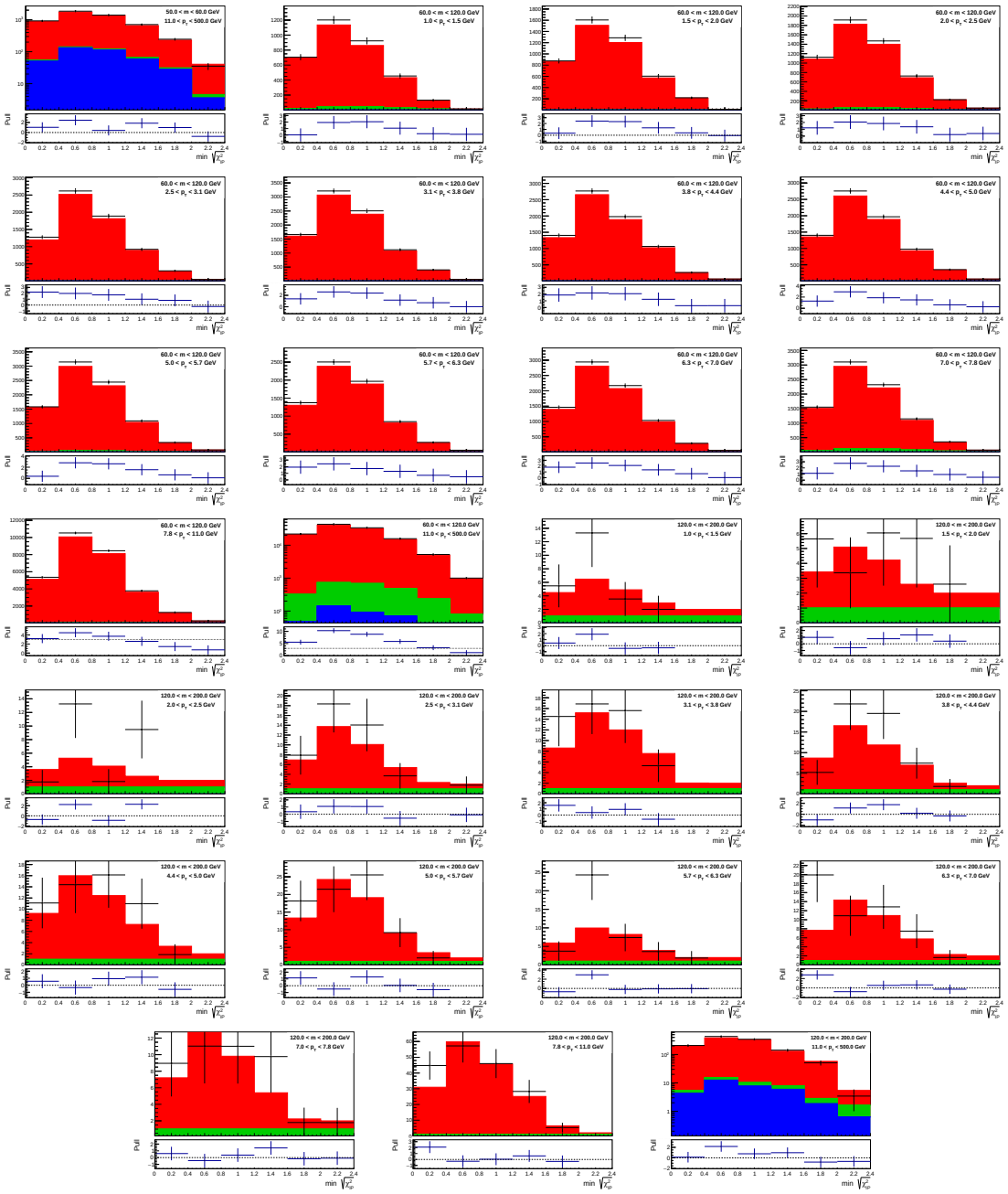
50.0 < m < 60.0 GeV
11.0 < p_t < 500.0 GeV
60.0 < m < 120.0 GeV
1.0 < p_t < 1.5 GeV
60.0 < m < 120.0 GeV
1.5 < p_t < 2.0 GeV
60.0 < m < 120.0 GeV
2.0 < p_t < 2.5 GeV
60.0 < m < 120.0 GeV
2.5 < p_t < 3.1 GeV
60.0 < m < 120.0 GeV
3.1 < p_t < 3.8 GeV
60.0 < m < 120.0 GeV
3.8 < p_t < 4.4 GeV
60.0 < m < 120.0 GeV
4.4 < p_t < 5.0 GeV
60.0 < m < 120.0 GeV
5.0 < p_t < 5.7 GeV
60.0 < m < 120.0 GeV
5.7 < p_t < 6.3 GeV
60.0 < m < 120.0 GeV
6.3 < p_t < 7.0 GeV
60.0 < m < 120.0 GeV
7.0 < p_t < 7.8 GeV
60.0 < m < 120.0 GeV
7.8 < p_t < 11.0 GeV
60.0 < m < 120.0 GeV
11.0 < p_t < 500.0 GeV
120.0 < m < 200.0 GeV
1.0 < p_t < 1.5 GeV
120.0 < m < 200.0 GeV
1.5 < p_t < 2.0 GeV
120.0 < m < 200.0 GeV
2.0 < p_t < 2.5 GeV
120.0 < m < 200.0 GeV
2.5 < p_t < 3.1 GeV
120.0 < m < 200.0 GeV
3.1 < p_t < 3.8 GeV
120.0 < m < 200.0 GeV
3.8 < p_t < 4.4 GeV
120.0 < m < 200.0 GeV
4.4 < p_t < 5.0 GeV
120.0 < m < 200.0 GeV
5.0 < p_t < 5.7 GeV
120.0 < m < 200.0 GeV
5.7 < p_t < 6.3 GeV
120.0 < m < 200.0 GeV
6.3 < p_t < 7.0 GeV
120.0 < m < 200.0 GeV
7.0 < p_t < 7.8 GeV
120.0 < m < 200.0 GeV
7.8 < p_t < 11.0 GeV
120.0 < m < 200.0 GeV
11.0 < p_t < 500.0 GeV
Pull
min √χ²_ip